Multivalent Programmable Interactions Between Lipid Vesicles: Towards Responsive Soft Materials

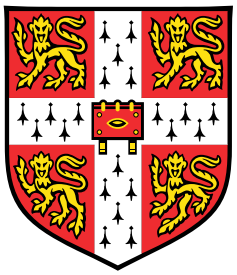

Omar Alexander Amjad

Cavendish Laboratory
University of Cambridge

This dissertation is submitted for the degree of
Doctor of Philosophy

Robinson College July 2019

To Joseph Grand: I empathise....

Declaration

I hereby declare that except where specific reference is made to the work of others, the contents of this dissertation are original and have not been submitted in whole or in part for consideration for any other degree or qualification in this, or any other university. This dissertation is my own work and contains nothing which is the outcome of work done in collaboration with others, except as specified in the text and Acknowledgements. This dissertation contains fewer than 60,000 words including appendices, bibliography, footnotes, tables and equations and has fewer than 150 figures.

Omar Alexander Amjad
July 2019

Acknowledgements

Firstly, I must thank my funding body, the EPSRC and more specifically the CDT for Sensor Technologies and Applications, as well as Robinson College for the financial support to undertake this PhD.

The most obvious and most important thank you must go to my supervisors, Prof. Pietro Cicuta and Dr. Lorenzo Di Michele, without whom none of this would be possible. I am very grateful for their role in my development and the support they have given, which has led to my growth as a scientist.

Within my work, I have been fortunate to have collaborated with and been helped by many other scientists. Within this group I must thank my secondary supervisor, Dr. Alexandre Kabla, Fergus Riche, and Dr. Bortolo Mognetti. A big thank you is needed for my friend Dr. Emma Talbot with whom I took on the dark arts of microfluidics, with some initial instruction from Dr. Jehangir Cama and Kareem Al-Nahas. Finally, a huge thanks to Dr. Lucia Parolini, for my lab-initiation into all things lipid-related, Dr. Jurij Kotar, for assistance with microscopes and hardware, and Dr. Luigi Feriani, for my education in DDM.

Thanks to all my friends from BSS not yet mentioned: Mia, Roberta, Sho, Shun, Will and all the others that have made the last few years so pleasant. A special thank you goes to Viola and Evelyn, for putting up with me in the office, and Alessio and Nicola for putting up with me at home. Finally, I have to thank Ryan for his friendship, help and just sitting next to me pipetting over the last few years.

I also thank the people in Cambridge who've kept me as close to sanity as possible; Jimmy, Rich, Campsie, Miriam, Alma, Dami, Izzy, easy-going Max, the MNDC, and numerous others who for brevity I don't include here, but certainly made life immeasurably richer.

I am very fortunate to have such a wonderful network of people outside of Cambridge to lend perspective and support. In particular I single out Tash and Fred, for their omnipresence

and terrible advice that I do not deserve. Thanks to my brother, Freddy, for always picking up the bill at dinner (it's my turn now) and your unwavering encouragement; and Sami, for being a phenomenal friend and a democratically elected member of our family. Finally, most importantly, and adhering to the expected clichés, I must thank my parents, Margaret and Tariq, for a lifetime of love and support. Nothing I achieve can ever be fully reflective of how much you have put in, but certainly anything of note I have ever done is down to you.

Abstract

Lipid membranes and lipid vesicles have been studied extensively in the last 50 years in order to characterise their biological, chemical and physical properties. Such work is of interest from a fundamental biological perspective, but also due to the applications that their biocompatibility affords: in biotechnological, pharmaceutical, food science and cosmetic applications. From this work, it is clear that lipid membranes display a large number of remarkable traits: they can form a wide range of sizes and morphologies, are deformable and can be functionalised with a variety of structures.

More recently, multivalent interactions have been exploited to drive self-assembly of nanoparticles, hard colloids and compliant units including emulsion droplets and lipid vesicles. By applying this to deformable lipid vesicles, formation of links between two membranes produces morphological changes unachievable in hard colloidal systems, and the liquid interface of liquid-phase bilayers allows for the diffusion of the multivalent constructs across the membrane of the lipid vesicle.

Against this background of membrane science and multivalent interactions, this thesis develops new experimental approaches to exploit these extra degrees of freedom to develop novel lipid-based soft responsive materials with potential 'real-world' applications, such as in molecular sensing. In Chapter 1, the motivations for this work are introduced, before introducing the requisite background literature and general experimental techniques in Chapters 2 and 3 respectively.

In Chapter 4 we show a system of single lipid vesicles adhering to a flat supported lipid bilayer through multimeric multivalent interactions, which we study to characterise the morphological and mechanical changes of the vesicles in response to external ligands. We show that the mechanical properties of the vesicles, in particular their membrane tension, change dramatically on adhesion, and that the number of adhering vesicles is dependent on the concentration of the external ligand due to combinatorial entropy, which we confirm

through consideration of a simple statistical mechanical model.

In Chapter 5 we use Differential Dynamic Microscopy to study the dynamics of a thermoreversible gel consisting of diffusive attractive soft colloids (large unimlamellar vesicles functionalised with complementary DNA constructs), and fit the dynamics with a stretched/compressed exponential model. From the fit parameters, we observe differing levels of spatial heterogeniety of the dynamics of the sample within different regimes below, above and around the gel/melting points, as well as differing length scales of the dynamics, which differ between quenching and melting experiments. From the statics and dynamics, we see evidence for multiple phenomena, including coarsening as well as ballistic events corresponding to strand breakages.

In Chapter 6 we propose a method for high-throughput vesicle production. We characterise the method and the vesicles produced, as well as demonstrating novel applications, most notably the high-throughput production of vesicles encapsulating responsive DNA circuitry, highlighting the potential of this method in bottom-up synthetic biology and the design of programmable materials. Furthermore, we demonstrate the possibility of on-chip functionalisation of membrane constructs into the lipid membranes, in this case cholesterol-anchored DNA constructs.

In Chapter 7 we study dense packings of vesicles assembled using multivalent complementary DNA interactions, through passive tracking of diffusive colloidal particles and active microrheology using magnetic tweezers. We observe changes in the structure in response to increased temperature, DNA concentration and aging leading to reduced pore sizes. From a rheological standpoint, we observe strain hardening of the material through repeated creep tests, with the ability to reset the material by increasing the temperature above the melting point of the system. The material stiffens and becomes more viscous, which we observe through the application of a constitutive and fractional rheological model respectively.

In this thesis we demonstrate the responsiveness of these multivalent construct functionalised lipid vesicle based soft materials by showing the ability to tune the structure, rheology and dynamics of such materials, as well as proposing a method for high throughput, monodisperse production of functionalised lipid vesicles. These results lead to further potential avenues of research, and demonstrate suitability for and preliminary steps towards applications of these responsive materials in fields such as molecular sensing.

Table of contents

Chapter 1

Introduction

1.1 Motivations

Over the last 200 years, a deep understanding of the biological, chemical and physical properties of lipids and lipid membranes has been accumulated through research motivated by applications in food science, consumer products, medicine and a fundamental understanding of biological systems [1–3]. From this work, it is clear that lipid membranes display a large number of remarkable traits: they can form a wide range of sizes and morphologies, are deformable and can have a variety of embedded structures within them [4, 5]. In biological systems, the richness of these traits is fully visible; of particular interest is the use of multivalent adhesion between cells, which mediates a number of events, including cell-sorting, migration, invasion and fusion [6–8].

Multivalent adhesion has been exploited in artificial systems; in particular, colloidal systems where adhesion is driven by selective interactions, often using synthetic DNA tethers, whose selective and reversible binding enables a fine control over the resultant multivalent interactions [9–11]. Despite the remarkable control over the structure of these materials, examples of phases exhibiting morphological response to external stimuli are limited. Existing approaches often rely on precisely engineered reactions between competing linkages that can be achieved only using synthetic DNA tethers, and are hardly applicable with naturally occurring linkers.

Here, biological systems offer inspiration; deformable sub-units (cells) adhering through multivalent interactions can respond to a range of external stimuli. Strong enough multivalent interactions cause significant deformation, and this can be observed in artificial systems when the functionalised particles become sufficiently soft; such as with emulsion droplets

and particularly lipid vesicles [5, 12, 13]. Therefore, in artificial self-assembled phases, the morphology can respond dramatically to small changes in the adhesion strength or the stiffness of the particles. This is independent of the details of the ligands. Large morphological variations allow for a specific and strong, nonlinear, amplification of external signals. These morphological changes can be observed optically, mechanically or through impedance measurements, enabling their transduction into an easily detectable response: these are major advantages for analytical sensing. The study of the physical properties of lipid-based self-assembled systems is of particular interest owing to their analogy with biological cells, providing a model to study cell and tissue morphology and rheology. Furthermore, such work can have implications on the study of compartmentalisation and therefore application to the fields of synthetic biology, nanoreactors, nanofiltration, and drug delivery. Finally, such systems are also of interest more fundamentally as a novel soft matter system.

In this thesis we present work on the bottom-up design and study of novel soft materials utilising lipid vesicles functionalised with multivalent constructs that mediate specific adhesion. We study the sensing properties of these materials, and the responsiveness to stimuli of different scale networks of vesicles through different methods, elucidating their fundamental physical properties, as well as presenting a microfluidic method of producing lipid vesicles. This work can be seen as fundamental to the study of such responsive materials, as well as the first step towards applications in sensing technologies of articial lipid-based phases.

1.2 Thesis Summary

In Chapter 2 we review and introduce the concepts of lipid structures, multivalency, microfluidics, gels and granular materials in order to contextualise this work. In Chapter 3 we introduce some heavily employed experimental techniques, with a brief background on the methods. In Chapter 4 we show a system of lipid vesicles adhering to a flat supported lipid bilayer through multivalent interactions, which we study to characterise the morphological and mechanical changes of the vesicles in response to external ligands, and propose this as a proof-of-concept biosensing system. In Chapter 5 we use Differential Dynamic Microscopy to study the dynamics of a thermoreversible gel consisting of diffusive attractive soft colloids (large unimlamellar vesicles functionalised with complementary DNA constructs), allowing probing of the spatial heterogeniety of the samples, and the time, temperature and q-mode dependency. In Chapter 6 we propose a method for high-throughput vesicle production. We characterise the method and the vesicles produced, as well as introducing some prelimi-

nary experiments, most notably the high-throughput production of vesicles encapsulating responsive DNA circuitry, highlighting the potential of this method in bottom-up synthetic biology and the design of programmable materials. In Chapter 7 we study dense packings of polydisperse GUVs assembled using multivalent complementary DNA interactions, through passive tracking of diffusive colloidal particles and active microrheology (the use of magnetic tweezers). This allowed for both the characterisation of the material for its use in artificial systems, as well as gaining insight through this biomimetic tissue into the physical, non-active mechanisms underlying the rheology of biological tissues. Finally in Chapter 8, we summarise our key findings, and propose future avenues of exploration on the back of this work.

Chapter 2

Design and Properties of Self-Assembled Soft Materials: A Background

In this chapter, we present a background to the multivalent adhesion mediated lipid-vesicle based soft materials on which this thesis is focused, from the scale of lipids to the properties of the biomimetic tissues they form. Initially, lipid vesicles and their properties will be discussed, specifically to demonstrate their suitability to application as the fundamental sub-unit for programmable soft materials. Multivalent interactions will also be considered, and discussed in the context of driving the formation of functional materials through mediating the self-assembly of soft subunits. Particular attention is paid to the use of DNA as a multivalent linker, due to its frequent use in this work. Gels consisting of colloidal scale sub-units and their dynamics are reviewed to give a background to the behaviour observed in our system in Chapter 5, and an introduction to microfluidics, droplet formation and applications in synthetic biology are also presented to support the work in Chapter 6. We touch upon the rheology of soft materials to contextualise the results in Chapter 7, before finally proposing a few applications and potential further studies for these soft materials, to make clear the long-term motivations of the work undertaken in this thesis.

2.1 Fundamental Concepts: Lipids and Vesicles

2.1.1 Lipids

Lipids have been studied for over 200 years [1], and since then have been extensively researched due to their fundamental structural, signalling and metabolic importance in biological systems [14], as well as applications in drug delivery and medical technologies [2]. Furthermore, lipids have been studied within the context of food science, and indeed in

consumer products such as cosmetics; soaps are lipid based products that have been produced since Babylonian times, and indeed much of the early research into lipid chemistry was driven by the study of saponification [15, 1].

Lipids are a heterogeneous group of hydrophobic or amphiphilic molecules [14]. In the case of amphiphilic lipid molecules such as phospholipids, these are made up of 2 hydrophobic tails and a hydrophilic polar head (Fig. 2.1d) [2]. Due to this amphiphilic nature, in water-oil solutions, lipids align on the interface, stabilising it through minimisation of the interfacial tension, with the hydrophobic tail exposed to the oil phase and the hydrophilic head group exposed to the water [16].

In an aqueous solution, individual lipid molecules are insoluble. Amphiphilic lipids can self-assemble into a variety of structures in order to protect the hydrophobic tails and expose the hydrophilic heads [17]. The clustering of hydrophobic residues together decreases the disruption to the hydrogen bonds between water molecules, which in turn increases the entropy of the system, minimising the free energy, making the self-assembly thermodynamically favourable [17]. As such, these materials represent an interesting sweetspot for applications in nano/microscale engineering of materials as, whilst the energy associated with these self-assembled structures is sufficient to keep them stable, it is also low enough that they are flexible.

2.1.2 Lipid Geometries and Bilayer formation

Self-assembled lipid structures can form a variety of geometries, which can be predicted by the following equation [18]:

$$R_{lipid} = v_0/a_0 l_c, \tag{2.1}$$

where v_0 is the volume of the hydrocarbon chain of the lipid, a_0 is the head group area of the lipid and l_c the critical chain length. This ratio indicates the shape of the lipids, which in turn allows us to consider how they would pack. From Eq. 2.1, it can be predicted as to whether the self-assembled structure would be a spherical micelle, cylindrical micelle, inverted micelle or a bilayer. Bilayers form when R_{lipid}>0.5 and up to when $R_{lipid} \sim$1, when the shape of the lipids is roughly a cylinder [4]. These bilayers are formed with two leaflets, with the hydrophobic tails from both leaflets pointing towards each other in the centre of the bilayer, where the water is excluded, with the hydrophilic heads exposed to the aqueous

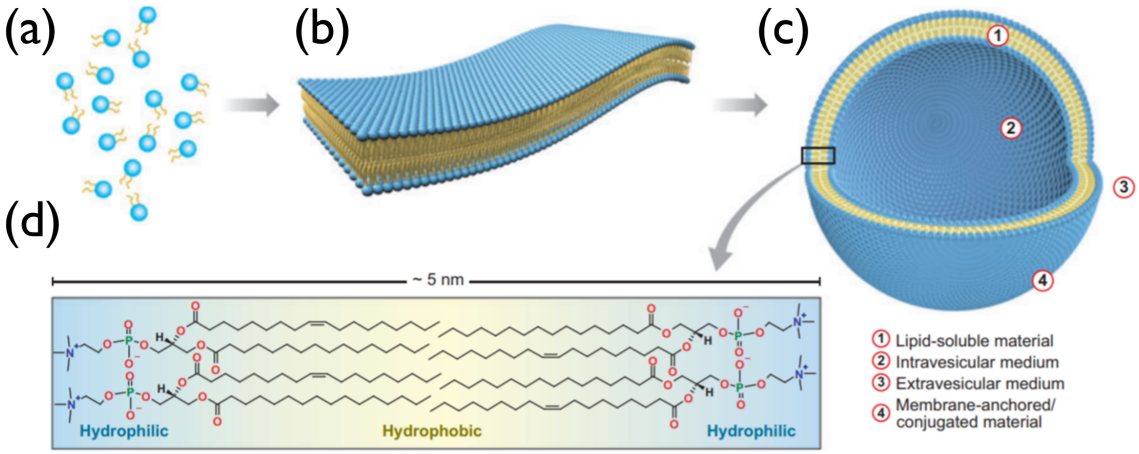

Fig. 2.1 The self-assembly process from (a) individual phospholipid molecules to (b) a bilayer membrane and (c) transformation into lipid vesicles. We show that (d) a single bilayer is typically $\sim$ 5 nm thick and consists of individual lipid molecules arranged with their hydrophobic tails facing each other and their hydrophilic headgroups facing toward the internal and external aqueous medium. Bilayers can consist of saturated and unsaturated lipids (as can be seen by the abscence or prescence of a double bond respectively), and consist of lipids with different headgroups conferring different properties. This image is adapted from [2].

phase (Fig. 2.1).

In a bilayer consisting of one lipid species, the short length scale behaviour is dictated by the phase behaviour of the bilayer. Below the melting temperature of the bilayer, it exists in a gel phase, whereas above this temperature a liquid phase occurs, and in this phase the bilayer can be thought of as fluid over short length scales as the lipids can diffuse within the bilayer [19]. Over longer length scales the bilayer behaves like an elastic membrane.

Bilayers can exist as 2D sheets, however in some conditions it is energetically favourable for the bilayer to bend and form a closed spherical structure at the cost of some bending energy but removing the energetic cost of the edges (Fig. 2.1b & 2.1c) [4]. Such a closed spherical bilayer is known as vesicle. Vesicles can be either multilamellar (several lamellar phase lipid bilayers creating an "onion"-like structure) or unilamellar (consisting of a single lipid bilayer) [20]. Unilamellar vesicles can exist at a range of sizes and are characterised as either Giant Unilamellar Vesicles (GUVs) with a size >1 µm, Large Unilamellar Vesicles (LUVs) with a size between 0.1-1 µm or Small Unilamellar Vesicles (SUVs) with a size <0.1 µm [20, 21].

As stated in Section 2.1.1, lipid structures, and more specifically vesicles, represent an exciting sub-unit for nanotechnology. However, there are further reasons vesicles are of keen interest to the wider scientific community: artificial lipid vesicles represent a fantastic model system for the fundamental study of lipid membranes and membrane bound proteins [3]. Additionally, vesicles are used for the study of compartmentalisation, and therefore have applications to the fields of synthetic biology, nanoreactors, nanofiltration and drug delivery [22–24].

2.1.3 Lipid Phases in Mixtures

The most simple composition for a lipid bilayer is one consisting of a single type of lipid. However, in biological systems this is not the case, and more pertinently to the applications of this work, the formation of vesicles with multiple types of lipids can lead to interesting properties that can be exploited in the design of programmable materials. Whilst phase separation is only briefly touched upon in this thesis, an understanding is helpful to appreciate fully the potential applications of the systems described here.

The effects on the partitioning and fluidity of a mixed lipid composition membrane relies on the differing chemical bonds (either fully or partially saturated) in the hydrocarbon tail groups and the chain length of the tail itself [25]. In particular saturated and unsaturated species can be seen to undergo demixing from a single phase at a high temperature, to phase separation below a critical temperature, with the formation of phase separated lipid "domains" [26, 25]. By choosing sufficiently well spaced melting temperatures of the saturated/unsaturated lipids gel-liquid coexistence and, with the addition of cholesterol to the lipid mix, liquid-liquid phase coexistence can be observed [27]. In the liquid-liquid coexistence case there is a disordered, L_d, and an ordered, L_o, phase. Different types of membrane bound structures, such as protein-receptors, cholesterol-anchored molecular constructs or dyes partition preferentially into different such domains. By controlling the patterning of the membrane with different domains [28], it is therefore possible to create functionalised vesicles where membrane bound constructs can be spatially constrained in regions of the bilayer.

2.1.4 Membrane Deformations

Much of the interest of lipid membranes in this work focuses on their ability to deform, which in turn is due to the energy associated with such structures being sufficient to keep them stable, but also low enough that they are flexible, and here we will consider the energetic costs of these deformations in a simple manner, as shown in Ref. [29].

Firstly we consider the behaviour within the confines of classic elasticity theory. However we find that, when the membrane is fluid (as in liquid phases), it does not support shear deformations as it can flow. It does, however, stretch and we can find the energy associated with stretching a membrane, $E_{stretch}$ with initial area A_0 to an area of $A>A_0$ given as

$$E_{Stretch} = \frac{1}{2} K_{stretch} \frac{(A - A_0)^2}{A_0}, \tag{2.2}$$

where $K_{stretch}$ is the stretching modulus. From Equation 2.2, we find the derivative of energy with respect to area, the lateral stress or tension, σ, to be

$$\sigma := \frac{\delta E_{Stretch}}{\delta A} := K_{Stretch} \frac{(A - A_0)}{A_0} := K_{Stretch} u, \tag{2.3}$$

where u is the dimensionless strain, $\frac{(A-A_0)}{A_0}$. Hence we have found Hooke's law for membrane stretching. Micropipette aspiration has been used to confirm this linear stress-strain relationship, and find the $K_{Stretch}$ of a phospholipid membrane to be around 250 mN/m, however membranes tend to rupture at only a few mN/m and therefore are not particularly stretchable [30].

In the limit of longer length scales, the thickness of the membrane becomes negligible to the area of the surface, and as such this can be considered as a 2D plane that can be bent into the third dimension. Considering the membrane as a thin sheet, such as in the case of paper, it is intuitive to imagine that, upon bending the inner leaflet will be under some compression, the outer will be stretched. We consider the membrane as elastic and then sum up the stretching energy contributions across the membrane section and get an expression for the bending energy density e_{bend},

$$e_{bend} = \frac{1}{2} \kappa \frac{1}{R^2}, \tag{2.4}$$

where

$$\kappa = \frac{1}{48} K_{stretch} h^2. \tag{2.5}$$

κ is the bending modulus, $K_{stretch}$ is the stretching modulus, R is the radius of curvature and h the membrane thickness. This is merely a simplified model but captures some key insights, including the dependency of κ on h. We find the bending modulus of lipid membranes to be tens of $k_B T$; large enough they are stable and do not break apart due to the "thermal breeze" but not so much bigger than thermal energy that they cannot be easily deformed [31].

2.1.5 Membrane Adhesion

The energy of the interactions between a membrane and a surface (or another membrane) is governed by generic features of adhesion, which locally suppress membrane undulations, reduce curvature, and modify tension, which result in the following interaction energy equation [32]:

$$U = U_{adh} + U_{str} + U_{und} + U_{bend}, \tag{2.6}$$

where U is interaction free energy, U_{adh} is the adhesion energy, U_{str} is the elastic stretching energy, U_{und} is the energy required to suppress thermally-induced shape fluctuations and U_{bend} is the bending energy. By setting $U_{adh} = 0$ in Eq. 2.6, we arrive at the shape equation for a free vesicle [33]. In the limit of strong adhesion, where U_{bend} and U_{und} are negligible, vesicles form spherical caps on adhesion, analogous to that in the Young-Dupré limit for droplets [34]:

$$U = K_a \frac{(A - \tilde{A})^2}{\tilde{A}} - A_f |W_p^{(0)}|, \tag{2.7}$$

where A is the final area of the bilayer, $\tilde{A}$ the unstretched area of the bilayer, A_f is the area of planar contact and $|W_p^{(0)}|$ is the adhesion potential [32]. Despite the positive stretching energy, with strong adhesion, it is energetically favourable for the vesicles to adhere [34]. From the minimisation of U shown here and using equations for volumes of both the non-adhering and adhering (spherical) cap geometries, and constraints on the vesicle's volume,

we can obtain the equilibrium contact angle of an adhering vesicle.

In the limit of strong adhesion $|W_p^{(0)}|$ is related to the lateral tension σ via the Young-Dupré equation, $|W_p^{(0)}| = \sigma(1 + cos\theta_{eff})$, where θ_{eff} is the effective contact angle [33]. Therefore if contact potential exceeds a threshold value of σ, this will lead to vesicle rupture and the closed sphere geometry will become a disk-like membrane segment [33]. Another possibility for vesicles experiencing area strain in excess of the characteristic rupture strain of bilayers is membrane fusion; adhesion makes fusion more energetically favourable than in the case of two unbound vesicles [34].

This brief insight shows how the deformability upon adhesion of vesicle based systems allows for configurations and outcomes (e.g fusion) which are impossible with traditional hard colloidal systems, as well as open a variety of opportunities for the design of novel soft materials and “smart” multi-vesicles systems.

2.2 Multivalent Interactions

2.2.1 Multivalency: Definition and Background

Broadly, multivalent interactions can be defined as the interactions between two objects mediated by a large number of linkers or ligand/receptor pairs [35]. Multivalent interactions are ubiquitous in biology and are fundamental to a diverse range of biological processes, such as cell-cell adhesion, cell-sorting, immune response, signal transduction, and tissue dynamics [6]. For example, cadherins, Ca^{2+}-dependent cell adhesion proteins, are found in many types of cell-cell contact regions, including adherens junctions [36]. Furthermore, multivalent interactions are also used for invasion of host cells by bacteria, viruses and parasites [7, 8, 37].

Here, we refer to multivalent ligand/receptor interactions when the particle-bound receptors on two surfaces are unable to bind and form a complex which contributes to adhesion without the presence of an external "bridging" ligand. We refer to linkers where the linkers on the particles simply need to be in proximity to another complementary linker on a different surface to stick to one-another and form an adhesive complex. In addition to the simple cases described above, multimeric linkers and multimeric ligands, where multiple binding sites for complementary linkers or receptor binding sites are present, exist, which leads to different

possible configurations of bridging complexes [38].

The combination of energetic contributions of multiple such non-covalent adhesive complexes allows for a stronger accumulated strength of interaction (avidity) between the entities involved, whilst the individual interactions themselves remain labile [39]. As such, they are exploited in a range of systems, both natural and man-made [37, 11, 40, 9].

Such multivalent interactions have since been shown to be a powerful tool with which to drive the self-assembly of Brownian objects and this method has been adopted to build materials whose local structure would be hard to replicate with top-down manufacturing approaches [11, 40, 9, 41, 10]. Advances in this area have been driven by the use of synthetic DNA tethers as the linkers, a material whose selective and reversible binding enables fine control over the resulting multivalent interactions [42, 43]. Such self-assembled phases have been applied to create materials for molecular diagnostics [44], photonics [45] and potential non-biological self-replicating systems [46]. Despite the remarkable control over these materials' structure, examples of phases displaying morphological response to external stimuli are limited, in part as the Brownian objects used are generally hard colloidal particles or gold nanoparticles, and their responsiveness often relies on precisely engineered reactions between competing linkages that can only be achieved using synthetic DNA tethers and are hardly applicable with naturally occurring linkers [47–49]. This limits the versatility and potential applications of these materials.

2.2.2 Multivalent Interactions between Compliant Substrates

When the particles become sufficiently soft, as for the case of emulsion droplets and particularly lipid vesicles [50, 13, 51–57, 12, 58], strong enough multivalent interactions can cause significant deformation. As a consequence, the morphology of the self-assembled soft phases can respond dramatically to small changes in the adhesion strength or the stiffness of the particles [51, 52]. Furthermore, for vesicles where the interactions bring the adhering membranes to close enough proximity, lipid mixing between the bilayers and fusion can occur, which allows the mixing of the contents of the vesicles [54]. Similarly to the case of hard colloidal particles, in the absence of specific multivalent interactions, there exist a gamut of non-specific interactions that mediate the interactions between soft particles, such as attractive van der Waals and hydrophobic interactions, and repulsive electrostatic and undulation forces, which in turn can lead to adhesion and aggregation under certain conditions. A schematic of adhering lipid vesicles mediated through an arbitrary pair of

complementary adhesive linkers is shown in Fig. 2.2a.

The interaction behaviour of adhering vesicles is also driven by other factors than just the deformability of the membrane, as entropic effects linked to the behaviour of the multivalent linkers themselves contribute significantly [52]. On a particle with a fluid interface, such as liquid-phase lipid bilayer, the multivalent receptors/linkers are free to diffuse and rearrange across the surface of the particle, adding a further degree of freedom to these systems. Additionally, the nature of the linkers or receptor-ligand constructs also drive the interaction of adhering membranes; through the conformational entropy in the case of flexible tethered linker constructs, and the combinatorial entropy (more pronounced with multimeric receptor-ligand systems) [52, 38]. Indeed, the design and associated dynamics of the tethering chains have been shown to strongly affect the strength, range and rate of adhesion [59]. Additionally, interesting interplay between the enthalpy and entropy occurs in these systems. Whilst the deformation of an interface may allow for optimal binding configurations between linkers that is favourable enthalpically, the deformation of the membrane, and suppression of thermal fluctuations, incurs an entropic cost [60].

The ability of the vesicle to deform is independent of the details of the linkers and can therefore be seen as a general means of sensing environmental changes, through the morphological and mechanical changes in lipid vesicles. Given a sufficient number of linkers, one such change is the formation of an adhesive patch. This is an area where adhesive interactions cause the formation of a quasi-flat disc-shaped adhesion patch within which the linkers are confined, leading to a region dense in linkers. Briefly we will consider the nucleation of this process. The sticking linker from one membrane to come in contact with sticking linker from the opposing membrane, allowing the formation of an adhesive bridge [61]. This nucleates the process of adhesion. There is a gain in free energy for the sticking molecules when they enter the contact area and form bridges across to the opposing membrane, thus these molecules will be "recruited" by this membrane and are thus enriched within the contact area [62]. This means that the density of linkers varies within the bound and unbound segments of the membranes. In the case of a vesicle with excess area, the localisation of bridges in close proximity to one another (i.e why a patch forms rather than multiple disparate binding sites) occurs due to the entropic cost of suppressing the fluctuations in the membrane (Fig. 2.2b). For the case of x bridges far away from each other, the membrane fluctuations must be suppressed at each spot, incurring an entropic cost of around w at each spot, where w is the work against the entropic repulsion of the membranes. Clearly, this would therefore incur an entropic cost of xw [63]. On the other hand, it is intuitive that when the two

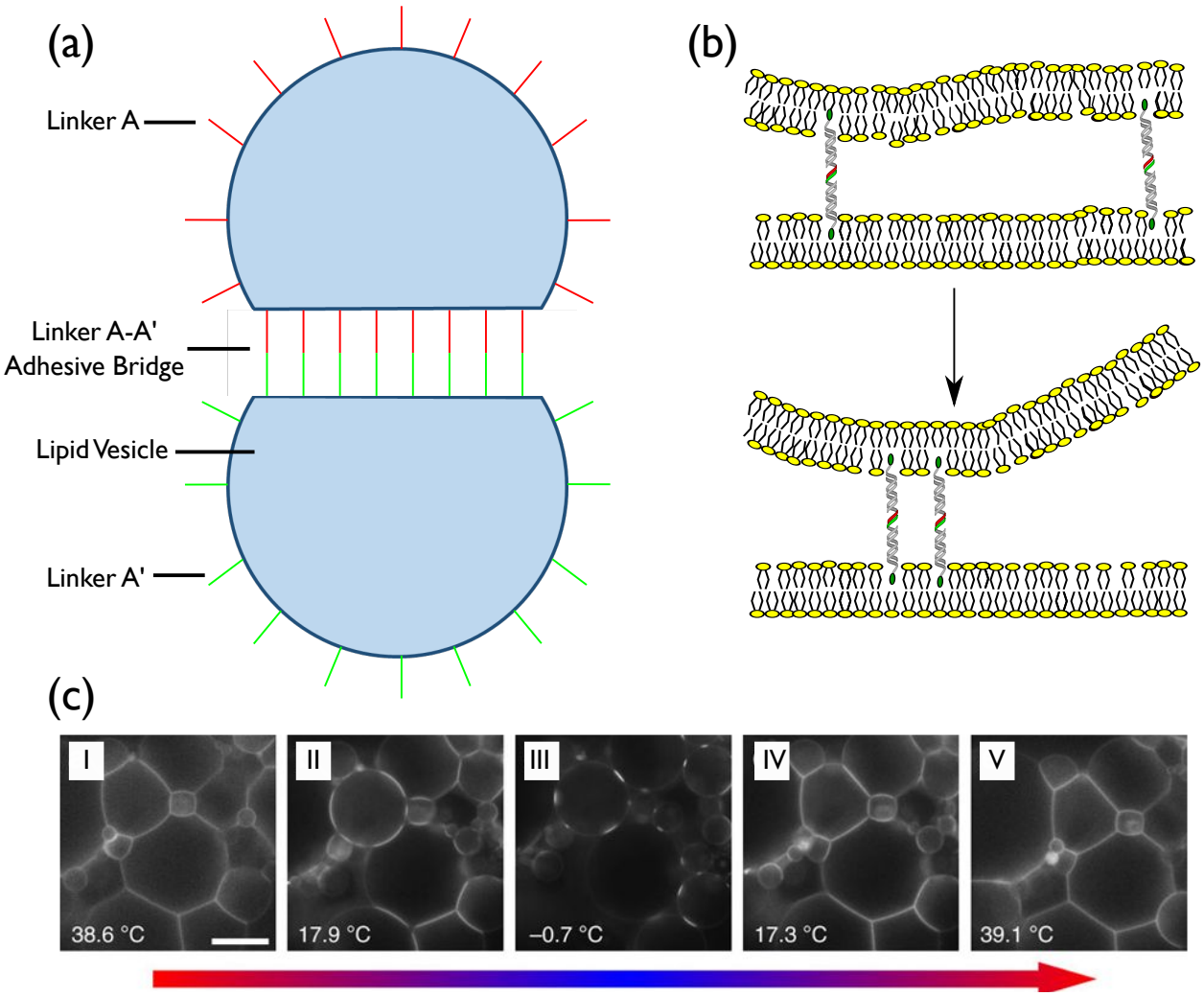

Fig. 2.2 An overview of multivalent adhesion between soft substrates, in this case vesicles, over a range of scales. (a) A schematic of the multivalency of a vesicle, with complementary linkers that can bind, causing adhesion and shape change. (b) Adhesive bridges move in the bilayer, and more specifically (from upper panel to lower panel), to localise close to each other within the adesion patch to minimise the entropic cost of suppressing fluctuations in the membrane. (c) A network of vesicles adhering through multivalent DNA-mediated interactions. As the temperature is cooled (I-III), the vesicles become stiffer and the adhesion patches become smaller, whereas when the temperature increases (III-V) the patches become larger and the packing becomes denser, as the vesicles become less stiff. This is adapted from [52].

membranes are pinned to one another by multiple bridges in close confinement the entropic cost would be $<< xw$. This causes there to be cooperative effects; a denser adhesion patch allows for the smoothing of the thermal roughness of the flexible membrane [64]. Linkers

can also come into contact and bind with complementary linkers on the same membrane; the complexes formed here are called "loops", and do not contribute to inter-vesicle adhesion.

Coupling soft sub-units with multivalent interactions is also of interest from a fundamental biophysical perspective, as vesicles can be considered as model cells in order to study the physics of cell-cell interactions [65]. This is due to their comparable size to cells, and also the potential to create vesicles with similar lipid composition and membrane protein content. Furthermore, vesicles also benefit from a lack of active cellular processes, enabling the effect of the passive multivalent adhesion to be disentangled from active processes, to enable a better understanding of the physical mechanisms of adhesion. Thus they can be used to provide useful insight into the physics of cell and tissue morphology, and could provide model systems to study their rheology [54].

Another application of systems coupling multivalent interactions with deformable sub-units is in the bottom-up construction of tissue-like materials. The use of controllable interactions, coupled with the ability to hold cargo within the particles, unlike with hard colloids, allows for precisely spatially orientated materials in conformations and packing fractions impossible to achieve with hard colloids.

Different interactions mediating compliant sub-unit adhesion will be reviewed in the following subsections, with a particular focus on work coupling the described interactions with lipid vesicles.

2.2.3 Streptavidin-Biotin Interactions

Streptavidin (SA) is a tetrameric protein that provides 4 binding sites for biotin, one pair on either side of the molecule [66]. The interaction between biotin and SA is well studied and, interestingly, the SA-biotin bond is the strongest non-covalent biological interaction known [67, 66]. Additionally, SA does not affect the stability of lipid vesicles [66]. In regards to studies using SA-biotin interactions to mediate adhesion of vesicles and soft substrates, a variety of functionalisation techniques have been employed. These include, but are not limited to, using commercially available lipids grafted with biotinylated PEG or the use of biotinylated DNA strands with cholesterol anchors [68, 38], which will be explained in more detail in Chapter 4.

Avidin-biotin interactions have been previously adopted to study adhesion of colloidal units including emulsion droplets and particularly lipid vesicles, starting with the seminal works of Zasadzinski and co-workers, who observed assembly of small lipid vesicles mediated by streptavidin bridges [69], and the formation of compartmentalised lipid vesicles [70]. A variety of properties of systems using avidin-biotin interactions have been elucidated. The association rates of avidin-biotin pairs have been shown to decrease in vesicles with increased membrane tension in the work of Bihr *et al.* [71]. An increase in the concentration of polymer brushes used to modulate unspecific GUV adhesion slowed down association rates [71]. The diffusion rates of both lipids and biotin-avidin complexes have been shown to decrease with increasing receptor concentration, due to molecular crowding and membrane viscosity [72]. Furthermore the morphology, formation kinetics, and overall binding strength of adhesive patches have been investigated for systems with deformable sub-units [73–75, 68]. Relevant work has been done on networks of soft objects assembled through avidin-biotin linkers: Pontani *et al.* showed that in a densely packed network of emulsion droplets mimicking biological tissues, droplet adhesion strengthens with increasing external pressure [50].

2.2.4 DNA-mediated Interactions

Due to the frequent employment of DNA-mediated interactions in this thesis, before introducing the literature on the assembly of soft particles through DNA-mediated interactions, we briefly consider the thermodynamics of DNA hybridisation.

DNA thermodynamics

Complementary DNA strands hybridise and bind selectively thanks to the Watson-Crick base pairing rules [76, 77]. For untethered DNA-strands at a reference concentration of 1 M to form a duplex, the standard hybridisation free energy is defined as:

$$\Delta G^0 = \Delta H^0 - T\Delta S^0 = -RT \log \frac{[AA']}{[A][A]} = -RT \log \frac{x}{C_0(1-x)^2}, \tag{2.8}$$

where ΔH^0 and ΔS^0 represent the enthalpic and entropic terms; ΔG^0 can be measured experimentally, for example using UV-vis absorbance spectroscopy [78], or calculated using the nearest-neighbour thermodynamic model proposed in Ref. [79]. T is the temperature, R the ideal gas constant, and $[A]$ and $[A']$ are the (free strand) equilibrium concentrations of complementary strands A and A', with the hybridised double stranded DNA equilibrium concentration $[AA']$, and x is the fraction of hybridised strands (i.e. $[AA']$=xC_0) whilst

$C_0 = [A] + [A'] + [AA']$. From Eq. 2.8, we can derive the melting/hybridisation temperature (T_{hyb}), defined as the temperature at which x=0.5 [80]:

$$T_{hyb} = \frac{\Delta H^0}{\Delta S^0 + R\log(\frac{C_0}{\rho_0 2})}, \tag{2.9}$$

where ρ_0 is the is the standard concentration (1 M). In the case of two complementary DNA linkers on a membrane, forming either bridges (b) between vesicles or loops (l) between linkers on the same membrane, the DNA hybridisation energy is defined as as [81]:

$$\Delta G_{b/l} = \Delta G^0 - T\Delta S^{conf}_{b/l}, \tag{2.10}$$

where ΔG^0 is the same as evaluated in Eq. 2.8, and the $T\Delta S^{conf}_{b/l}$ term represents the loss of configurational freedom following the formation of a complex, consisting of the loss of rotational and translational entropy. The loss of translational entropy is more pronounced in bridges, where the complex is confined to the adhesion patch whereas loops are free to diffuse across the surface of the vesicle. From the hybridisation free energy between membrane bound linkers for both bridges and loops (Eq. 2.10), the overall hybridisation free energy between vesicles can be estimated analytically, as in Ref. [52].

Multivalent DNA-mediated Adhesion

DNA-mediated interactions have been used to drive colloidal self-assembly for over 20 years, where the specificity of interactions between complementary base pairs in DNA strands was first exploited for colloidal self-assembly by Mirkin and Alivisatos respectively [42, 43]. The DNA construct used normally consists of an inert ssDNA/dsDNA (single-stranded or double stranded DNA) spacer, with a (complementary to another strand) ssDNA component/overhang or "sticky end". ssDNA has a persistence length significantly smaller than that of dsDNA, therefore the inert ssDNA, and indeed the sticky end, can be thought of as flexible, whereas the dsDNA is considered a rigid rod [82]. In order to add some flexibility to dsDNA spacers a short ssDNA "hinge" region can be introduced.

The selectivity and thermal reversibility of the hybridisation interaction of Watson-Crick base pairing, the ease of design and cost of DNA oligonucleotides, ease of functionalisation as well as the possibility for grafting onto colloids makes DNA a very good mechanism for driving self-assembly. In soft systems, such constructs can be inserted into the membrane in

a variety of ways. Cholesterol anchoring of the constructs is extremely common; it is commercially available as a functionalisation of the DNA strands and inserts into the membrane with an off-rate of the bond between a cholesterol-tethered DNA molecule and a lipid bilayer of 5.8×10^{-4} s^{-1} [83]. Another method of vesicle functionalisation is the use of DNA-lipid conjugates, where thiol-derivatised DNA strands are covalently attached to lipids, which will spontaneously insert when mixed with lipid vesicles [5]. Finally, biotinylated lipids can bind streptavidin, which in turn can bind biointylated DNA constructs, allowing coating of a vesicle. The long lasting nature of the biotin-streptavidin bond has been shown to mitigate the loss of specificity of the linking mechanism over time in precisely spatially engineered aggregates [58].

In 2007, Beales & Vanderlick demonstrated a system where the assembly of clusters containing two populations of vesicles was mediated by complementary cholesterol-anchored DNA-constructs for vesicles of length scales from 100 nm to 5 µm [84]. These aggregates were reversible; clusters could be broken apart through heating above the hybridisation temperature of complementary strands or reducing salt concentrations formed between lipid vesicles (which causes the repulsive electrostatic interactions to not be sufficiently screened and thus dominate the inter-strand Watson-Crick base pairing interactions that lead to adhesion). The valency of the vesicles was also varied, showing only higher valency vesicles were able to cause the formation of large aggregates, presumably as only above a certain valency will there be excess linkers outside of the patch to nucleate adhesion of more than two vesicles. Valency of DNA functionalised emulsion droplets has also been varied, and shown that one can precisely engineer single pairs of droplets, flexible chains of droplets, and amorphous 3D aggregates through controlling the valency of the soft sub-units [85]. Furthermore, this has been corroborated experimentally and in simulations, where it has been shown that a minimum number of DNA constructs per vesicle is required to overcome configurational entropic costs for membrane deformation and produce stable aggregation [86]. A system of "Janus" vesicles, whereby ternary mixtures of lipids prepared correctly lead to a bilayer that phase separates into two distinct regions, a co-existing L_o and L_d phase, has shown interesting aggregation properties [87]. The cholesterol-anchored DNA preferentially partitions into the L_o domains, leaving the rest of the vesicle relatively devoid of DNA. When such Janus vesicles with complementary DNA strands are mixed, they assemble into size-limited clusters, with central adhesion plaques inside the clusters formed through the L_o domains, with the DNA-poor L_d domains unbound on the outer surface of the clusters. Different length DNA tethers in the same region of a bilayer within an adhesion patch have also been shown, however they partition into regions with DNA tethers of the

same length: local bending of the lipid membrane is energetically unfavourable, therefore the DNA-tethers segment into self-sort into domains of equal DNA length in order to minimise the total curvature energy in the adhesion patch [88]. Interestingly, for the longer strands studied (48 and 72 bp respectively), domain formation did not occur, presumably due to the increased flexibility of the tether chain/the ability for the strand to tilt to allow the coexistence of both strands due to low membrane suppression costs. Using a system divorced from particle compliance, van der Meulen *et al.* studied networks of micron-scale colloids coated in a lipid bilayer functionalised with mobile specific DNA constructs, and found a much broader association/dissociation transition than is common for hard colloids with grafted and immobile linkers [13].

Parolini *et al.* utilised mobile specific DNA constructs to drive the adhesion of GUVs, showing significant shape adjustments on adhesion of pairs of vesicles in response to temperature due to the change in stiffness of the vesicles, which in turn led to tunable porosity in networks of GUVs [52]. Indeed, these networks showed negative thermal expansion, highlighting a rare case of structural responsiveness to external stimuli in DNA-assembled materials, made possible by the interplay between the temperature-dependent deformability of the vesicles and the DNA-mediated adhesive forces (Fig. 2.2c). Further work on DNA-mediated adhesion of vesicles was achieved using both models and experiments employing a simplified geometry of vesicles adhering to a supported lipid bilayer, which allowed the probing of how vesicle adhesion is affected by the interplay between DNA coverage and temperature [51]. At high DNA coverage, the adhesion contact angle peaked between 30°C-40°C before decreasing at low temperatures (due to stiffness of the vesicles), and at high temperatures (due to the weakening of the DNA bonds). This is less pronounced for lower DNA coverage, as non-specific interactions continue to mediate vesicle adhesion in this regime, whereas in high DNA coverage regimes these are prevented due to the DNA strands acting as steric inhibitors.

Aggregation kinetics of such system of GUVs have also been controlled using toehold-mediated strand-displacement mechanisms [89], whereby an ssDNA toehold transiently colocalises an "invading" ssDNA molecule to two hybridised strands, catalysing a branch migration reaction in which the invading strand displaces one of the strands from the hybridised pair [90]. The toehold-mediated strand-displacement mechanisms in general also allows for the ability to control structural rearrangements, as has been shown in DNA-coated colloidal systems [91, 92], in response to external stimuli (the addition of free invading strands). As such, they represent a powerful potential mechanism for controlling self-assembled vesicle-

based materials.

Multivalent interactions have also been shown to drive adhesion as a transient stage on the way towards fusion. The Boxer group has utilised complementary lipid-conjugated DNA strands as a model system for SNARE proteins [93, 94], which mediate fusion of lipid membranes in biological systems. Docking was shown to increase with the number of DNA-strands per vesicle, and whilst docking also occurred more for longer DNA-strands, shorter DNA-strands were better at causing membrane fusion. Such work has interesting applications to ideas of creating assemblies of vesicles where some adhering vesicles can be programmed to fuse, possibly through a toehold-exchange mechanism, as discussed previously.

Indeed, whilst these tools and methods of adhesion and assembly are fundamentally of interest, basic applications have already been shown: binary and ternary mixtures of complementary and non-complementary DNA-functionalised vesicles containing gene expression machinery have been shown to be able to self-assemble into spatially controlled macroassemblies [57], indicating the suitability of such systems for novel functional biomaterials. Furthermore, targeting of DNA-coated cells targeting using similarly functionalised lipid vesicles has also been shown [95].

2.2.5 Other Multivalent Interactions

As stated previously, coupling multivalent interactions to vesicles can serve as an interesting model system for adhesion in biological tissues and, in service of this, vesicles interacting through biologically-relevant multivalent linkers have already been considered [96]. A variety of lectin-glycan systems have been used to model the adhesion properties of cells: for example, to tease out the effect of the repulsive Glycocalyx layer, as well as to demonstrate bond energy reduction of protein linker pairs in the membrane compared with when free in solution [97, 98]. RGD-capped (where RGD is an arginine–glycine–aspartic acid peptide sequence) lipids can bind to integrins, and have been used to study both the statics and dynamics of adhesion [99, 100], with one study elucidating that force-induced growth of adhesion domains is controlled by receptor mobility, suggesting a physical and passive (non-cytoskeletal) mechanism of cells for mechanosensing in cells [100].

Responsive phases have also been created using other multivalent interactions. Vesicles have been functionalsied with either a tetrameric lectin molecules or their conjugate, glycans, in order to cross-link vesicles into tissue like structures [101]. Using different

glycan and lectins on the same vesicles showed segregation of similar lectins into domains in the adhesion patches between vesicles. This material was also shown to be responsive to concentrations of calcium ions, which are prerequisite for lectin-glycan binding. Other such systems exist which are responsive to external stimuli: lipid vesicles containing using metal-chelating lipids have shown to form complexes (in the presence of copper(II)) which can bind L-histidine residues. These can be themselves functionalised on another population of vesicles [102], or be added as an external multimeric poly-L-histidine which bridges vesicles functionalised with metal-chelating lipids [103]. In either case, addition of poly-L-histidine and external Copper(II) was shown to increase aggregation of lipid vesicles. Adhesion between lipid vesicles containing functionalised lipids, such as complementary cyanuric acid and melamine functionalised lipids or complementary barbituric acid and triaminopyrimidine group functionalised lipids, have shown adhesion through hydrogen bond driven recognition [104, 105]. In the case of cyanuric acid and melamine, this occurs when the functional groups have multimeric hydrogen bonding, which allows enough stability for ahdesion despite low molar concentration of functionalised lipids and solvent competition for hydrogen bond donor/acceptor sites [104].

Other studies utilise multivalent adhesion, using receptors such as aptamers [106] and antibodies [107], from a medical/targeting perspective rather than physical perspective and thus are beyond the scope of this section.

2.3 Soft Glassy Materials

2.3.1 Colloidal Scale Particles

Colloidal particles are insoluble particles dispersed in a fluid phase, in the range of 10 nm to 10 µm. This makes them small enough to be suspended in the fluid by thermal motion, provided the density mismatch with the particles is not too large, and thus individual particles diffuse in a Brownian manner [108]. These colloidal scale particles can be created monodisperse and their interparticle interactions can be tuned very precisely.

2.3.2 Gels

Gels are low-density disordered states which have solid-like properties, such as a yield stress, and do not flow, yet are disordered states, similar to a liquids and glasses [109]. The process of gelation occurs at the sol-gel transition whereby the sol particles, initially separated and

suspended in a solvent, aggregate into a percolating network under specific conditions due to attractive potentials. Whilst gels lack long range order, the specific mechanism of gelation dictates the length scales of the material and the fractal dimension.

Gels can be broadly defined into two categories: chemical or physical gels. In the case of chemical gels, gelation occurs through the formation of bonds $\geq 100k_BT$ which can be deemed irreversible throughout observable timescales. As such, the gel point coincides strictly with the appearance of a space spanning structure. Physical gels on the other hand are held together with bonds of the order of k_BT. In this type of gel, bonds are reversible over the experimental timescale (although they can nonetheless be relatively long lasting) breaking and reforming many times during the course of an experiment. However, the corollary of this is that a percolating structure is not sufficient for gelation to have occured; transient clusters can continuously break and reform, and at high enough densities this can lead to transient percolating networks which are unstable over experimental times scales [109]. At higher densities of sol particles, we enter the "glassy" region of the phase diagram, where dynamic arrest causes the formation of metastable solid phases: attractive glasses at low termperatures, and respulsive glasses in high temperature system. At reduced temperature, the glass transition occurs at lower volume fraction. Interestingly, at intermediate temperatures between repulsive and attractive glasses, the weakened attractive interactions can lead to a reduction in the distance between particles, leaving more room for diffusion and therefore allowing the glass line to move to higher volume fractions, which then reduces again due to repulsive interactions dominating [110].

2.3.3 Gelation in colloidal systems through arrested phase separation

At low enough temperatures, a colloidal system with attractive interactions crosses both the binodal, where phase coexistence is thermodynamically favoured but the homogenous phase is metastable, and the spinodal line, where the homogenous phase is unstable and any fluctuations lead to phase separation via spinodal decomposition [109].

If this occurs at temperatures above the T_{glass}, this leads to macroscopic separation between the two equilibrium phases through completed phase separation. If the temperature is reduced to $<T_{glass}$, the spinodal decomposition begins but, as soon as the density of the aggregates reaches the glass line, the dynamics becomes arrested and the phase separation interrupts (Fig. 2.3) [109]. If the overall density of the mixture is high enough, the structures left from this arrested phase separation can form a (over experimentally probable timescales)

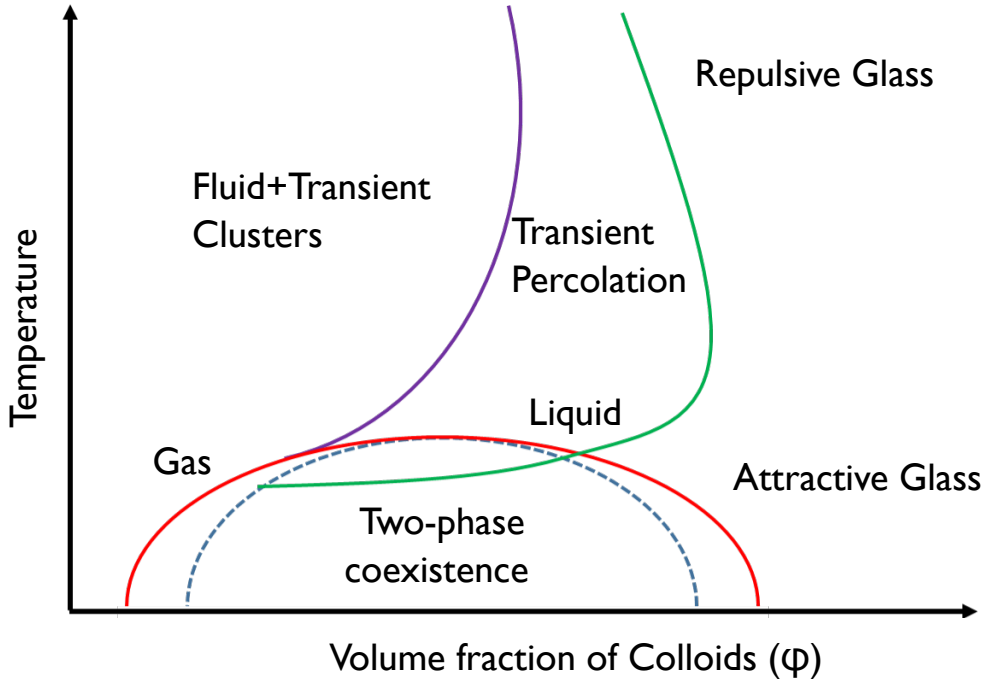

Fig. 2.3 Sketched phase diagram for a system of attractive colloids. Increasing temperature corresponds to decreasing the attraction of the system. The red line is the binodal line, and the blue dashed line the spinodal. The green line represents the glass transition; quenching to below this line within the spinodal region leads to arrested phase separation. The purple line indicates the percolation transition.

permanent network, non-equilibrium gel.

In the limit of very large attraction strength (ie. deeply quenched) and arbitrarily low volume fraction, this scenario crosses continuously to diffusion-limited cluster aggregation (DLCA). DLCA is a purely kinetic process; particles stick on contact and no thermal relaxation is allowed at any stage; as such the aggregation process if mediated by the diffusion of clusters and particles which leads to the formation of fractal gels with a fractal dimension of df< 1.9 [111].

2.3.4 Aging and Dynamics of Gels

As can be inferred by the mechanisms of gelation expanded upon in Section 2.3.3, gels or glassy-systems are often thermodynamically out of equilibrium. Such materials still want to

achieve equilibrium, and do so through physical aging [111], where their structure evolves to lower the free energy. Such aging is only possible due to the mobility of the individual subunits in colloidal systems, and the possibility of bonds rearranging on accessible timescales. Often these gels are examples of non-ergodic systems: they are able to explore only a restricted portion of the total phase space. However, experimentally, determining the non-ergodicity of a system is non-trivial, as only a limited range of length and time scales can be probed [112]. Here, as we consider the dynamics of soft "glassy" materials, we describe a broader ranger of systems, including materials that are ergodic but still exhibit very slow relaxations.

Density correlation functions can be found using scattering experiments, and give a measure of the structure in a system being studied, allowing the probing of system dynamics as a function of the scattering q-vector (which can be thought of as the resolution of the observation) and time. Experiments have shown two step relaxation, in systems using colloidal suspensions, emulsions, surfactant vesicles, and polymer gels [113–116]. This is corroborated by the theoretical work of Bouchaud and co-workers [117, 118]. In such systems the first relaxation corresponds to the diffusion of particles in cages by the local structure: it has been shown that diffusive-like behaviour in colloidal gels can arise from overdamped fluctuations of the collective motions within clusters [119].

This long-time relaxation has been attributed to a range of behaviours experimentally. Scattering experiments have shown several different q-dependencies of the characteristic time τ for the slow relaxation have been measured. Abou *et al.* found $\tau \sim q^{-2}$ for a suspension of Laponite particles, as expected for a diffusive process, such as cage-escape mechanisms [120], though in the same material, but a different aging regime, Bellour and c-oworkers have found that $\tau \sim q^{-1.3}$ [121]. However, less intuitive scaling laws have also been obtained by several groups on various samples. Solomon *et al.* reported $\tau \sim q^{-0.5}$ for a colloidal gel of adhesive particles [122], and subdiffusive final relaxations have also been reported [113, 123].

Ballistic motion has frequently been observed: this corresponds to $\tau \sim q^{-1}$ scaling, and has been measured for a wide variety of materials, including both attractive (i.e fractal colloidal gels) and repulsive systems (ie. arrangements of soft elastic spheres and emulsion droplets), as well as with both dilute and concentrated volume fractions [124, 116, 125]. This scaling is accompanied by the presence of a compressed exponential to fit the decay of intermediate scattering function, $f(q, \tau)$ (or mathematically described $f(q, \tau) \sim e^{-\left(\frac{t}{\tau}\right)^{\beta}}$), where $\beta \geq 1$. The relaxation is faster than exponential, therefore due to non-diffusive scaling,

this cannot be due to a cage-escape process. It is thought that the relaxation of randomly distributed internal stresses is what drives these dynamics, and leads to spatial and temporal heterogeneity of relaxation times and scaling [124, 116, 126, 127]. Scattering experiments coupled to rheology show that an external oscillatory shear strain can help the system evolve towards a more relaxed configuration, presumably by relaxing internal stress [128–130]. In systems with soft and thermally responsive colloidal subunits, this has been hypothesised to be due to the expansion and contraction of the colloids in response to small thermal fluctuations, which in turn cause localised shears [115, 131]. Another possible contributing mechanism to these dynamics is the slow directional motion of individual colloid-rich domains driven by interfacial coarsening [114]. Indeed, the nature of ballistic events themselves in dilute gels has been further studied. It has been shown that the ballistic behaviour in the final relaxation can be due to intermittent events rather than being a continuous process [126].

2.4 Rheology and Soft Granular Materials

2.4.1 Rheology

Rheology is the study of the deformation and flow of matter, both solids and liquids, achieved by extending continuum mechanics to describe materials whose behaviour cannot be described by classical theories. Rheological properties of soft materials are often described by either linear viscoelasticity or (non-linear) power-law rheology. Power-law models give a single value to characterise a sample, the exponent, as it models the rheological behaviour of a sample as a distribution of time constants. Whilst this value does not have an intuitive physical explanation, power-law analysis has been very successful in yielding good fits for soft materials under a variety of conditions [132]. In the case of linear viscoelasticity, the viscoelastic behaviour can be described by mechanical equivalent circuits consisting of networks of Hookean elastic springs and Newtonian viscous dashpots arranged in series or in parallel. These can be used to describe the system in an intuitive fashion, giving time constants and parameters that can be physically interpreted to properties of the material (eg. the viscosity of the solvent, the stiffness of a vesicle etc.), and compared between samples and systems [132]. However, this approach is not able to accurately model the behaviour of all non-Newtonian materials. An extension of this approach which allows improved fitting is the use of a fractional derivative of a spring/dashpot, often called a spring-pot or a Scott-Blair element, which allows for the modelling of materials with time-dependent viscosity [133]. These can be substituted into existing consitutive models to better model complex materials with time-dependency, through the power-law response inherent to the

fractional derivative [134].

Rheological measurements are commonly achieved using rheometers, which fundamentally work through the application of extensional or shear stress, where either stress or strain is kept constant and the responsive strain or stress is measured. However, such devices require millilitres of sample, which can be prohibitive for certain systems, and do not allow local probing of viscoelastic properties. Instead, one can use microrheology, well described in [135], where the measurement of the trajectory of a tracer particle is used to find the rheological properties of a medium. This can be done passively, where the mean-squared displacement (MSD) of Brownian tracer particles can be used to calculate the viscoelastic moduli using the generalised Stokes–Einstein relation. Additionally, this can be done actively, where a known force is applied to a particle, and the response can be observed. This force can be applied in an oscillatory manner to derive frequency-dependent viscoelastic moduli, or as a pulse, where the deflection of the particle can be measured to derive the creep-response.

2.4.2 Rheological Considerations for Soft Materials

To the best of our knowledge, no literature currently exists that describes the rheology of tissue-like materials consisting of adhering lipid vesicles. However, soft materials, granular materials and biological tissues, on which there is a vast existing literature, all provide some context to lipid vesicle based systems.

Networks of particles that make up granular materials are non-Brownian, and can form jammed, metastable, non-ergodic states that can resist shear through adhesive, frictional and repulsive forces [137]. Therefore the application of force is required to perturb the initial configuration; this will not occur through thermal fluctuations. Thus the motion of an object through a granular material requires breaking and reformation of force chains, resulting in temporally intermittent, stick-slip dynamics [137]. Forces are transmitted inhomogenously and anisotropically throughout the network (Fig. 2.4), on one hand causing enriched dynamics, on the other making theories on rheology challenging [138]. Cellular tissues have some similarities to granular systems and thus can be viewed as a soft granular system, where the orientation and aligment of the sub-units (cells) can lead to similar rheological properties to those observed in granular systems. However, one key difference is that that the properties of cellular tissues are coupled to active and heterogeneous substructures within cells that contribute to their mechanical properties and respond to external stimuli [132].

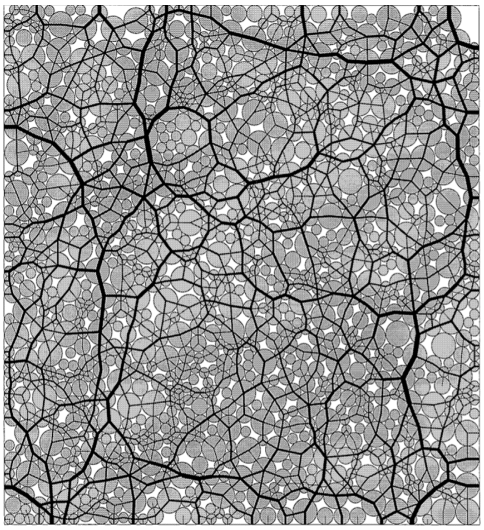

Fig. 2.4 Force chains in a 2D granular material as calculated from contact dynamics simulations, where the width of the intercentre connecting segments indicate the magnitude of the force. It is clear to see that the forces are inhomogenously and anisotropically distributed. Figure taken from [136].

2.5 Microfludics

2.5.1 Microfluidics Overview

Microfluidics is the scaling down of fluidic processes to the microscale. To understand the uniqueness of the technique, we consider the Reynolds number (*Re*), a dimensionless ratio which compares the inertial forces to the viscous forces

$$Re = \frac{\rho u L}{\mu}, \tag{2.11}$$

where ρ is the density of the fluid, u the velocity, L the characteristic length (for flow in a pipe this is the diameter) and μ the dynamic viscosity. At L of the order of μm, we find that *Re* becomes low enough that the flow regime becomes laminar rather than turbulent, allowing molecular transport to be through diffusion and advection and thus relatively predictable throughout the channels. This and the small channels allow for a variety of benefits: low reagent consumption, rapid heat transfer and precise heat control and fast and accurate reactions [139]. Using this relatively simple principle, complicated designs of microfluidic devices have been achieved, allowing for previously difficult or inconceivable processes to be realised [140]. Work on microfluidics often utilises pressure pumps which allow precise control of flow rates. Furthermore, whilst microfluidic devices can be fabricated from a variety of materials, including silicon, glass, metals, ceramics and hard plastics, in a laboratory

setting most frequently Polydimethylsiloxane (PDMS) is employed as it is cheap, easy to make, bio-compatible, optically transparent, easy to mold and gas permeable [139].

One method of microfluidics is segmented-flow, where immiscible fluids are used to create discrete pico to nanolitre-sized droplets, that exist in an external phase. As such, the conditions in each droplet are far more consistent and controlled, negating issues with continuous-flow microfluidics, and allowing each droplet to be thought of as a separate, well-controlled nanoreactor for the experimental system. These droplets can be created at kHz formation rates, and can be made highly monodisperse, therefore also giving large statistics for experiments [141]. Whilst no strict definition exists, consensus from the literature suggests a definition of GUV monodispersity as a sample which has a standard deviation of the distribution of GUV diameters of <10% [41, 142–144]. Furthermore, these droplets can be split, mixed, merged, and sorted through a variety of microstructures [145–147], which is important to facilitate the integrable nature of microfluidics that makes it so applicable for "lab on a chip" devices, allowing the multiplexing and integration of multiple processes to simply achieve outcomes that would otherwise be multistep and time consuming.

In addition, the contents of microfluidic devices can be assessed using optical or electrochemical methods, with integration of electrodes into PDMS devices possible [148]. As such, there is potential to create low-cost disposable devices with electronic read-outs using microfluidics, and though not fully realised, this thesis presents some foundational work towards this.

2.5.2 Microfluidic GUV formation

Methods have been proposed to create monodisperse GUVs using microfluidic devices, which overcome the issues of encapsulation and polydispersity that plague other techniques [149, 143, 144, 150, 151]. Many of the microfluidic GUV techniques in the literature involve the creation of a lipid stabilised water-in-oil-in-water (w/o/w) double-emulsion droplet as a primary step, though often with the downside that resiudal solvent (oil or another organic solvent) can remain in the bilayer which can additionally affect the physical and chemical properties of the membrane [143], which in turn can affect processes such as membrane functionalisation. Promisingly, Karamdad *et al.* proposed a microfluidic method which produced monodisperse vesicles with bending rigidities within the margin of error of values from the literature, despite residual solvent present in the bilayer [143]. Deshpande *et al.* proposed a high-throughput method utilising a double-emulsion-droplet-based approach

(Fig. 2.5a) using an alcohol based solvent, octanol, instead of the commonly used oil-based lipid carrying phases [144]. In this method, the solvent extraction time is only a few minutes as the octanol buds off the vesicle, and furthermore the method is robust for variation in membrane composition and inserted constructs in the membrane. Other methods exist for reducing the solvent from double emulsion droplets: by forming constrictions post-double emulsion junction channel width, Vian *et al.* showed that up to 93% of the solvent could be removed from the double emulsion droplet [152]; numerous groups have referenced the use of ethanol in the outer aqueous solution as the organic solvent's high solubility in ethanol causes it to dissolve into the solution, reducing the distance betweeen monolayers which in turn allows for self-assembly into a bilayer [153, 142, 149]; Deng *et al.* reported that the use and careful tuning of a hexane-chloroform mixture as the lipid carrying phase, coupled with a triblock copolymer surfactant in the outer phase, allowed for complete dewetting of the oil phase [154]; and finally by the use of serpentines downstream from the w/o/w droplet formation junction, which gives both time and shear stress for the oil pocket to bud off [144]. However, even in these cases, solvent separation is still a problem but methods exist to get around this issue; by adding a separation hole downstream of the formation junction, the oil droplets rise into the hole due to their lower density, while vesicles are sucked into a post-hole channel [155].

Emulsion transfer methods are another method of creating vesicles [158], and this has been achieved in a microfluidic context in the the work of Matosevic *et al.* [159, 160]. Lipid-stabilised water-in-oil (w/o) were created, and co-flowed with an aqueous stream; at a certain point they were displaced by a ramp-shaped obstacle, forming a bilayer as they passed from the organic into the aqueous phase (Fig. 2.5c). This critical stage reduces the yield to as little as 1% of the w/o droplet production stage [159].

From the double-emulsion and emulsion transfer methods a variety of interesting architectures and experiments have been performed; studies which produce multicompartment vesicles free from residual oil by careful tuning of interfacial energies of w/o/w droplets [154], structures with defined compositional asymmetry and lamellarity [160], broad ranges and careful tuning of vesicle size, as well as encapsulation of dyes, beads, cells and simple genetic circuitry [161, 142, 154].

Another promising method of creating monodisperse unilamellar vesicles is through microfluidic jetting [162, 156]. A liquid jet of the inner aqueous solution is directed into a unilamellar lipid bilayer formed between two aqueous solutions. This in turn deforms

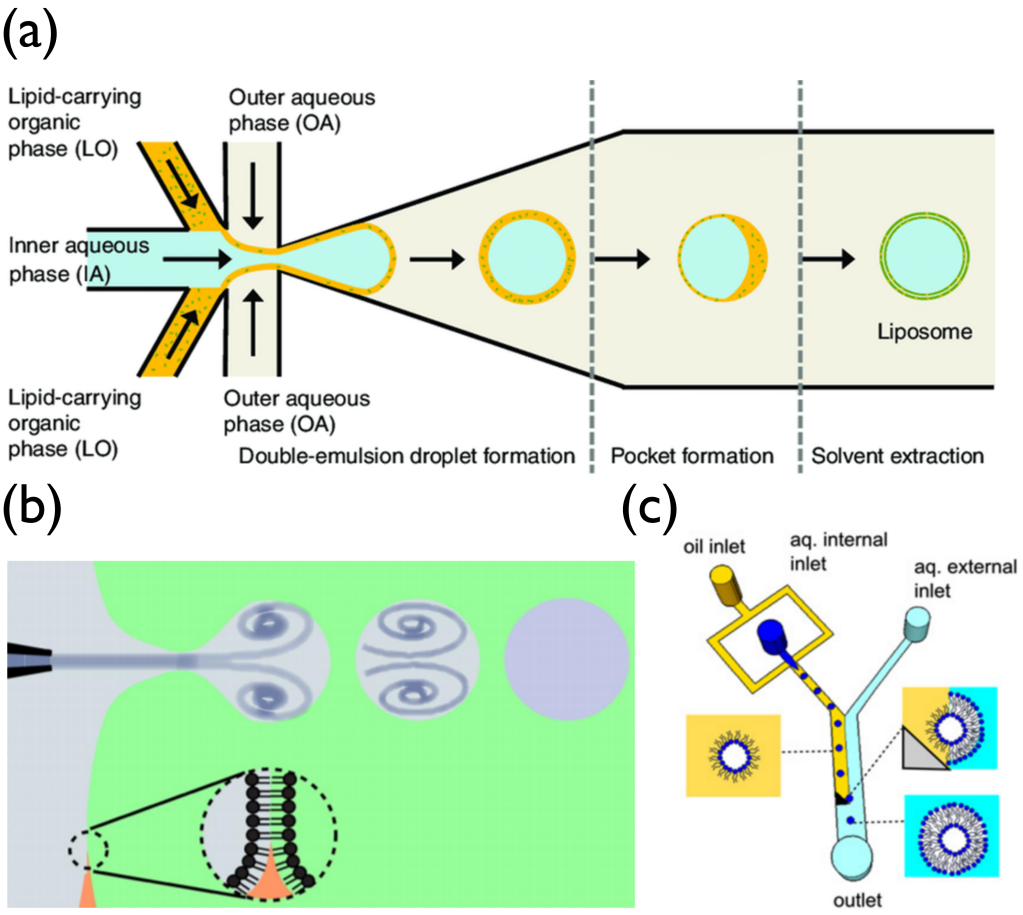

Fig. 2.5 Examples of three microfluidic methods for the generation of GUVs. (a) Shows a double emulsion method, utilising the "bubble-blowing" junction technique, where an aqueous component forms a bubble, which is pinched off by another aqueous phase, forming a double emulsion which eventually becomes a vesicle, taken from [144]. (b) The microfluidic jetting method, where a liquid jet of the inner aqueous solution deforms a unilamellar lipid bilayer, between two aqueous phases, into a vesicle that is filled with the inner aqueous solution and buds off into the aqueous phase on the other side of the bilayer, taken from [156]. (c) An example of the emulsion transfer method, where lipid stabilised water-in-oil droplets are co-flowed with an aqueous stream until being displaced by a ramp-shaped obstacle, forming a bilayer as they passed from the oil into the aqueous phase, taken from [157].

the bilayer into a vesicle that is filled with the inner aqueous solution and buds off into the aqueous phase on the other side of the bilayer (Fig. 2.5b). The bilayer remains intact, and this process can be repeated. Due to the fast formation time, this method could yield thousands of GUVs per minute. Intuitively, by varying bilayer composition and functionalisation, one can vary the functionalisation and composition of the vesicles, making it a more versatile technique than many of the previously explored techniques [156]. Furthermore, the interior

solution is unrestricted in composition, allowing encapsulation. However, precise control of domain distribution/lipid composition is made difficult due the imprecision of the jetting relative to the distribution of domains on the bilayer.

Other microfluidic vesicle-producing techniques, such as the flow focusing method of Jahn *et al.* exist to create high-throughput monodisperse vesicles, but are limited to vesicles sizes in the nanoscale [163].

2.6 Applications

In the previous sections we have given the reader a brief background to the fundamental science underpinning the work that will be explored here. But what is the purpose of studying multivalent linker-mediated vesicle based self-assembled systems?

Such systems have clear analogies with biological cells. Thus they can provide a model to study cell and tissue morphology and rheology [54], as well as representing a novel soft granular system to study. Cells have incredibly complicated rheological responses, thus using such systems one can employ a bottom-up approach to create a minimal biomimetic model [137]. Complexity can then be added by utilising various biologically relevant ligands.

The properties of such self-assembled systems are also interesting from a biosensing point of view, creating materials responsive to external stimuli whose macroscopic properties can respond to small (nM/pM) concentrations of analytes [38]. Studying the response of vesicle adhesion to such changes would give us single vesicle resolution on the sensing capabilities of such a system. For standardised engineering applications such as in biosensing, vesicles would need to be uniform, monodisperse sub-units in order to decouple the understanding of morphological changes in vesicles from size effects. To do this, and indeed to create dense packings in a consistent matter, the use of microfluidics to generate vesicles represents a powerful tool. Furthermore, vesicles generated through microfluidic techniques can also easily encapsulate other substances and as such can be seen as a method to produce high-throughput artificial cells.

Additionally, multiple lipid vesicles can be held together by linkers to form multi-compartment assemblies. Engineered linkers can be used to change the morphology of the assemblies and/or the distance between the lipid bilayers. If agents (chemical or biological) in different compartments are to communicate *via* permeation of species across the bilayers,

such morphological changes can serve as a means of spatially controlling communication. Furthermore DNA linkers can be used to induce fusion between bilayers, effectively merging different compartments [93, 94]. This could have implications to the study of compartmentalisation, and therefore application to the fields of synthetic biology, nanoreactors, nanofiltration and drug delivery [22–24].

Chapter 3

General Experimental Methods and Techniques

In this chapter the main aspects of fundamental and frequently employed methods will be described; in addition, a brief background for each method will be put forth. The following sections will be utilised as a reference for future chapters.

3.1 Electroformation of Giant Unilamellar Vesicles

Electroformation allows for the fast ($\sim$3 hour) preparation of large numbers of vesicles in the 10 µm-100 µm range. Broadly speaking, electroformation follows a protocol of forming dry lipid films on an electrode, hydrating the lipid films in a chamber between another electrode (which forms a capacitor cell), and applying an oscillating field, which in turn causes the swelling of the films which bud off at lower frequencies to form vesicles [164].

This method has been shown to give unilamellar vesicles free from organic contaminants or oil in the membrane that other methods can suffer from. Electroformation allows the simple formation of multicomponent vesicles and functionalisation with membrane bound constructs such as membrane proteins [165, 166]. That being said, electroformation has its limitations, such as significant polydispersity and the inability to produce asymmetric vesicles, and is thus not perfect for all applications of vesicles, for reasons considered further in Section 6.1. Despite this, some limitations of electroformation have been overcome in certain implementations; vesicle formation at high and physiologically relevant salt concentration, vesicles with cationic lipids in the membrane and more tuned distribution of sizes through micropatterning have all been achieved [167–169]. Nonetheless, the simplicity

of the method and relatively high yield, as well as the range of sizes and compositions possible, make electroformed GUVs well suited for studies on fundamental biophysics and membrane physics.

3.1.1 Electroformed lipid vesicle protocol

DOPC (1,2-dioleoyl-sn-glycero-3-phosphocholine, Avanti Polar Lipds) and a fluorescent dye-lipid conjugate (such as Texas Red-DHPE or Oregon Green 488 DHPE) are dissolved in chloroform in a 99.3:0.7 molar ratio and overall concentration of 3.57 mg ml^{-1}. An indium tin oxide (ITO) coated microscope slide is spin-coated on its conductive side with 160 µl of the lipid solution for 2 minutes to create a uniform film. The lipid-coated slide is dried out in a vacuum desiccator for 1 hour. The dried lipid-coated slide and a clean non-lipid-coated slide are arranged together to form a capacitor cell. Both conductive sides faced inwards and were overlaid using a U-shaped 0.5 mm thick silicone rubber spacer (Altec) creating a chamber. The chamber is filled with a de-gassed inner solution (this solution will be inside the vesicles), and sealed using plastic paraffin film (Parafilm) and paper clips. Electroformation is then carried out using a function generator. A 10 Hz sinusoidal potential with a 1 V peak-to-peak amplitude is applied across the chamber for 2 hours, after which the frequency is reduced to 2Hz for 1 hour, in order to aid the detachment of the vesicles from the ITO slide. The vesicles are extracted from the chamber using a pipette and stored in a vial (Eppendorf) at room temperature in the dark. GUVs are used within 7 days.

3.2 Extrusion of Small and Large Unilamellar Vesicles

Small unilamellar vesicles (SUVs) and large unilamellar vesicles (LUVs) can be created through extrusion: a simple technique whereby unilamellar vesicles from hundreds of nanometers to a few microns in size can be produced through sequential filtering of a multilamellar vesicles (MLVs) solution through a polycarbonate membrane [170]. The MLVs are themselves formed by the hydration of a lipid film and subsequent sonication which allows the budding off of polydisperse multilamellar vesicles, which are rendered sequentially more unilamellar and monodisperse through successive filtering.

This technique produces vesicles that are mostly unilamellar and that have a size distribution centred around the membrane pore size, with a standard deviation of $\sim$8% about the mean for filters with a 100 nm pore size, though this is larger for larger pores [171]. Unilamellarity also decreases with pore size; to counteract this a freezing and thawing procedure is applied to

the MLVs solution before extrusion is used to improve the unilamellarity of the vesicles. This is thought to work due to differential freezing of the water in the spaces between lamellae, due to the interlamellar space being too small for a water crystal nucleus of larger than the critical size to develop [172]. This leads to large osmotic stresses as a result of freeze induced dehydration, and structural changes in vesicles with small fluid spaces, such as those which are multilamellar, causing vesicles to become inreasingly unilamellar with freeeze/thaw steps.

Whilst the size range for extrusion is limited, the fact that it produces relatively monodisperse unilamellar vesicles, doesn't require the use of organic solvents, allows for a range of lipid compositions, is remarkably simple and can be used as a robust method for encapsulation makes extrusion a widely used method of vesicle formation.

3.2.1 Extruded lipid vesicle protocol

200 µl of a 25 mg ml^{-1} chloroform solution of DOPC + a lipid conjugated dye (99.3:0.7 molar ratio) is injected in a glass vial and desiccated for 15 minutes to let the chloroform evaporate. The dried lipids are then resuspended in 500 µl of the solution which is desired to fill the inside of the vesicle, and vortexed to ensure hydration. Four freezing/thawing cycles are then carried out using liquid nitrogen and 40°C water to break up large lipid structures. To prepare SUVs/LUVs, the lipid solution is processed with a Mini-Extruder kit (Avanti Polar Lipids) equipped with a track-etched polycarbonate membrane with defined pore sizes in the nm- µm range (Whatman) and operated according to the manufacturer's instructions. The SUV/LUVs are then stored at 4°C and used within 7 days.

3.3 Differential Dynamic Microscopy

Differential Dynamic Microscopy (DDM) is a powerful video analysis tool that was first introduced in 2008 by Roberto Cerbino and Veronique Trappe [173]. It allows for scattering experiments to be conducted simply using an optical microscope. DDM itself is a near-field technique that is predicated on the Fourier analysis of the differences between frames to eventually arrive at an intermediate scattering function (ISF) (Fig. 3.1), the same information normally accessible via Dynmic Light Scattering (DLS) [174, 175]. DDM has been shown to be particularly useful in assessing multiscale dynamics, often encountered in soft matter and bio-physics [176].

DDM can be used, and has been applied to, a variety of imaging systems. Additionally, unlike DLS, it allows for for the simultaneous inspection of dynamics of the sample at multiple q-vectors with good statistics, which significantly reduces the experimental time in regards to DLS [176]. Furthermore, it can be used to sample a larger sample volume, giving better statistics and also an ability to better probe the sample spatial heterogeneity. DDM affords a wider range of wave-vectors to be considered than DLS, where smaller scattering angles are inaccessible due to stray light from imperfections in the optical path perturbing the signal. In DDM this stray light represents a static contribution in the microscope images between frames and thus cancels out in the difference images, allowing DDM to be robust to such imperfections, and also still viable in systems with poorly cleaned elements/low-quality optics. Indeed, similarly, an experimental system with a dense array of nanoposts demonstrated the ability to accurately assess dynamics of confined particles even in the presence of static contributions [177].

DDM can also be used instead of particle tracking, such as to assess the diffusion coefficient field for dispersions where the Brownian motion is heterogeneous in space [178]. DDM negates the need for tracking particles between frames, removing the significant combinatoric problems which occur with increasing density of tracer particles. By being agnostic to anything other than the difference between images, DDM does not require the significant fine tuning of parameters required in particle tracking experiments (displacement between frames, size of particles, brightness of particle, minimum number of frames to analyse track etc.).

Since the initial presentation of the technique to characterise colloidal dynamics, DDM has been adapted to a wealth of applications [173, 176]. In addition to systems of colloidal dispersions, DDM has been applied to extract the mean-squared displacement for a dispersion of particles without the need for tracking, and from this infer microrheological measurements for the frequency-dependent loss and storage moduli [179]. DDM has also been applied to study the intermittent dynamics during spinodal decomposition in a colloidal gel by not considering the ensemble average, and finding a time-resolved Image Structure Function (see Section 3.3.1) [180]. Aspects of colloidal aggregates, such as their kinetics and estimates for their fractal dimension, have also been found [174].

DDM also has been applied in biological and active systems: Wilson *et al.* used DDM to measure *Escherichia coli* motility and Drechsler *et al.* used DDM to study the dynamics of cytoskeletal filamentous actin and endogenous vesicles within a Drosophila oocyte [181, 182]. Indeed DDM has even seen applications in biophysics with a possibility as a diagnostic tool;

Chioccioli *et al.* showed the application of a new DDM variation, multiDDM, to detect changes in ciliary dynamics that can be used to assess respiratory diseases and for drug screeninng [183].

3.3.1 DDM methodology

A visual description of the DDM process is shown in Fig. 3.1. The first step in DDM analysis is obtaining a differential signal as a function of position and time lags, $d(\vec{r},t_0,\tau)$ of set of frames making up a video:

$$d(\vec{r},t_0,\tau) = F(\vec{r},t_0+\tau) - F(\vec{r},t_0), \tag{3.1}$$

where $F(\vec{r},t_0)$ and $F(\vec{r},t_0+\tau)$ are frames at t_0 and $t_0+\tau$ respectively. We then define the spatial 2D Fourier transform of $d(\vec{r},t_0,\tau)$ as $d(\vec{q},t_0,\tau)$. We square this and average over all difference images with the same lag time, τ to find the Image Structure Function

$$I(\vec{q},\tau) = \langle |d(\vec{q},t_0,\tau)|^2 \rangle_{t_0}. \tag{3.2}$$

If the assumption that the image is isotropic is true, $I(\vec{q},\tau)$ can be azimuthally averaged as it will have circular symmetry in q, which permits us to instead consider the Image Structure Function $I(q,\tau)$, dependent on only the magnitude of the scattering vector ($q = \sqrt{q_x^2+q_y^2}$) and τ.

In this implementation of DDM, we average over the azimuthally averaged Fourier transforms of up to the first 200 difference images for a given τ (or $n/(\tau+1)$ difference images if $n/(\tau+1)<200$ where n is the total number of frames in the video). The windows are non-overlapping to give better statistics and prevent artificial smoothing. From an $N \times N$ pixel image, we calculate $I(q,\tau)$ for N/2 q-modes.

It has since been shown theoretically that the $I(q,\tau)$ can take the form

$$I(q,\tau) = A(q)[1-f(q,\tau)] + B(q). \tag{3.3}$$

The function $f(q,\tau)$ is the aforementioned ISF usually found from DLS experiments, and gives cumulative probability that the displacement of a material element over time τ will lie within a distance equal to the length scale $\lambda(=2\pi/q)$. Therefore the time evolution of the ISF encodes information as to how quickly the structure at the length scale of λ is lost, or, alternatively, how the sample configurations decorrelate. $A(q)$ is the product of the

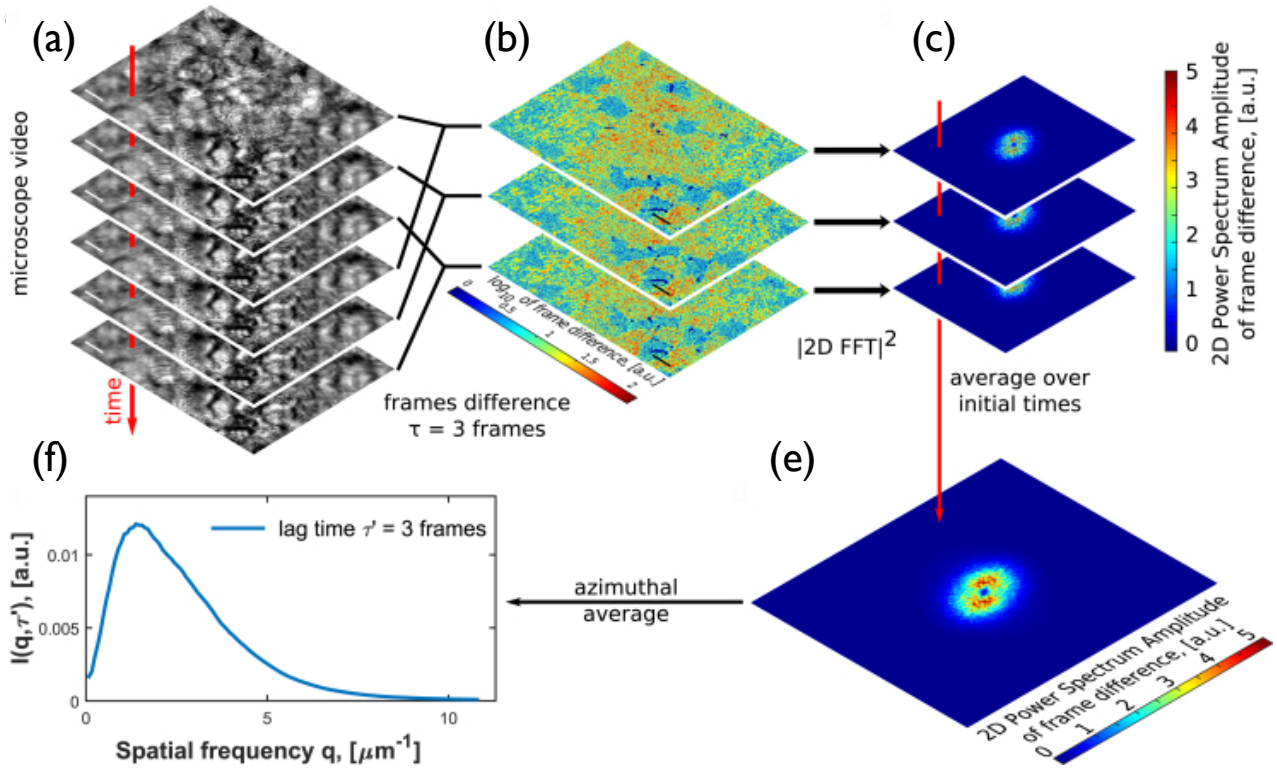

Fig. 3.1 Image acquisition and analysis process for DDM: initially there is an (a) acquisition of bright field microscopy videos from which (b) difference images are generated by subtracting frames separated by a time interval (lag time) τ. (c) The 2D FFT of the differential images is found and then (d) averaged over all the Fourier transforms of the differential images. (e) The 2D power spectrum is then azimuthally averaged to yield a 1D power spectrum for a given τ. This image is reproduced from Ref. [184].

intensity static scattering of the sample and a microscope dependent transfer function . $B(q)$ is background term accounting for the detection noise. $A(q)$ and $B(q)$ can be retrieved as parameters of the fit, and this, along with the fitting of $f(q,\tau)$, will be considered more fully in Section 5.4.

3.4 Flickering Analysis

Flickering analysis derives information on the mechanical properties of a membrane through the consideration of the thermal fluctuations of the membrane [185]. The theory on membrane fluctuations which leads to this technique is beyond the scope of this thesis, however the fundamental equation governing the membrane fluctuations that allows this analysis is detailed in Ref [186]. Significant work applying this technique has already been achieved, with applications to studying such phenomena as vesicle bending moduli [187, 185], vesicle membrane tension on adhesion [51], line tension of domains on lipid vesicles [188] and tension of cells such as erythrocytes [189]. Here, a simpler case of the application to adhering GUVs in order to probe adhesion mediated forces, as in Chapter 4, is considered. Other methods of measuring membrane tension exist, such as micropipette aspiration, however this method requires precise control of a pipette and a vesicle, making it significantly more complicated.

3.4.1 Flickering Spectroscopy implementation

Videos of the GUVs' equator are recorded in a fluorescent channel using a Leica TC5 SP5 Confocal Microscope. The equatorial plane is defined by the z-position with the largest vesicle diameter.

The vesicle contour is determined from the videos using a customised version of the MATLAB algorithm described in [51], and this process is shown in Fig. 3.2. Briefly, an initial estimate of the centre of the vesicle and a point on the membrane are used as a first approximation for the radius and vesicle centre using a user input. From this an annular region of a preselected width is defined that contains the membrane. This is mapped into polar coordiates, $c(r,\phi)$, using a cubic interpolation where r is the distance from the centre and ϕ is the azimuthal angle. The vesicle rim is defined as the maximum $c(r,\phi)$. For each ϕ, the contour location is refined by evaluating the centroid of $c(r,\phi)$ within an interval of 6 pixel centered around the initial estimate for the contour location. This interval is chosen as

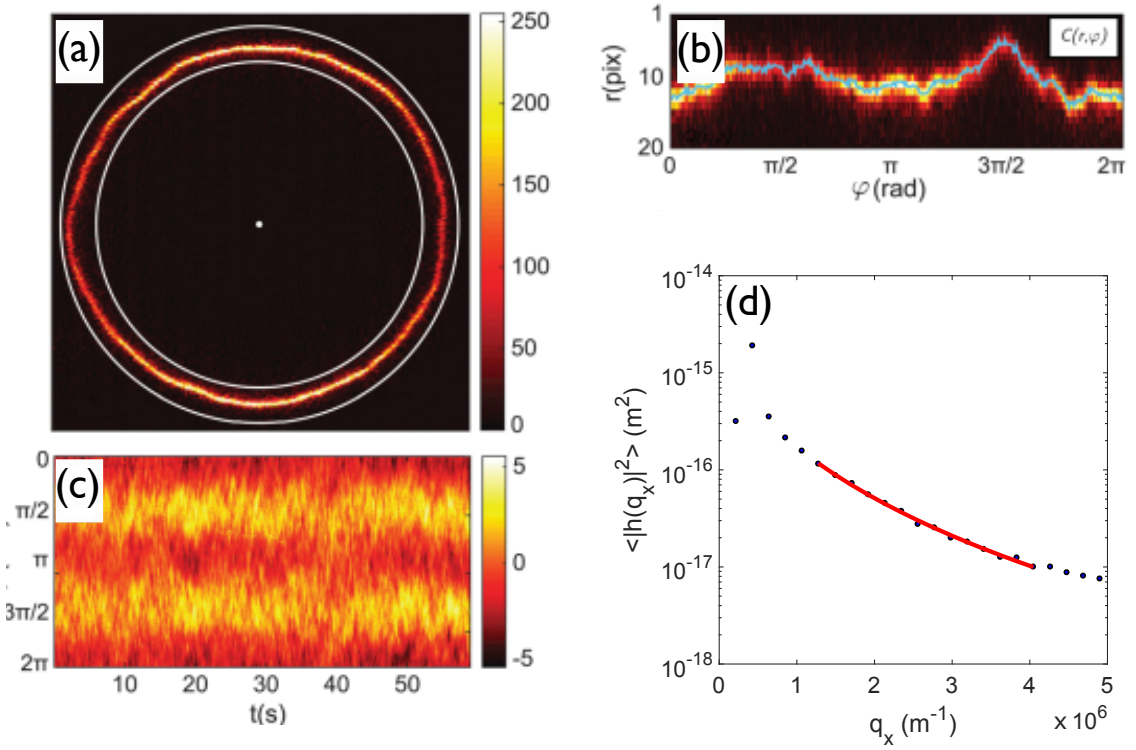

Fig. 3.2 Image analysis process for flickering spectroscopy. (a) The centre and the mean radius are detected to create an annular region in the frame. (b) The maximum of the annular region $c(r,\phi)$ is used to find the membrane contour with sub-pixel precision. The extracted contour is shown in the blue line. (c) Considering this for each image over time we can derive the radial profile ($r(\phi,t)$), and the colourmap representation of $r(\phi,t)$ shows the fluctuations of $r(\phi,t)$ relative to the average radius, where the colourbar shows the relative fluctuation as percentage. (d) The $r(\phi,t)$ is used to derive the power spectrum which can then be fitted (red line) using Eq. 3.5 to extract the membrane tension and bending modulus. (a-c) are adapted from Ref. [51].

about 3 times the spatial resolution of the microscope to include the entire radial section of the membrane. The centroid calculation is repeated 5 times, each time using the centroid found in the previous step as the initial centre for the calculation. This procedure allows for sub-pixel resolution. The whole process is repeated 3 times to further refine the results, with the vesicle's centre and mean radius from the previous iteration replacing the user-input estimates/previous centre and mean radius. The centre and radius from the previous frame are then used at the starting points for the analysis of the next frame in the algorithm.

The procedure is repeated for every frame in a video of the fluctuating membrane, with the centre and mean radius from the previous frame used as the initial centre and mean

radius for the next frame. This allows us to find the membrane radial profile $r(\phi,t)$. From this, using the MATLAB Fast Fourier Transform algorithm, the mean-squared amplitude of the power spectrum is calculated $\langle|h^2(q_n)|\rangle$, where $q_n = (2\pi/\ell)\,n$ $(n = 1,2,3,\dots)$ is the wavevector along the equatorial contour of length and M is the number of points used to map the contour ℓ [51]:

$$\langle|h^2(q_x)|\rangle = \frac{\langle|FFT(r(\phi,t))|^2\rangle_t}{M^2}. \tag{3.4}$$

The power spectrum amplitude can then be fitted within a user defined range to an established model to extract membrane tension σ and bending modulus κ (Fig. 3.2d) [190]:

$$\langle|h^2(q_x|\rangle = \frac{k_bT}{L}\frac{1}{2\chi}\left[\frac{1}{q_x} - \frac{1}{\sqrt{\frac{\sigma}{\kappa}+q_x^2}}\right], \tag{3.5}$$

where $\langle|h^2(q_x)|\rangle$ is the mean-squared amplitude of the power spectrum, q_x is the wavevector, κ is the bending modulus, L is the contour length, σ is the membrane tension, T is the absolute temperature and k_b is the Boltzmann constant.

3.5 DNA Preparation

Annealing of complementary DNA strands takes advantage of Watson-Crick base pairing to form duplexes. Quantification of the concentration of the strands is achieved via a small volume UV-visible absorbance spectrophotometer NanoDrop2000 (Thermo Scientific) that allows quantification of DNA concentrations from as little as 1 µl of sample through measuring the absorbance at 260 nm and the application of the Beer-Lambert law

$$A = \varepsilon c l, \tag{3.6}$$

where A is the measured absorbance, ε the molar extinction coefficient specific to the strand and provided by the manufacturer, c the concentration and l the pathlength.

3.5.1 DNA hybridisation protocol

DNA is designed and the equilibrium base-pairing properties analysed using NUPACK [191], and subsequently purchased with/without functionalisation (IDT or Eurogentech). Purchased DNA strands are reconstituted in TE buffer (Tris-EDTA, Sigma Aldrich) and vortexed for 4 minutes to allow mixing. Concentrations are then quantified using a nanodrop, in order to know the precise concentration of the stock solutions. These are then aliquoted, and stored at

-20°C. For hybridisation, each complementary single strands are diluted equal amounts in TE buffer containing 100 mM NaCl, and added together. To help hybridization, the solution is heated up to 90°C then slowly cooled down in a PCR machine (Eppendorf MasterCycler).

Chapter 4

Membrane Adhesion through Bridging by Multimeric Ligands

In this chapter we consider a biosensing system in which single lipid vesicles adhere to a flat supported lipid bilayer, both decorated with membrane-anchored biotinylated receptors. Adhesion is driven by multimeric streptavidin ligands forming bridges between the vesicles and the supported bilayer. Upon changing the concentration of ligands we characterise morphological and mechanical changes of the vesicles, including the formation of a stable adhesion patch, membrane tension and the kinetics of bridge rupture/formation. We observe vesicle binding only within a specific range of ligand concentrations; adhesion does not occur if the amount of streptavidin is either too low or too high. A theoretical model is presented, elucidating the mechanism underlying this observation, particularly the role of streptavidin multivalency in determining the onset of adhesion. We elaborate on how the behaviour of membranes studied here could be exploited in next generation (bio)molecular analytical devices. This chapter contains work published in the following journal publication: Ref. [38].

4.1 Multivalency: engineering responsive soft materials

Ligand/receptor multivalent interactions have been exploited to drive the self-assembly of nanoparticles, hard colloids, and more recently compliant units including emulsion droplets and lipid vesicles [42, 43, 50, 58, 51]. In deformable lipid vesicles, the formation of links between two membranes produces morphological changes depending on the concentration of inter-membrane adhesive bridges.

Recent work has demonstrated a pronounced response to temperature changes in the morphology of DNA-tethered Giant Unilamellar Vesicles (GUVs), and thereby in the porosity of vesicle networks [51, 52]. More specifically, structural change in these tissues results in a negative thermal expansion [52]. Such response emerges from the interplay between the thermal expansion of the GUVs' surface area and the rearrangement of the mobile tethers. Considering this, and the foundational theory of such systems [51, 52, 89, 192], in this chapter we test the response of adhering GUVs to changes in the concentration of free ligands in solution that mediate the adhesion, thus exploring the potential for biosensing. In view of their well understood interactions, we choose to functionalise the membranes with biotin "receptors", bridged by tetravalent streptavidin (SA) "ligands". A variety of studies on systems of vesicles utilising streptavidin-biotin interactions have been reported and discussed in Section 2.2.3, however, a detailed characterisation on the dependency of the adhesion behaviour on ligand concentration, highlighting the effect of streptavidin multivalency, has not been reported.

To unambiguously assess the response to changes in SA concentration we consider a simplified architecture in which isolated GUVs adhere to large supported lipid bilayers (SLB), and measure morphological, mechanical and kinetic features related to adhesion and deformation. In particular, the probability of GUVs forming a stable adhesion "patch" with the SLB and the resulting membrane tension are measured. Bond lifetime is accessed through Fluorescence Recovery After Photobleaching (FRAP). We propose a simple statistical-mechanical model capable of capturing the experimental phenomenology. Specifically, we demonstrate that entropic contributions deriving from the tetrameric nature of SA ligands play a crucial role in determining the onset of adhesion upon increasing ligand concentration and the trend observed in bond breakup kinetics.

The sensitivity of GUV adhesion to ligand concentration could be harnessed to design (bio)molecular detection devices featuring packings of receptor-decorated GUVs that sharply change their adhesion probability. Patch formation can then be detected optically or through electrical measurements following the change in the packings' porosity and thereby its resistance to ionic current.

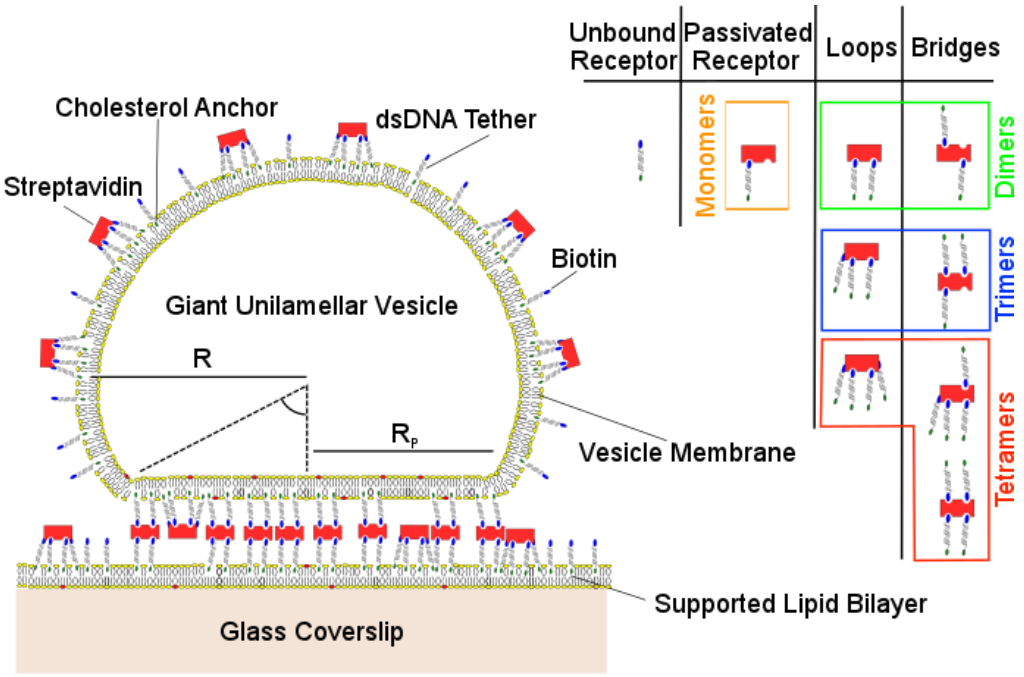

Fig. 4.1 Schematic vertical cross section of a GUV adhering to an SLB. Adhesion is mediated by intermembrane bonds formed by tetravalent SA molecules connecting multiple membrane-anchored DNA–biotin receptors. Various multimeric ligand–receptor complexes are shown in the top-right corner.

4.2 Experimental

4.2.1 Experimental Design

A schematic of the experimental system is sketched in Fig. 4.1. Following Ref. [51], we consider isolated GUVs adhering to a SLB. Compared to the study of GUV-GUV interactions, this simplified geometry enables an accurate characterisation of the membrane tension of the GUVs, as well as morphological changes. At the same time, the underlying physical mechanism of GUV-SLB and GUV-GUV adhesion are largely shared [52, 51].

Both the GUVs and the SLB are functionalised with cholesterol-anchored double-stranded DNA (dsDNA) constructs. Cholesterol anchors on the DNA allow the insertion of the construct into the lipid membrane. Interactions are not mediated by DNA-overhangs. Instead, dsDNA receptors are tipped by a biotin molecule, and streptavidin (SA) molecules dispersed in solution act as multivalent ligands. Streptavidin is a tetrameric protein that provides 4 biotin-binding sites, one pair on either side of the molecule [66]. Therefore the protein can connect multiple receptors and create molecular "bridges" between GUVs and SLB, driving

adhesion. Likewise, complexes in which a single SA connects multiple receptors bound to the same membrane are possible, indicated as "loops" (see Figs. 4.1, 4.2). SA does not affect the stability of the vesicle, making it ideally suited for our proof-of-principle experiments [66].

One may argue that simple biotin-functionalised lipids could have been used instead of biotin-tipped DNA tethers, which have long been adopted in membrane systems [69]. However, our design choice enables two key functions specifically fulfilled by the dsDNA spacers. First, they provide a steric repulsion between bilayers, stopping the membranes from getting into close contact and thus adhering through non-specific forces (e.g. van der Waals) or even undergoing fusion. We demonstrated in a recent publication how these rigid spacers force approaching bilayers at distances $> L$, where $L \sim 10\,\text{nm}$ is the length of the dsDNA [52]. Second, in the absence of dsDNA spacers, geometrical constraints due to the spatial arrangement of the binding sites on the bulky SA ligands would affect the formation of certain types of loops, as further discussed below. Long spacers relax these constraints.

4.2.2 GUV preparation

DOPC GUVs are prepared according to the protocol in Section 3.1.1, with fluorescent Oregon Green DHPE (1,2-dihexadecanoyl-sn-glycero-3-phosphoethanolamine, Thermo Fisher) used to label the vesicles, and an inner solution of 300 mM Sucrose solution in MilliQ water.

4.2.3 SLB preparation

Experimental chambers are prepared by adhering silicone rubber $6.5\times6.5\times3.2\,\text{mm}^3$ multi-well plates (Sigma-Aldrich) onto microscope coverslips ($24 \times 60\,\text{mm}^2$, No. 1, Menzel-Glaser), previously cleaned according to the protocol of Ref. [193]. The surface of the coverslip is hydrophilized by plasma cleaning (Femto, Diener Electronic), at a frequency of 40 kHz, pressure of 30 Pa, and power input of 100 W for 5 minutes. Each chamber is then immediately filled with 100 µl of a SUV solution, prepared as in Section 3.2.1 obtained by diluting the extruded samples in a ratio of 1:9 in a solution containing 5 mM $MgCl_2$ and 272 mM glucose in TE buffer. The contents of the chambers are incubated for 30 minutes at room temperature to form a defect free supported bilayer from the rupture of SUVs onto the hydrophilic glass. Excess lipids and magnesium are then removed from the chambers by two rinses with the buffer used in the experiment (hereafter indicated as "experimental buffer", TE + 100 mM NaCl + 87 mM glucose). Chambers are then filled with a known amount of experimental buffer, 110 µl below the overall capacity of the wells. Formed SLBs

are then inspected under the confocal microscope to check for uniform fluorescence and used immediately for sample preparation (Section 4.2.5).

4.2.4 DNA preparation

Double-stranded DNA tethers are assembled from two complementary 33 nucleotide long single-stranded (ss)DNA molecules purchased lyophilized from Integrated DNA Technology. One of the DNA strands is functionalised with a cholesterol molecule at its $3'$ end via a TEG linker, whilst the other has a biotin on its $3'$ end. These are prepared and hybridised according to Section 3.5.1, to create 1.6 µM of the construct in TE buffer containing 100 mM NaCl. The sequences of the two ssDNA strands are *i*) $5'$–CGT GCG CTG GCG TCT GAA AGT CGA TTG CGA AAA–$3'$–Cholesterol–TEG and *ii*) $5'$–CGC AAT CGA CTT TCA GAC GCC AGC GCA CGA AAA–$3'$–Biotin. Note that to improve flexibility, single-stranded A_4 spacers are included between the duplex and the functional groups. DNA strands were designed with high G-C content in order to enhance the thermal stability of the hybridised constructs, and without self-complementary sequences to prevent the formation of hairpins.

4.2.5 Sample Preparation

The experimental chambers prepared as described in Section 4.2.3 are filled with 90 µl of experimental buffer containing 22.2 nM of the previously hybridized DNA constructs (Section 5.3.1), immediately followed by 10 µl of the GUV solution (Section 4.2.2), previously diluted down 1:19 in 300 mM glucose solution. The DNA is expected to uniformly partition on the SLB and the GUVs. We estimate a surface density of receptors $\rho_R = 2.3 \times 10^4\ \mu m^{-2}$.

We prepare solutions at different concentrations c_{SA} of Streptavidin – Alexa Fluor 647 (Thermo Fisher) in experimental buffer, and add 10 µl to the wells before carefully mixing with a pipette, sealing with a Flexwell Seal Strip (Grace Bio-Labs), and incubating for 1 hour. The final bulk concentration of DNA receptors in the chamber is $c_{DNA} = c_0 = 18.2\,nM$. The stoichiometric ratio used as control parameter is calculated as $\chi = c_{SA}/c_0$, and ranges between 8×10^{-6} and 80. The final osmolarity of the solutions outiside and inside the GUVs is equal to 300 mM resulting in osmolarity matched samples.

4.2.6 Imaging and Image Analysis

Imaging is carried out on a Leica TCS SP5 II laser-scanning confocal microscope equipped with a Leica HCX PL APO CS 63× 1.4 NA oil immersion objective. A 633 nm He-Ne

laser and a 488 Argon-ion laser are used to excite respectively Alexa 647 labelling the SA molecules and Oregon Green labelling the membranes. Emission is collected between 497 nm and 600 nm for the Oregon Green and 639 nm and 780 nm for the Alexa 647 channels.

A customised script written in MATLAB is used for image analysis. Morphological changes in the vesicle are assessed by taking confocal Z-stacks from below the SLB to above the vesicle. Figure 4.4 shows 3D reconstructions obtained from typical Z-stacks using the 3D Viewer plugin of ImageJ [194]. The SLB plane is determined as the Z-slice with the maximum average intensity on the He-Ne channel. The presence/absence of a stable patch is determined visually. For vesicles displaying a bright adhesion patch, a Gaussian filter is applied to remove pixel-level noise. Thresholding is then used to reconstruct the patch. From the area of the patch, the patch radius R_p is derived (see Fig. 4.1). We measure the equatorial radius R (see Fig. 1) of the vesicle by analysing the Z-stack recorded on the Oregon Green channel. A circle is fitted to the vesicle contour for each Z-slice above the SLB plane. The frame with the largest circle is defined as the equatorial plane; from this the equatorial radius R is measured. The contact angle is then calculated as $\theta = \arcsin\left(R_\mathrm{p}/R\right)$.

Whenever a patch is present, from the SLB plane we also determine the ratio $\mathscr{I}$ between the average fluorescence intensities measured within and outside the patch. This ratio, measured on the Alexa 647 channel, is used to determine the ratio between the concentration of SA attached to the free standing SLB and that present on the GUV-SLB contact region. The same measurement is carried out also on the Oregon Green channel as a control.

4.2.7 Flickering spectroscopy

We use flickering spectroscopy as described in Section 3.4.1 to assess membrane tension in adhering and non-adhering GUVs. 1000 frame long videos of the GUVs' equator are recorded on the Oregon Green channel at 10.3 frames per second (fps). Adhering vesicles have much higher tension than non-adhering ones [51] reducing the amplitude and correlation time of the fluctuations [190]. Due to limited spatiotemporal resolution of our instrument we are therefore unable to access $\langle|h^2(q_n)|\rangle$ within a sufficiently broad range of q_n for the fitting to be reliable. Thus for adhering vesicles we use the mean squared-amplitude of the low-q equatorial mode 3 as a qualitative indicator for membrane tension. Mode 3 is the longest wavelength undulatory mode carrying unbiased information on the membrane tension, with mode $n = 1$ being associated to vesicle translation and mode $n = 2$ describing changes in eccentricity and being heavily biased by imaging artefacts [189]. The longest

wavelength undulatory mode is necessary as the tense adhering vesicles' high-q mode, short wavelength membrane fluctuations decorrelate faster than the spatiotemporal resolution of the microscope; therefore longer wavelength, low-q modes are required to acquire a non-biased signal.

4.2.8 Fluorescence recovery after photobleaching

Fluorescence recovery after photobleaching (FRAP) is carried out to determine binding/unbinding kinetics of inter-membrane bonds using the dedicated Leica software. FRAP is a method for quantifying lateral diffusion, well suited for studies of effects confined on lipid membranes. The method involves imaging a defined area containing a specific fluorescent molecule, photobleaching said area, and imaging the area again over time to observe the recovery of fluorescence.

We consider adhering GUVs, and after imaging the adhesion area on the SLB plane for 10 s, we bleach the SA molecules within the adhesion patch by exposing it to high-intensity excitation light for 9.7 s. We then monitor the fluorescence recovery of the bleached area for 1235 s. For the first 10 seconds we image at 10 fps and thereafter at 0.5 fps for 4 minutes and subsequently at 0.1 fps. The ratio $\mathscr{I}(t)$ between fluorescence intensities measured within and outside the adhesion patch is measured as a function of time as described in Section 4.2.6, with $t = 0$ corresponding to the first frame taken after bleaching. The recovery in $\mathscr{I}(t)$ carries information about loop-like complexes and passivated receptors rapidly diffusing in and out the adhesion patch, as well as bridge-like complexes that require unbinding events in order to leave the adhesion area (see Fig. 4.1).

4.3 Modeling streptavidin/DNA complexation

Much of the phenomenology discussed in the remainder of this chapter arises from the possibility of each SA ligand to bind between one and four biotin-DNA receptors. We indicate the resulting multimeric complexes as *monomers*, *dimers*, *trimers*, and *tetramers*, as sketched in Fig. 4.2. Given its strong affinity, it is safe to model SA/biotin linkages as irreversible, meaning that the fraction of ligands involved in each of the multimeric complexes is fixed at the moment of sample preparation and remains unchanged throughout the experiment. In turn, as discussed in Section 4.4.5, cholesterol anchors can detach and reinsert to/from the

bilayers (with the off-rate of the bond between a cholesterol-tethered DNA molecule and a lipid bilayer of $5.8\times10^{-4}s^{-1}$ [83]), enabling equilibration of the populations of loop-like and bridge-like complexes over accessible time-scales.

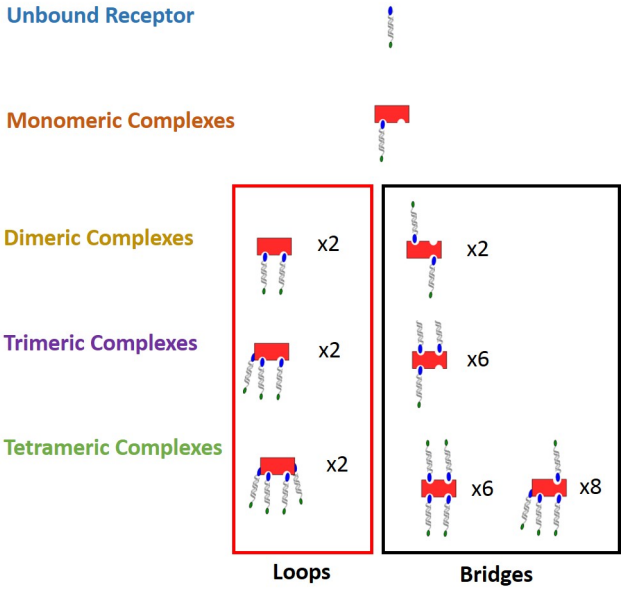

Fig. 4.2 Possible configurations of the SA-Biotin complex. Free receptors are unbound to a SA molecule, whereas momeric, dimeric, trimeric and tetrameric complexes are SA's with 1, 2, 3 or 4 of their binding sites occuppied by a receptor respectively. The number of configurations of each type of conformation are also indicated thereby demonstrating the probability of either a loop or bridge forming.

We label the total bulk concentration of DNA-receptors and SA as $c_{\mathrm{DNA}} = c_0$ and $c_{\mathrm{SA}} = \chi c_0$, while $c_{1,k}$ (with $k = 1,\cdots 4$) denotes the concentrations of complexes made by k DNA strands binding a SA (see Fig. 4.2). For a given stoichiometric ratio χ, $c_{1,k}$ can be calculated using equilibrium chemical reactions

$$c_{1,k} = K c_{1,k-1} c_{0,1} \qquad\qquad k \in [1,4], \tag{4.1}$$

where $c_{1,0}$ and $c_{0,1}$ are the concentrations of unbound DNA and SA, and K is the association kinetic constant of the SA-biotin complex (in this work $K \to \infty$). The conservation of total number of DNA and SA molecules implies

$$\begin{aligned} c_0 &= c_{0,1} + c_{1,1} + 2c_{1,2} + 3c_{1,3} + 4c_{1,4}\,, \\ c_0\chi &= c_{1,0} + c_{1,1} + c_{1,2} + c_{1,3} + c_{1,4}\,. \end{aligned} \tag{4.2}$$

Two concentration regimes can be identified $\chi > 1/4$, and $\chi \leq 1/4$.

$\underline{\chi > 1/4}$. Because association between DNA and SA is maximized ($K \to \infty$ in Eq. 4.1), at high χ no unbound DNA is left in solution ($c_{0,1} = 0$) while free SA is present ($c_{1,0} > 0$). From Eq. 4.1, taking $Kc_{0,1}$ constant, we obtain

$$\alpha = \frac{c_{1,4}}{c_{1,3}} = \frac{c_{1,3}}{c_{1,2}} = \frac{c_{1,2}}{c_{1,1}} = \frac{c_{1,1}}{c_{1,0}}, \tag{4.3}$$

and using Eq. 4.2 with $c_{0,1} = 0$ we obtain

$$c_{1,0} = \frac{c_0}{\alpha + 2\alpha^2 + 3\alpha^3 + 4\alpha^4}, \tag{4.4}$$

$$\chi = \frac{1 + \alpha + \alpha^2 + \alpha^3 + \alpha^4}{\alpha + 2\alpha^2 + 3\alpha^3 + 4\alpha^4}. \tag{4.5}$$

Equation 4.5 admits a unique solution for α that can be used to calculate $c_{1,0}$ first (see Eq. 4.4), and then $c_{1,k}$ by using Eq. 4.3 and the value of $c_{1,0}$.

$\underline{\chi \leq 1/4}$. When $\chi = 1/4$ only tetramers are present in solution ($c_{1,4} = \chi c_0$), while $c_{1,0} = 0$. For $\chi \leq 1/4$ the amount of SA is not sufficient to bind all the available receptor strands resulting in a finite concentration of free DNA with concentration $c_{0,1} = c_0(1 - 4\chi)$.

Assuming that biotin-SA association is much faster than cholesterol adsorption into the lipid bilayers [195, 83], we now estimate the concentration of bridge-like complexes within the patch area. We neglect interactions between different complexes and calculate the probability of finding a complex in the patch area given the concentration of the same complex on the lipid bilayer outside the patch area, that is modelled as an infinite reservoir. The surface densities ρ_X ($X = \{1,0\}, \{0,1\}, \{1,k\}, k = [1,4]$) are proportional to the bulk concentration $\rho_X = a \cdot c_X$, with a that does not depend on the type of complex. Neglecting the surface area of the GUVs as compared to that, much larger, of the SLB, and assuming that all of the receptors partition on a lipid membrane [83], we estimate $a \simeq 2.1 \times 10^3$ μm^{-2} nM^{-1}. Whilst this is only strictly true if all of the cholesterol anchors absorb onto the bilayer, this should be the case given the dissociation constant of 17nM.

Complexes found within the patch area can have either a loop-like or a bridge-like character as sketched in Fig. 4.2. We assume that configurational costs of adsorbing a complex in loop-like or bridge-like configurations are equal. Recent work suggests that this is the case for distances between the GUV patch and the SLB comparable with the DNA strand length

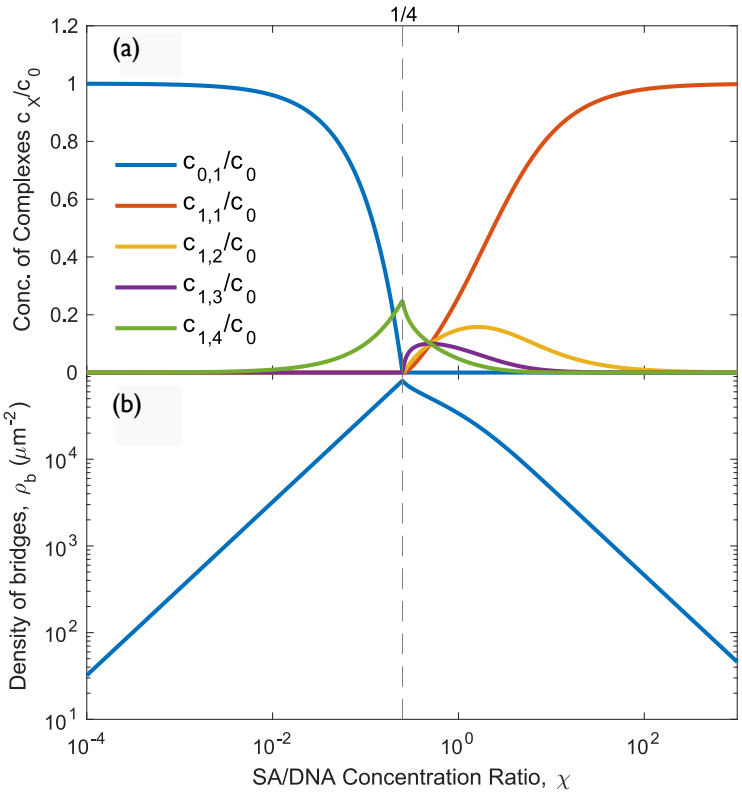

Fig. 4.3 Modeling distribution of multimeric complexes. (a) Fraction of receptors involved in different complexes with SA ligands as a function of the relative ligand concentration χ. For $\chi \geq 1/4$, only tetramers are present. Trimers, dimers, and monomers appear for $\chi > 1/4$. If the SA concentration is further increased, the majority of the receptors are passivated by a single ligand. (b) Surface density of bridge-like complexes ρ_b as a function of χ. ρ_b peaks at $\chi = 1/4$ and drops upon increasing or decreasing the SA concentration, compatible with the observation on GUV adhesion.

employed here [51–53]. In particular, this assumptions is also justified by the configurational freedom enabled by the use of freely rotating dsDNA spacers. Since pairs of binding sites are arranged on opposite sides of the SA molecules, if biotin receptors were directly grafted to the lipids [69] the formation of loops with tetrameric complexes would be highly hindered. However, since dsDNA spacers ($L \sim 10\,\mathrm{nm}$) are longer than the diameter of SA ($\sim 5\,\mathrm{nm}$), and cholesterol and biotin are connected through flexible spacers made of four unpaired bases, all possible binding configurations are geometrically accessible.

Each complex of type $\{1,k\}$ in the patch region has 2^k possible ways of arranging the k DNA "arms" between the two bilayers. Out of these, 2 configurations are loop-like, and the remaining 2^k-2 are bridge-like (Fig. 4.3). It follows that dimers ($k=2$) have equal chances of forming loops or bridges, but trimers ($k=3$) and tetramers ($k=4$) are more likely to form bridges than loops by a factor 3 and 7 respectively.

In Fig. 4.3b we therefore show the surface density of bridge-like complexes within the patch, calculated as $\rho_b = a\sum_{k=1}^{4}(2^k-2)c_{1,k}$. We observe a region of intermediate SA concentrations with a high density of bridges that peaks at $\chi = 1/4$.

4.4 Results and Discussion

4.4.1 Morphological response to ligand concentration

The 3D reconstructions from confocal Z-stacks shown in Fig. 4.4 as recorded on the Oregon Green (lipid) channel, exemplify the morphological difference between an adhering vesicle having the shape of a truncated sphere (Fig. 4.4 b) and a more spherical non-adhering one (Fig. 4.4 a). The clear shape difference enables to distinguish easily between adhering and non-adhering vesicles, as also demonstrated in Fig. 4.5a where we show vertical confocal sections of the GUVs, the equatorial cross sections and the SLB plane, all recorded on the SA (Alexa 647) fluorescence channel. Figure 4.5b shows the observed fraction of adhering GUVs as a function of the bulk concentration ratio between SA ligands and receptors (χ).

Three regimes can be clearly identified: *low* ($\chi \lesssim 3\times10^{-4}$), *intermediate* ($3\times10^{-3} \lesssim \chi \lesssim 20$), and *high* ($\chi \gtrsim 20$) SA concentration. The theoretical estimate of Section 4.3 indicate that in the low ligand concentration regime all of the SA receptors give rise to tetrameric complexes, but the number of bridges formed between the GUV and the SLB is still too low to cause the formation of a stable adhesion patch (see Fig. 4.3b). Within the broad range of

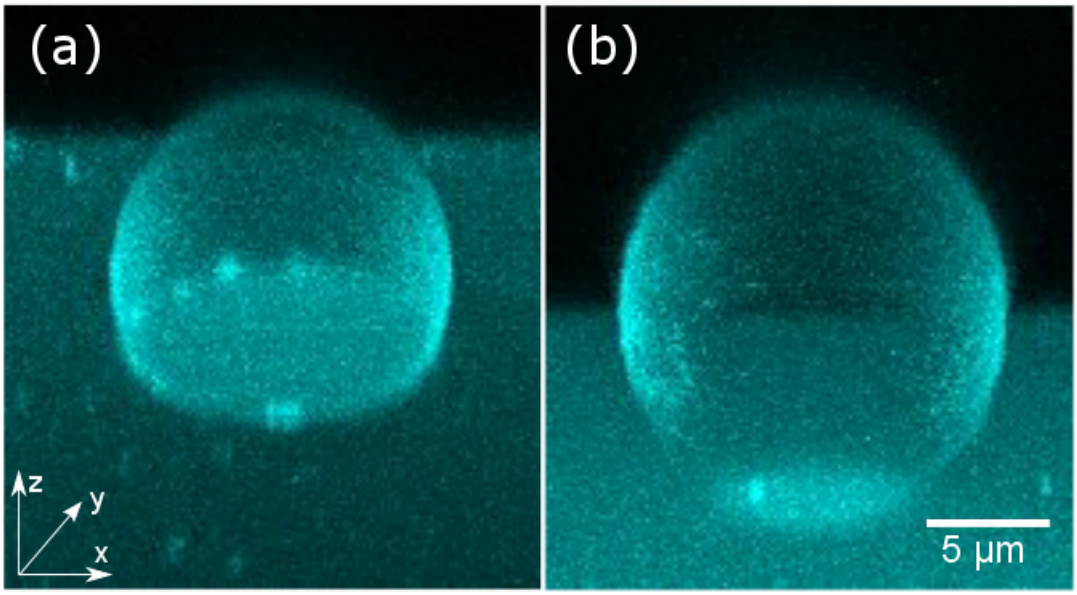

Fig. 4.4 (a) Confocal 3D reconstruction of a GUV adhering to an SLB, as acquired by imaging fluorescently labeled lipids. (b) Confocal 3D reconstruction of a non-adhering GUV.

intermediate SA concentrations a stable adhesion patch is observed for the majority of the GUVs. Here the confocal lateral and equatorial sections demonstrate the presence of SA molecules on the GUV and SLB membranes.

Adhesion sets in already at $\chi \approx 3 \times 10^{-4}$ where only a small fraction of the receptors are bound to ligands. However most of the receptors form tetrameric complexes with large chances of bridge formation, resulting in a sufficiently high number of GUV-SLB bonds (see Fig. 4.3b). The strong tendency towards bridge formation of tetrameric complexes also produces a significant accumulation of SA within the adhesion patch, as compared to non-adhering areas of the SLB and GUV. Indeed, the ratio between Alexa 647 fluorescence intensity measured within and outside the patch at $\chi = 8 \times 10^{-4}$ is $\mathscr{I} = 16.7 \pm 8.1$. When the number of SA molecules exceeds 1/4 of that of the DNA receptors, all of the binding sites are saturated, and some of the SA ligands are bound to three or fewer receptors. As we approach the high-concentration regime, for $\chi = 8$, the SA fluorescence intensity ratio between the adhesion patch and the free SLB drops to $\mathscr{I} = 2.18 \pm 0.33$. Here, most of the DNA receptors are passivated by single SA and therefore uniformly distributed across the membranes within and outside the patch, hence explaining the intensity rato approaching the limit of non-interacting membranes (i.e. 2). Only a small number of ligands are involved in

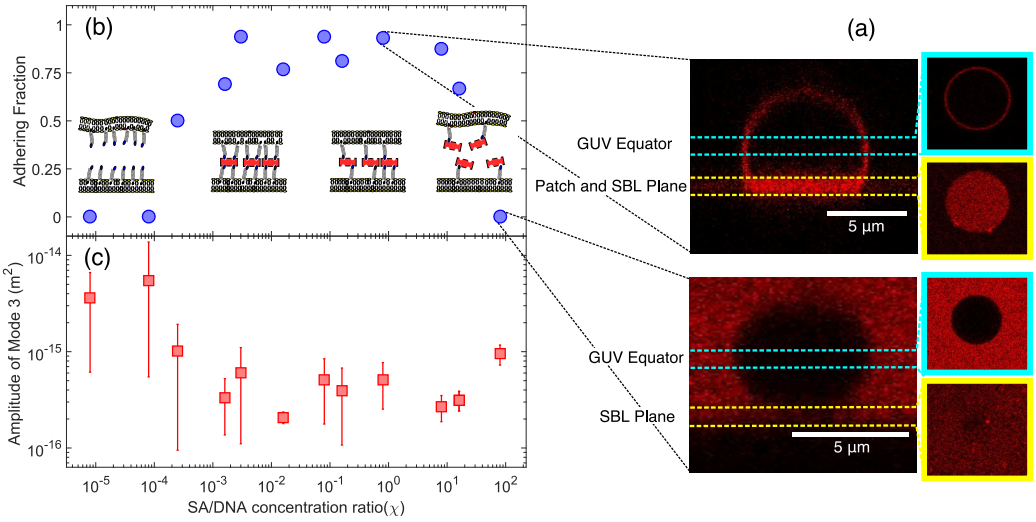

Fig. 4.5 Quantifying GUV adhesion and induced membrane tension. (a) Confocal cross section, equatorial section, and SLB plane in an adhering GUV (top, $\chi = 8 \times 10^{-1}$) and a non-adhering GUV (bottom, $\chi = 8 \times 10^{1}$). (b) Fraction of adhering GUVs as a function of the relative ligand concentration χ, as determined by visual inspection in a sample of $>$ 15 GUVs. The insets sketch the architecture of complexes expectedly present within the adhesion patch. Adhesion is observed within an *intermediate* range of concentrations, where the surface density of bridges is sufficiently high (see Fig. 4.3b). (c) Mean-squared amplitude of equatorial fluctuation mode $n = 3$ as measured *via* flickering spectroscopy. The amplitude drop in the intermediate regime corresponds to an increase in membrane tension induced by adhesion. Experimental points and errorbars are calculated as the mean and standard deviation in a sample of $>$ 15 measurements.

mutlimeric complexes stabilising the patch.

For $\chi \gtrsim 20$ we enter the high-concentration regime, where nearly all SA are either free in solution or tethered to a single receptor, and number of multimeric SA complexes is too low for stable adhesion. Confocal lateral and equatorial sections confirm that in the high concentration regime most of the SA molecules remain free in solution (Fig. 4.5a).

4.4.2 Contact angle

Measurements in the contact angle (taken only for adherent vesicles) as a function of χ showed no dependency on χ (Fig. 4.6b). Large error bars point to the large variation in contact angles recorded. This was hypothesised to be due to the variation of tension between adhering vesicles, and plotted the tension of the vesicles ($\langle |h^2(q_3)| \rangle$ values) against the

contact angle (Fig. 4.6 a). Again there was no relationship.

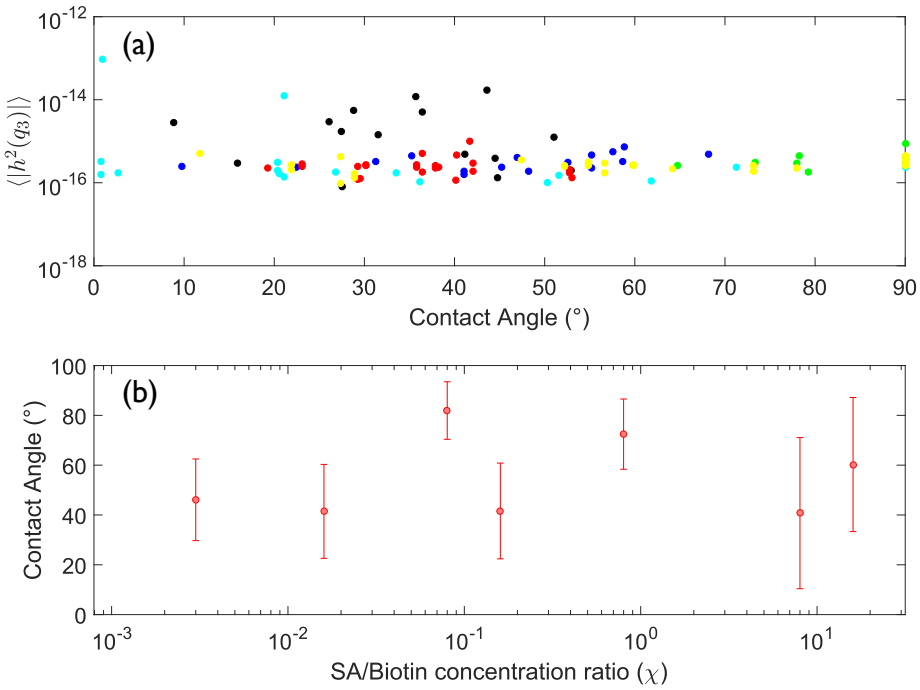

Fig. 4.6 Adhering Vesicle Contact Angle. (a) Response of a subset of vesicle's contact angle to tension, measured here by the mean-squared amplitude of equatorial fluctuation mode $n = 3$, proportional to 1/membrane tension. Colours represent adhering vesicles at different χ. (b) The response of contact angle to varying χ. Experimental points and errorbars are calculated as the mean and standard deviation in a sample of > 15 measurements.

This lack of variation in contact angle as function of any of the aforementioned parameters can be explained by the polydispersity of the vesicles formed through electroformation. This causes there to be variations in the excess area of each vesicle. The excess area is the difference between the surface area of the vesicles and the area, given the internal volume if the vesicle were a perfect sphere. Vesicles that are more floppy (smaller internal volume, larger excess area) can therefore take the shape of truncated spheres with relatively larger patches, which corresponds to a larger contact angle. In the limit of unstretchable membranes the size can be computed from the reduced volume, and would be independent from the strength of the adhesion. In reality, the adhesion forces stretch the membrane slightly, causing the patch and contact angle to be a slightly larger than it would be for unstretchable membranes. However, since the membranes are hard to stretch, this deviation in contact angle is small and negligible compared to the deviation caused by these variations in excess areas of the vesicles. Were the excess area of the vesicles equal or known, this deviation may be have been measur-

able. Therefore having monodisperse vesicles, with constant excess area, would enable a more accurate study of the effect of adhesion at varying ligand concentration on contact angle.

Some techniques for measuring the excess areas of vesicles do exist: Pommella *et al.* measured the excess area by analysing vesicle deformation in a capillary flow [196], whereas Zhou *et al.* studied the relaxation back to a sphere of vesicles after they equilibrium after deformation far from equilibrium by optical tweezers [197]. However, this would only allow for taking enough measurements to measure average excess areas in the sample (as the methods could not be applied to adhered vesicles), but the variation in excess area in polydisperse samples will be large, rendering the measurement uninformative.

4.4.3 Mechanical response: Membrane tension

Figure 4.5c shows the mean-square amplitude $\langle|h^2(q_3)|\rangle$ of equatorial fluctuation mode $n = 3$ as a function of χ. In the high-tension limit, the rough proportionality $1/\sigma \propto \langle|h^2(q_3)|\rangle$ holds, that however cannot be used to quantitatively extract σ [190]. Nonetheless, the three adhesion regimes are clearly reflected in $\langle|h^2(q_3)|\rangle$. In the low-SA-concentration regime non-adhering vesicles display $\langle|h^2(q_3)|\rangle \approx 10^{-14} - 10^{-15}$ m^2. In the intermediate regime, from the onset of adhesion, we observe a drop in fluctuation amplitude, with $\langle|h^2(q_3)|\rangle$ decreasing by approximately one order of magnitude. Within this regime where most vesicles are adhering we observe $\langle|h^2(q_3)|\rangle$ decreasing with χ. As we approach the high-SA-concentration regime, the lack of adhesion causes an increase in fluctuation amplitude due to their membranes not adhering.

The sharp changes in tension at the boundaries between the three regimes demonstrate the correlation between GUV morphology, i.e patch formation, and mechanical properties for the membranes.

Although, as explained in Section 4.2.7 the membrane tension σ cannot be reliably measured within the intermediate regime, in the low- and high-SA-concentration regimes an accurate estimate can be extracted by fitting $\langle|h^2(q_n)|\rangle$. At χ=8×10^{-6}, we obtain $\sigma = 1.8 \times 10^{-6} \pm 5 \times 10^{-7}$ Nm. The large errorbar is partially a consequence of the broad distribution of excess areas typical of electroformed lipid vesicles, as discussed in Section 4.2.2. In adhering vesicles differences in excess area result in changes in the size of the adhesion patch, which has a smaller influence on membrane tension [51].

4.4.4 Quantifying Ligand Distribution

Within the broad range of intermediate SA concentrations a stable adhesion patch is observed for the majority of the GUVs. Here the confocal lateral and equatorial sections demonstrate an accumulation of SA molecules on the GUV and SLB membranes (Fig. 4.5a, left). Conversely, at very high concentrations of SA, when the vesicles do not adhere, confocal lateral and equatorial sections confirm that in the high concentration regime most of the SA molecules remain free in solution (Fig. 4.5 (a), right), and at very low concentrations of SA, no SA can be observed.

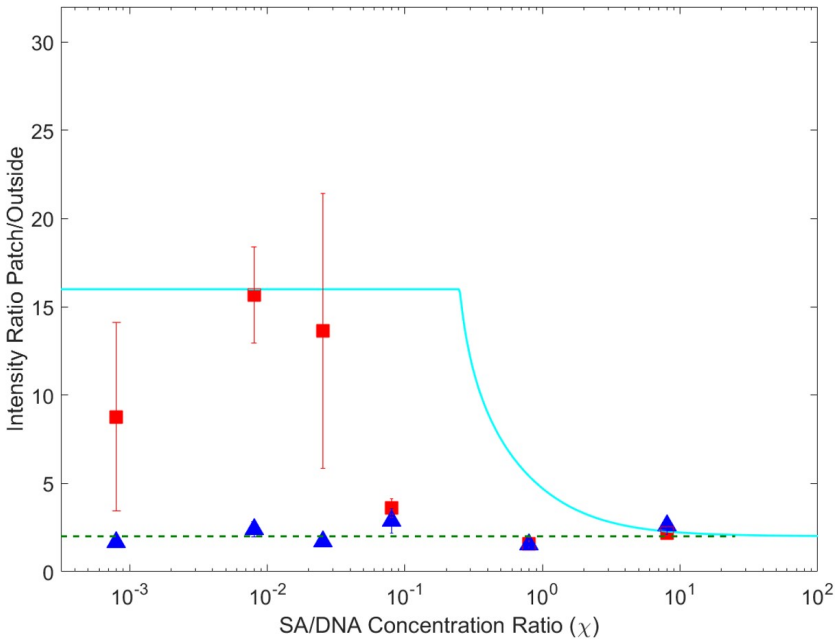

Fig. 4.7 Quantifying ligand distribution. Red squares indicate the ratio between the fluorescence intensity I of Alexa 647 tagged ligand molecules between the adhesion patch and the surrounding free SLB. The solid line marks the theoretical prediction of I, estimated as detailed in the Section 4.3, based on the proportion of different multimeric SA complexes. Insets sketch complexes' distribution in different regimes. Blue triangles mark the fluorescence intensity ratio between the patch and the surrounding SLB as measured using the Oregon Green dye labelling the lipid membranes. Experimental points and errorbrars are calculated as the mean and standard deviation in a sample of >15 measurements.

In the intermediate regime a stable circular adhesion patch is present between SLB and GUVs. The image of the SLB plane shows that in the intermediate regime adhesion patches are significantly brighter than the surrounding SLB, indicating an overall accumulation of the SA molecules being trapped in bridge-like multimeric complexes. By comparing the

fluorescence intensity of the adhesion patch with that of the surrounding SLB, as measured on the Alexa 647 channel, we can quantify the fraction of SA receptors trapped within the adhesion patch in bridge-like complexes. As a control, we also considered the distribution of fluorescently tagged lipids. Figure 4.7 shows the measured patch/SLB intensity ratio I as a function of χ. Following the arguments of Section 4.3 we can predict

$$I = \frac{\sum_{k=1}^{4} \left(2^k + 2\right) c_{1,k}}{2\sum_{k=1}^{4} c_{1,k}}, \tag{4.6}$$

where the numerator accounts for the concentration of bridge-like complexes and loop like complexes tethered to both membranes within the patch. The denominator accounts for the loop-like complexes on the free SLB. For $\chi \leq 1/4$ only tetramers are present ($c_{1,4} = c_0, c_{1,1\ldots3} = 0$), and Eq. 4.6 predicts a constant $I = 16$. As χ increases above 1/4, the presence of complexes with $k < 4$ causes a drop in I. Upon further increase in SA concentration the majority of the receptors are be passivated by a single SA molecule ($c_{1,2\ldots4} \approx 0, c_{1,1} \approx c_0$) which, similarly to loop-like complexes, are uniformly distributed across both membranes. Here I approaches its asymptotic value $I \simeq 2$, corresponding to uniform distribution of SA molecules on receptors within and outside the patch for both the SLB and the GUV membranes. In fact, since the inter-membrane distance ($\approx$20nm) is much smaller than the vertical resolution of the microscope, the apparent brightness of an adhesion patch between two membranes featuring the same density of fluorophores is twice that of a singe membrane. The patch/SLB intensity ratio also on the Oregon Green (lipid) channel was also measured and find as expected $I_{lipid} \simeq 2$, due to the same uniform distribution of fluorophores coupled with the vertical resolution of the microscope.

4.4.5 FRAP measurements of bond reversibility

Figure 4.8a shows a sequence of confocal images of an adhesion patch as taken in the Alexa 647 (SA) channel over a typical FRAP experiment. Before the bleaching step, a clearly defined bright patch is visible, with a patch/SLB intensity ratio equal to $\mathscr{I}_{\mathrm{PB}}$. Exposure of the adhesion area to high-intensity excitation causes an almost complete bleaching of the SA molecules. Recovery is then followed over time by monitoring the patch/SLB intensity ratio $\mathscr{I}(t)$.

The adhesion patch is populated by both loop-like and bridge-like complexes (see Fig. 4.1). The former, together with passivated receptors, can freely move in and out the patch area through lateral diffusion on either SLB or GUV membranes, resulting in a

quick recovery of part of the fluorescence signal. In turn, the bridge-like complexes are confined within the patch area being able to leave only upon bond breakup. Full recovery of the fluorescent signal therefore occurs on timescales dependent on the breakup of GUV-SLB bonds. In view of these two time-scales, we fit the patch/SLB intensity ratio $\mathscr{I}(t)$ with a double exponential

$$1-\frac{\mathscr{I}(t)}{\mathscr{I}_{\mathrm{PB}}}=A\exp\left(-\frac{t}{\tau_1}\right)+(1-A)\exp\left(-\frac{t}{\tau_2}\right), \tag{4.7}$$

where τ_1 is the fast recovery time associated to diffusion of loop-like complexes and passivated receptors, τ_2 ($>\tau_1$) is the slow recovery time associated to bridge breakup, and A is a parameter quantifying the fraction of the initial fluorescence intensity undergoing fast recovery.

Figure 4.8b shows recovery curves collected at different χ and fitted with Eq. 4.7, while Fig. 4.8c summarises the dependency of τ_2 on χ. Two processes could be involved in the bridge breakups leading to full recovery of the signal: the breakup of biotin/SA bonds or the yielding of the connection between the cholesterol anchor and the lipid bilayers. The off-rate of biotin/SA bonds, as estimated according to the parametric formula of Koussa *et al.* [195] is $k_{\mathrm{off}}=6.3\times10^{-7}$ s^{-1}. The off-rate of the bond between a cholesterol-tethered DNA molecule and SBL, as evaluated by Pfeiffer and Höök [83], is comparatively much higher: $k_{\mathrm{off}}=5.8\times10^{-4}$ s^{-1}, and compatible with the recovery timescales we measure. We can therefore deduce that the process responsible for bond rearrangement in our systems is the thermal extraction of cholesterol anchors from the lipid bilayers.

Figure 4.8b demonstrates a drop in τ_2 as χ increases within the intermediate-SA-concentration regime. This behaviour can once again be qualitatively explained by the χ-dependence of the valence of multimeric complexes. For $\chi\leq1/4$ ligands form only tetrameric complexes and, as discussed in section 4.3, 7 out of 8 tetramers are in a bridge-like configuration. Among these, 4/7 have three receptors anchored to the one membrane and one to the other, while 3/7 have two receptors on each membrane. The latter complexes therefore need to break and reform at least two bonds in order to turn into loop-like complexes and diffuse out of the membrane, resulting in a slow fluorescence recovery. As χ is increased above $1/4$, a fraction the bridge-like complexes are trimers or dimers, that can exit the adhesion patch by breaking and reforming only one bond, hence fluorescence recovery is faster.

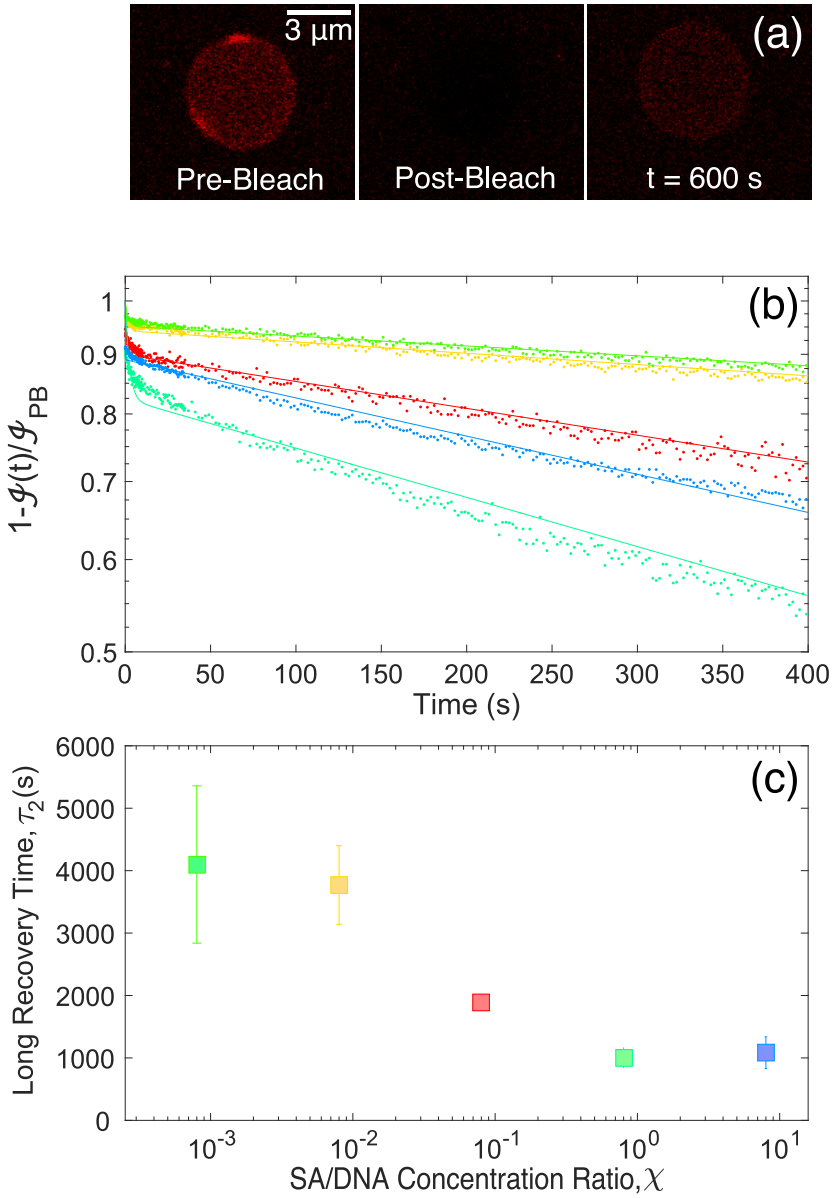

Fig. 4.8 Fluorescence recovery after photobleaching measurements of bridge unbinding kinetics. (a) Sequence of images of the adhesion patch before the SA molecules are bleached (left), immediately after bleaching (middle), and after partial recovery of the fluorescence intensity has occurred (right). (b) Fluorescence recovery profiles: $1-\mathscr{I}(t)/\mathscr{I}_{\mathrm{PB}}$. Solid lines are best fits using Eq. 4.7. (c) Slow-recovery time constant τ_2 (see Eq. 4.7) as a function of relative SA concentration χ. Experimental points and errorbars are calculated as the mean and standard deviation in a sample of >7 measurements.

4.5 Conclusion

We have studied morphological and mechanical response in single giant lipid vesicles adhering to a flat supported lipid bilayer, caused by changes in the concentration of the ligand molecules mediating the attraction. Biotin-functionalised DNA receptors are tethered to the membranes through a cholesterol anchor. Streptavidin ligands dispersed in solution bind the receptors forming multimeric complexes that feature one to four receptors *per* ligand. The complexes can either take a loop-like arrangement, when all of the bound receptors are anchored to the same membrane, or bridge between the GUVs and the SLB.

For a fixed concentration of ligands, we observe stable adhesion only when the concentration of SA receptors falls within a well-defined range. Adhering vesicles display a large increase in membrane tension, which is shown can directly probe the SA-mediated adhesion strength. Furthermore, we find the contact angle to be independent of the concentration of SA within the adhering regime, which can be understood through the dominating effect of suppression of the excess area compared to the contributions of adhesion induced stretching. We find an accumulation of SA receptors within the adhesion patch as compared to the concentration of those tethered to free membranes, which becomes less pronounced at higher SA concentrations. The unbinding kinetics of intermembrane bridges, caused by the reversibility of cholesterol insertion, is probed *via* FRAP. The average unbinding rate of bridges is lower at low SA concentrations.

The observed phenomenology can be rationalised with a simple model that accounts for the tetravalent nature of SA-biotin complexes. Re-entrant unbinding upon increasing linker concentration is a general phenomenon, but here the effect is rationalised for the case of diffusive multimeric linkers.

We argue that the sharp onset of vesicle adhesion could be exploited to build (bio)molecular sensing devices the purpose of which would be to sense the presence of an analyte above a certain concentration threshold that triggers membrane adhesion and changes in shape and tension of the vesicles. The detection threshold can potentially be tuned by including synthetic linkers (e.g. made of DNA) forming a small number of permanent bridges, enough to bring the membranes very close to the onset of adhesion. From there, a very small amount of the target ligand would trigger adhesion and therefore be detected. Readout can be done optically or via impedance measurements using microfluidic devices featuring integrated electrodes.

Furthermore, the findings presented here are relevant to the study of multivalent interactions in adhesion between cells, in particular those dependent on linker molecules such as cadherins and selectins.

Chapter 5

Assessing Microdynamics of DNA-LUV Gels with Spatially Resolved DDM

In this chapter we study a gel consisting of Brownian Large Unilamellar Vesicles (LUVs), adhering together through attractive interactions of membrane-functionalised complementary DNA. Temperature and aging dependent properties are studied using a spatially resolved Differential Dynamic Microscopy (DDM) technique. More specifically, we probe the dynamics and statics of the system; both on melting of a gel, and quenching of a sol. By utilising spatially resolved DDM, we gain insight into the spatial heterogeneity of these processes. All of this is contextualised within existing work on vesicles adhering through multivalent DNA-mediated interactions.

5.1 Gels and DDM

A brief overview of the underlying theory on gel dynamics, specifically in colloidal systems, is provided in Section 2.3.3. The literature is comprehensive for systems with hard colloids, however, it far sparser on systems built upon aggregating soft particles. Whilst work using soft particles exists [115, 114, 198–200], to our knowledge, no study on the dynamics of vesicle-based gels at low volume fractions has been undertaken. The mechanics of interacting vesicles adhering through selective interactions, such as the use of DNA linkers, as well as the statics of self-assembled structures, has been probed through experiment and simulation [52, 86]. However, the bulk dynamics of self-assembled structures based on adhering lipid vesicles remain unexplored. Studying the dynamics of these self-assembled materials in response to an external variable such as temperature, would elucidate another degree of responsiveness of the material and marry our existing understanding of the underlying

mechanisms of vesicle-vesicle adhesion with bulk properties of the material. Furthermore, microrheological insight garnered through this is particularly informative given that creating sufficient volume of samples for conventional rheological measurements is non-trivial. As such, we utilise a system of diffusive vesicles functionalised with a thermoresponsive linker; cholesterol anchored dsDNA constructs with complementary ssDNA sticky ends, to probe the response of the material to temperature change.

We achieve this using a relatively recent technique, covered more extensively in Section 3.3; DDM. DDM has been applied to study gels [114, 201, 202], and offers the ability of deriving scattering measurements from simple optical microscopy images, and the simultaneous probing of a wide range of scattering angles advantageous when compared to DLS, as well as the ability to correlate dynamics and statics with visualisation of structure [176]. Indeed, by using spatially resolved DDM, whereby we consider subsections of the image, we can assess the different dynamics present in the sample; particularly useful for probing spatially heterogeneous structures.

5.2 DNA-LUV gel

The gel consists of vesicles made through extrusion as in Section 3.2, through membranes with 1 μm diameter pores. These vesicles are Brownian, and as such, freely diffuse at sufficiently dilute volume fractions. A similar system was studied, with specific focus on the linker concentration dependency of the phase transition in Ref. [86].

These vesicles are functionalised with a dsDNA construct with a short ssDNA overhang, with the construct anchored in the bilayer with a double cholesterol anchor, and given flexibility with 4 unpaired adenine bases (Fig. 5.1c). Two types of constructs are used; an A construct and A' construct which have ssDNA overhangs that are complementary to one another, but non-complementary to themselves. These constructs cause an attractive potential between vesicles allowing for vesicle-vesicle adhesion below the gel point (T_g), and the formation of a gel (Fig. 5.1a). At temperatures above the melting temperature of the gel (T_m), the ssDNA overhangs will not bind, and in fact act as polymer brushes with short-range repulsive steric effects, removing the attraction between the vesicles and causing the system to be in a sol rather than gel state. The cholesterol anchors allow for the free diffusion of the constructs across the surface of the vesicle, and therefore, combined with the deformability of the vesicle upon adhesion, allows for more flexibility in the potential geometries that can be formed, and denser packing when compared to hard colloidal gels with grafted

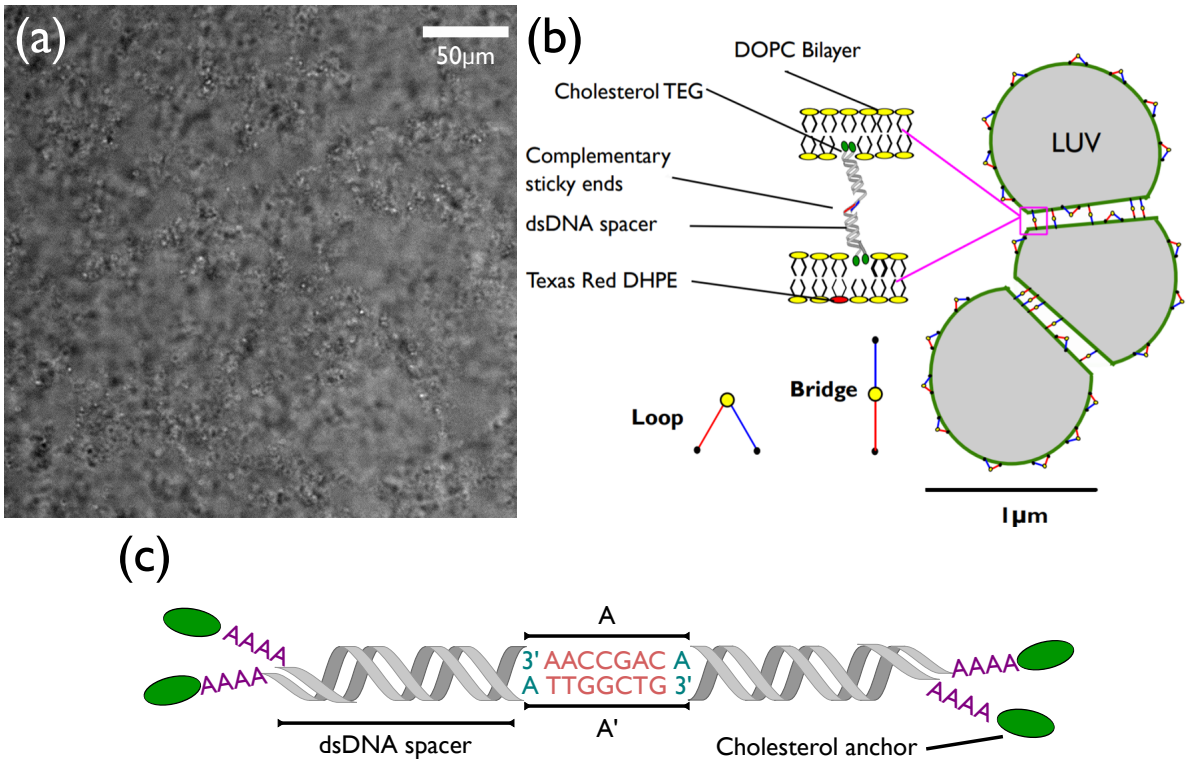

Fig. 5.1 (a) Brightfield image of a LUV-DNA gel, showing a clear network of vesicles spanning the frame of the image. (b) A schematic of the interactions mediating the formation of the gel, whereby complementary ssDNA overhangs on dsDNA membrane bound constructs form adhesive bridges between lipid vesicles. (c) An adhesive bridge between the two membrane bound constructs, A and A', with complementary ssDNA overhangs indicated in red.

attractive DNA/polymer interactions where the degrees of freedom are more limited. The double-anchor ensures that the construct remains in the bilayer during the timescales at which we consider; from the work of Pfeiffer and Höök the insertion of a double cholesterol anchor into a lipid biylayer is effectively irreversible for experimentally relevant timescales [83].

5.3 Methods

5.3.1 DNA preparation

Type A and A' dsDNA constructs containing either an A or A' sticky-ends and a double cholesterol anchor were both produced using the same 3'-cholesterol anchor ssDNA template strand, purchased lyophilized from Integrated DNA Technologies. The anchor

strand consisted of 5′–CGT GCG CTG GCG TCT GAA AGT CGA TTG CGA AAA–3′–Cholesterol–TEG. The A and A' ssDNA strands were bought from Eurogentec and consisted of *i*) Cholesterol–TEG–5′–AAA ACG CAA TCG ACT TTC AGA CGC CAG CGC ACG ACA GCC AA–3′ and *ii*) Cholesterol–TEG–5′–AAA ACG CAA TCG ACT TTC AGA CGC CAG CGC ACG ATT GGC TG–3′, respectively.

The double-stranded construct was assembled from the anchor and either an A or A' single-stranded ssDNA. These are prepared and hybridised according to Section 3.5.1, to create 1.6 μM of the construct in TE buffer containing 100 mM NaCl. The ssDNA backbones of anchor, *i* and *ii* strands were designed with high G-C content in order to enhance the thermal stability of the hybridised constructs, and without self-complementary sequences to prevent the formation of hairpins. The ssDNA overhangs of the constructs were designed for the system to have an $T_m \simeq 35 - 55°$C, giving access to a range of temperatures to study the gel dynamics whilst not damaging the vesicles.

5.3.2 Sample Preparation

LUVs were prepared according to the method in Section 3.2 with the use of a membrane filter with 1 µm diameter pores. Cholesterol-anchored constructs of type A and A' prepared as in Section 5.3.1 were added to a buffer solution of TE + 100 mM NaCl + 87 mM glucose as well as the SUVs, in ratio of 1:1:7:1, creating a solution with a vesicle volume fraction of $\sim 5\%$, and an average number of 2039 DNA-constructs per vesicle. This is estimated from the amount of DNA and the available surface area of vesicles, assuming all lipids became monodisperse vesicles with a diameter of 1 µm, and that all DNA is inserted in the bilayers.

Rectangular glass capillaries (Inner Dimensions= 0.2mm×0.5mmx×0mm, CM Scientific) were cut into ∼13mm long smaller capillaries. Each capillary was washed through filling and emptying the capillary with DI water 10 times through capillary action. Subsequently, this was repeated with isopropanol 10 times. A single wash with DI water was repeated, before the capillary was dried by blowing nitrogen through the capillary. The glass was passivated to prevent rupturing of the vesicles by repeating the washing step (10 times) with 1% BSA in DI water. This was followed by a single wash with DI water to remove any aggregates.

The sample solution in an Eppendorf was kept above the T_m, on a heating block at 60°C, to prevent aggregation. The eppendorf was briefly taken off the heating block and shaken to further ensure a homogeneous sol sample. The capillaries were then filled from this solution.

A few µl of sample was removed from either side of the filled capillaries, and this space was filled with mineral oil. The oil sealed capillaries are then placed on a cover slide (20×70mm), and the ends are sealed using an adhesive. Direct application of an adhesive without the oil seal could lead to the adhesive interfering with the sample, hence the oil buffer. The sample was checked for air bubbles, due to their expansion and contraction upon heating causing drift in the sample, and not used if there were any present.

5.3.3 Experimental Control & Imaging

Imaging was conducted with a Nikon Plan Apo VC 20x 0.75 NA Objective in both fluorescence and brightfield. The sample was placed on a peltier device consisting of a peltier element with a hole to allow brightfield imaging. Feedback from a thermocouple attached to the sample allowed for control of the temperature through a PID controller. This device was designed by Jurij Kotar. The hole was covered by a transparent sapphire window to prevent uneven heat distribution over the sample not directly in contact with the peltier element (the region of the sample placed over the hole).

The microscope and peltier settings were controlled using Temika, a custom interface designed by Jurij Kotar. Temika allows for the control of the microscope using XML scripts, which were written and customised for different experiments. Specifically, here this allowed the custom variation of the position in the sample, illumination and temperature. In order to mitigate axial focus fluctuations due to movement in x and y, Nikon Perfect Focus was employed, whereby a reference plane is set at the interface between the coverslip and the aqueous environment of the sample. 1024×1024 pixel brightfield images (0.292 µm pixel length) were taken at 100fps.

The sample was heated up to 60°C, above the hybridisation temperature of the complementary ssDNA overhangs, preventing the vesicles to bind to one another. In this regime they are diffusive, and are left for 1 hour to homogenise the density of the sample. In the case of the melting experiments, the temperature of the sample is reduced to 29°C near instantaneously (limited by the feedback from the peltier device). This is then left for 1 hour. From there, the temperature is increased by 1°C every 21 minutes, with 3 evenly separated 4 minute videos taken within this time, with a 30 s buffer at the start to ensure that the temperature is constant, and 3 minutes 10 seconds taken between videos. This is repeated until we reach 50°C, giving 3 videos at 3 different aging times (t_{age}) for each temperature reading. In the case of the quenching experiments, the temperature of the sample is reduced

to 51°C near instantaneously (limited by the feedback from of the peltier device). From there, the temperature is reduced by 1°C every 21 minutes, with 3 evenly separated 4 minute videos taken within this time, with a 30 s buffer at the start to ensure that the temperature is constant, and 3 minutes 10 seconds taken between videos. This is repeated until we reach 30°C, giving 3 videos at 3 different aging times (t_{age}) for each temperature reading.

5.3.4 DDM Implementation

DDM, as explained in Section 3.3, was achieved using a customised and built upon version of the code written by Luigi Feriani, utilised in [184]. This implementation of the DDM algorithm allowed for spatially resolved DDM measurements. This was used to analyse the videos from the experiments.

DDM was also applied to analyse smaller regions of the sample of different length scales (l_{box}) within the full-frame image to spatially resolve dynamics. 1024 × 1024 pixel ($l_{box} = 299\mu m$), 512 × 512 pixel ($l_{box} = 149.5\mu m$), 256 × 256 pixel ($l_{box} = 74.8\mu m$) and 128 × 128 pixel ($l_{box} = 37.4\mu m$) sized boxes were all considered (Fig. 5.2), allowing for probing of the dynamics at different length scales with increased statistics (as the different box sizes gives 1, 4, 16 and 64 boxes respectively to analyse).

5.4 Data Analysis

5.4.1 Extracting Static Structure

The static structure factor, $S(q)$, can be found through the Fourier analysis of a single image, where q is the spatial frequency. For an aggregating homogeneous suspension, the peak of $S(q)$ occurs at q_{peak}, where $\frac{2\pi}{q_{peak}}$ can be used as an approximation for the average length scales of the gel clusters.

From the static structure function, we can also find the normalised first moment of the static structure factor (norm. m_1 $S(q)$), which gives further insight into the structure.

$$norm.m_1 S(q) = \frac{\sum qS(q)}{\sum S(q)}, \tag{5.1}$$

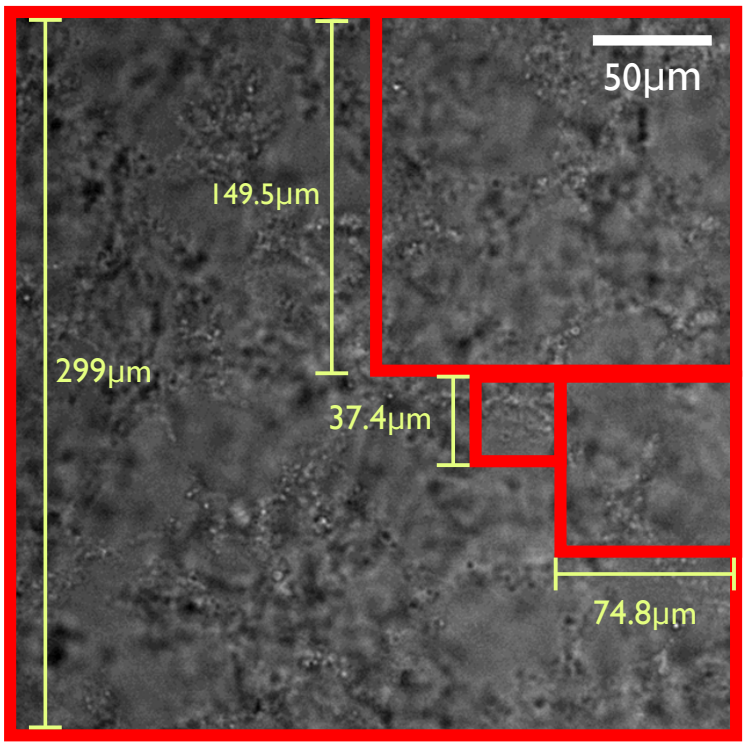

Fig. 5.2 Different sizes of the regions of interest considered in the spatially resolved DDM implemented in this work. Red boxes of 4 different sizes are shown, with lengths (l_{box}) of 299 µm, 149.5 µm, 74.8 µm and 37.4 µm, which give 1, 4, 16 and 64 boxes respectively to analyse from a 1024×1024 pixel full-frame image.

In order to gain better statistics, the normalised first moment was calculated for each frame in a 200 frame video and averaged to remove sampling noise.

5.4.2 Fitting DDM Analysis

Fitting of the image structure factor, $I(q,\tau)$, derived from the DDM analysis of the videos was implemented by varying the model to describe the Intermediate scattering function (ISF). By varying the model describing the ISF and fitting this to the $I(q,\tau)$ the q-dependent parameters describing the relaxation of the different Fourier modes are found. As stated in Section 3.3, which for simplicity is included here again

$$I(q,\tau) = A(q)[1 - f(q,\tau)] + B(q). \tag{5.2}$$

These fitting parameters were allowed some flexibility in the main model, but significantly constrained to reduce the complexity of the fitting. The $I(q,\tau)$ was then fitted using different models for the ISF, $f(q,\tau)$, by using a non-linear least-squares method. Fitting the model to an exponentially spaced series of bins of $I(q,\tau)$ rather than the raw data was found to minimise the residuals of the fit, and was therefore employed here.

5.4.3 Finding a good and robust ISF

Various functions for the ISF term were used in order to attempt to fit the $I(q,\tau)$. Existing work on gel dynamics has utilised some variation of a stretched/compressed exponential, either alone or in conjuction with a single exponential, to model the ISF [124, 127, 114, 118]. The addition of a single exponential term, and a coefficient of proportionality, allows the inclusion of a second relaxation time that can be seen in the $I(q,\tau)$ upon heating, and applying these models yielded good fits. However, it remains unclear whether these models are suitable; small movements of individual vesicles, which are polydisperse compared to colloidal sample cannot be described by an unstretched exponential, whilst adding the extra term adds extra complexity to the model, and increases the potential for overfitting. Therefore instead, we subscribe to Occam's razor, and use a simplified fit

$$f(q,\tau) = e^{-\left(\frac{\tau}{\tau_1(q)}\right)^{\beta(q)}}, \tag{5.3}$$

where $\tau_1(q)$ is the relaxation time of the density correlation fluctuations for a given q-value, and $\beta(q)$ is an exponent, which gives a measure of the distribution of relaxation times. An exponent $\beta < 1$ is referred to as a *stretched* exponential, and describes the distribution of the relaxation times corresponding to either the polydisdispersity of diffusive particles or subdiffusive behaviour [118]. On the contrary, behaviour characterised by an exponent $\beta > 1$ has been observed and is referred to as a *compressed* exponential and describes superdiffusive behaviour, such as microcollapse events [117, 124]. In the implementation of the fit, the Image Structure Function data is binned in exponentially increasing bin sizes which allows for better statistics on longer lag time (τ) values of the $I(q,\tau)$.

5.4.4 Fitting the relaxation timescale, τ_1

The q-dependent decay of the relaxation timescale, τ_1, extracted from fititng the ISF, characterises the dynamics of the sample. τ_1 decays as a power-law with increasing q. As such,

we take the logarithm of the data, in order to scale the contributions of the residuals for a non-linear least squares fit. Initially, some of the data shows a plateau before exhibiting a power-law decay, demonstrating a "knee" like function (Fig. 5.3a, with the plateau corresponding to the region which can be fitted by $\tau_1 \approx constant$). This plateau could correspond to q-values representing length scales greater than the mesh size (the characteristic length scale of the gel); at these q-values, the system can be seen as being an elastically-connected solid, and as such, the corresponding time correlations of the density fluctuations can be considered "locked-in", relatively unaffected by the local rearrangements probed at higher q-values [127].

Additionally, τ_1 at certain temperatures shows two q-dependent decays, indicating multiple length scale-dependent transitions in the decay rates of the material's relaxation times. To model this, we employed an empirical function, based on a combination of logistic functions coupled with linear decays

$$\tau_1(q) = a_1 - \frac{a_2(q-a_3)}{1+e^{-k(q-a_3)}} + \frac{a_2(q-a_4)}{1+e^{-k(q-a_4)}} - \frac{a_5(q-a_4)}{1+e^{-k(q-a_4)}}. \tag{5.4}$$

This equation is based on using a logistic function to approximate a Heaviside step function, and a representative fit is shown in the black line in Fig. 5.3a. The first term a_1 is a constant, which corresponds to a starting constant plateau for a range of q-values up to the first knee. When q>a_3, there is the start of a decay from an initial plateau as set in the logistic function, the first knee. A tuning constant k (set at 1000) ensures a sharp step approximating a Heaviside step, and the gradient of this decay is set by the a_2 term. At q>a_4, we add another decay with an a_2 term to cancel out the contribution from the first decay. Finally, the second decay is added when q=a_4, with a gradient of a_5. This allows for the fitting of two knee points. We then simply fit the following power law for $\tau_1(q)$ between where q=10^{a_4}, where a_4 is extracted from the previous fit and represents the second knee in log scale, and the upper limit of our accessible q-modes (Fig. 5.3a, green line):

$$\tau_1(q) = kq^{\Upsilon}, \tag{5.5}$$

where k is a scaling constant, and Υ is the exponent of q in the given q-range. The q-range suitable for fitting is limited by a variety of factors. Theoretically, DDM probes a q-range from $q_{min} = 2\pi/L_{im}$, where L_{im} is the image size , to an upper bound of $q_{max} = 2\pi/L_{px}$, where L_{px} is the pixel size. In practice, this range becomes limited by the statics (e.g. low signal to noise ratio) and the dynamics (e.g. the sampling frequency is too low to sample fast dynamics or the experimental time too short to probe dynamics of slowest modes). The

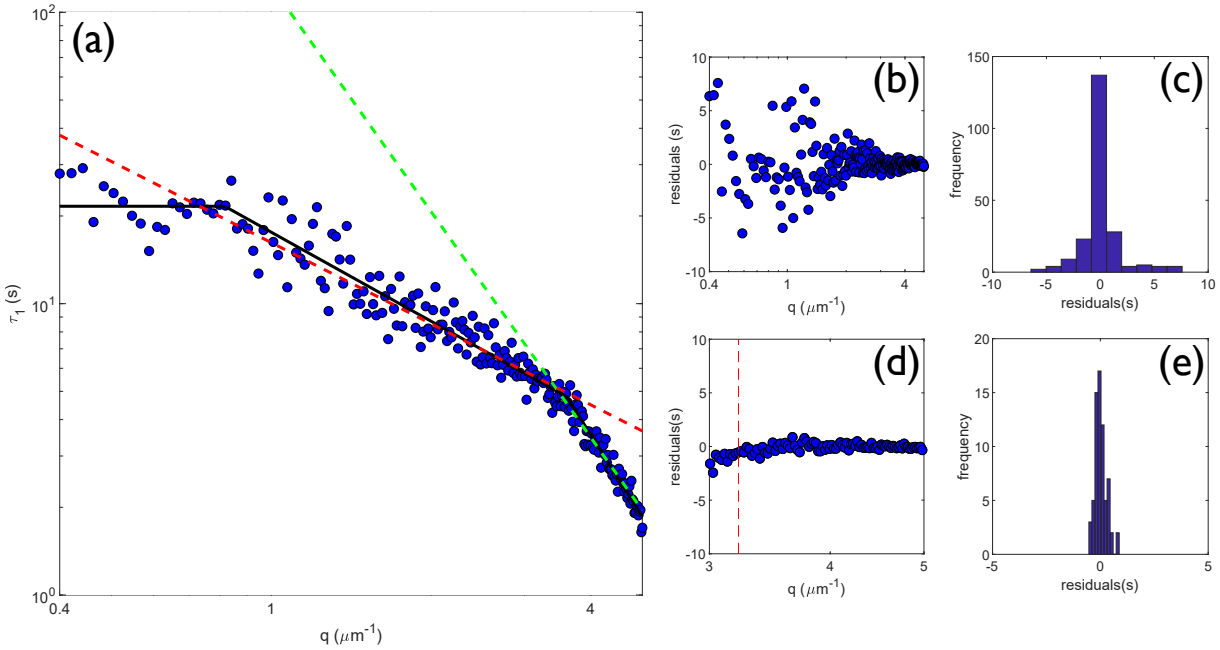

Fig. 5.3 (a) A representative fit of the relaxation time, τ_1 to Equation 5.4. The fit of this model is shown in black, with a power law fit of the first knee to the second knee, and the second knee to the maximum accessible q-value shown in red and green respectively. The plateau is visible before the onset of the first knee. (b) The residuals as a function of the q-values of the fit of Equation 5.4 and (c) a histogram of the residuals of the aforementioned fit, showing a broadly normal distribution. (d) The residuals of a power law fit between the second knee and the highest accessible q-value, with the intersection of the green and red dashed line representing the location of the second knee. (e) A histogram of the residuals of the aforementioned fit, showing a broadly normal distribution.

signal to noise ratio is defined as the ratio between static scattering dependent term, A(q), and the background noise term, B(q). A low signal to noise ratio leads to errors in the fitting of the ISF, and therefore the derived parameters.

To assess the appropriate q-range, we considered only the case of diffusing LUVs; which occur in samples above the melting temperature of the DNA. Using a cumulant analysis to derive a $\tau_1 \sim q^{-2}$ dependency, we can find the diffusion coefficients at each q-value. When $q > q_{max}$, we find the derived diffusion coefficient becomes unreliable. The A(q)/B(q) ratio at these q-modes was 0.25. To allow for comparison of dynamics between all samples, q_{max} was set as the minimum q-value for all 1024 $\times$ 1024 pixel images where A(q)/B(q)>0.25, which occurs when $q = 4.45\,\mu\text{m}^{-1}$. A similar method of determining a q_{max} is reported in Ref. [203]. To define q_{min}, we take the maximum q-value for diffusive samples where the ISF

saturates, corresponding to complete decorrelation, which we found to occur at $0.39\,\mu m^{-1}$, in a manner similar to Ref. [204].

5.4.5 Cumulant Analysis at High Temperatures and Polydispersity Measurements

In order to consider the polydispersity in a sample of Brownian colloidal particles, a single exponential alone cannot be used to represent the ISF. Instead, the ISF can be expressed as an integral over a distribution of decay rates, which can itself be expressed in terms of a series expansion [205]. This is known as a cumulant fit. The terms in the expansion correspond to moments about the mean. We utilise a modified cumulant fit, as shown in Ref.[206], which considers only the second moment about the mean, which corresponds to the variance of the sample

$$f(q,\tau) = \left(1 + \frac{\mu\tau^2}{2}\right) e^{-\left(\frac{\tau}{\tau_1(q)}\right)}, \tag{5.6}$$

where τ_1 is the relaxation time of the density correlation fluctuations for a given q-value and μ is the second moment of the mean, which gives a measure of the distribution of relaxation times. We can find the diffusion coefficient (D), as $D = 1/(q^2\tau_1)$. Through these results we can find the mean vesicle radius, by applying the Stokes-Einstein relationship

$$D = \frac{k_B T}{6\pi\eta r}, \tag{5.7}$$

where k_B is the Boltzmann constant, T the temperature, η the viscosity and r, the vesicle radius. A polydispersity index, $\mu\tau_1^2$, is found to be equal to $(\sigma/r)^2$, where σ is the standard deviation of the distribution. Therefore using cumulant analysis we can find the mean size and width of the distribution of vesicles, as previously demonstrated for scattering data in other systems [205, 206].

5.5 Results and Discussion

5.5.1 Visual Assessment of System

Visual inspection of the system yielded qualitative understanding of the processes underlying the dynamics described quantitatively later, and was explored through assessment of the

videos, demonstrative frames of which are shown in Fig. 5.4.

In melting experiments, at temperatures below the melting temperature (T_m) of the gel, a clearly set percolating gel can be observed, which spans the sample (Fig. 5.4a&b). Observing the videos, a structure with small "in-place" movements of branches of the structure significantly greater than the length scale of the vesicles is seen. Upon heating to just below the T_m, the structure has become coarser, with more fibrullar branches, and the structure is less held in place, with greater movement observed. Indeed, breakage events of connected branches of the gel can be observed, as well as structures coming into focus sharply, possibly indicating the breaking of branches in the z-direction. Just above the T_m, smaller diffusive clusters can be observed, which rapidly break up at higher temperatures to form a homogeneous sample of diffusive vesicles (Fig. 5.4c).

Upon quenching, the system was observed to start as freely diffusing vesicles (Fig. 5.4f), before starting to form diffusive clusters. With decreasing temperature, these clusters began to diffuse less, before eventually a sample-spanning gel is observed to form (Fig. 5.4d&e). This temperature is called the gel point (T_g).

This is made more clear by generating motion maps of the videos, where the standard deviation of the pixel values over the entire movies is shown, indicating how much the pixel values change, and thus the motion of the sample at different temperatures in different regions of the sample (Fig.5.5). At 44°C, the pixel standard deviation is relatively uniform throughout the sample, indicating diffusive motion of the vesicles (Fig.5.5c&f). Differences are again seen between the samples on heating and cooling respectively. At 36°C, only small fluctuations were observed, whereas at 40°C for both experiments, we see the largest values of pixel standard deviation, which broadly correspond in their location to the structures observed in Fig. 5.4b&e.

5.5.2 Polydispersity

Cumulant analysis of vesicles at temperatures corresponding to the diffusive regime of the system yielded good fits across the range of accessible q-modes, with residuals that were normally distributed around 0, as can be seen in the representative fits and residual plots shown in Fig. 5.6a-f. Indeed, the cumulant analysis gave a scaling exponent of the of the q-dependent τ_1 decay, $q \sim \tau_1^{\Upsilon}$, $\Upsilon \approx$-2, in good agreement with the experimentally and theoretically observed $q \sim \tau_1^{-2}$ relationship. Using the diffusion coefficient derived from this fit

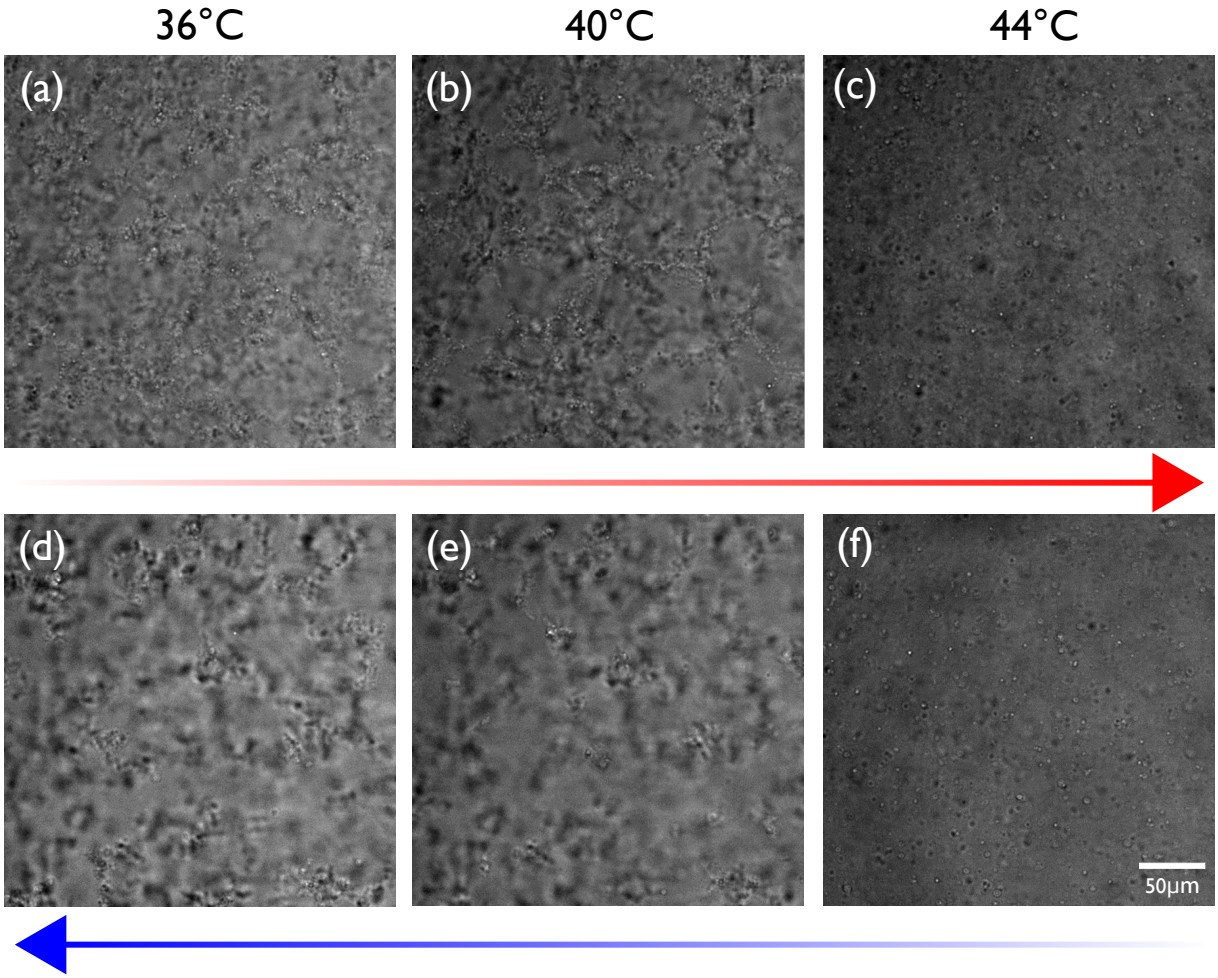

Fig. 5.4 Brightfield images of LUV-DNA gels at for the gels on heating (a-c), and cooling (d-f), at 36°C, 40°C and 44°C respectively. The arrows represent the direction of temperature ramps; red for heating (a-c) and blue for cooling (d-f). At 44°C, the system is diffusive, whereas the other two temperatures represent different stages in the gel-sol/sol-gel transition.

$D = 1/(q^2\tau_1)$ and the Stokes-Einstein equation (Eq. 5.7), we find the mean radius across the three temperatures to be $0.66 \pm 0.08 \mu m$. This is above the radius of the pore (0.5 µm), though it has been shown that extruded vesicles will be larger than the diameter of the pores they are extruded through [207]. The cumulant analysis allows for the calculation of the standard deviation of the distribution of particle sizes, which we find to be consistently $\sim$4% of the radius.

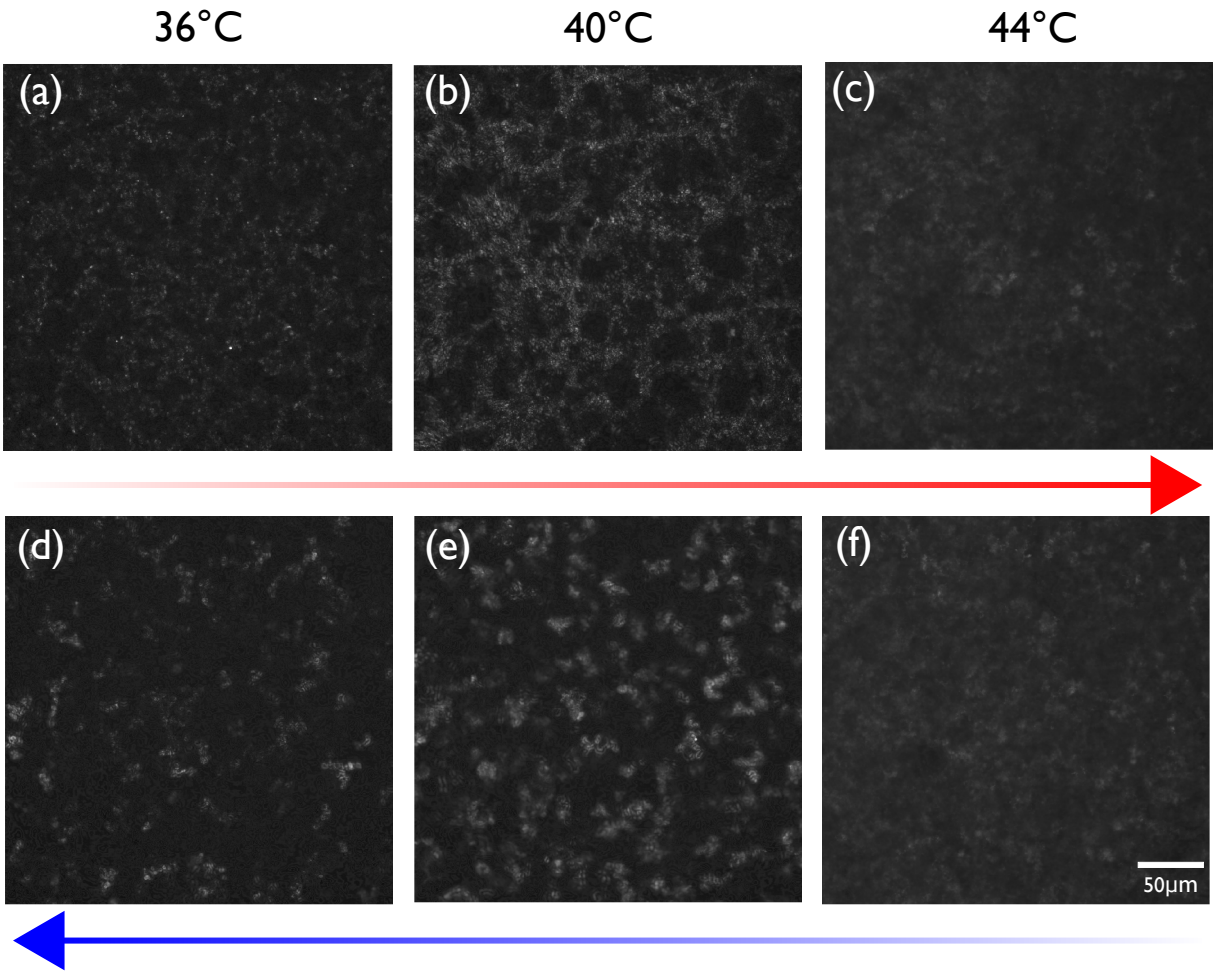

Fig. 5.5 Motion Maps images of LUV-DNA gels at for the gels on heating (a-c), and cooling (d-f), at 36°C, 40°C and 44°C respectively. The arrows represent the direction of temperature ramps; red for heating (a-c) and blue for cooling (d-f). At 44°C, the system is diffusive, whereas the other two temperatures represent different stages in the gel-sol/sol-gel transition. The intensity of the pixels in the images corresponds to the standard deviation of each pixel's value over the entire movie.

5.5.3 Static Structure

The normalised first moment of $S(q)$ (norm. $m_1\ S(q)$) allows us to see the transition of the material containing larger structures (lower norm. $m_1\ S(q)$ values) to smaller structures (higher norm. $m_1\ S(q)$ values) as a function of temperature, and indicates the gel-sol transition temperature for both cooling and heating. The gel-sol transition is markedly sharper in the case of heating, similar to the results on a similar system reported in Ref. [86], whereas on cooling, this transition occurs over a broader range of temperatures (Fig. 5.7a&b). Through the consideration of the norm. $m_1\ S(q)$, the melting of the gel can be seen to begin once

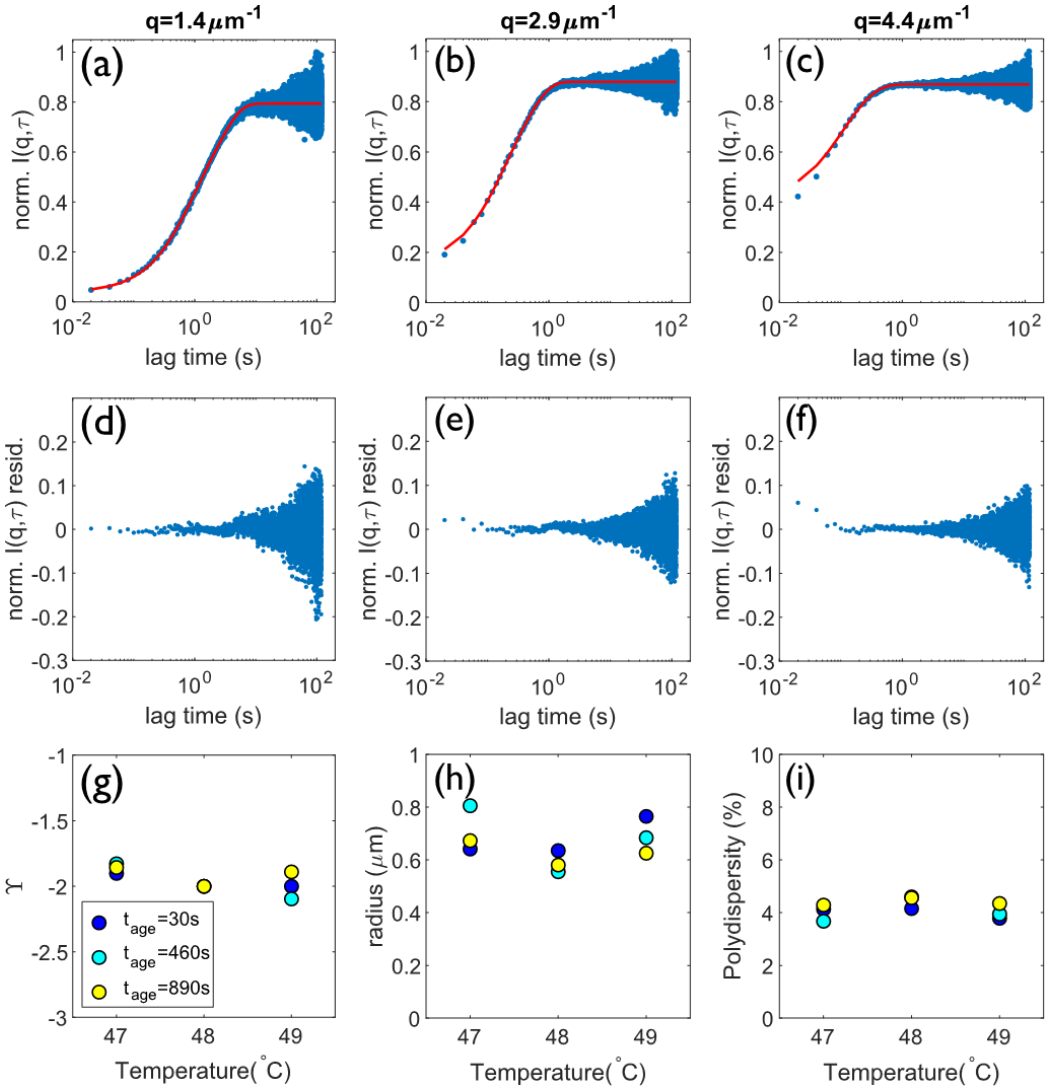

Fig. 5.6 Cumulant analysis of the system in the diffusive regime. (a-c) Show the fits and (d-f) the residuals of fitting a cumulant fit to the ISF at $q = 1.4\,\mu\text{m}^{-1}$, $2.9\,\mu\text{m}^{-1}$ and $4.4\,\mu\text{m}^{-1}$ respectively. Derived parameters from the fit, (g) Υ, the scaling exponent of the q-dependent decay of τ_1, (h) the extracted particle radius and (i) the polydispersity, shown as the standard deviation of the radii as a percentage of the mean radius, are also shown to characterise the diffusive system at 47°C, 48°C and 49 °C respectively.

the temperature is elevated above 39°C and reaches a relatively constant (corresponding to smaller structures, in this case diffusive vesicles) state at 42°C. We therefore say that the $T_m \approx 40°C$. On quenching, a gel is formed by 39°C, which can be observed by the decrease in norm. m_1 $S(q)$, but the system shows evidence of aggregation from 44°C. From considering this, the aging dependence of the norm. m_1 $S(q)$ as well as the rheological insight from the

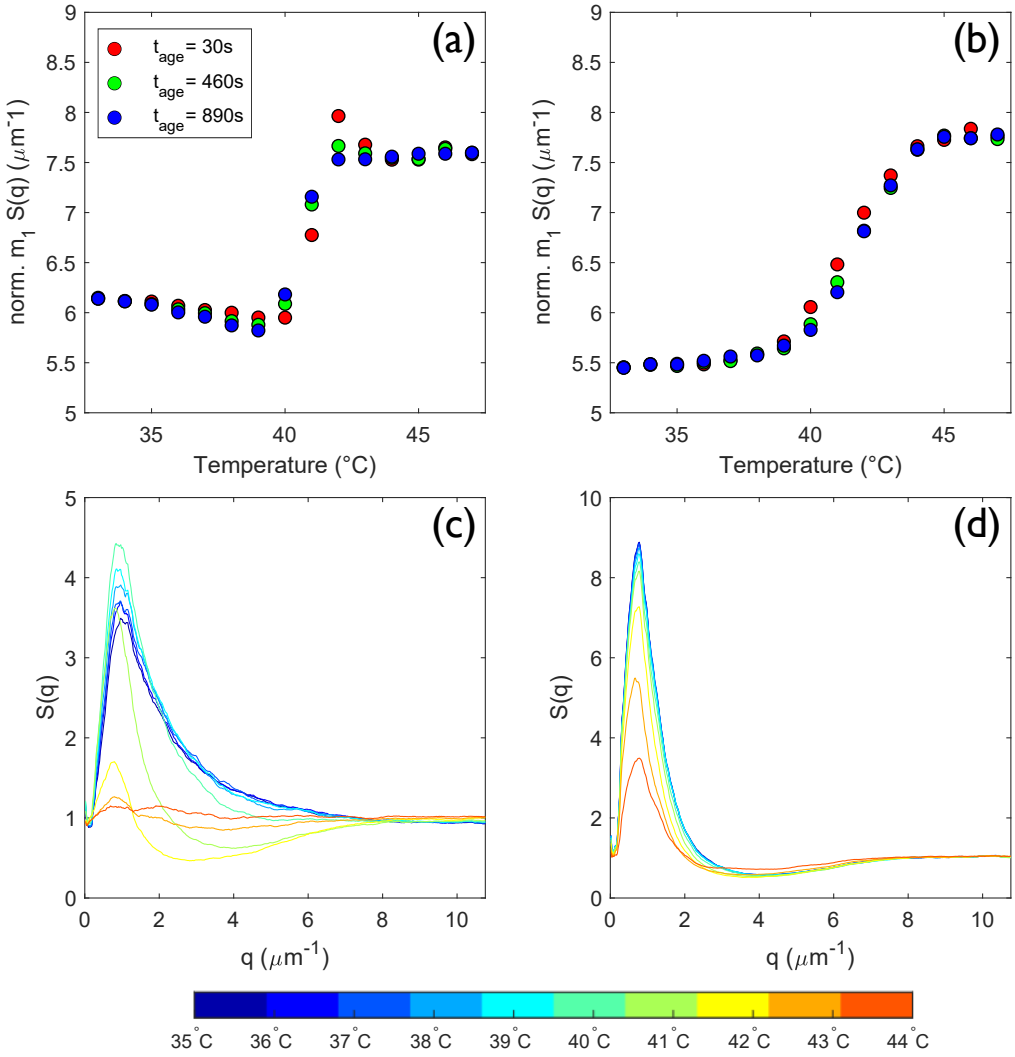

Fig. 5.7 The normalised first moment of $S(q)$ (norm. m_1 $S(q)$) for (a) melting and (b) quenching experiments. Additionally the static structure factor ($S(q)$) is shown as a function of the wave vector, q, for (c) melting and (d) quenching experiments for temperatures between 35°C-44°C.

relaxation times (Fig. 5.14b), we find that $T_g \approx 40°C$. It would generally be hypothesised that, due to the increased local concentration of the linker within the gel, $T_g < T_m$. However this shift to lower values could be due to vesicle degradation caused by repeated exposure to high temperatures [86].

Interestingly, we see evidence of coarsening with increasing temperature in Fig. 5.7a; indeed there seemingly is also an aging dependent coarsening which is observed. Coarsening with aging and temperature is well-known in colloidal gels [108], but this system has the

added property that, below the melting temperature, vesicles are more deformable, and the adhesion patches between them can grow [52], causing the network of vesicles to transition from packings similar to hard-sphere packing, to a wet foam-like structure with reduced interstitial spaces.

A coarsening gel shows a peak in $S(q)$ that grows in magnitude and shifts towards low-q values. This can be observed on heating, where the peak grows in magnitude (Fig. 5.7c), but no significant shift of the peak towards low-q values as we approach T_m is observed. On cooling this shift to low-q values is also not observed; whilst coarsening occurs near the transition temperature, it is also an aging dependent process and as such is perhaps difficult to disentangle these competing effects in cooling experiments (Fig. 5.7d). The gel studied on melting represents a much more deeply quenched gel than the one studied on quenching; we see that the $S(q)$ for the less deeply quenched gel is larger, as observed in Ref. [208], due to the shallow quenched gel being more structured.

5.5.4 Analysis of Fits

We analyse the fit of the $I(q,\tau)$ with the stretched/compressed exponential by inspecting both the fit of the data, and the residuals of the fit, as shown in Fig. 5.8 & 5.9 for quenching and melting experiments respectively at three q-values spanning the accessible range. We consider three temperatures; 36°C, 40°C and 44 °C, which correspond to the system being in three broadly defined regimes of i) gel ii) close to the sol-gel/gel-sol transition and iii) sol, respectively.

We observe very good agreement with the data with our model (Eq. 5.3) at 36°C and 44°C on quenching (Fig. 5.8a-f & Fig. 5.8m-r). At $q = 1.4\mu m^{-1}$ for the fit at 40°C at long lag times, we find that the residuals are not normally distributed (Fig. 5.8j). It is possible that this is due to the presence of another dynamic process unaccounted for in our simple model, occurring at longer times during the gelation process at low q-values and therefore large length scales. However, fundamentally fitting the data at longer lag-times is less accurate; as we reach lag-times approaching the duration of the experiment we have fewer points to ensemble average for each value of the $I(q,\tau)$.

On melting (Fig. 5.9), we observe a good fit for the data by our model (Eq. 5.3) at 44°C. In the gel and transitional regimes (Fig. 5.8a-l), we have a reasonable fit at small-intermediate lag times. As we reach lag-times (τ) approaching the duration of the experiment, where we

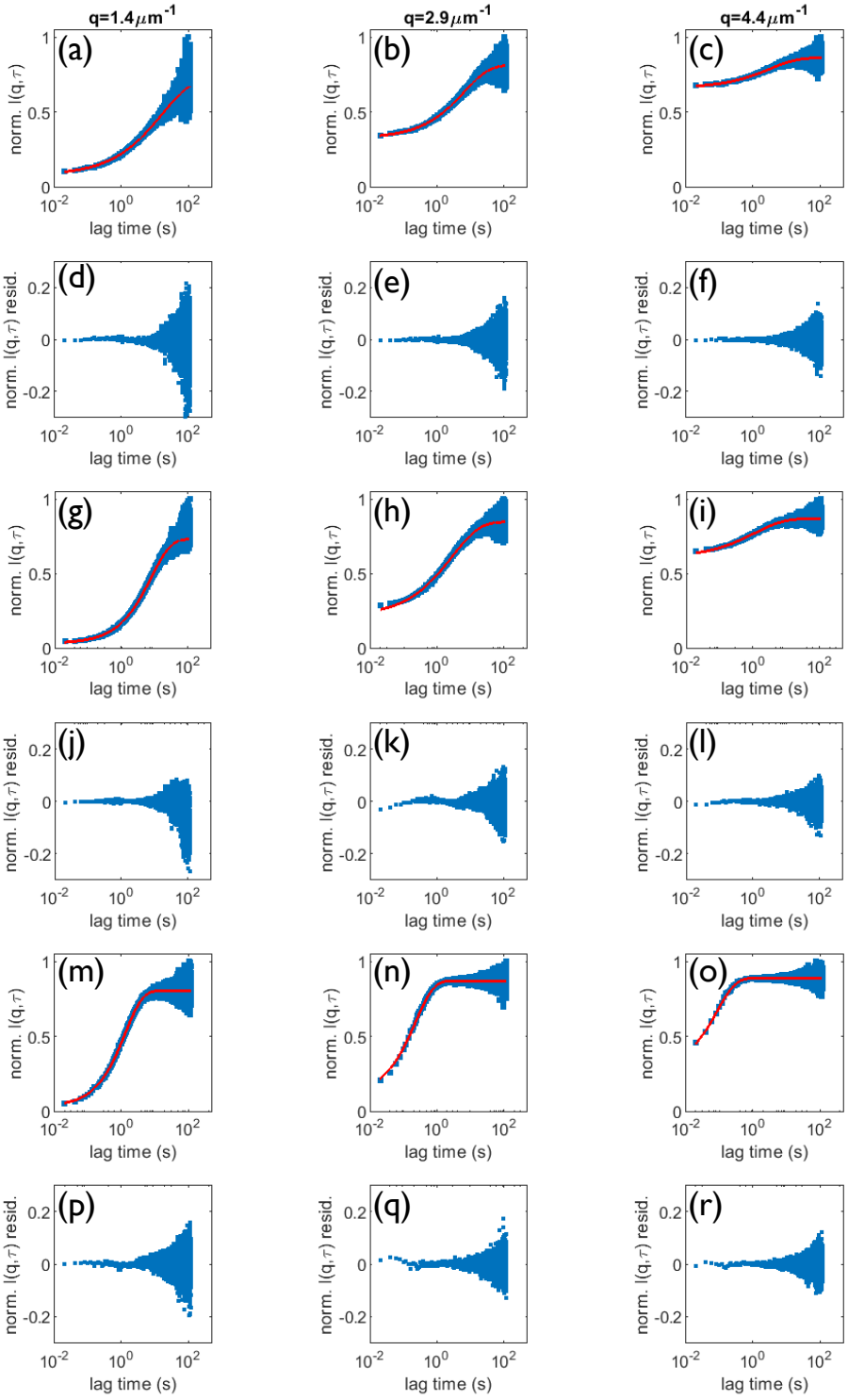

Fig. 5.8 Representative fits of the normalised $I(q,\tau)$ (Image Structure function) with the stretched/compressed exponential model at 3 q-values for experiments on quenching: (Left to Right) 1.4 µm^{-1}, 2.9 µm^{-1} and 4.4 µm^{-1}; and 3 temperatures: (a-c) 36°C, (g-h) 40°C and (m-o)44°C. Additionally the residuals are also shown at (d-f) 36°C, (j-l) 40°C and (p-r) 44°C.

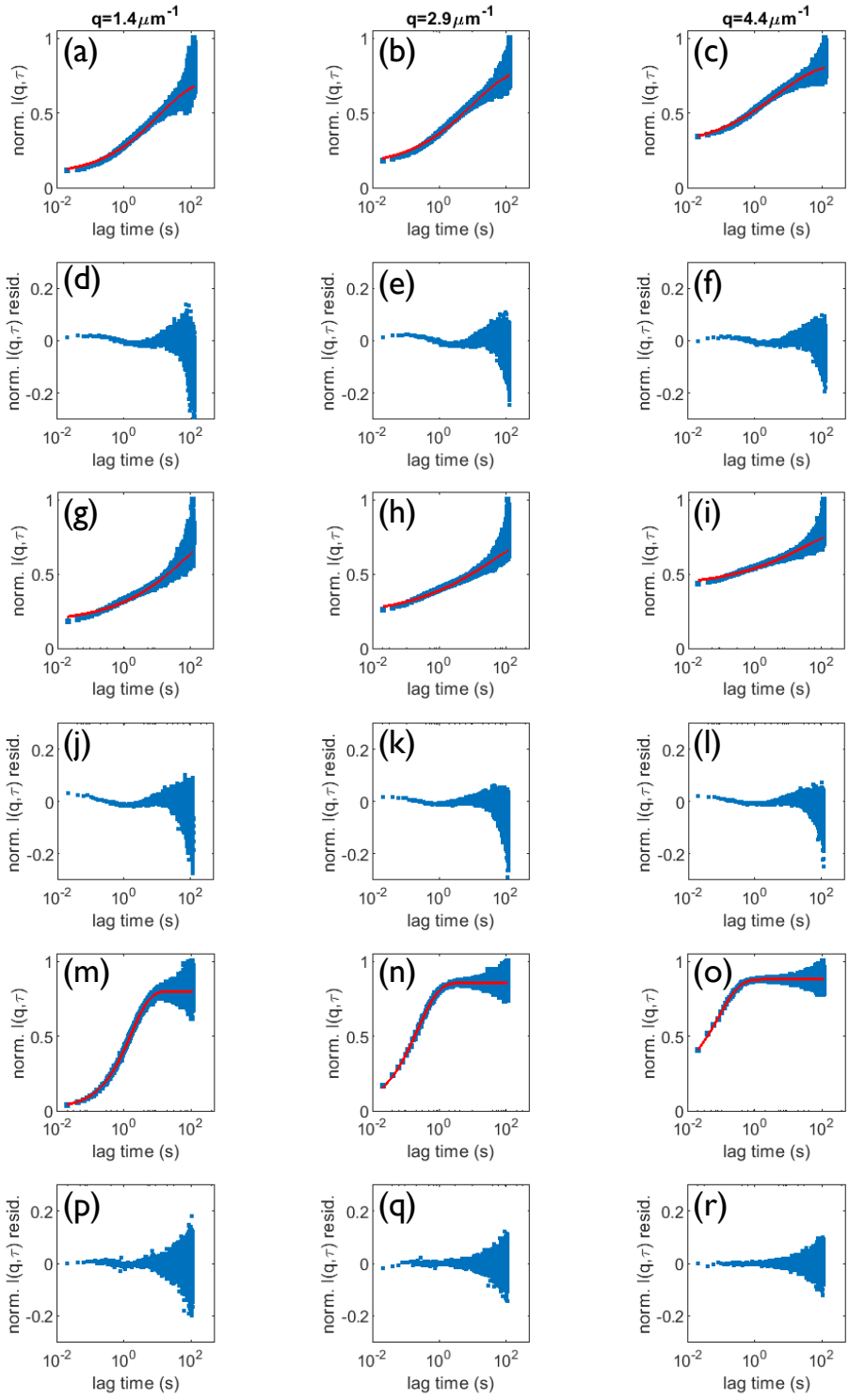

Fig. 5.9 Representative fits of the normalised $I(q,\tau)$ (Image Structure function) with the stretched/compressed exponential model at 3 qs for experiments on melting: (Left to Right) 1.4 µm^{-1}, 2.9 µm^{-1} and 4.4 µm^{-1}; and 3 temperatures: (a-c) 36°C, (g-h) 40°C and (m-o)44°C. Additionally the residuals are also shown at (d-f) 36°C, (j-l) 40°C and (p-r) 44°C.

have fewer points to ensemble average for each value of the $I(q,\tau)$, we observe a tail of the distributions of the residuals, which can be explained by the use of exponentially spaced bins to mitigate the low statistics of longer lag time $I(q,\tau)$ data. Additionally, whilst the onset of a plateau can be observed, or at least inferred, within the experimental time in Fig. 5.9a-c, the $I(q,\tau)$ does not plateau in Fig. 5.9g&h. It is possible that our experimental time is too short to probe the longer relaxation times present in the system which would lead to complete decorrelation and plateauing of the $I(q,\tau)$. It is also probable that there are other dynamic process unaccounted for in our simple model, however, we subscribe to Occam's razor; fits involving more parameters did yield better fits, but suffered with overfitting, converging to results with no sensible physical interpretation.

From these fits and Eq. 5.3, we derive the relaxation time, τ_1, and the exponent, β, which we use to charaterise the properties of the system in the subsequent chapters.

5.5.5 Dynamics: Quenching

In the case of cooling experiments, we can observe a single scaling of the q-dependent decay of the relaxation time τ_1, above 42°C (Fig. 5.10k-l), which is similar to the $q \sim \tau_1^{-2}$ decay expected for diffusive particles. At 42°C, we see the onset of a plateau. At and below $T_g(\approx 40°C)$, we see two distinct regimes of decay (Fig. 5.10d-h); a slower decay at $q \lesssim 2\,\mu m^{-1}$, and a faster decay at $q \gtrsim 2\,\mu m^{-1}$, with the initial decay slowing for lower temperatures, until the first decay plateaus. This plateau precedes a single decay at high $q \gtrsim 2\,\mu m^{-1}$ (Fig. 5.10a-c).

The corresponding stretching/compressing exponent, β gives further insight into the dynamics of the system on cooling. Initially, the system consists of diffusive vesicles. The exponent captures the distribution of relaxation times, and in a monodisperse sample $\beta = 1$. However, the vesicles are polydisperse, so we expect and observe $\beta \lesssim 1$ (Fig. 5.11l), as the distribution of relaxation times should be relatively narrow [209]. As we decrease the temperature, the initial (at $q = 0.4\,\mu m^{-1}$) β decreases. Furthermore, we observe that β decreases as a function of the q-value (Fig. 5.11e-l), until the temperature regime where there was a plateau in the τ_1 as a function of q-value ($T \leq 36°C$, Fig. 5.10a-d). Here, the β increases as a function of the q-value (Fig. 5.11a-d), until reaching a constant value around the q-value ($q \lesssim 2\,\mu m^{-1}$) at which we observe the onset of the post-plateau τ_1 decay.

If we consider only the β corresponding to the q-values representing the initial slow decay of τ_1, and also consider smaller regions of the sample, by using spatially resolved DDM (as

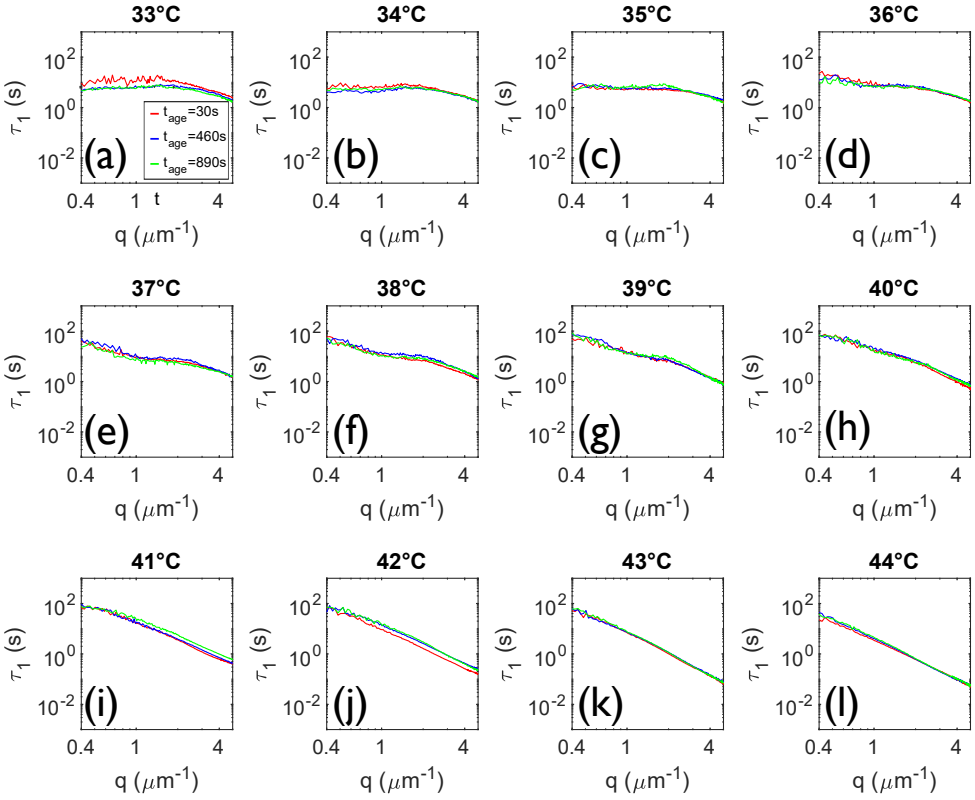

Fig. 5.10 The relaxation time, τ_1, derived from the fit of the ISF with Eq. 5.3 of an experiment on cooling the LUV-DNA system derived from videos taken at aging times (t_{age}) of 30 s, 460 s and 890 s after a 1°C temperature step. The temperature quench started from 50°C and ended at 30°C but (a-l) only shows 33°C-44°C.

described in Section 5.3.4), we observe the presence of q-values at which β>1, indicating superdiffusive/ballistic dynamics [124, 116, 210–212]. Multiple mechanisms have been proposed for such behaviour. In the case of gelation, this has been thought to be indicative of interfacial coarsening of large domains [213]. It seems, however, these dynamics might be discernible from the background subdiffusive/diffusive behaviour only on relatively small length scales, as hypothesised in other systems with such rearrangements [214]. Considering smaller boxes could help, however we find that the small number of accessible q-modes at smaller boxsizes (l_{box}) than those employed here, where the signal from such events may dominate the background of subdiffusive/diffusive behaviour, makes fitting unreliable. Subdiffusive behaviour of the structure is predicted for the behaviour of an aging gel, due to effects such as bonding/caging and larger-scale cooperative rearrangements in the structure due to thermal fluctuations [215, 118, 216, 199]. This behaviour is also representative of glassy behaviour, supporting the mechanism of arrested spinodal decomposition for the

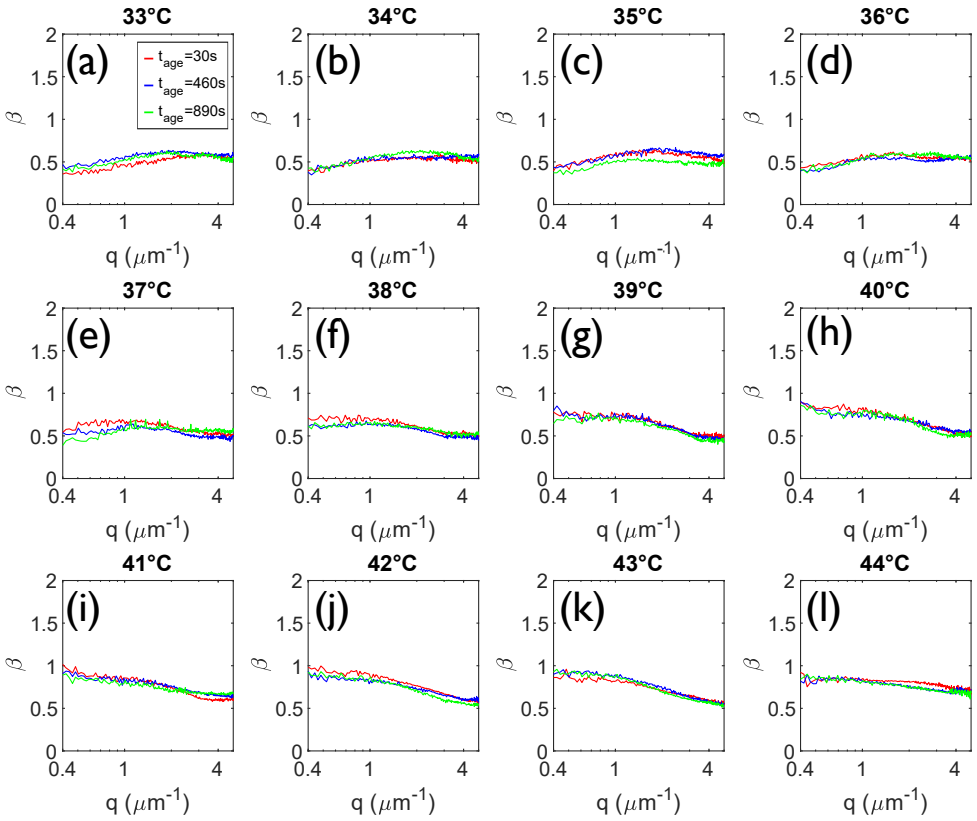

Fig. 5.11 The stretching/compressing exponent of the exponential, β, derived from the fit of the ISF with Eq. 5.3 of an experiment on cooling the LUV-DNA system derived from videos taken at aging times (t_{age}) of 30 s, 460 s and 890 s after a 1°C temperature step. The temperature quench started from 50°C and ended at 30°C but (a-l) only show 33°C-44°C.

formation of the gel studied here [217].

In concert, the evolution of these parameters suggests our fits capture q-dependent dynamics on gelation, whereby the initial regime contains only diffusive particles. On cooling, polydisperse but diffusive clusters form with a range of relaxation times, which are captured by the stretched exponential. Additionally we observe, by considering smaller regions of the sample (as described in Section 5.3.4) to probe the spatial heterogeneity of the dynamics, some superdiffusive dynamics at low q-values in some regions, which we hypothesise is due to spatially localised interfacial coarsening events occur between these clusters leading to the formation of a space-spanning gel, as in Ref. [114]. At lower temperatures we see subdiffusive dynamics, which represent the thermal motion of the gel at higher q-values, and thus small length scales. This corresponds well with the formation of a gel through arrested spinodal decomposition, as seemingly gelation is merely diffusion limited, with the

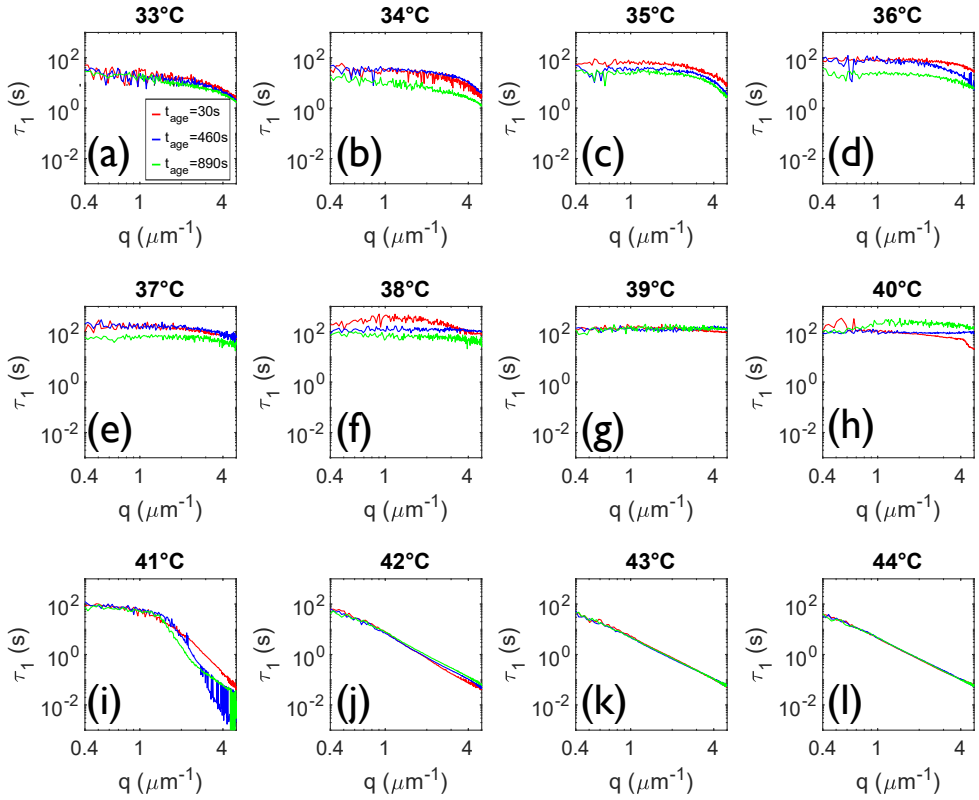

Fig. 5.12 The relaxation time, τ_1, derived from the fit of the ISF with Eq. 5.3 of an experiment on heating the LUV-DNA system derived from videos taken at aging times (t_{age}) of 30 s, 460 s and 890 s after a 1°C temperature step. The temperature ramp started from 30°C and ended at 50°C but (a-l) only show 33°C-44°C.

subdiffusive motion of the gel at lower temperatures indicative of glassy dynamics [218]. At low temperatures, we also see that τ_1 plateaus at $q \lesssim 2\,\mu\text{m}^{-1}$. This could be because we are probing length scales at which the gel behaves like an elastic solid, or that we are unable to access ultra-slow dynamics of coarsening within our experimental window, and capture only the diffusive motion within clusters.

5.5.6 Dynamics: Melting

In the melting experiments, we see noticeably different dynamics. Except for the high temperature/diffusive regime, the initial τ_1 is close to an order of magnitude larger than that seen in the quenching experiments. Above the T_m of the gel, we see a single decay which we find to scale on average as $\tau_1 \sim q^{-2.6}$ (Fig. 5.12j-l). From 33°C onwards, we see the formation of a plateau before the onset of a final decay of τ_1 with respect to the q-value (Fig. 5.12a-e).

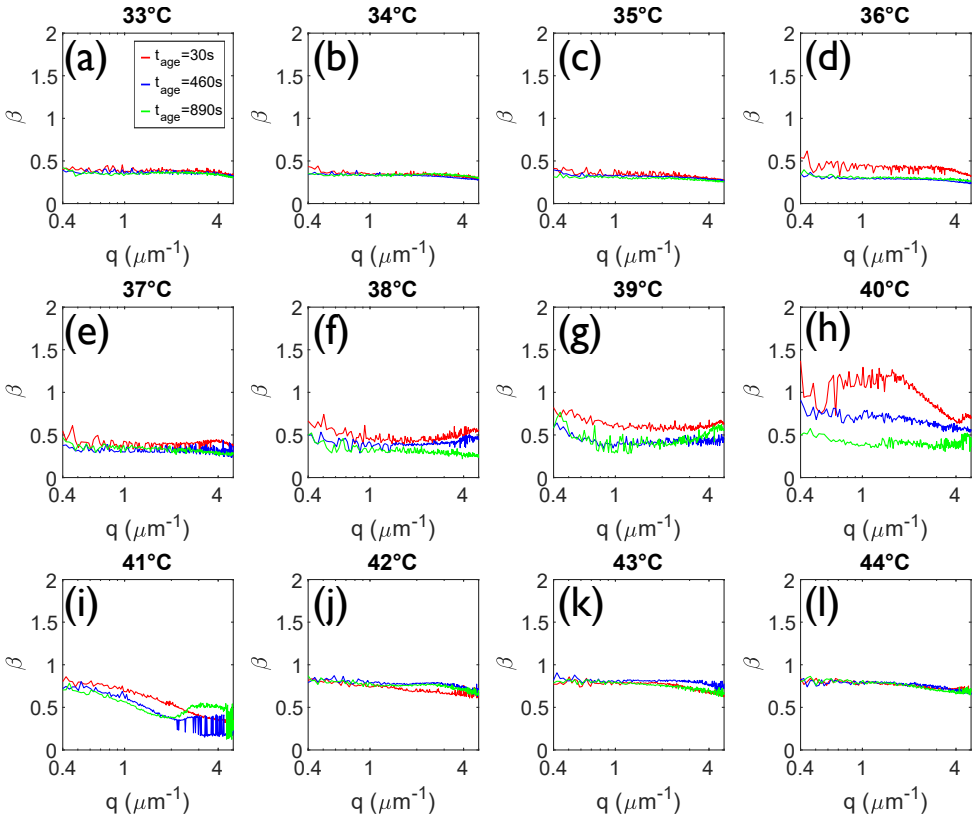

Fig. 5.13 The stretching/compressing exponent of the exponential, β, derived from the fit of the ISF with Eq. 5.3 of an experiment on heating the LUV-DNA system derived from videos taken at aging times (t_{age}) of 30 s, 460 s and 890 s after a 1°C temperature step. The temperature ramp started from 30°C and ended at 50°C but (a-l) only show 33°C-44°C.

The final decay is similar to $\tau_1 \sim q^{-2}$ and, coupled with a $\beta < 1$ (Fig. 5.13a-e), describes the subdiffusive movements of the structure. As stated previously, this is predicted for an aging gel, due to effects such as bonding/caging and larger-scale cooperative rearrangements in the structure due to thermal fluctuations [215, 118, 216, 199]. At lower q-values (corresponding to longer wavelengths and larger lengthscales) the material is solid and elastically connected, therefore the time correlations of the density fluctuations over the length scales probed at such q-values can be considered "locked-in" [127]. This "locked-in" behaviour shifts to higher q-values as temperature is increased to 39°C (Fig. 5.12f&g), indicating the coarsening driven increase in elastic-solid like properties of the material at smaller length scales. At 40°C, at $t_{age} = 30$ s, we see a region of $\tau_1 \sim q^{-1}$, indicative of superdiffusive events and rearrangements. The decay of τ_1 at 41°C for $q \lesssim 2\,\mu\text{m}^{-1}$ is slow ($\sim q^{-1}$), before transitioning to $\tau_1 \sim q^{-4}$ dynamics at 41°C. This has been shown to represent caged dynamics at high q-values [219, 220]. We hypothesise this could be due to the presence of the gel structure

and the confined motion of broken clusters within the gel-network during gel melting.

The observed β shares some similarities with the β observed on cooling at low and high temperatures, but differs around the T_m. Above 41°C, $\beta \lesssim 1$ which, when coupled with the corresponding τ_1, indicates a polydisperse diffusive sample (Fig. 5.13j-l). At low temperatures we see $\beta \sim 0.4$, corresponding to the broad range of relaxation times in this amorphous material (Fig. 5.13a-e), and therefore dynamic heterogeneity. As we increase the temperature towards the T_m, corresponding to coarsening as discussed in Section 5.5.3, β increases (Fig. 5.12a-g), indicating the reduction in the heterogeneity of the dynamics which we ascribe to the homogenisation of the characteristic length scales of the material due to coarsening. At 40°C, when $t_{age} = 30$ s, at low-q-values we see a $\beta \geq 1$, indicating a compressed exponential, which corresponds to microcollapse events, in this case the beginning of the breakage of the gel-structure. The coarsening events, or rearrangements can induce long-range strain fields [117], and in turn lead to the presence of "earthquakes" or "avalanches" [118, 221]. These have been shown to occur intermittently in a gel, and are responsible for granular collapse in glassy materials with a similar compressed exponential behaviour of the ISF [214]. The gel here has been deeply quenched and thus contains "frozen-in" stresses [222, 223]; close to the transition temperature experimentally unavoidable small fluctuations in temperature can lead to the breakages of inter-vesicle bridges [115], which can cause rearrangements that can lead to the relaxation of these internal stresses through failure/breakage of strands [223], which corresponds to the observed dynamics, and indeed what we see visually in the raw videos. The later aging steps at $40°C$ show a lower β, perhaps due to the breakage of the structure into more heterogeneous clusters, and the loss of the characteristic length-scale of the gel. Above 42°C, $\beta \sim 0.8$ at all q-values, indicating the transition to a polydisperse diffusive sample (Fig. 5.13j-l).

5.5.7 Relaxation and Rheological Insight

Whilst we do not directly extract rheological measurements from these experiments, some of our results can be understood within the framework of gel rheology, as the behaviour of the viscoelastic materials at the gel transition have been well described by power-laws [224]. We examined the relaxation times at q=1 μm^{-1} for the system on both heating and quenching, and define this as $\tau_{1_{q=1\mu m^{-1}}}$. For all temperatures where a gel was present, this q-value was within the "plateau" regime. Both the relaxation times and the viscoelastic properties can be understood through the framework of percolation theory.

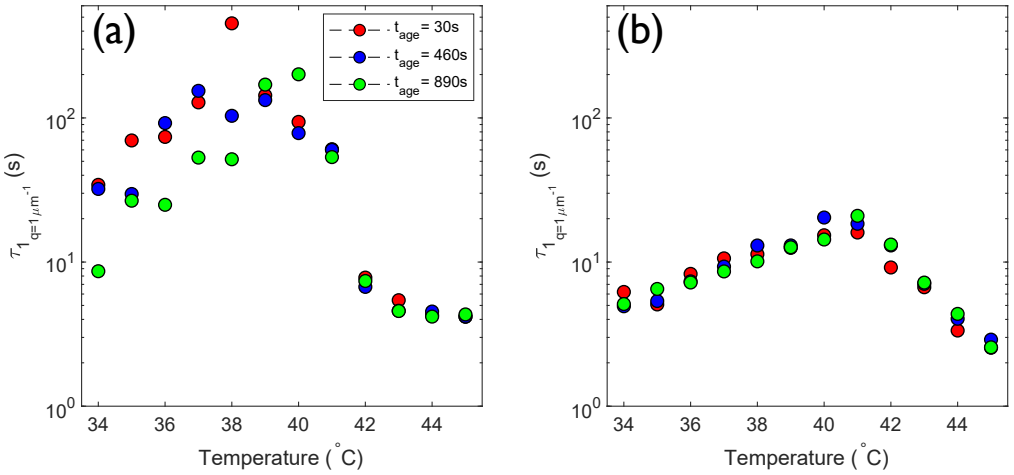

Fig. 5.14 The relaxation time, τ_1, considered at q=1 µm^{-1} ($\tau_{1_{q=1\mu m^{-1}}}$) for (a) experiments on a deeply quenched system on heating and (b) an initially diffusive system on cooling. Red, blue and green correspond to aging times (t_{age}) of 30 s, 460 s and 890 s respectively.

Percolation theory dictates that the relaxation of a system with critical value of connectivity, p_c, of the network (above which the system is a gel and below it is a sol), scales as a power law of the difference between this value and the connectivity of the system $\tau_1 \sim (p_c - p)^{-\alpha_+}$ for a sol and $\tau_1 \sim (p - p_c)^{-\alpha_-}$ for a gel [225]. This occurs as, approaching the gel point, the connectivity increases and the largest cluster grows, increasing the largest finite relaxation time [226]. Post-gelation, this decreases as the smaller clusters with finite relaxation times are incorporated into the gel, which has a relaxation time that cannot be probed within the timescales of our experiments, and instead we capture the faster relaxation of unbound vesicles/vesicle aggregates. Whilst our system represents a physical gel, the additivity of the multivalent interactions gives sufficiently long-lived inter-particle associations relative to the experimental timeframe to allow these scaling relationships to maintain their relevance. Additionally the elastic modulus exhibits power-law divergence away from the transition temperature (within the gel regime) and the viscosity diverges approaching the transition temperature [227].

In the case of the melting experiment where the temperature is increased, $\tau_{1_{q=1\mu m^{-1}}}$ increases up until 38°C, where the value peaks (Fig. 5.14a). This gradually decreases until 42°C, by which point there is a significant discontinuity, which can be explained by the gel-sol transition having occurred, which can be observed visually and through the norm. m$_1$ $S(q)$ (Fig. 5.7a), by 42°C. This can be understood through the transition from probing the relaxation time of large clusters with longer relaxation times, to a system of fluidised

vesicles. In the case of fluidised vesicles, the relaxation time scales is no longer due to the breaking of large clusters, as the p is constant (i.e particles are not connected), but simply represents the temperature dependency of the vesicle diffusion, which is due to the change in the fluid viscosity. As such, $\tau_{1_{q=1\mu m^{-1}}}$ decreases slower after this discontinuity between 41°C-42°C. Below the transition temperature, where a gel is present (T<40°C), the longest finite relaxation time decreases as diffusive aggregates with finite relaxation times are incorporated into the gel. Additionally, the stiffness of the vesicles increases with decreasing temperature [52]; therefore we imagine an increased elastic modulus of the sample. In the regime in which the system is in a gel phase (T < 40°C), we see clear aging; the relaxation time decreases with aging time. Intermittent dynamics leading to stress relaxation have been observed in colloidal systems [126, 228, 216, 229], which could explain this aging behaviour of the relaxation time. Whilst the stiffness of the vesicles and stability of the multivalent interactions leads to a gel close to an elastic solid, and the application of percolation theory would imply that the elastic modulus would increase with decreasing temperature, we also see a coarsened structure at temperatures close to the T_g (Fig. 5.7), due to the ability of the vesicles to undergo sintering-like coalescence, due to the increase in their excess area and thus patch size at higher temperatures [52]. That the elastic modulus does not seem to correspond to the coarsening is an interesting property of this material within this quenching regime.

In the case of the quenching experiment (Fig. 5.14b), we observe a peak at 41°C corresponding to the formation of diffusive clusters, which is also observable in the videos and Fig. 5.4e. $\tau_{1_{q=1\mu m^{-1}}}$ is much faster than that in the melting experiment. The q-mode used to probe the relaxation time is relatively arbitrary, and longer relaxation times are observed at lower q-modes for cooling, however it is possible that the relaxation time of the gel formed through cooling is faster due to the comparative lack of "frozen-in" stresses that occur following a deep or rapid quench [223], as in the gel in the melting experiment. This in turn leads to very different relaxation times, but also yielding behaviour.

5.5.8 Length scale and Spatially-dependent Dynamics

DDM was also applied to analyse smaller l_{box} within the full-frame image, giving multiple regions of interest within the image, as discussed in Section 5.3.4. This allowed for the exploration of spatial heterogeneity, observed in colloidal gels [230], of the β and τ_1 parameters of the gel, as well probing the length scale dependent-onset of the dynamics through the evaluation of the knee representing the start of the final decay within the accessible

q-modes (q_{knee}), as defined in Section 5.4.4. To compare the q-dependent τ_1, we considered Υ, the exponent describing the power-law q-dependency of the final (post-q_{knee} decay of the relaxation time τ_1 ($\tau_1 = kq^{\Upsilon}$). We were unable to fit the q-dependency of β in a reproducible fashion, and instead use a β averaged across all accessible q-modes, which we call $\overline{\beta}$. Whilst this removes the resolution on its q-dependency, it allows us to see trends in the data; specific trends in β that indicate interesting dynamics at specific q-modes are referred to directly.

Quenching

Clustering of the parameters on quenching showed a consistent trend of decreasing $\overline{\beta}$ and Υ, with decreasing temperature, across all l_{box}, indicating the movement from a diffusive and relatively monodisperse system to the formation of larger polydisperse aggregates, which continue to diffuse and aggregate (Fig. 5.15), before forming a gel. The q_{knee} shifts to higher q-values (Fig. 5.18) with decreasing temperature, and this indicates that onset of the final decay τ_1 is shifted to smaller wavelengths and thus length scales. The plateau that exists before the onset of q_{knee} (Fig. 5.10), indicates the gel's solid like properties extending to even smaller lengths scales (higher q_{knee}) at which we observe the onset of subdiffusive dynamics. The spatial variation within the temperatures can be particularly observed in Fig. 5.15c&d, where the parameter clusters grow larger, particularly with decreasing temperature, due to the heterogeniety of dynamics between different regions of the gel structure. At low-temperatures, we also see parameter clusters where $\Upsilon \approx -1$ coupled with $\beta < 1$ (Fig. 5.15); this type of anomalous dynamics has been observed in colloidal glasses [231].

With decreasing temperature, as aggregates form, $\overline{\beta}$ shifts from being tightly clustered to a larger spread at smaller l_{box}, with a decreasing $\overline{\beta}$ as a function of temperature (Fig. 5.16). At and below 39°C, β begins to increase upon decreasing l_{box} (Fig. 5.16a-g). This is to be expected; at higher temperatures when clusters have formed, these are still diffusive, so the distribution of relaxation times both within a subsection and over the entire sample should be relatively narrow. Upon the formation of a gel and the ensuing time-dependent coarsening, the heterogeneity of the distributions of relaxation times should drive $\overline{\beta}$ down across the full sample ($l_{box} = 299\,\mu m$); however, locally (at smaller l_{box}) it is possible for the distribution of relaxation times to be narrower, and as such have higher $\overline{\beta}$ than when $l_{box} = 299\,\mu m$.

Υ shows no l_{box} dependency, but the standard deviation shows the range of heterogeneity in the sample when considering smaller l_{box} (Fig. 5.17). Υ decreases from ~ -2.8 to ~ -1.5 on cooling from 43°C-33°C suggesting a slowing down of the average decay of the relaxation

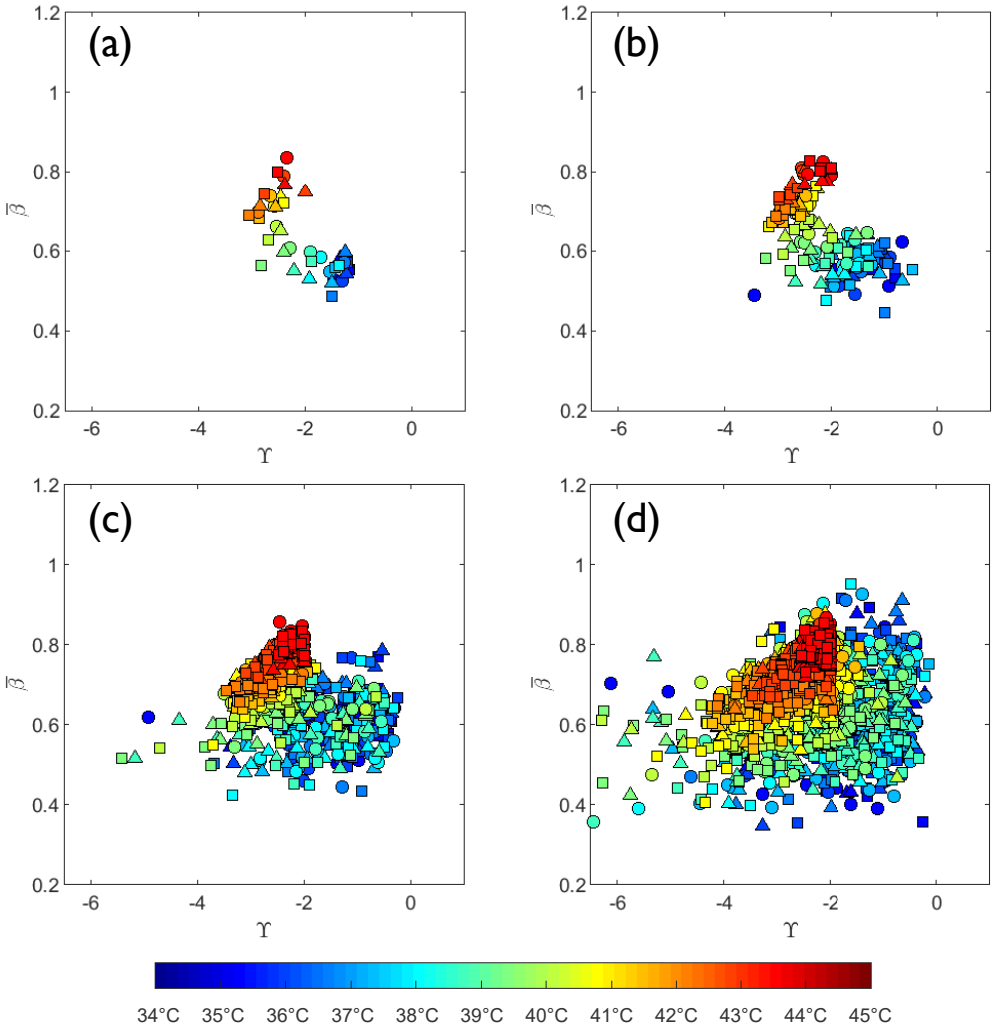

Fig. 5.15 Clustering between the mean across all accessible q-modes of the exponent of the stretched/compressed the exponential used to fit the ISF, $\overline{\beta}$, and the corresponding Υ, the exponent of the power-law q-dependency of the final decay of the relaxation time τ_1, for an initially diffusive sample on quenching. Square (sub)sections of the image of length (l_{box}) (a) 299 µm, (b) 149.5 µm, (c) 74.8 µm and (d) 37.4 µm are shown. ◯, △ and □ correspond to parameters extracted from videos at aging times (t_{age}) of 30 s, 460 s and 890 s respectively, and the colourbar indicates the temperature of each point.

time, τ_1.

The delayed onset of the q_{knee}, the q-value where the start of the final decay of τ_1 is observed, is $\gtrapprox 2.1$ with minimal l_{box}-dependence below 41°C (Fig 5.18a-h). While q_{knee} is relatively invariant below this temperature, as discussed in Sections 5.5.5 & 5.5.6,

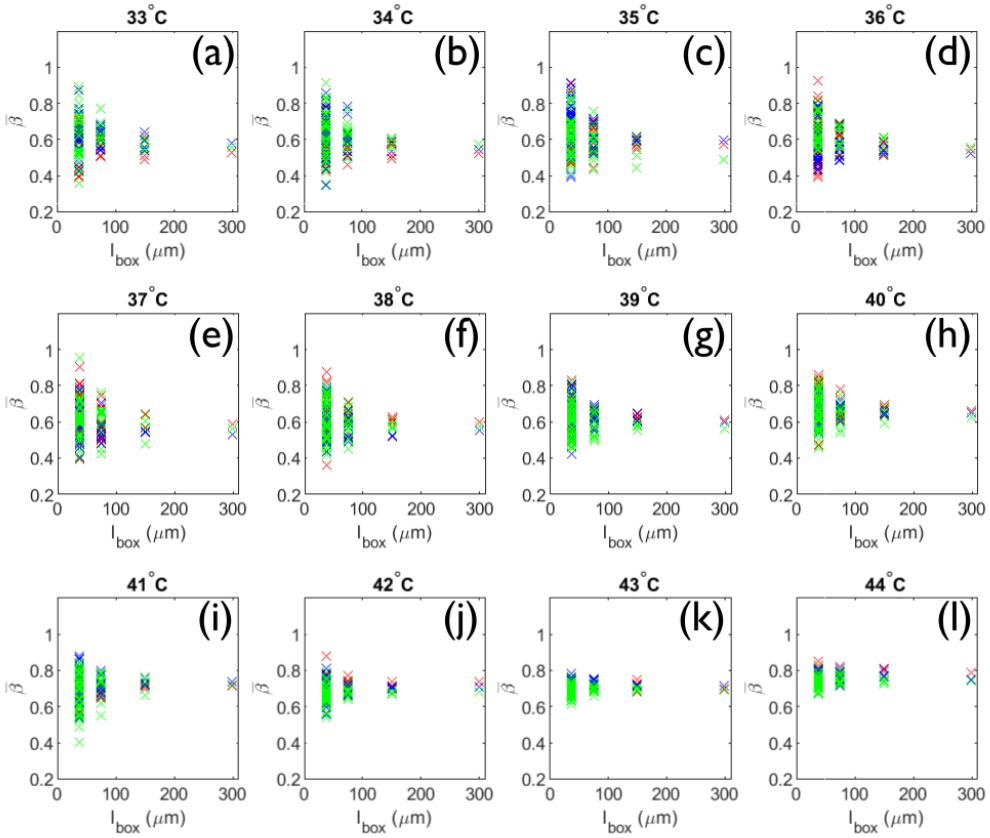

Fig. 5.16 The mean across all accessible q-modes of the exponent of the stretched/compressed exponential used to fit the ISF, $\overline{\beta}$, for an initially diffusive sample on quenching. Spatial resolution on the length-scale dependent heterogeneity of this parameter is achieved through considering square (sub)sections of the image of dimension (l_{box}) 299 µm, 149.5 µm, 74.8 µm and 37.4 µm respectively. Red, blue and green markers correspond to parameters extracted from videos at aging times (t_{age}) of 30 s, 460 s and 890 s respectively.

the dynamics before the second knee vary considerably. Above 40°C, $q_{knee} \lessapprox 1.9\,\mu m^{-1}$ (Fig 5.18i-l), with q_{knee} increasing for decreasing l_{box}. This is due to the predominance of diffusive motion at and above the transition temperature.

Melting

On melting we see noticeably different trends. At high temperatures diffusive measurements are similarly clustered to what we observe in the quenching experiment, as seen in Fig. 5.15. The dynamics at temperatures around the T_m of the gel are best visualised in Fig. 5.19d where we can see a parameter cluster where β is ≥ 1 and $\Upsilon \sim -1$, indicative of the presence of ballistic/superdiffusive dynamics indicative of micro-collapse events at 40°C. These can

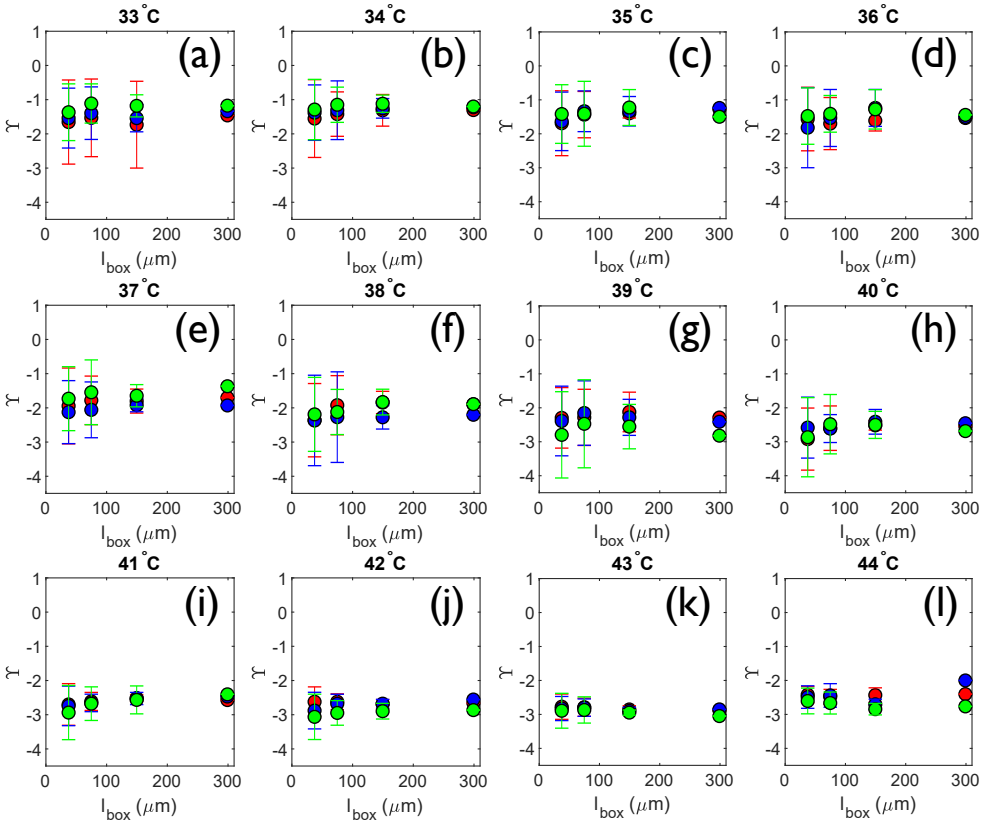

Fig. 5.17 The exponent (Υ) of the power-law q-dependency of the final decay of the relaxation time τ_1 for an initially diffusive sample on quenching. Spatial resolution on the length-scale dependent heterogeneity of this parameter is achieved through considering square (sub)sections of the image of dimension (l_{box}) 299 µm, 149.5 µm, 74.8 µm and 37.4 µm respectively. Errorbars correspond to the standard deviation of Υ for each l_{box}. Red, blue and green markers correspond to parameters extracted from videos at aging (t_{age}) times of 30 s, 460 s and 890 s respectively.

be seen in the videos through the breakage of fibrous structures in the gel, but could also correspond to smaller rearrangements in the structure. Indeed, it is hypothesised that these rearrangements are due to experimentally unavoidable thermal fluctuations that are randomly spatially and temporally distributed, leading to small shear forces to cause the micro-collapse events [131, 223]. This allows the vesicles to restructure locally to create denser packings, causing local strain fields that cause longer-range rearrangements in the structure itself [118]. In the case of the heated gel we hypothesise that, in addition to the presence of local strain fields, the breakage of large strands of the gel is sufficient to cause flow-induced local rearrangement of structure. As we can see in Fig. 5.9g-i, the long time behaviour of the

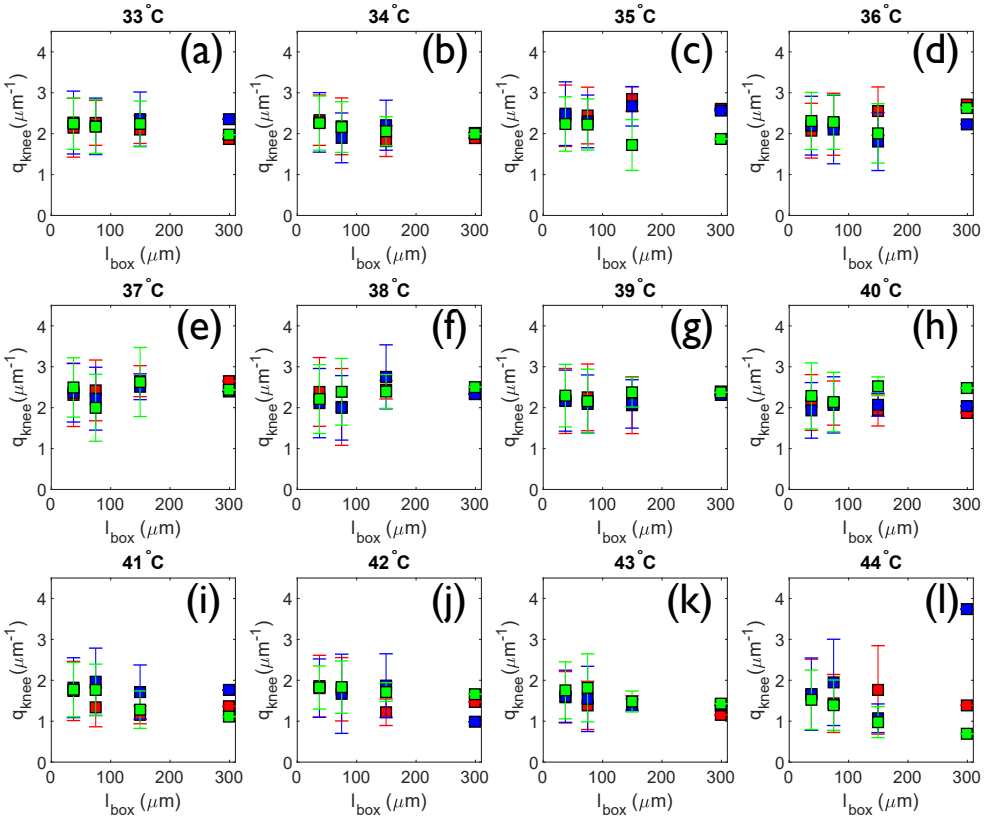

Fig. 5.18 The mean wave-vector where the knee (q_{knee}), describing the onset of the final decay of the relaxation time τ_1, occurs for an initially diffusive sample on quenching. Spatial resolution on the length-scale dependent heterogeneity of this parameter is achieved through considering square (sub)sections of the image of dimension (l_{box}) 299 µm, 149.5 µm, 74.8 µm and 37.4 µm respectively. Errorbars correspond to the standard deviation of q_{knee} for each l_{box}. Red, blue and green markers correspond to parameters extracted from videos at aging times (t_{age}) of 30 s, 460 s and 890 s respectively.

$I(q,\tau)$ does not lead to the formation of a plateau, indicating that in this intermediate regime the time to the decorrelation of the system is longer than the experimental window. Below 39°C, a broad parameter cluster where $-4 \leq \Upsilon \geq 0$ (with a mean $\Upsilon \sim -2$) is observed for all $l_{box} \geq 74.8\mu m$ with a $\beta \leq 0.5$ (Fig. 5.19a-c), showing the extent of the spatial heterogeneity of the material behaviour at temperatures below the T_m; the range of Υ indicates the presence of caged, subdiffusive, "locked-in" behaviour and other experimentally observed anomalous diffusion [231]. Immediately after the T_m, at 41°C, we see a clustering in Υ indicating a rapidly decorrelating $I(q,\tau)$. As mentioned previously, for high q-values, caged dynamics have been shown to follow a $\Upsilon \sim -4$ relationship [219, 220]. Finally when the temperature

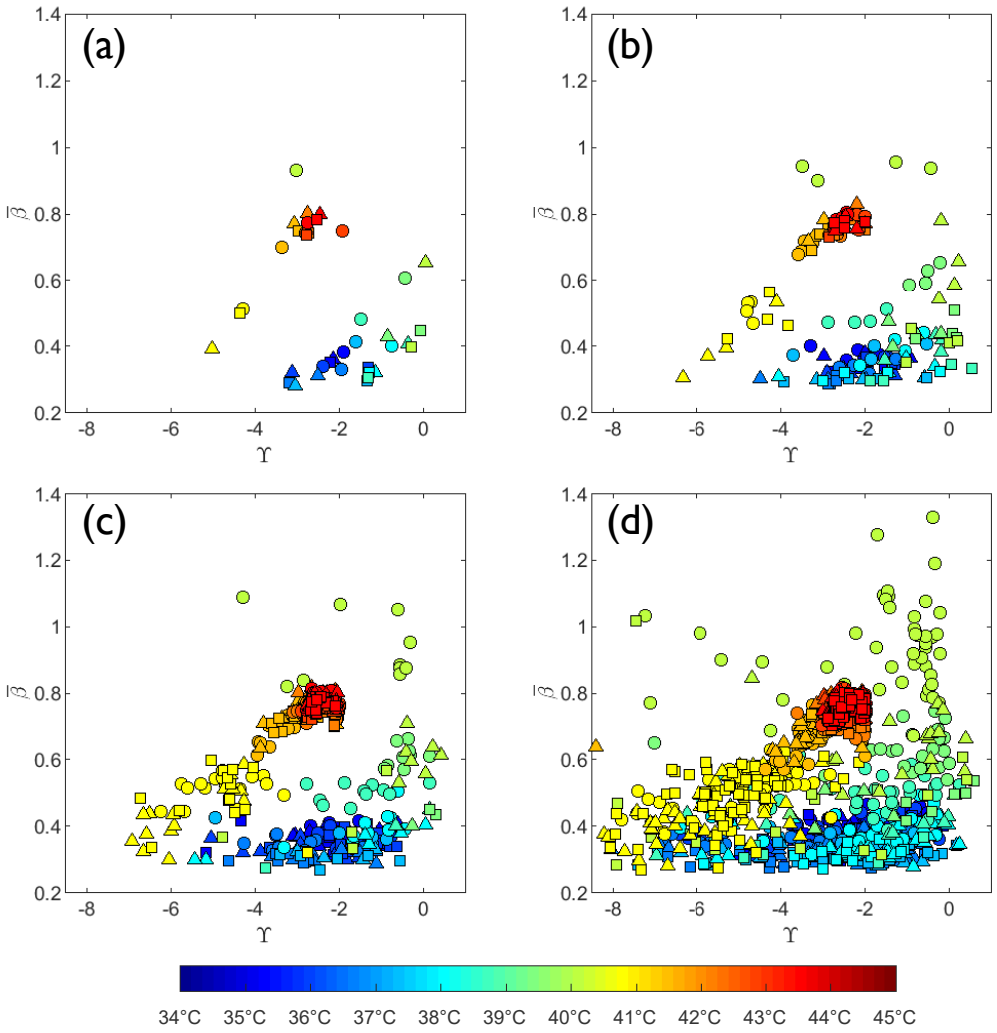

Fig. 5.19 Clustering between the mean across all accessible q-modes of the exponent of the stretched/compressed the exponential used to fit the ISF, $\overline{\beta}$, and the corresponding Υ, the exponent of the power-law q-dependency of the final decay of the relaxation time τ_1, for a deeply quenched gel on heating. Square (sub)sections of the image of length (l_{box}) (a) 299 µm, (b) 149.5 µm, (c) 74.8 µm and (d) 37.4 µm are shown. ◯, △ and □ correspond to parameters extracted from videos at aging times (t_{age}) of 30 s, 460 s and 890 s respectively, and the colourbar indicates the temperature of each point.

is $\geq$42°C, we see a cluster demonstrating the expected Υ and $\overline{\beta}$ for a polydisperse diffusive sample (Fig. 5.19).

At temperatures $\leq$ 36°C, $\overline{\beta}$ is tightly clustered, and increases with decreasing l_{box} (Fig. 5.16a-d), indicating that the spatial heterogeneity is somewhat localised; however,

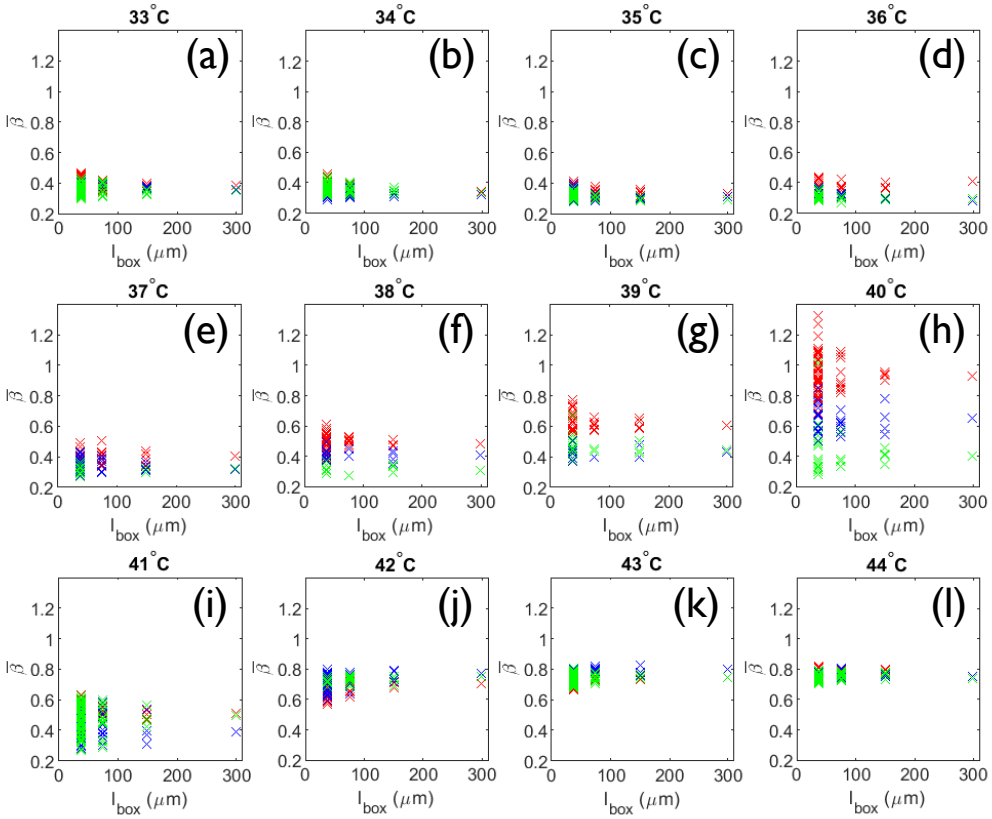

Fig. 5.20 The mean across all accessible q-modes of the exponent of the stretched/compressed exponential used to fit the ISF, $\overline{\beta}$ for a deeply quenched system on heating. Spatial resolution on the length-scale dependent heterogeneity of this parameter is achieved through considering square (sub)sections of the image of dimension (l_{box}) 299 µm, 149.5 µm, 74.8 µm and 37.4 µm respectively. Red, blue and green markers correspond to parameters extracted from videos at aging times (t_{age}) of 30 s, 460 s and 890 s respectively.

even when considering the smallest l_{box} $\beta \leq 0.5$ which indicates a broad range of relaxation times (Figure 5.20). This is distinct from the β observed on quenching (Figure 5.16), which was consistently higher, indicating less heterogeneity in relaxation times. This could be due to the deeply quenched nature of the gel in the melting experiment, causing the freezing in of stresses with different relaxation times. For gels forming through arrested spinodal decomposition, it has been shown that a slower quench rate across the spinodal would lead to more ordered and less heterogeneous gels [208], which would support our observation between the heating and quenching experiments. As the gel coarsens, we still see the increasing $\overline{\beta}$ with decreasing l_{box}, however $\overline{\beta}$ also increases as a function of temperature, indicating coarsening-dependent local homogenisation of structure. Additionally, between 38°C and

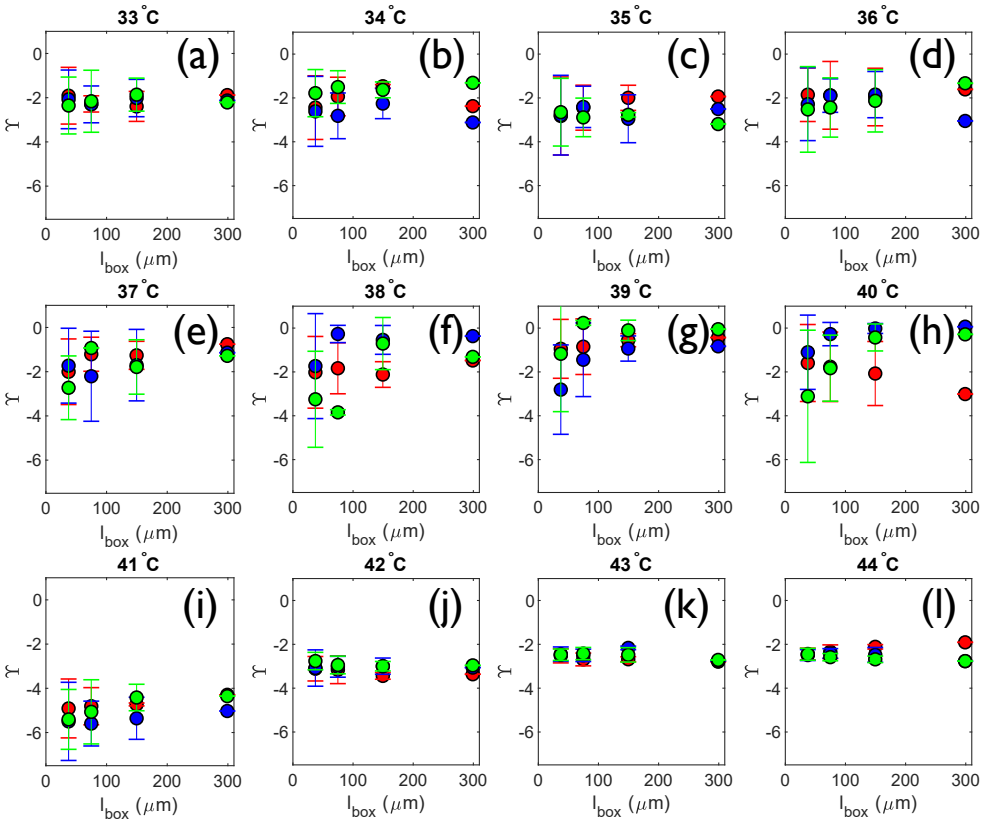

Fig. 5.21 The exponent (Υ) of the power-law q-dependency of the final decay of the relaxation time τ_1 for a deeply quenched system on heating. Spatial resolution on the length-scale dependent heterogeneity of this parameter is achieved through considering square (sub)sections of the image of dimension (l_{box}) 299 µm, 149.5 µm, 74.8 µm and 37.4 µm respectively. Errorbars correspond to the standard deviation of Υ for each l_{box}. Red, blue and green markers correspond to parameters extracted from videos at aging times (t_{age}) of 30 s, 460 s and 890 s respectively.

40°C, we observe clear signs of aging, with decreasing $\overline{\beta}$ with increasing time (Fig. 5.20f-h). At 40°C see $\overline{\beta}$>1, predominantly for $t_{age} = 30$ s. We see a transition from microcollapse events described by this compressed exponent, to a stretched exponential, where $\overline{\beta}$<1, at $t_{age} = 460$ s and $t_{age} = 890$ s. The compressed exponential is only observed with smaller l_{box} (Fig. 5.20h); it has been shown that these rearrangement events in low-volume fraction systems are the main relaxation mechanism only at lengths scales corresponding to a few particle sizes and at longer length scales the dynamics are described by a stretched exponential [218]. A compressed exponential has been attributed to the presence of intermittent anomalous diffusion events, rather than continuous processes. To explore these intermittent dynamics,

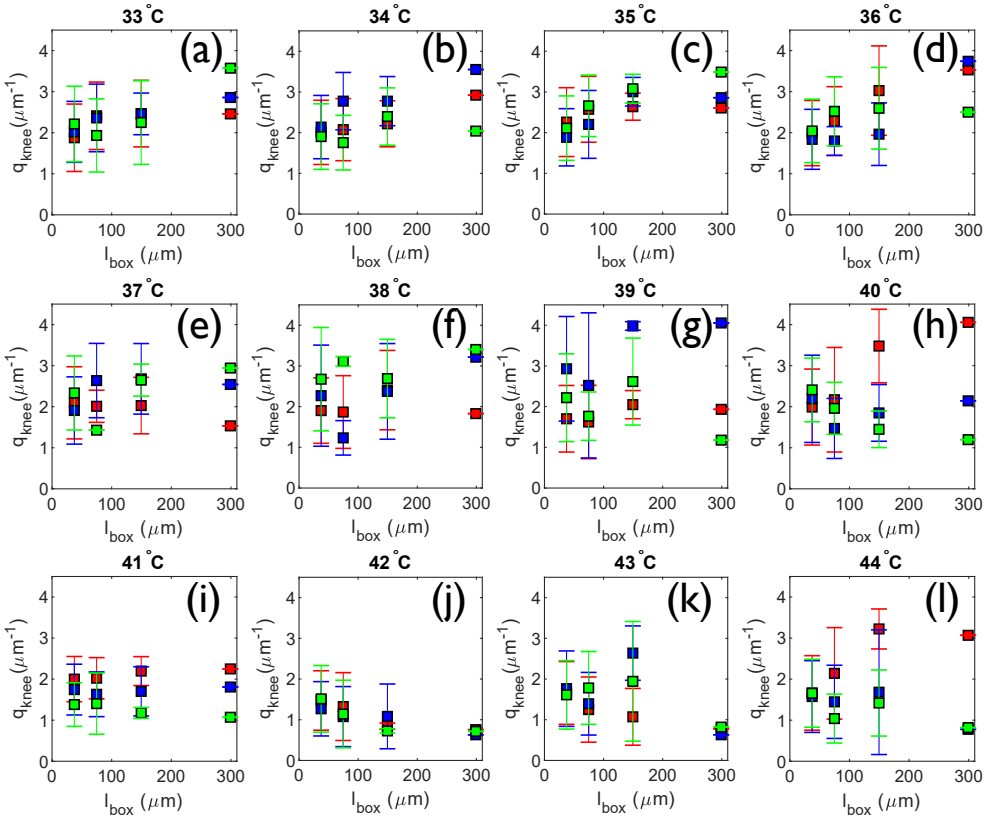

Fig. 5.22 The mean q-value where the knee (q_{knee}), describing the onset of the final decay of the relaxation time τ_1, occurs for a deeply quenched system on heating. Spatial resolution on the length-scale dependent heterogeneity of this parameter is achieved through considering square (sub)sections of the image of dimension (l_{box}) 299 µm, 149.5 µm, 74.8 µm and 37.4 µm respectively. Errorbars correspond to the standard deviation of q_{knee} for each l_{box}. Red, blue and green markers correspond to parameters extracted from videos at aging times (t_{age}) of 30 s, 460 s and 890 s respectively.

we considered the FFT power fluctuation $\Delta I(q,\tau,t)^2$ (the instantaneous value of the $I(q,\tau)$ before being ensemble averaged) as in Ref. [114], where they found the intensity fluctuations exhibit occasional excursions to higher values, and skewed distributions at shorter lag times. We looked at boxes where $\beta \geq 1$ to see whether skewness decreased as a function of lag time, however the results were inconclusive.

Υ shows no discernible l_{box} dependency between 35°C and 41°C (Fig. 5.21). Within the region described as a coarsening gel in Section 5.5.3 ($T \leq 40°C$), with "locked-in" relaxation times representative of a connected-gel structure, we observe a decrease in Υ, and

a large increase in the standard deviation, indicating a range of dynamics present at these temperatures when considering smaller l_{box}. The behaviour of q_{knee} followed that of the normalised first moment of $S(q)$, by increasing whilst approaching the start of the gel-sol transition at $\sim 41^{\circ}$C (Fig. 5.22a-i). Above this temperature, q_{knee} decreases as the gel breaks into diffusive vesicles. In particular, between 33°C-38°C, we see that the q_{knee} decreases as a function of the l_{box}. This is in the region where the relaxation time increases to its maximum value as a function of temperature (Fig. 5.14a). Immediately preceding the T_m, the q_{knee} has a large standard deviation, indicating that the rearrangement processes which occurs at these temperatures has led to a range of heterogeneous local structural properties of the gel.

Spatial Dependency and Heterogeneity of Dynamics

It has been shown that a measure of the heterogeneity of the dynamics, the four-point dynamic susceptibility, scales with the system relaxation time [232, 126]. Indeed, spatially heterogeneous dynamics are observed in systems demonstrating longer relaxation times [233]. This fits well with our observed dynamics; in both the quenching and the melting experiments we see that there is a range of Υ and $\overline{\beta}$s that indicate the spatial heterogeneity through the comparison of regions of a range of l_{box}. Analogously to the case of high-volume fraction gels, we see smaller $\overline{\beta}$ for the more deeply quenched gel (observed in the melting experiment), due to it being deeper into its glass phase; therefore the deviations from diffusive behaviour are correspondingly larger, translating to a smaller subdiffusive exponent $\overline{\beta}$ [216]. Furthermore, the length scale-dependent heterogeneity of colloidal gels has previously been reported, showing the scaling of increasing heterogeneity with increasing q-values and thus smaller length scales [126], which we observe in the errorbars in Figs. 5.17& 5.21. From a structural point of view, this heterogeneity has previously been observed in low-volume fraction attractive colloidal systems [234]. The structural heterogeneity of individual clusters within a network of interconnected clusters, accounts for the local homogeneity (which we see through the higher $\overline{\beta}$ at smaller l_{box}) within the gel regime. In the gel regime for the melting experiment, we see an l_{box} dependency of the q_{knee} which is not observed in the quenching experiments, leading us to hypothesise that this behaviour is specific to more deeply quenched gels.

5.6 Conclusions

We implemented spatially resolved DDM in order to probe the previously unstudied dynamics of a temperature responsive gel consisting of DNA-functionalised LUVs. We found evidence of spatial heterogeneity corresponding to different dynamics within the gel, which correspond to visible structural changes. When we consider the entirety of the image, we find that the dynamics of our amorphous material are "averaged" out; the use of DDM on subsections of the image reveals the richness of the dynamics across the sample.

At high temperatures, above transition temperature for either sol-gel or gel-sol, we find the dynamics of the diffusive system well fit by the stretched/compressed exponential model. Fitting the ISF of diffusive systems using cumulant analysis, gives results in agreement with those theoretically expected, and additionally allows for insight into the polydispersity of a sample. The derived Υ from this analysis is in good agreement with that expected from a diffusive sample, and confirms the size of the particles to be similar to those expected from extrusion, with similar polydispersities. From the stretched exponential fit $\Upsilon \simeq -2.4$, not quite representative of the $\tau_1 \sim q^{-2}$ decay expected. This could be due to bleeding between parameters in the fitting.

We find markedly different relaxation times for the gel formed through quenching the sol or melting the (deeply-quenched) gel. We hypothesise that this is due to the increased presence of "frozen-in" internal stresses due to the rapid quenching in the melting experiment. We see divergence of the relaxation times, which can be understood through percolation theory, which gives insight into the development of the viscoelastic properties of the material. This, coupled with the static measurements, allow us to find the T_g and T_m of the system, which both occur at approximately 40°C.

In both experiments, we find that we can describe the dynamics through clustering of two parameters derived from of our stretched exponential model, $\overline{\beta}$ and Υ, which we find leads to the presence of defined clusters which correspond to the phenomenology.

On melting of the gel, we find a transition from subdiffusive dynamics, corresponding to the small thermal movements of the gel structure, to a slower decay in the relaxation time. We see clear evidence of the coarsening through the normalised first moment of $S(q)$, of the structure approaching the melting temperature of the gel. This can be explained by the temperature dependency of the mechanical properties of the vesicles, which allows for the tighter packing of vesicles at higher temperatures below the transition temperature. As we

approach this we see a "locked-in" relaxation plateau extending to higher q-values, indicative of the material behaving like an elastic solid. Around the gel-sol transition, at 40°C, when considering smaller subsections we find local dynamics which indicate the presence of microcollapse events, which can be visually observed as branch breaking of the gel structure. At 41°C, we see relaxation times which decay as $\tau_1 \sim q^{-4}$, which has been observed in granular and jammed systems approaching the gel transition. Finally, as the gel-sol transition is complete we observe dynamics capturing the diffusive behaviour of the vesicles and their polydispersity.

On quenching, conversely to the behaviour seen in the melting experiments, the gel coarsens with decreasing temperature. This, however, may be misleading; coarsening is also a function of time, and thus it would be difficult to tease out the temperature and time dependencies of coarsening. We initially see the same high-temperature behaviour observed in the melting regime. This continues with a slowing down of the relaxation time and a decrease in β as the sample forms clusters with a distribution of relaxation times. As the gel forms, we see two distinct regimes of τ_1 decay; at low q-modes we observe $\tau_1 \sim q^{-1}$, wheras at higher q-modes we see $\tau_1 \sim q^{-2}$. When we look at low q-modes in smaller regions of the image, we can see evidence of some $\beta \geq 1$ possibly indicating the presence of interfacial coarsening as the diffusive clusters aggregate. As the temperature quench increases, and the clusters stop diffusing and the gel network is formed, the low q-mode behaviour of $\tau_1 \sim q^{-1}$ tends towards being a plateau, indicating that the dynamics are "locked-in" across length scales probed at these $q-modes$, which corresponds to the presence of a gel with elastic properties.

The broad range of relaxation times present in the gel can be seen in an increase in the $\overline{\beta}$ at low temperatures. The general increase of $\overline{\beta}$ with decreasing l_{box} within the gel regime, indicates that the dynamics are locally more homogeneous. On quenching this is also observed. In both cases, with coarsening (as defined by the normalised first moment of $S(q)$; with increasing temperature until T_m for melting experiments and with decreasing temperature after T_g for quenching experiments), we see a trend of increasing of $\overline{\beta}$; structural changes on coarsening should lead to a more homogeneous structure. The relaxation decay parameter, Υ, on the other hand, remains relatively constant with l_{box} for both quenching and melting experiments, however the standard deviation increases significantly, indicating differing local dynamics. The q_{knee} shifts to higher q-values at lower temperatures in the quenching experiment. In the melting experiments, coarsening occurs with increasing temperature approaching the gel-sol transition, and we see an increase in q_{knee} approaching this

value, which would correspond to an increase in the characteristic length scale of the material. Higher values of q_{knee} are seen in the (initially deeply quenched) melting experiments, indicating the gel in this experiment behaves as an elastic solid at shorter length scales than the gel formed through the slower quench in the quenching experiment. Whilst no strong l_{box}-dependency is seen in terms of the mean value, the standard deviation increases with decreasing l_{box} again pointing to the spatial heterogeneity of such materials.

To summarise we find that we can use DDM to assess and spatially resolve the dynamics of systems of attractive DNA-functionalised LUVs. We find these dynamics are spatially heterogeneous, though can be locally homogeneous, to an extent determined by route to gelation. This phenomenology, and its temperature dependence, can be reconciled with the existing work on low-volume fraction attractive colloidal systems, as well as novel behaviour driven by the changes in the mechanics of the vesicles themselves.

Chapter 6

Microfluidic Device for GUV production: Design, Fabrication and Application

This chapter details work conducted on the development of a new high-throughput method for GUV production using microfluidics which allows for encapsulation and functionalisation of lipid vesicles. Here, the design and fabrication process will be considered, along with characterisation of the method: both the properties of the vesicles produced, as well as the tunability of the device. Lastly, applications to bottom-up synthetic biology and biomimetic material fabrication will be explored.

6.1 Why Microfluidic GUVs?

As discussed in Section 2.5, and Chapter 3, there are myriad of different techniques with which to create lipid vesicles. These methods include electroformation, phase transfer and sonication [164, 235, 20]. Such methods are limited by suffering from one or more of the following: low-yield encapsulation, non-uniform functionalisation with surface bound receptor constructs, polydispersity, imprecise control of phase domains and being low-throughput [149, 143, 144, 150, 151]. Microfluidics offers the ability to control or improve on the problems listed above (for reasons considered in Section 2.5) and, more specifically a demonstrated or potential ability to: produce monodisperse vesicles of a range of sizes, form multicompartment vesicles, form asymmetric bilayers, efficiently encapsulate cargo (including charged constructs) and functionalise vesicles in a single process [154, 236, 237]. For applications to engineering disciplines and more specifically for the use in biosensing, which much of this thesis is in service to, it will be essential for vesicles to be as homogeneous

as possible, in terms of size, excess area and functionalisation in order to have consistency between devices. Vesicles with controllable size, membrane and internal content, and other properties are also of keen interest for work in biophysical studies, to remove experimental variance from the heterogeniety of vesicle production in existing methods.

6.2 Method Overview & Design

6.2.1 Mechanism of GUV generation

We employ a double emulsion method for the creation of lipid vesicles which integrates the solvent choice from Ref. [144] with a commonly used double emulsion template forming channel geometry, with a design inspired by those in Refs. [149, 238–240]. The device consists of 3 input channels containing three different phases: an inner aqueous phase (IA), an outer aqueous phase (OA) and a lipid-carrying organic solvent phase (LO), as shown in Fig. 6.1. Briefly, an IA phase is flowed through an intersection between two channels containing the LO phase. This forms a water-in-oil droplet (w/o) at this first junction (J_1) (Fig. 6.1b), with the lipid molecules forming a monolayer, exposing the hydrophilic head-groups to the inner aqueous phase. A long post-J_1 channel allows visualisation of this process to ease the tuning of pressures to control vesicle formation. At the next junction (J_2), the w/o droplet meets two channels containing the OA solution. Passing through this allows the stream of w/o droplets to be pinched off into either single or multi-compartment water-in oil-in water (w/o/w) double emulsion droplet (Fig. 6.1c), with a second monolayer formed at the interface between the OA and LO phases. Due to the minimisation of the interfacial energies, this double emulsion transitions to a lipid bilayer formed around the IA phase with a small solvent pocket, which buds-off downstream, leaving lipid vesicles (Fig. 6.1d).

In order to realise this mechanism, there are some key considerations in phase composition and device coating. In the OA phase we add glycerol, which has been shown to aid the shearing/pinching off of the LO phase by the OA phase as well as stabilising the membranes of the liposomes [142]. Additionally, the aqueous phases contain Kolliphor, a nonionic tri-block copolymer surfactant (Poloxamer 188), which reduces the interfacial tension between the two monolayers in the double emulsion leading to the dewetting and removal of the solvent from the bilayer, discussed further in Section 6.2.3, as well as preventing fusion of double emulsion droplets [154]. The choice of lipid-carrying organic solvent is octanol, which allows dewetting of the solvent from the bilayer for reasons discussed more fully in Sections 6.2.2 & 6.2.3. The post-J_2 channel and the OA phase containing channel are

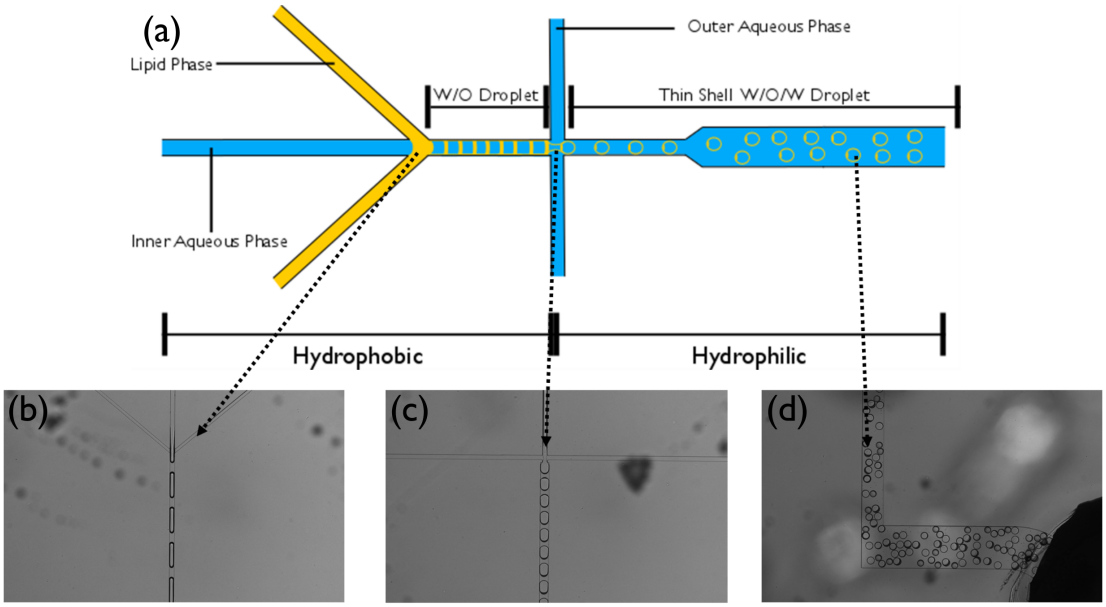

Fig. 6.1 (a) Schematic of the mechanism of GUV production we employ. An Inner Aqueous stream is flowed through a junction, which is the intersection of two streams of a lipid-carrying phase, forming aqueous water-in-oil droplets. These drops are then pinched off to form thin-shelled water-in-oil-in water droplets. Arrows showing brightfield images of the chip respresentative of the parts of the schematic: (b) the junction (J_1) where the water-in-oil droplet is formed, (c) the junction (J_2) where the water-in-oil-in water double emulsion droplet is formed and (d) vesicles/oil-droplets/unseparated double emulsion droplets entering the outlet after passing through the serpentine.

rendered hydrophilic through a polyvinyl alcohol (PVA) coating. This is done to prevent the LO phase wetting these channels, which can lead to reduced yield at J_2 and rupturing of the vesicles on the channel surfaces [241].

6.2.2 Choice of Carrier Fluid

The limiting factor in many microfluidic techniques is the presence of residual solvent in the bilayer of the vesicles [143], which affects the properties of the vesicles and thus their applicability to their hypothesised applications. In order to prevent this we settled on octanol as our organic solvent, as used in Ref. [144] where they showed separation of the solvent to allow vesicle formation.

Though other solvents such as squalene or oleic acid have been used, we settled on octanol due to its high interfacial tension with water, which should aid the dewetting of the

solvent from the bilyaer [143, 142, 144, 154]. Initial testing with oleic acid confirmed that octanol afforded improved dewetting of the solvent from the bilayer. Other solvents, such as hexane/chloroform mixtures have been shown to have been employed successfully, but are not compatible with biological systems [154]. Furthermore, we were unable to produce stable vesicles using hexane/chloroform mixtures, in particular struggling to form the initial w/o droplet at J_1. These preliminary experiments conducted with other organic solvents were less promising that those with octanol.

The octanol is removed from the bilayer due to energy minimisation. Octanol in a bilayer causes defects in the ordered structure of the lipids, disrupting the interactions between hydrophobic tails, which is energetically unfavourable [242]. More importantly, octanol and water have a significantly higher interfacial tension than the membrane tension of a vesicle, and as such it makes it energetically favourable for the octanol to be removed [243, 244].

6.2.3 Tuning solutions for optimal dewetting

Dewetting of double emulsions

To tune the dewetting of the double emulsions to allow for the formation of a lipid bilayer from the two monolayers through the expulsion of the oil from the double emulsion "shell", we consider the spreading coefficient as followed in Ref. [154]. The spreading coefficient is defined as follows:

$$S_i = \gamma_{jk} - (\gamma_{ij} + \gamma_{ik}), \tag{6.1}$$

where for two solutions i and j, γ_{ij} is the interfacial tension. In order to tune the dewetting of the double emulsions we first consider when the spreading coefficient of the oil-phase, S_o<0:

$$S_o = \gamma_{w1w2} - (\gamma_{ow1} + \gamma_{ow2}) < 0, \tag{6.2}$$

here, the interfacial tension between the two aqueous phases is less than the interfacial tensions between each aqueous phase and the oil phase, causing spontaneous dewetting to minimise the total interfacial energy. O is the LO phase, w_1 is the IA phase and w_2 is the OA phase.

However, this consideration is insufficient for the formation of lipid vesicles; instead we must also achieve the complete dewetting of the O phase over the w_1 phase, which requires S_{w1}<0, therefore

$$S_{w1} = \gamma_{ow2} - (\gamma_{ow1} + \gamma_{w1w2}) < 0, \tag{6.3}$$

and that S_{w2}>0, therefore

$$S_{w2} = \gamma_{ow1} - (\gamma_{ow2} + \gamma_{w1w2}) > 0. \tag{6.4}$$

Pendant Drop Analysis

To test what compositions and combinations of IA, OA and LO phases would be sufficient to achieve dewetting of the solvent from the bilayer according to the criteria in Section 6.2.3, we conducted pendant droplet measurements to find the interfacial tensions between the LO and the two aqueous phases respectively (the OA and IA phases). By varying the compositions of these phases, we can tune the interfacial tensions and thus the potential for dewetting of the solvent from the lipid bilayer. Pendant droplet measurements were achieved by suspending a drop of an LO phase from a needle in a bulk liquid phase (Fig. 6.2a). The shape of the drop results from the relationship between the interfacial tension and gravity. Interfacial tension is calculated from the shadow image of a pendant drop whereby we threshold the image and extract the contour [245], and make use of the Young-Laplace equation:

$$\Delta p = \gamma(\frac{1}{r_1} + \frac{1}{r_2}), \tag{6.5}$$

where Δp is the pressure difference between the two liquid phases, γ is the interfacial tension and r_1 and r_2 are the radii of curvature for the surface. From this we can arrive at the following expression for interfacial tension:

$$\gamma = \frac{\Delta\rho g d_e^2}{H}, \tag{6.6}$$

.

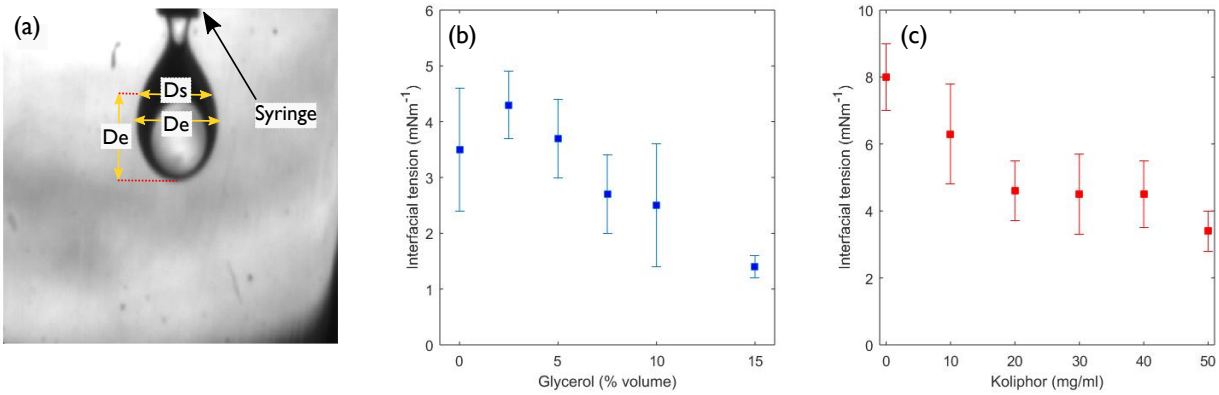

Fig. 6.2 Results from pendant droplet measurements. (a) An LO phase drop from a syringe nozzle in a bulk aqueous phase, annotated with the parameters we extract to find the interfacial tensions. The interfacial tensions between the OA and LO phase vary in response to two drivers of interfacial tension: (b) glycerol and (c) Kolliphor respectively. For each data point, $N = 20$.

Where $\Delta\rho$ is the density difference, g the gravitational constant and where H is a correction factor derived in Ref. [246] defined as:

$$H = 0.02664 + 0.62945\alpha^2, \tag{6.7}$$

where $\alpha = \frac{D_s}{D_e}$, with D_e being the equatorial diameter of the drop and D_s being the width of the drop a distance D_e away from the apex, which can be found from the drop profile (Fig.6.2a).

Iterating aqueous solutions with dewetting considerations

Testing different solutions for IA and OA phases, we found that salt and sugar compositions of the aqueous phases had no noticeable effect on the interfacial tension (Table. 6.1), which allows us to change compositions to allow for the encapsulation of cargo or functionalisation of DNA constructs with minimal effect on the extraction of residual octanol. Indeed, the interfacial tension between the LO phase and either an IA phase containing Cell-free extract (discussed further in Section 6.5.2) or a 200mM sucrose solution varied by only 2.5%. We also found no noticeable effect of the use of ethanol in the OA on the interfacial tension. Octanol has a high solubility in ethanol, causing it to dissolve into the solution, reducing the distance betweeen monolayers which in turn allows for self-assembly into a

Description	**Aqueous Solution Composition**						
	γ $(mN\,m^{-1})$	*Sucrose* *(mM)*	*NaCl* *(mM)*	*Kolliphor* $(mg\ ml^{-1})$	*Glycerol* *(v%)*	*EtOH* *(v%)*	*Lipid* $(mg\ ml^{-1})$
Octanol in IA	3.5±1.1	200	0	50	0	0	0
LO in IA	3.3±0.6	200	0	50	0	0	2
LO in IA	3.5±0.8	87	100	50	0	0	2
LO in IA	8.0±1.8	87	100	0	0	0	2
LO in OA	1.4±0.2	200	0	0	15	0	2
LO in OA	1.4±0.2	87	100	0	15	20	2

Table 6.1 The variation of interfacial tension (γ) between the LO solution and various IA and OA solutions, demonstrating the interfacial tension dependency on these parameters.

bilayer [149, 153, 142, 239]. The addition of ethanol did lead to vesicles with no visually observable residual octanol in the membrane, however these vesicles were short lived, and tended to fuse with other vesicles, removing the monodispersity of the sample. The presence of lipids in the LO phase reduces the interfacial tension with the OA phase by $0.2\,\mathrm{mNm}^{-1}$ compared to the interfacial tension with Octanol without the addition of lipids (Table. 6.1). The minimisation of the interfacial tension between the LO and OA phases can also be driven by the use of glycerol and Kolliphor (Fig. 6.2b-c), and this is exploited to drive the dewetting process. This is considered more thoroughly in Table 6.2.

Reducing the glycerol or Kolliphor content led to a larger interfacial tension between the LO and OA phases (Fig. 6.2b-c), making it less energetically advantageous for the spontaneous dewetting of the solvent from the bilayer to occur (Eq. 6.4). Glycerol and Kolliphor have been shown to stabilise membranes, and prevent non-specific vesicle aggreation [142], and glycerol increases the viscosity of the OA phase, increasing the shear stresses at the junction leading to improved pinching-off and thus better double-emulsion production [239]. However, high glycerol content interferes with the DNA and the increased Kolliphor in the membrane may decrease the surface area of the membrane available for functionalisation of membrane bound constructs, as well as stabilising microemulsions [154].

Preliminary results corroborated the stabilising effects of the Kolliphor: in the range of 0-10 mg ml^{-1} of Kolliphor, vesicles quickly ruptured, and the yield was noticeably reduced compared to higher concentrations; indeed, dewetting is unable to occur with no Kolliphor or Glycerol (Table. 6.2). From Table. 6.2 we observe that the spreading coefficients show $S_o < 0$ and $S_{w2} > 0$, the criteria for spontaneous dewetting for all compositions shown except in the

OA Phase Composition		**Calculated Spreading Coefficients**	
Glycerol (%v)	*Kolliphor (mg ml^{-1})*	S_o *(mN m^{-1})*	S_{w2} *(mN ml^{-1})*
0	0	-15.0	-1.1
0	10	-13.2	0.7
0	20	-11.5	2.4
0	30	-11.5	2.5
0	40	-11.4	2.5
0	50	-10.4	3.6
2.5	50	-11.3	2.7
5	50	-10.7	3.3
7.5	50	-9.7	4.3
10	50	-9.5	4.5

Table 6.2 The variation of the Kolliphor and Glycerol compositions of the OA phase affect the spreading coefficients and thus the dewetting of octanol from the bilayer. The value in red corresponds to an insufficient spreading coefficient for spontaneous dewetting. For these values, the interfacial tension between the LO phase and IA phase containing 200 mM sucrose was used, and kept constant.

absence of both Kolliphor or Gylcerol. In particular, increasing the concentrations of either leads to an increased S_{w2}, which results in a higher driving force for dewetting, and thus a faster dewetting transistion [154]. This demonstrates that a range of Kolliphor/Glycerol concentrations should be sufficient for spontaneous dewetting. Therefore, we find trade-off between the stabilising effects of Kolliphor and glycerol in the OA phase, and their negative effects on membrane functionalisation, can be made by carefully tuning the phase compositions depending on the use of the vesicles. Experiments with Kolliphor in the IA phase were attempted, as in the method of Ref. [144], but did not aid dewetting, as predicted by the theory (Section 6.2.3).

6.2.4 Iterating the design to optimise solvent removal

We iterated a variety of post-J_2 channel geometries to optimise the solvent removal from the produced lipid vesicles. All initial chips suffered from the same flaw: roughness in the post-J_1 channel due to the use of film mask and UV exposure for the lithographic process. This roughness affected the wetting, frequently preventing the formation of w/o droplets after J_1. As such we moved to a multiphoton lithographic method described in Section 6.3, which enabled the creation of smooth channels and w/o droplets.

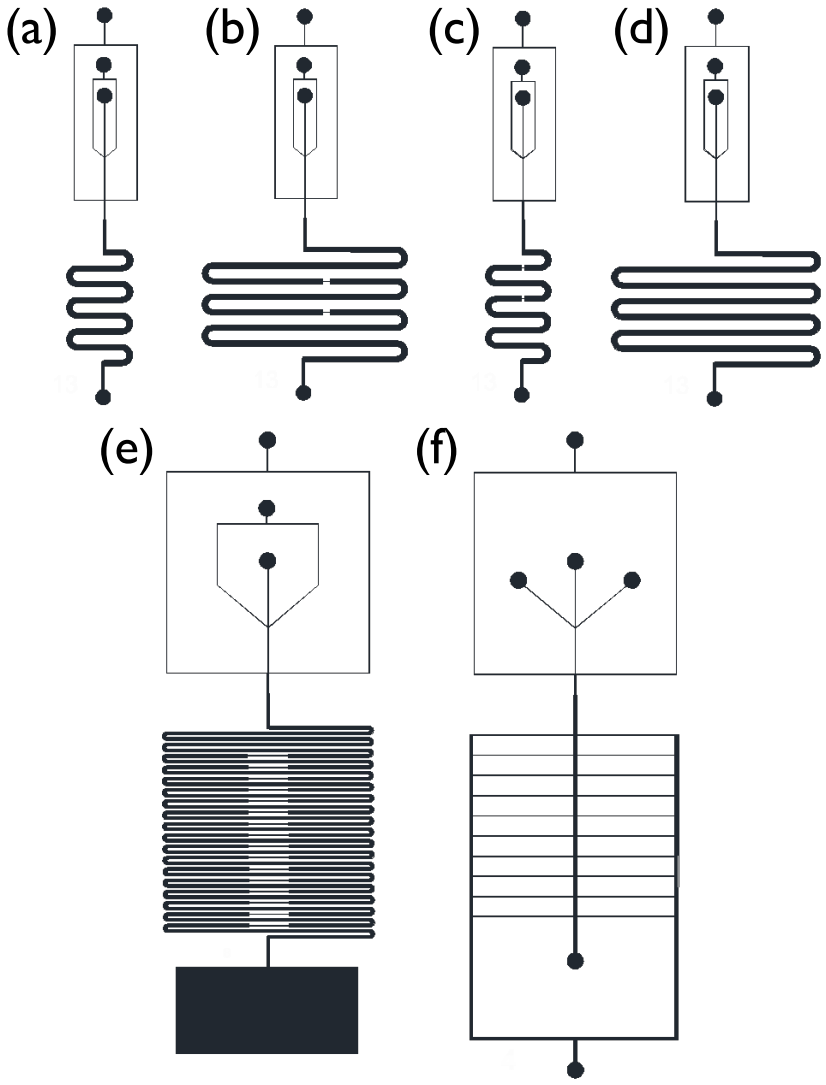

Fig. 6.3 Example designs of microfluidic devices that were tried and tested during this work. Geometries from the inlets up to and including J_2 were eventually standardised to those seen in (a-d). Downstream of J_2, (a) and (d) represent the simplest designs, with two serpentine channels differing in length. (b) and (c) represent the same designs with constrictions, which were varied in size in different designs between 5 µm-15 µm in diameter. (e) A much longer serpentine, incorporating longer and many constrictions, which were similarly varied between designs. (f) A straight post-J_2 channel, with thin channels coming off the sides. These thin channels were connected to a separate input, from which suction would be applied. Other designs incorporating combinations of these basic themes were also tested.

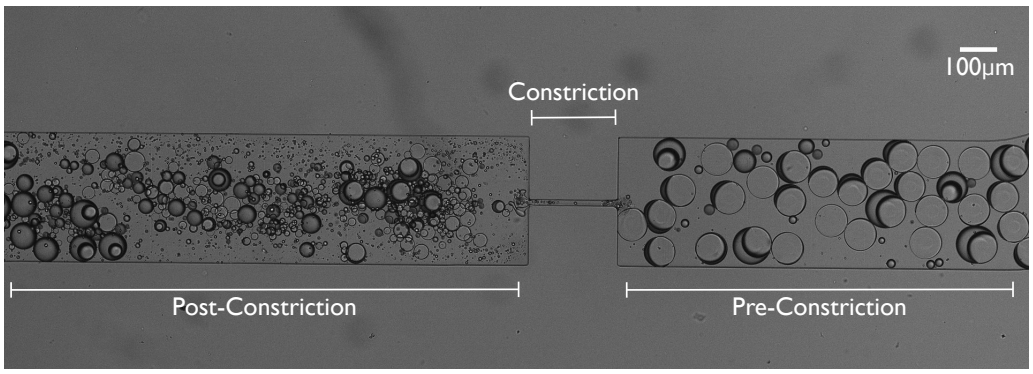

Fig. 6.4 An example of a 10 μm constriction, and its effects on passing lipid vesicles of ∼85 μm diameter. Vesicles passing through the constriction can be seen to have split post-constriction, removing solvent from some of the resultant vesicles, but also creating polydisperse vesicles.

Alteration of the geometry of the junctions did not noticeably affect the ability to form w/o droplets at J_1 or w/o/w droplets at J_2. Simple practical considerations therefore drove our design: inlets for the IA, OA and LO channels were designed to be in enough space to enable punching without splitting the channels, as well as making them compact to enhance the number of designs per master, and enable more chips to fit on each PDMS coated slide (described in Section 6.3), all enabling quicker testing of designs.

For the post-J_2 channel, a variety of geometries were employed. We designed serpentine channels which allowed for time and exposure to flow induced shear to promote the budding-off of the residual octanol droplets (Fig. 6.3a-d). Shorter serpentine channels were not always sufficient for all solvent droplets to bud off the vesicles. However, we found longer serpentine channels harder to coat with PVA, lowering the yield in our chip production stage. For this reason, we avoided longer serpentine channels and compromised with shorter designs. We also varied PVA concentration, and of exposure of the channels to PVA for coating, however, lower concentrations of PVA led to chips which stopped working relatively quickly. Our coating method was sufficient to utilise the same chip for the longest continuous runs we attempted (∼7 hours).

We also implemented constrictions (Fig. 6.3b,c & e). Vian *et al.* showed the ability to reduce the solvent content in the membrane of a double emulsion through deformation in a constriction, which increases the interfacial energy to sufficiently high enough to favour the splitting of the double emulsion to a thinner shelled double emulsion and an oil droplet [152].

We attempted this with our vesicles, implementing constrictions of 5 µm-30 µm at lengths from 250 µm-2500 µm. The deformation is caused through the application of a shear stress, which is a function of the constriction dimensions and the flow rate [152]. We could not adjust the flow rate without affecting the size of the vesicles themselves (which itself feeds into different velocity and dimension requirements for budding off of the excess solvent) or the rate of vesicle formation. Constrictions >15 µm wide, visually did not seem to promote the budding off of the oil droplet for the flow rates we tried. However, constrictions <12 µm wide, caused budding off, although this was accompanied by the vesicles breaking into a smaller vesicle and thick shelled double emulsion (Fig. 6.4), negating the monodispersity of the vesicles. We also attempted longer constrictions (1000 µm and 2500 µm long), however, again, this was problematic from a PVA coating perspective; we found that extracting the PVA after initial coating, as well as preventing the PVA from coating the LO channel whilst exposing J_2 and the OA channel, was difficult and returned a very low yield of chips; successful testing of the constrictions was only demonstrated with 250 µm and 500 µm long constrictions. An alternative would be to remove the vesicles from the first chip, and add them to a second chip where the flow rate would be independent of the flow rates needed for GUV formation, and the excess solvent could be removed in this second chip. This would also allow for the consideration of longer constrictions, as PVA coating would be simpler as this second chip would be completely coated.

We also tried designing a system with a straight post-J_2 channel (Fig. 6.3f), with thin channels coming off the sides similar to a method from Ref. [247]. These thin channels were connected to a separate input, from which suction would be applied, in theory removing the smaller octanol droplets from the main channel, allowing the removal of vesicles without octanol from the outlet. We found this method to be ineffective with few vesicles observed to have octanol removed, perhaps because it required a longer channel for most of the octanol to bud off than was tested. Alternative methods for extraction of organic solvent droplets to allow for the removal of purified vesicles from the chip have been reported [155]. However, we found a simple solution was to cut a large chamber at the outlet, and fill it with a osmolarity matched but density mismatched solution (in this case glucose), causing the sucrose filled vesicles to sink to the bottom of the chamber, and the octanol droplets to float to the top (Fig. 6.5). These could be removed through pipetting, allowing the extraction of "purified" (solvent droplet free) vesicles.

The final device design had the following measurements and followed the design in Fig. 6.3a: the LO channels were 25 µm wide and the IA and OA channels were 35 µm wide.

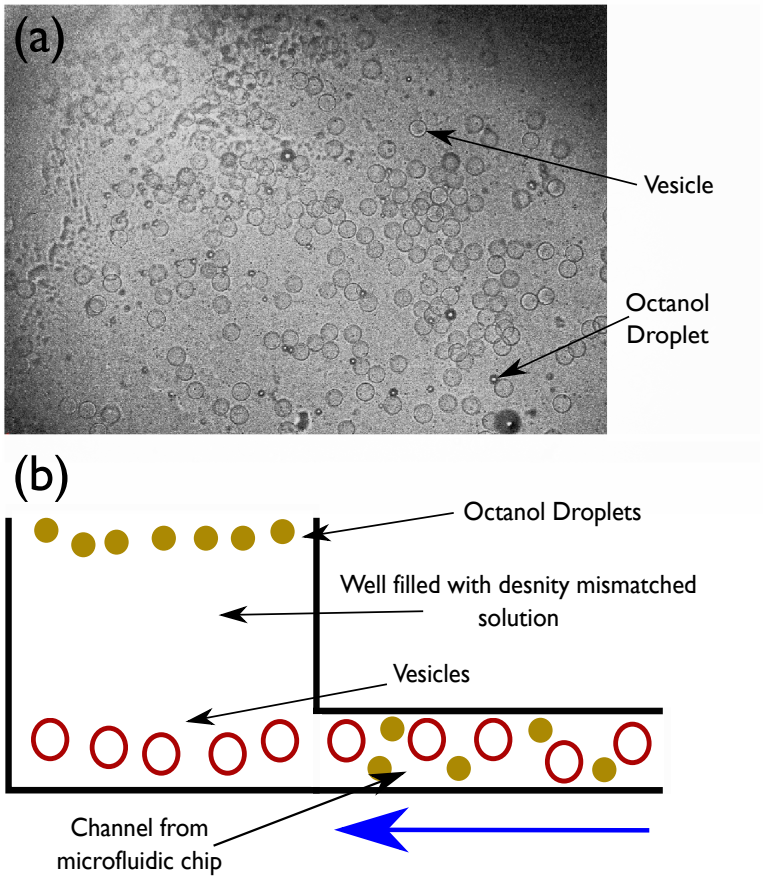

Fig. 6.5 Separation Method employed for extraction of vesicles. (a) Vesicles at the botttom of a well, with minimal octanol droplets present due to their lower density causing them to float to the top of the well and be extracted through pipetting. (b) A schematic showing this process, the blue arrow showing the direction of flow through the microfluidic chip. Density mismatched vesicles sink to the bottom, and octanol droplets and double emulsions droplets float to the top, and can be removed by pipetting.

A 25 µm long segment after the second junction was 35 µm, before expanding to 70 µm wide for 1250 µm, then to 175 µm for 2000 µm, before finally widening to 350 µm. Constrictions, where present, varied in length between and 250-2500 µm, and in width from 5-10 µm, but were not included in the most frequently used design. The channel depth from the fabrication procedure (Section 6.3) was 50 µm.

6.3 Device Fabrication and Operation

Following designs created in AutoCAD for the formation of double emulsions, microfluidic chips for octanol-assisted liposome assembly are fabricated by setting Polydimethylsiloxane (PDMS) on a master of the design on a Silicon wafer to create the microfluidic channels. This leaves a network of unsealed channels, which is sealed using a PDMS coated slide to create the final device.

6.3.1 Protocol for Master Fabrication

A soft lithographic process using epoxy-based negative photoresists was followed in order to create a design master on 4" Silicon Wafers (Pi-Kem Reclaim).

The wafer was pretreated by placing it on a hotplate at 200°C for 10 minutes, and then exposed to oxygen plasma for 10 minutes (Femto, Diener electronic). Next, 4 ml of SU-8 2000.5 was spread across from one side of the wafer to the other, with all bubbles removed. Subsequently, this was spin coated at 3000rpm for 30 s, and then baked for 3 minutes at 95°C. All baking steps in this section followed a pattern of increasing temperature by 5°C every 45s until the required temperature, and cooling at the same rate down to 40°C. The 5°C resolution is due to the resolution of the heat block. This slow ramp up and ramp down prevents cracking of the SU-8. After this, the whole wafer was exposed to UV for 120 s, and then baked again for 3 minutes at 95°C before development by agitation with PGMEA (propylene glycol monomethyl ether acetate, Sigma Aldrich) for 1 minute, before washing with isopropanol and drying with nitrogen. This thin layer of SU-8 2000.5 was deposited on the wafer in order to improve the adhesion of the design to the substrate further later on in the process.

The wafer with the adhesion layer was again placed on a hotplate at 200°C for 10 minutes, and then exposed to oxygen plasma for 10 minutes. Next, 4 ml of SU-8 2050 was spread across from one side of the wafer to the other, with all bubbles removed. Subsequently, this was spin coated at 500rpm for 30 s with an acceleration 100rpm/s, and an initial 5s to facilitate achieving the desired spin speed. Subsequently this was increased at 100rpm s^{-1} for 15s, until a spin speed of 2000rpm was reached, at which speed its was kept for 60 s.

A soft bake was then carried out at 65°C for 5 minutes, where the temperature was first ramped up at 5°C/45s from 30°C. This was then raised at 5°C/45s to 95°C, where it was held for 10 minutes. Subsequently this was cooled to 40°C at 5°C/45s.

At this point the wafer is ready for the for the multiphoton lithographic step. The wafer was placed in the Direct Laser Writer (Protolaser LDI) and, after uploading and checking the designs, using the proprietary software the negative photoresist was patterned with sub-micron control of feature size.

Next came the hard bake step, where the patterned wafer is baked for 2 minutes 65°C, where the temperature was first ramped up at 5°C/45s from 30°C. This was then raised at 5°C/45s to 95°C, where it was held for 10 minutes. Subsequently this was cooled to 40°C at 5°C/45s, and then developed by agitation in PGMEA, before washing with isopropanol and drying with nitrogen.

Finally, the Silicon Wafers were rendered hydrophobic by placing Trichlorosilane (ABCR GmbH & Co.) on 4 glass slides surrounding a silicon wafer all within a desiccator. By applying a vacuum for 2 hours, vapor deposition and silanisation of the silicon wafer was achieved.

6.3.2 Protocol for PDMS Chip Fabrication

PDMS is prepared in a plastic cup at at a mass ratio of 10:1 polymer:curing agent, and mixed until full of bubbles, at which point it is degassed for 20 minutes in a vacuum desiccator. The PDMS is then added to the silicon wafer relief of the device in a petri dish to create a mold, and left to set for 1 hour at 60°C. The designs in PDMS are cut out so each PDMS block contains one design. Holes are then punched at the IA, OA, LO and outlet channels using 750 µm diameter biopsy punch (World Precision Instruments).

As in Section 6.3.1, we silanised 4' Silicon wafers. A thick layer of PDMS is poured on top of the wafer, and 2 (50×24mm, type 1 thickness) slides were pressed hard onto the wafer and submerged in the PDMS. This is then incubated at 60°C for 2 hours. The PDMS layer is peeled off, and the glass slides are removed, leaving a thin PDMS layer on the underside. The earlier silanisation prevents any water getting between the wafer and the PDMS which is to be added. When placed in the oven to set, this would evaporate causing wrinkling and therefore a non-uniform layer of PDMS on the slide.

Subsequently both the PDMS block from the epoxy mold and the PDMS coated slides are exposed to oxygen plasma for 20 s (Femto, Diener Electronic). They are then bonded together, with the PDMS coated side of the slide acting as the seal to the open pattern on the PDMS block, yielding the microfluidic chip.

A 5% PVA in milliQ water solution is prepared using a 1:19 mass ratio of PVA (87–90% hydrolysed, molecular weight 30,000-70,000 MW, Sigma Aldrich) to milliQ water in a glass flask. This mixture is vortexed for 20 minutes before a magnetic stirrer is added. This is left on a magnetic stir plate overnight at 80°C. By adding this solution through the OA channels, and preventing entry to the LO and IA channels by applying air pressure in them, this renders the OA channel and post-J_2 channels hydrophilic (Fig. 6.1). After a 1 minute incubation period to permit PVA polymers assemble on the surface, air is applied from the OA, IA and LO channels in order to clear the channels. The device is then baked at 120°C for 15 minutes to heat immobilise the PVA polymers onto the surface of the channels.

6.3.3 Aqueous and Lipid-Carrying Phase Preparation

A general method for aqueous and lipid carrying phase preparation is as follows, however, solution compositions, particularly the gycerol and Kolliphor concentrations, were/can be varied according to the results in Section 6.2.3, both in terms of their ability to facilitate dewetting, and their effects on fuctionalisation and vesicle stability.

The IA phase consists of a 300 mM Sucrose solution. For the OA phase, a solution of 300 mM Sucrose, 15% by volume solution of glycerol and Kolliphor (50 mg/ml) is used. For the lipid-carrying LO phase, a solution of ratio 1:49 100 mg/ml stock lipid solution:octanol is used. Oregon green-DHPE was added to the stock lipid (DOPC) at a ratio of 0.7:99.3.

6.3.4 Device Operation and Imaging

A microfluidic flow control system (Fluigent GmbH) along with the MAESFLO software (version 3.2.1) controls a pump (Elveflow MUXFlow Switches Standard 3/2) that is used to drive and control to flow the solutions into the microfluidic device using appropriate connectors and tubings (Tygon Microbore Tubing) attached to the previously punched holes. Solutions were added through each of the specific inlet channels. The pressure in the OA inlet (OA_p) is increased to 50 millibar, and if no solution could be observed to fill the channel, this was increased more. Subsequently, the same process is repeated with the pressures applied at the IA and LO inlets (IA_p and LO_p), both of which should have the same pressure values. The pressures are then tuned until yielding monodisperse droplets, which occurred at 58 millibar for IA_p and LO_p, and 75 millibar for the OA_p. Increasing the OA_p causes a faster rate of "pinching-off" of the w/o emulsions, which allows control of both size and number of compartments. LO_p can be reduced to lower values to create double emulsions with thinner shells, whereas tuning the IA_p allows for varying the size of the w/o droplets.

Imaging of vesicle generation on the microfluidic device itself is achieved using a Nikon Ti-E inverted microscope using a Nikon Plan Apo VC 20× 0.75 NA objective and recorded using a IIDC Point Grey Research Grasshopper3 GS3-U3-23S6M camera. When imaging the vesicles removed from the microfluidic device, we use a Leica TCS SP5 II laser-scanning confocal microscope equipped with a Leica HCX PL APO CS 40× 0.85 NA dry objective. A 633 nm He-Ne laser and a 488 Argon-ion laser are used to excite respectively Texas-Red or Oregon Green labelled membranes respectively. Emission is collected between 497 nm and 600 nm for the Oregon Green and 639 nm and 780 nm for the Texas-Red channels.

Vesicles were found and measured using a simple algorithm written in MATLAB to analyse fluorescent confocal images. Circles within the image were found using a circular Hough transform. These circles were then iteratively thresholded to assess whether the circle was a vesicle, where the mean pixel value within the circle should be similar to the mean pixel intensity of the image outside the circle, or an emulsion drop, where the mean pixel value within the circle would be higher than the mean pixel value of the image outside the circle. The circles assessed as vesicles were then presented for visual inspection, at which point the user would confirm if each circle was indeed a vesicle through a user input. From these circles defined as vesicles, the radii were extracted.

6.4 Characterisation

6.4.1 Monodispersity, Size Control and Throughput

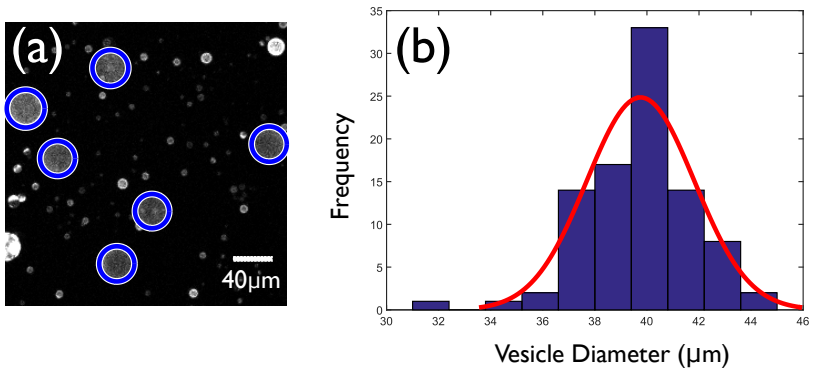

Fig. 6.6 (a) Example of vesicle detection in a octanol droplet contaminated sample, showing the robustness of the algorithm to non-vesicle spherical particles (b) histogram and normal fit of a run of vesicles where IA=58 mbar, OA=75 mbar and LO=58 mbar (N=96).

We were able to produce monodisperse vesicles, and show vesicles with an average diameter of 39.8 µm with a standard deviation of 2.06 µm (or 5.38%) (Fig. 7.1). These results came from applying pressures in the channels at IA_p=58 mbar, OA_p=75 mbar and LO_p=58 mbar.

Through controlling the flow rates, it was demonstrated that a range of vesicle sizes were achievable at a range of diameters between $\sim$ 25 µm-90 µm. Additionally, analysis of videos showed high throughput production of vesicles, with vesicles produced at a rate as high as >80Hz, significantly above the 10-15Hz demonstrated in other systems [143, 144].

6.4.2 Towards Multi-Compartment Vesicles

By adjusting the flow rate, specifically reducing the OA_p to slow the pinching of the incoming stream of w/o droplets, it was demonstrated that a range of multi-compartment double emulsions could be produced. Removal of the solvent without the compartments fusing proved to be non-trivial, however, the ability to produce multi-compartment w/o/w droplets is demonstrated (Fig. 6.7). Though we only show 2 and 3 compartments here, we were able to produce multicompartment droplets of up to 9 compartments which were stable enough to be removed off-chip. Further work into the stabilisation of the compartments as well as

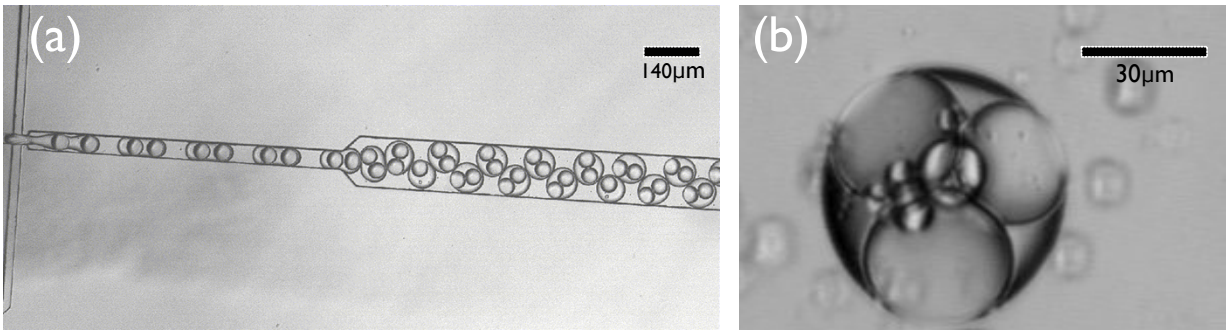

Fig. 6.7 Multicompartment vesicles (a) on chip and (b) off-chip. Vesicles here have 2 and 3 compartments respectively, but by reducing the OA flow rate this could be varied considerably.

the oil removal is necessary for optimisation of this process, however, for simple work on encapsulation and communication between compartments, this is sufficient. We hypothesise that using different lipid compositions, which have more stable monolayers, such as DPhPC (used in other works on microfluidic vesicles) [237], might allow the complete dewetting of solvent from the bilayer without fusion of the compartments.

6.5 Device Applications towards Functional Materials

6.5.1 Encapsulation and Coating

We were able to encapsulate a fluorescent dye, as an initial proof of principle that the microfluidic device could support the vesicles being generated whilst simultaneously being encapsulated with a cargo. Fluorescein was added to the IA solution at a concentration of 50 mM in 700 mM Sucrose solution. An OA 700 mM Sucrose solution with 15% glycerol and 50 mg/ml Kolliphor was used. This was run through the chip to produce monodisperse vesicles, which were then extracted (Fig. 6.8). These vesicles were taken off chip with no significant reduction in yield, and were stable for > 3 hours during which time we were able to see fluorescence localised within the vesicles off-chip (Fig. 6.8b). Other cargo was also encapsulated within the vesicles; for example, we also created SUVs in 300mM sucrose through extrusion (as in Section 3.2), and used this solution as the IA, and showed the ability to encapsulate SUVs within microfluidic formed GUVs.

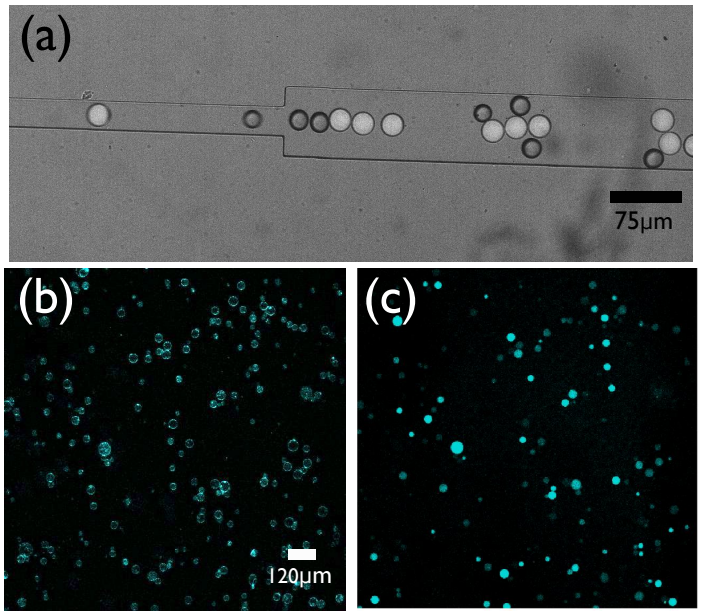

Fig. 6.8 Vesicles containing fluorescein. (a) The vesicles produced on chip, with the non-fluorescing octanol droplets. (b-c) The vesicles taken off chip, with (b) the Texas-Red labelled membrane, and (c) the fluorescein loaded inner compartments still present after 3 hours.

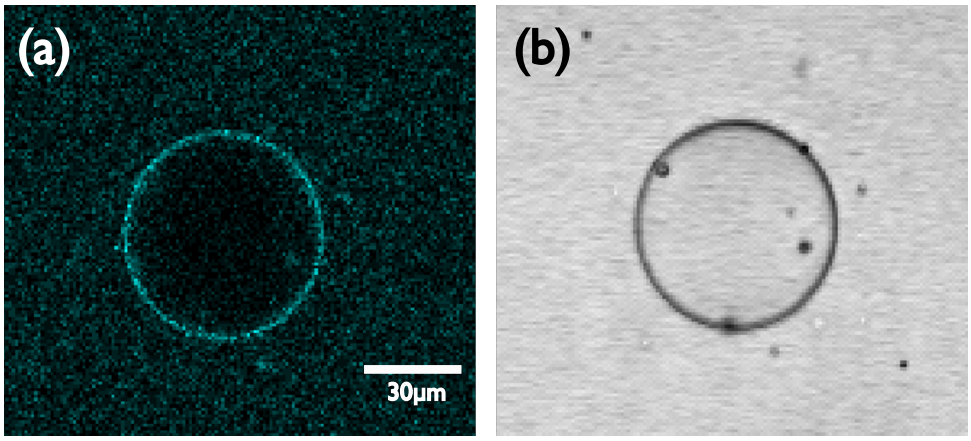

Fig. 6.9 Vesicles coated with a fluorescent DNA construct on chip in both (a) fluorescence, where the fluorophore is fluorescent molecule conjugated to the DNA construct and (b) and brightfield.

In addition to encapsulating cargo, another step towards creating functional/responsive materials with lipid vesicles involves the use of vesicles functionalised with membrane bound constructs, such as multivalent linkers to drive adhesion or receptors on artificial cells. Controlling the number of constructs per vesicle more accurately than with existing methods is possible with microfluidics due to the ability to functionalise vesicles one at a

time with controlled volumes of OA phase for each vesicle. Another benefit is the ability to conduct the entire process of creating, encapsulating and functionalising vesicles simultaneously, reducing the steps required to achieve the functionalised, cargo-containing vesicles.

In order to see if these vesicles could be functionalised on-chip, we used a fluorescently labelled dsDNA construct, which was able to insert into a bilayer through a cholesterol anchor. We changed the composition of the OA to allow for the DNA, maintaining the 15% glycerol and 50 mg ml^{-1} Kolliphor, but using a 100 mM NaCl+87mM Glucose+TE buffer, and adding the desired amount of DNA to the OA phase. The salt is necessary to maintain the integrity of the DNA constructs.

Only at concentrations of DNA of 50 µM in the OA were we able to see insertion into the membrane (Fig. 6.9). Indeed, at lower concentrations fluorescence was visible outside of the vesicle, but not on the membrane, showing that this was not due to insufficient DNA, but a lack of insertion.

We hypothesise that this could be due to 3 reasons. Firstly, the presence of the Kolliphor could influence insertion of the construct: it forms repulsive-brush like structures and also, if saturated in the membrane, could exclude the addition of the DNA constructs [248, 249]. Secondly, small oil droplets stabilised with a lipid monolayer sequestering some of the fluorescent DNA constructs away from the vesicles might also play a role. Finally, the presence of glycerol can cause DNA to precipitate due to the disruption of the solvation coat around nucleic acids molecules, removing water from around these molecules. Functionalisation of the vesicle was possible, but in order to have more precise control over the surface concentration of constructs, and prevent the need for a washing stage to remove the non-membrane bound constructs, further work into these considerations must be explored. The work in Section 6.2.3 implies that there are a range of Kolliphor and glycerol combinations that still should lead to the formation of vesicles without residual octanol in the membrane, and should be considered further to optimise the functionalisation process.

6.5.2 Artificial Cells

We created artificial cells, vesicles encapsulating a cell-free extract with either the p70-T7-C6N-mRFP plasmid or the p70-T7-C6N-mRFP plasmid. The plasmid constructs and cell-free extract were prepared by Dr. Emma Talbot. The plasmid and cell-free extract were used as the IA phase, which we found to be osmolarity matched with 700 mM sucrose, which was thus used as the OA phase with 15% by volume solution of glycerol and Kolliphor

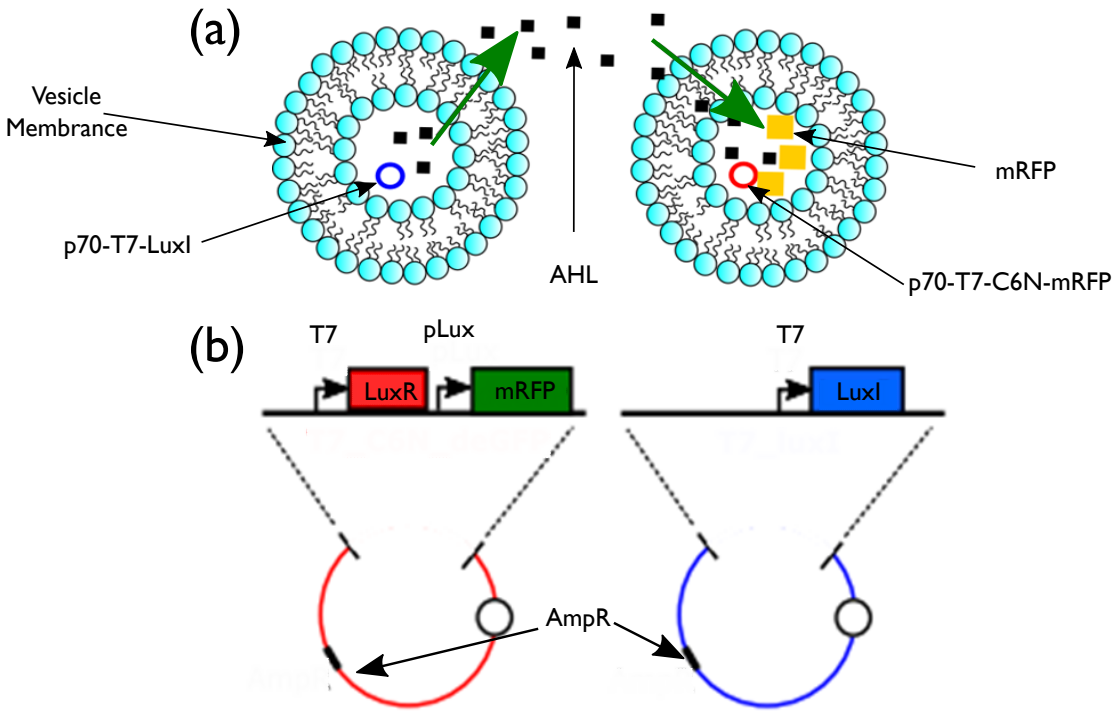

Fig. 6.10 Mechanism and constructs used in artificial cell experiments. (a) Communication between two populations of artificial cells. Membrane encapsulated solutions of plasmids (either p70-T7-LuxI (L) or p70-T7-C6N-mRFP (R)) communicate when a small molecule is produced from one vesicle (L), which diffuses (Green arrows) out of the vesicle and allows for transcription of a fluorescent protein in another vesicle (R). This can be achieved with the addition of the small molecule independent of the presence of the p70-T7-LuxI plasmid containing artificial cells. (b) Schematic of the p70-T7-LuxI (R) and p70-T7-C6N-mRFP (L) plasmids.

(50 mg ml^{-1}). The LO phase remained as in Section 6.3.3.

We found that the cell-free extract in the IA solution eventually sticks in the channels past the first junction, leading to wetting and the absence of the formation of w/o droplets. This however could be solved by washing this section of the chip from the IA channel with 700 mM sucrose solution, allowing vesicles encapsulating the cell-free and construct to be produced once again. Nonetheless, this caused a reduction in yield. Additionally, the yield of extraction of vesicles off-chip was noticeably lower than when encapsulating other solutions, presumably due to rupture of vesicles upon being pipetted. To improve on this we used wider tip pipettes to reduce shear, and coated them with BSA to prevent rupture inside the pipette tip.

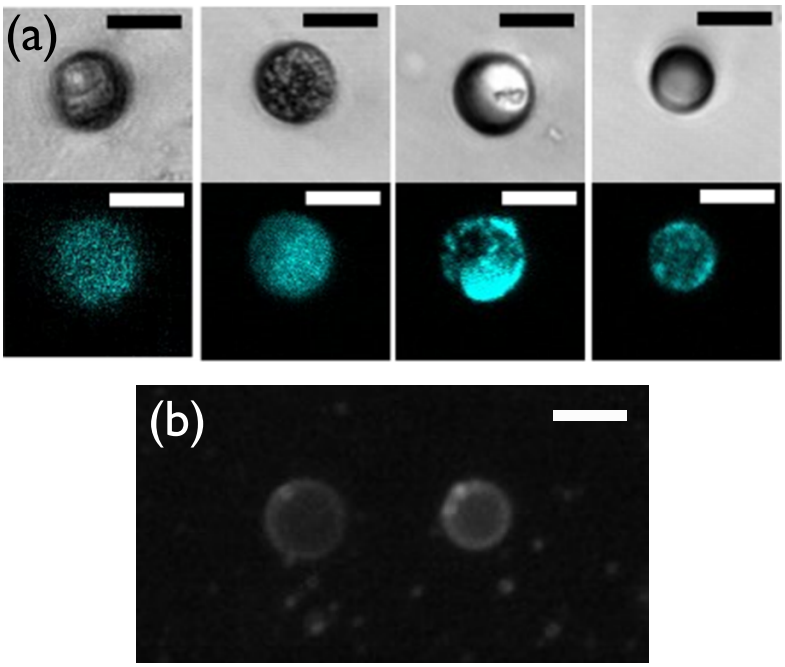

Fig. 6.11 Artificial cells shown on chip and off chip. (a) Brightfield (upper) and fluorescent (lower) images of vesicles produced using the microfluidic method described in this chapter, encapsulating cell free extract and a p70-T7-C6N-mRFP plasmid, incubated for 3 hours in a solution containing 10mM C6-AHL. These images were taken off-chip using a Leica TCS SP5 II laser-scanning confocal microscope. (b) fluorescent images of vesicles taken on-chip after 3 hours.These images were taken using a Nikon Ti-Eclipse inverted microscope. Scale bars are 25 μm.

Vesicles were produced with the cell-free extract and a p70-T7-C6N-mRFP plasmid encapsulated within them. As can be seen in Fig. 6.10, p70-T7-C6N-mRFP contains constitutive T7 promoter for the expression of the *luxR* gene which produces the LuxR activator protein. In the presence of the autoinducer C6-AHL, this forms a complex that acts as an activator on the inducible promoter pLux. 3 hours after the introduction of 10 mM C6-AHL, the inducer for RFP expression, vesicles were observed to show fluorescence at 583 nm, indicating that the small molecule was able to pass through the membrane and activate transcription of the fluorescent RFP within the vesicle (Fig. 6.11). As a control we conducted the same experiment without the addition of 10 mM C6-AHL, and were unable to see any vesicles showing fluorescence within a 3 hour period

Additionally, we created another population of vesicles, encapsulated with the cell-free extract and a p70-T7-LuxI plasmid. This plasmid produces C6-AHL. Placing vesicles from both populations together, we hypothesised that we should similarly see expression of RFP due to diffusion of the C6-AHL produced in the p70-T7-LuxI containing vesicles in to the

p70-T7-C6N-mRFP containing vesicles. However this was not observed, presumably due to there being insufficient production of C6-AHL to induce transcription of RFP.

6.5.3 Vesicles with lipid mixtures

Lipid mixtures can be used to create phase separated vesicles; by choosing lipid mixtures containing lipids with different melting temperatures, we can create vesicles with different domains containing only certain lipids and different properties within these domains [27]. This can be achieved with binary or ternary mixtures, often with a saturated and unsaturated lipid species and, in the case of a ternary mixture, cholesterol [25]. In binary mixtures, in addition to single phases, we can see gel/liquid coexistence, whereas in ternary mixtures we also see coexisting liquid ordered (with cholesterol and saturated lipids) and liquid disordered (with mainly unsaturated lipid) domains [25]. Phase separated vesicles allow for preferential segregation and thus patterning of membrane bound constructs into specific domains, creating patchy soft particles with controllable (patch) valency, whilst the transition temperature adds another level of control to the system which can be exploited to change the "patchiness" of the vesicles and allow membrane bound constructs to mix, which could be exploited to initiate down-stream chemical events within the vesicle [235].

We attempted to create phase separated vesicles, by placing the chip on a peltier element, and increasing the temperature to 60°C, above that of the phase transition temperature of the lipid with the highest melting temperature, which in this case was DPPC, where T_m=41.3°C. We substituted a 40:40:20 mixture of DOPC:DPPC:keto-cholestenol for simply using DOPC in the preparation of the LO phase (Section 6.3.3), which should lead to the formation of phase separated liquid-liquid coexistence. Whilst some vesicles showed something akin to gel/liquid phase separation, results were inconclusive and we did not observe the the desired liquid-liquid coexistence phase separation we would expect from the compositions used. However, this demonstrated the ability to create vesicles using different lipid compositions using our method.

Work on vesicles produced by the emulsion transfer method has shown that phase separation in lipid vesicles in systems where the vesicles have been produced using a lipid-carrying oil phase leads to very different phase behaviour due to lower incorporation of cholesterol into the membrane [235], as cholesterol is predominantly a hydrophobic molecule, and as such is has a higher probability compared to amphiphilic lipids to remain dissolved in the oil rather than partitioning at the oil-water interface. As such, further experimentation

with ternary mixtures incorporating greater proportions of cholesterol would allow us to better probe this technique's ability to produce phase separated vesicles.

6.6 Conclusions

We have demonstrated and described a method for the high-throughput production of monodisperse lipid vesicles through microfluidics with the ability to functionalise and encapsulate the vesicles on-chip, using a double-emulsion template and octanol as an organic lipid-carrying solvent. This method builds upon and integrates concepts from previous work utilising octanol as the lipid-carrying solvent, and microfluidic channel geometries for the production of double emulsion templates, in addition to integrating solvent removal steps. We find this to be a robust and high yield method for high-throughput (>80Hz) monodisperse single and multi-compartment vesicles.

We initially described the considerations for tuning the dewetting of the solvent from lipid, where the pendant droplet measurements and theory indicated a wide range of compositions of IA and OA solutions that should lead to dewetting. This allows for other considerations, such as stability or functionalisation, to be accounted for in choosing solution compositions. We found that the glycerol and Kolliphor content are the drivers of the dewetting process, with salt, sugar, and even ethanol concentrations having comparatively minimal effects. We considered a range of designs, and briefly addressed the limitations in implementations in certain instances.

The vesicles produced from our chips have been shown to be very monodisperse with a standard deviation of 5.38% in radius, formed with different lipid compositions, and able to be produced in a range of diameters between $\sim$25-90 µm. Throughput was able to be varied up to >80Hz, and we were able to encapsulate fluorescent dyes, SUVs as well as cell-free extract and plasmids within the vesicles on chip, in addition to the functionalisation of vesicles with DNA constructs. We showed permeability of the membrane through the transcription and protein expression from a plasmid through the addition of a C6-AHL small molecule that acts as an activator of the promoter for RFP, LuxI. Furthermore, we describe the formation of multi-compartment vesicles, however the solvent does not completely dewet in these instances.

We find therefore that this method produces vesicles well suited to our desired applications in the formation of artificial cells and as a building block for functional materials, as

these sub-units allow for encapsulation, functionalisation, size control and permeability of the membrane to small molecules.

Chapter 7

Rheological Properties of Biomimetic GUV-based tissues

In this chapter, work is presented on the study of a biomimetic tissue consisting of GUVs adhering through complementary DNA-mediated interactions. The rheological properties of the sample are probed through the use of magnetic tweezers perturbing a magnetic bead in the bulk; through measuring the response of both the bead and the tissue directly. Additionally, the porosity of the material is examined through particle tracking of small, diffusive, sterically stabilised particles. These results inform a phenomelogical understanding of this amphorous material, which can be broadly understood through the underlying theory on granular and soft-tissue like materials, as well as our understanding of DNA-mediated adhesion of lipid vesicles. This work was undertaken in collaboration with Fergus Riche and Dr. Alexandre Kabla, who provided the experimental set-up for the work on magnetic tweezers and collaborated directly on the experiments and analysis.

7.1 Biomimetic GUV-based tissues

The system is based on the work described in Chapter 4 and Ref. [51], where we move from a simplified geometry of vesicles adhering to a supported lipid bilayer through multivalent interactions, to networks/tissues of vesicles adhering through multivalent interactions [38]. Here, instead of multimeric ligand/receptor interactions, we use vesicles functionalised with a single cholesterol-anchored dsDNA construct with an short palindromic ssDNA overhang (Fig. 7.1c), to facilitate adhesion between vesicles, akin to the work in Ref. [51]. Above the melting temperature (T_m) of the system, the ssDNA overhangs will not bind, and the DNA constructs instead contribute short-range steric repulsion. Below the T_m, DNA constructs

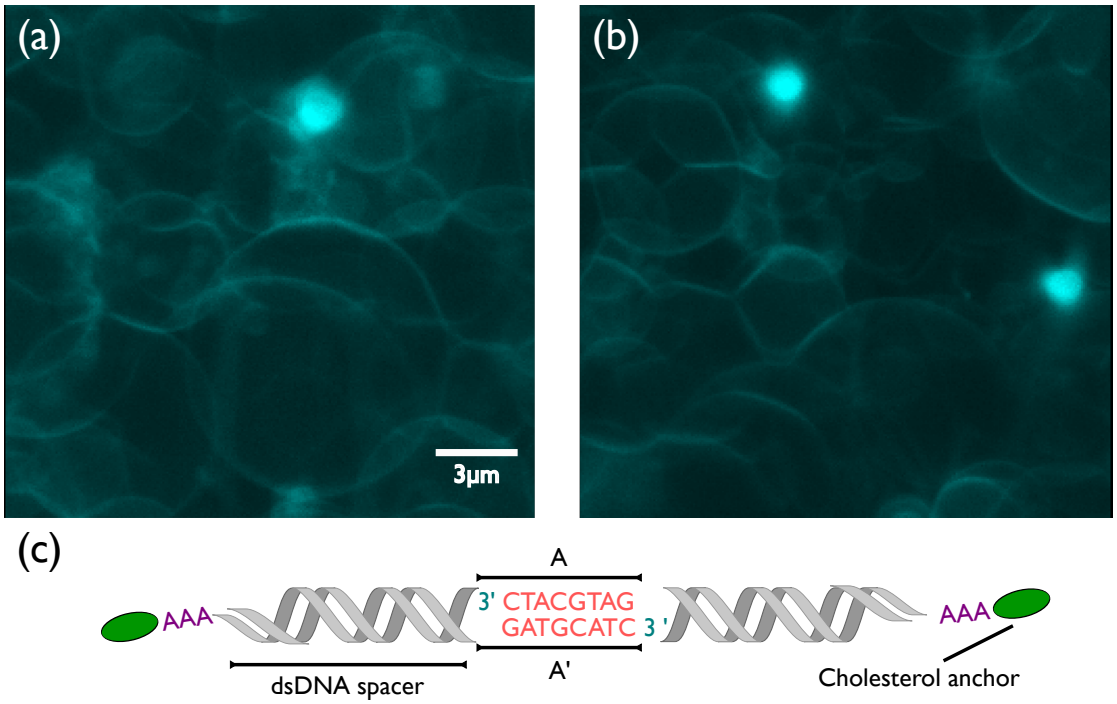

Fig. 7.1 A 3D rendering of 1 μm sterically stabilised bead (which can be observed as dense brightly fluorescent spheres) in a DNA-mediated vesicle "tissue". (a-b) Different local configurations within the "tissue" are shown and (c) a diagram of the palindromic DNA construct mediating adhesion between the vesicles.

will bind, and thus vesicles can adhere forming tissue like structures as in Fig. 7.1a&b. The temperature control on binding allows for us to "reset" the material; by increasing the temperature above the T_m and removing adhesion, we hypothesise that we can allow the material to relax from stress induced configurations. In addition, varying temperature allows us to probe the effects of temperature dependent adhesion of vesicles, where the effects of temperature on the vesicles deformability plays a driving role [52]. The cholesterol anchors allow for diffusion of the construct across the surface, and thus the formation of adhesion patches in areas of close proximity to other vesicles. The vesicles are formed by electroformation and thus polydisperse. Unlike in the system in Chapter 5, these vesicles are GUVs and thus large, non-diffusive and relatively heavy particles, so we are able to create dense packings/tissues through centrifugation.

We study this system in order to further understand the potential of soft materials based on such compliant sub-units coupled to multivalent interactions, which are of interest for a variety of reasons. Characterising the mechanical properties of the material for the purpose of understanding the responsiveness of the network to external stimuli is of great interest to our ongoing work towards creating responsive soft materials; here we characterise the rheological and structural responsiveness of the materials consisting of multivalent linker functionalised lipid vesicles in response to mechanical perturbation, temperature and linker concentration. More broadly, our system allows for a highly tunable model system for fundamental studies on the rheology of soft materials, and more specifically cell-tissue like soft materials, an area with a significant existing literature as reviewed in [137]. The DNA-mediated multivalent interactions employed here can also be used to mimic similarly multivalent interactions that drive the adhesion of cells in tissues. Biomimetic tissues consisting of cell-sized GUVs lack the active processes which govern the collective motion of cells within a tissue; rearrangements of the actin cytoskeleton in collective migration and interactions with the extracellular matrix through focal adhesions [250, 251]. Removing active processes that also integrate chemical signals allows for a model to investigate the physical processes governing the rheological and mechanical properties of cells decoupled from active processes [50]. Physical processes are hypothesised to have significant roles in cell sorting and morphenogenesis, through mechanisms described by the Differential Adhesion Hypothesis [252].

In order to study these rheological and mechanical properties we employ two distinct methods. The primary focus is the work conducted using quadrupolar magnetic tweezers, which were used to drive the movement of a 50 μm magnetic bead embedded in the network of vesicles (Fig. 7.4a&b). Both the response of the bead and the tissue can be recorded

giving minimally invasive measurements of mechanical properties resolved in space and time. In particular, the response of the bead allows for the derivation of creep and recovery measurements. This represents a method to quantitatively characterise the local rheology and thereby gain insight into the local microstructural response of the model tissue. Additionally, we briefly considered a passive measurement, tracking sterically stabilised diffusive beads to gain insight into the porosity of the networks in response to temperature, DNA functionalisation density and aging.

7.2 Magnetic Tweezer Rheology

As stated in Section 2.4.1, low-volume samples are unsuitable for conventional rheological measurements, therefore we employ an active microrheological method, using a quadrupolar magnetic tweezer set-up designed within the group of Dr. Kabla, and optimised by Fergus Riche. The theory is described below.

A magnetic field is used to apply a time dependent force *f(t)* to a bead containing ferromagnetic particles [253],

$$f(t) = M(t) \cdot B(t) = \chi_{bead} V_{bead} \frac{\Delta(B(t))^2}{2}. \tag{7.1}$$

where $M(t)$ and $B(t)$ are the magnetisation and corresponding flux density as a function of time, and χ_{bead} and V_{bead} are the bead's magnetic susceptibility and volume. By adjusting the flux density around the bead, a known force can be applied to the bead. These fields are created by a quadrupolar electromagnetic tweezer set-up (Fig. 7.4a). By inducing fields with combinations of the poles, a range of field gradients can be achieved. By dragging the bead at different positions in the sample, with different applied currents to the electromagnets, we can calibrate the force through knowing that the viscous drag of the bead due to motion is equivalent to the applied magnetic force,

$$F_{mag} = F_{vdrag} = 6\pi\eta r v. \tag{7.2}$$

With forces calibrated in a known media, we can conduct creep tests in an unknown media using the magnetic tweezers by applying a constant force over a set duration, during which the displacement of the bead is measured as a function of time. From this we find the creep compliance $J(t)$; a measure of the material's progressive deformation in response to constant stress. In tests performed in one dimension only, such as uniaxial extension,

$$J(t) = \frac{\varepsilon(t)}{f_0}, \tag{7.3}$$

where $\varepsilon(t)$ is the time-dependent strain and f_0 the applied force. This is not sufficient in the case of deformation by sphere, as the deformation occurs in 3-dimensions. By assuming that the strain field outside the bead is equal to that of a point force, for small displacements, the displacement of the bead of radius r, subject to a constant force f_0, in a solid of shear modulus μ is given by

$$x(t) = \frac{f_0}{6\pi\mu r}, \tag{7.4}$$

from this the viscoelastic correspondence principle can be applied to transform the elastostatic solution into a viscoelastic solution by making the substitution $\mu(t)^{-1} \simeq J(t)$, forming the final relationship shown in Ref. [254]:

$$J(t) = \frac{6\pi r}{f_0} x(t). \tag{7.5}$$

This creep function can be fitted with a variety of models to describe the creep behaviour. The first model chosen for this analysis, termed the Jeffrey's model in rheological literature and shown in Fig. 7.2a, developed using the spring and dashpot framework, from which it can be shown that the creep function is given by

$$J(t) = \frac{t}{\eta_1} + \frac{1}{k_1}(1 - e^{-\frac{\eta_2}{k_1}t}). \tag{7.6}$$

This model is hypothesised to give insight into the microscopic origins of the mechanical properties experienced at the scale of the bead, where single dashpot η_1 corresponds to fluid motion, thought to be due to the slipping between vesicles, rendering η_1 a measure of the interfacial viscosity [255]. The spring-dashpot pair η_2 and k_1 correspond to solid deformation, which we attribute to the internal properties of the vesicles; k_1 related to the surface tension of the vesicle, and η_2 arising from the viscosity of the fluid contents of the vesicles.

The spring-pot, or Scott-Blair element was also considered (Fig. 7.2b). The spring-pot comes from the work of Scott-Blair who pioneered the use of fractional calculus in rheology [256]. The spring-pot is an element interpolating between a Hookean spring, in which the stress in the spring is proportional to the zero-th derivative of the strain and the Newtonian dashpot, in which the stress in the dashpot is proportional to the first derivative of the strain, through a constitutive equation with a fractional derivative [257]:

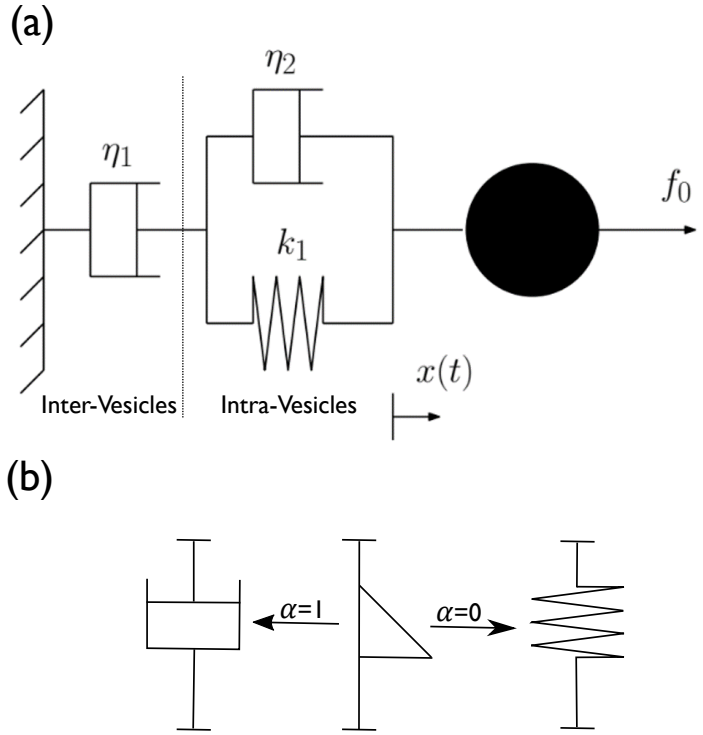

Fig. 7.2 The two models employed to gain rheological understanding of the data. (a) A linear model known as the Jeffrey's model, which is also described as the three parameter viscoelastic fluid. (b) The spring-pot, a fractional derivative model which allows the description of power law behaviour, and gives quasi-rheological insight, where the exponent of the fractional derivative, α, varies between 1 and 0, describing more dashpot- or spring-like behaviour respectively.

$$\sigma(t) = c_\alpha \frac{d^\alpha \varepsilon(t)}{dt^\alpha}, \tag{7.7}$$

where α is the exponent of the fractional derivative of the strain, set between 0 and 1, and c_α is a material property often referred to as a quasi-property [133]. That α is between 0 and 1 effectively creates an element that describes responses limited to those between the constitutive responses of either spring or a dashpot [133]. Quasi-properties do not describe true material properties as they depend on α and therefore non-integer powers of space and time. However, it is suggested that they describe textural parameters such as the "firmness" of a material, and furthermore give numerical measures of dynamical processes in materials, such as creep, rather than descriptions of equilibrium behaviour [258].

From this constitutive equation for a spring-pot, we can arrive at the expression for the creep compliance:

$$J(t) = \frac{t^\alpha}{c_\alpha \Gamma(1+\alpha)}, \tag{7.8}$$

where Γ is the gamma function, and $\Gamma(n) = (n-1)!$. The use of the spring-pot allows for the description of behaviours that cannot be easily modelled using traditional linear viscoelasticity, where constitutive rheological models result from combinations of elastic springs and viscous dashpots. Whilst power-law behaviour can be modelled using large number of linear elements [259], this becomes impractical and uninformative, as it is difficult to intuitively attribute the resultant parameters to the material's properties. Conversely, empirical power-law functions, whilst often fitting such non-linear creep responses well, lack an ability to have a physically significant interpretation [133]. The spring-pot allows for both the description of quasi-rheological properties as well as the ability to describe power-law behaviour. Specifically, in tissue-like materials such as the one considered in this chapter and cellular materials, this element captures, with two parameters, the broad distribution of timescales typical of their mechanical response [260]. Whilst this element has been combined with other linear elements, or in combination with other fractional derivative based elements, to model more complex rheological behaviours [261–263], here we consider the simple case of the spring-pot.

7.3 Methods

7.3.1 DNA preparation

A double-stranded DNA tether was assembled from two (ss)DNA molecules purchased lyophilized from Integrated DNA Technology. Both DNA strands contain a complementary region of 33 base pairs. The shorter strand (36 base pairs) also has a cholesterol molecule on the 3′ end via a TEG linker, with a ssDNA triple A sequence, which gives flexibility to the construct. The longer strand has an 8bp palindromic sequence, rendering the ssDNA overhangs on the constructs derived from these strands self-complementary. These are prepared and hybridised according to Section 3.5.1, to create 1.6 µM of the construct in TE buffer containing 100 mM NaCl. The sequences of the two ssDNA strands are *i*) 5′–CGC ACG TCC CGT CGA AGC GTT CCC GGA GTC TCG AAA –3′–Cholesterol–TEG and *ii*) 5′–CGA GAC TCC GGG AAC GCT TCG ACG GGA CGT GCG GAT GCA TC–3′. The construct is shown in Fig. 7.1c. The ssDNA backbones of *i* and *ii* were designed with high G-C content in order to enhance the thermal stability of the hybridised constructs, and without self-complementary sequences to prevent the formation of hairpins. The 8 base pair palindromic ssDNA overhang was designed for the tissue to have $T_m \simeq 55$, allowing for the ability to reset and tune the porosity of the tissue over a range of temperatures that would not damage the vesicles.

7.3.2 Sample Preparation

0.2 mm × 0.4 mm × 40 mm (Inner Dimensions) capillaries (CM Scientific) are filled to approximately half way through the capillary from one end with UV-curing glue, to create a seal minimising negative curvature, in order to prevent slipping at the walls upon application of force to the sample through the magnetic bead. These capillaries are then UV-exposed for 1 hour. Subsequently, the chamber with a single opening that is formed between the glue "plug" and the open end is washed by filling and sonicating in DI water for 15 minutes, and then filling and sonicating in Isopropanol for 15 minutes, before drying with nitrogen. The chamber is then filled with 1% (w/w) BSA solution, and left in an oven at 60°C for 1 hour to coat. The BSA-coated chamber is then washed through pipetting in and out of the capillary with the experimental buffer to remove excess BSA and aggregates to leave a passivated capillary.

GUVs are prepared as in Section 4.2.2 with Texas-Red DHPE as the fluorophore on the vesicles. GUVs were then sedimented in 300 mM glucose solution, to allow a region dense

in GUVs at the bottom of the Eppendorf tube.

We take 10 µl of GUVs extracted from the dense region and dilute them in 70 µl of TE+100 mM NaCl+87 mM glucose solution in an Eppendorf tube. To this mixture, 20 µl of a single cholesterol anchored dsDNA sequence with a palindromic overhang is added, in order to functionalise the vesicles. The eppendorf was turned upside down 10 times to aid mixing, and subsequently placed on heat block at 65°C, significantly above the melting temperature of the complex the overhangs form. As some of the cholesterol attached to the wall of the eppendorf, the elevated temperature prevents any vesicles sticking to DNA constructs on the side of the eppendorf by preventing binding of the DNA constructs, and due to the density mismatch, they sink to the bottom to create a dense region of vesicles. The temperature is reduced to room temperature, considerably below the melting temperature, to allow inter-vesicle adhesive connections to form.

The chambers are loaded with the sample with narrow pipette tips (VWR Pippette tips with microcapillary for loading gels). Sample is loaded into the chamber, and spun down in a centrifuge at 8000 rcf for 3 minutes, to create a dense packing at the bottom of the chamber. The supernatant is removed, and more sample is added and spun down a further four times, to ensure the packing is large enough that it spans the width and height of the chamber with sufficient length that it can be assumed that there will be no slippage that could affect our measurements in the bulk. Finally, 5 µl of supernatant is removed, and replaced with 5 µl of mineral oil. The sample is sealed using an adhesive, to leave a capillary sealed on both ends.

In the experiments with the magnetic beads, 50 µm diameter magnetic beads are isolated under a microscope and individually suspended in 1 µl drops of TE+100 mM NaCl+87 mM glucose solution. This is added with the vesicle network before the spinning down, to leave the magnetic bead in the bulk of the network of vesicles. Only one bead was added per sample, both to prevent interactions between beads as well as not being able to resolve contributions of forces from multiple beads to our measurements.

In the experiments with sterically-stabilised polystyrene colloids (Section 7.3.5) colloids were diluted 1:199 in TE+100 mM NaCl+87 mM glucose, and 70 µl of this solution is used instead of the normal TE+100 mM NaCl+87 mM glucose, when making the experimental sample, allowing the pores in the network to be filled with diffusive particles.

7.3.3 Magnetic Tweezers and Imaging

We utilise a quadrupolar magnetic tweezer set-up designed within the group of Dr. Kabla. Imaging was conducted in brightfield and achieved using a bespoke set up created by Dr. Radu Tanasa and optimised by Fergus Richie. A more detailed description of an earlier iteration of the setup is found in Ref. [255]. Images are taken at 2.2 fps.

7.3.4 Tweezer Calibration

The calibration technique employed is described in detail in Ref. [255]. Briefly, the force on the bead at a particular point is estimated from the set of points the bead passes through during a calibration experiment, where a magnetic bead is moved through a sample of known viscosity, in this case mineral oil, to calculate the force vectors acting on the bead. This is repeated from multiple start positions, and a Gaussian Process regression model is used to establish a magnetic force map from the calibration/training data. We found that, with a 50 µm diameter bead, at 1A current applied to the electromagnetic tweezers, we produced a 11.5 nN magnitude force which varied within the region that the bead moved by 0.28%. The accuracy of the forces derived from the calibration are highly dependent on the accuracy of the viscosity of the calibration oil. In order to ensure this, rather than using the manufacturer's value, we assessed the viscosity of the calibration oil using a rotational shear rheometer. We found the real value of the viscosity to be 1.5% less than stated by the manufacturer.

7.3.5 Sterically Stabilised Colloids

Sterically stabilised colloids are created for particle tracking within the biomimetic tissue using a method adapted from Ref. [264]. Steric stabilisation is necessary due to the need to reduce nonspecific binding and keep the particles dispersed in high ionic strength solutions, such as those required in samples with DNA including the samples studied here.

Briefly, the method works through the adsorption of a triblock copolymer to the particle surface, subsequent swelling with an organic solvent which allows the hydrophobic residue block of the triblock copolymer to insert beneath the surface, and finally the stripping of the solvent and deswelling through heating to leave stable, surfactant functionalised particles.

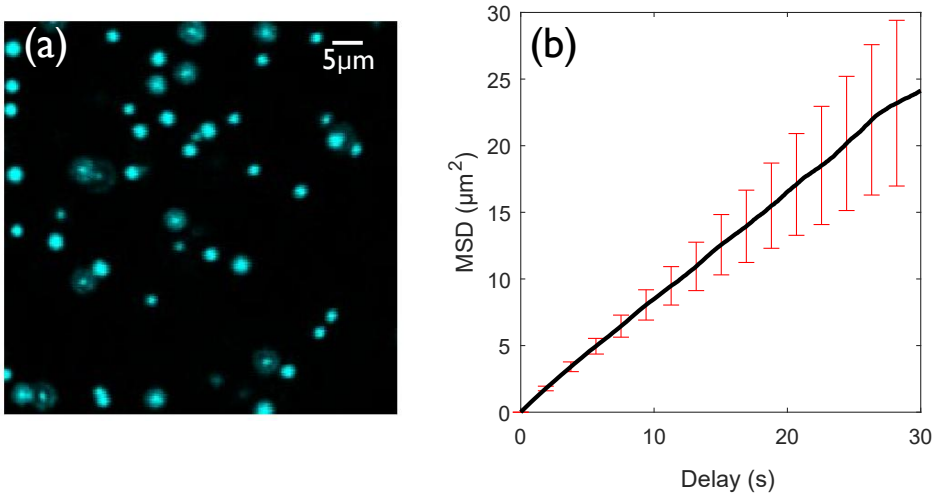

Fig. 7.3 Characterisation of free beads in solution: (a) confocal image of sterically stabilised, non-aggregating fluorescent 1 μm diameter beads, (b) mean-squared displacement (MSD) of the freely diffusive beads in the experimental medium, showing a straight line indicating diffusive behaviour. Errorbars are the standard deviation of the (MSD) for each delay time.

0.3 ml of 1% (w/w) triblock copolymer, Pluronic F108 (poly(ethylene glycol)-b-poly(propylene glycol)-b-poly(ethylene glycol)), in deionised water is added to 0.2 ml of 1% (w/w) of 1 μm, yellow-green fluorescent (505/515) polystyrene beads (FluoSpheres™ Carboxylate-Modified Microspheres) in deionized water. 0.5 ml of Toluene (99.8%, Aldrich) is added in a 1:1 volume ratio and gently mixed on stirrers for 12 hours.

Toluene is removed by steam stripping the dispersion due to its large miscibility gap with water, by heating an open container of the sample in a silicone oil bath at 98 °C in a fume hood, causing the deswelling of the particles. Finally, to remove excess surfactant, the particles are washed ten times by centrifugation and redispersion in deionised water. To ensure that the stabilisation was successful and that the particles were freely diffusing, particles were placed in the experimental buffer (TE+87 mM glucose+100 mM NaCl) and analysed to ensure they were diffusive and not aggregating (Fig. 7.3).

7.3.6 Imaging and Particle Tracking: Sterically Stabilised Diffusive Particles

Fluorescence imaging is carried out on a Leica TCS SP5 II laser-scanning confocal microscope equipped with a Leica HCX PL APO CS 63× 1.4 NA oil immersion objective.

A 633 nm He-Ne laser and a 488 Argon-ion laser are used to excite respectively Texas Red-DHPE labelling the vesicles and the Yellow-green fluorescent(505/515) FluoSpheres. Emission is collected between 510 nm and 560 nm for the FluoSpheres and 639 nm and 780 nm for vesicles. Images were taken of the vesicles to assess the local packing of the structure, whilst movies were taken taken at 12 fps for particle tracking/MSD calculations.

Each frame of each stack has a bandpass filter applied to smooth the image and subtract the background. A peakfinding algorithm detects a peak for each particle, via a threshold dependent on the maximum pixel value and an estimated particle size in pixels to prevent multiple pixels from one particle being represented as multiple particles. This is applied to each frame to find a peak corresponding to each particle. To find the centre of the particles with sub-pixel accuracy, we find the centroid of each region defined as a particle. Subsequently the positions were linked together using a customised version of the Particle Tracking Code published by Blair and Dufresne to find the particle tracks [256]. This is achieved by considering the n particles found previously at time (i), and m possible new positions at time $t(i+1)$. The function maps the n postitions at $t(i)$ to m positions at $t(i+1)$, minimising total squared displacement. For particles which are lost (going out of frame in x,y or lost in z) and not associated with one of the m particles in $t(i+1)$ due to there not being an m within the maximum between-frame displacement threshold of n, the total squared displacement is penalised by the maximum displacement threshold squared. Tracks with fewer than a defined number of points were then removed. These tracks were then analysed by reformatting the data to be compatible to a customised method built upon the existing @msdanalyser MATLAB per-value class for MSD analysis, first employed in the work of Tarantino *et al.* [265]. From the tracks, the MSD was calculated with drift correction using velocity correlation.

7.4 Uniaxial Creep: DNA-mediated Vesicle Network

7.4.1 Experimental Design

To test the rheological properties of the DNA-mediated vesicle network, a series of uniaxial creep and recovery tests were performed using magnetic tweezers. Preliminary testing indicated that the material stiffened after successive cycles of stress were applied. The cause of this behaviour was thought to be due to the rearrangement of the vesicles into positions in which they would jam, or otherwise obstruct the motion of the bead. This system allowed the probing of this hypothesis, as the material is held together by the formation of DNA bridges

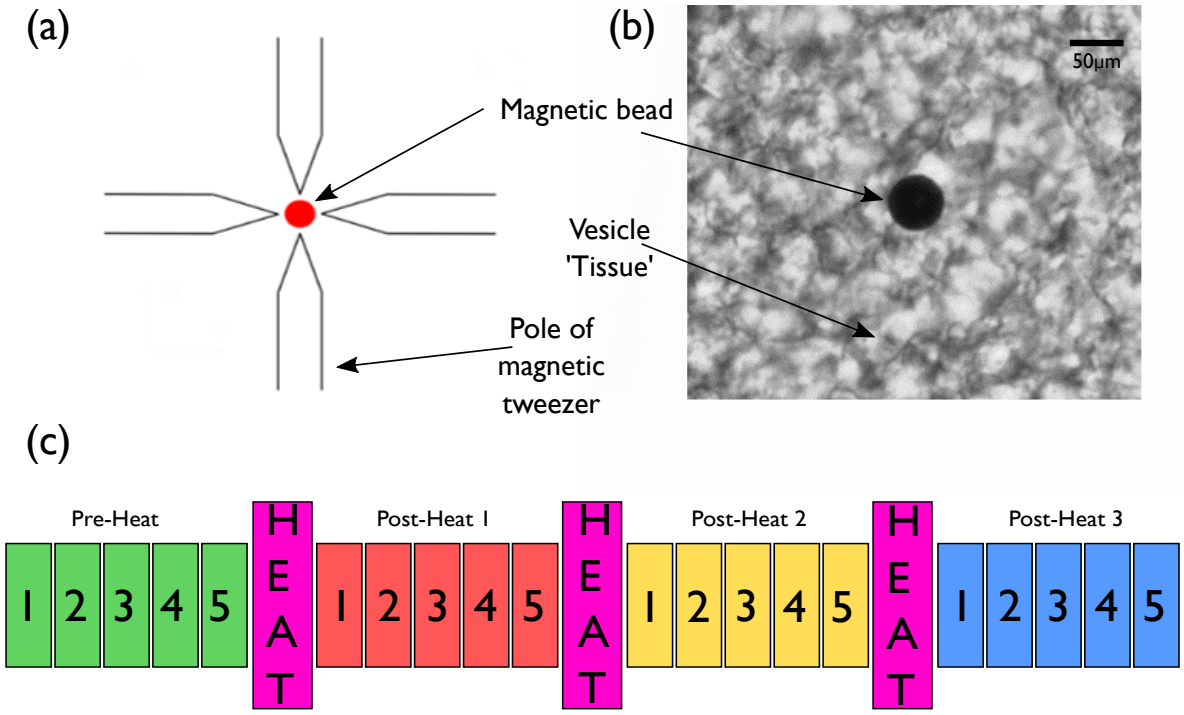

Fig. 7.4 (a) A simple diagram of a magnetic bead shown between the four poles of the magnetic tweezer, indicating how a combination of the poles control the bead directionality. (b) a brightfield image of the magnetic bead in the vesicle tissue. (c) a schematic to show the experimental procedure, with heat steps of 65°C, and each numbered creep test performed back to back within each stage between heat cycles.

between vesicles. By heating the sample above the melting temperature of the material, we remove adhesive forces between vesicles and in turn lower the effective viscosity, thus enabling the vesicles to move out of the strain induced configuration.

Creep tests were carried out in a series of stages, with each stage consisting of five consecutive creep tests, or runs (Fig. 7.4c). Each run consisted of three phases totalling 3 minutes; the pre-creep phase before the force was applied (10s), the creep phase during which force was applied with constant magnitude of 11.5 nN (60s), and the recovery phase (110s), at the start of which the force was (instantaneously) removed and the material was allowed to recover from its deformation, as observed by the movement of the bead. At the end of each run, we moved straight into the next. After five runs, a heating step was performed by placing the sample on a hotplate at 65°C and covering it to ensure equal heat distribution across the sample. The heating step lasted five minutes, after which the sample was placed back into the tweezer setup, and two further minutes were observed before starting a new stage of experiments, in part to allow the sample to cool down and the vesicles time to adhere (though this is a very fast process so this time is more than sufficient), but also to ensure adequate time to remount the sample.

7.4.2 Creep and Recovery

Figure 7.5 shows the results obtained from the creep and recovery experiment outlined in Section 7.4.1. It can be observed that, within each stage, the displacement is reduced with each subsequent run, with the difference between the first run and second predominantly the largest. The notable exception is in the case of the pre-heated experiment (Fig 7.5a), where the maximum displacement of the bead does not decrease monotonically as a function of run number. We also see that the maximum displacement decreases between stages after the initial pre-heat stage (Fig 7.5b-d).

Our results indicate a strain hardening effect, through the successive decrease in displacement of the bead. This effect is reset to an extent by the heating process; the maximum displacement increases above that seen at the end of the previous heating stage, however not to as large a value as in the first run of the previous stage. We hypothesise that the movement of the bead through the network of vesicles causes local rearrangements. Such "jamming" of the microstructure has been posited as a mechanism for creep in dense Laponite suspensions [266]. Indeed, shear induced bond formation has been proposed as the mechanism for stiffening in soft colloidal materials undergoing deformation [267]. In our system, such

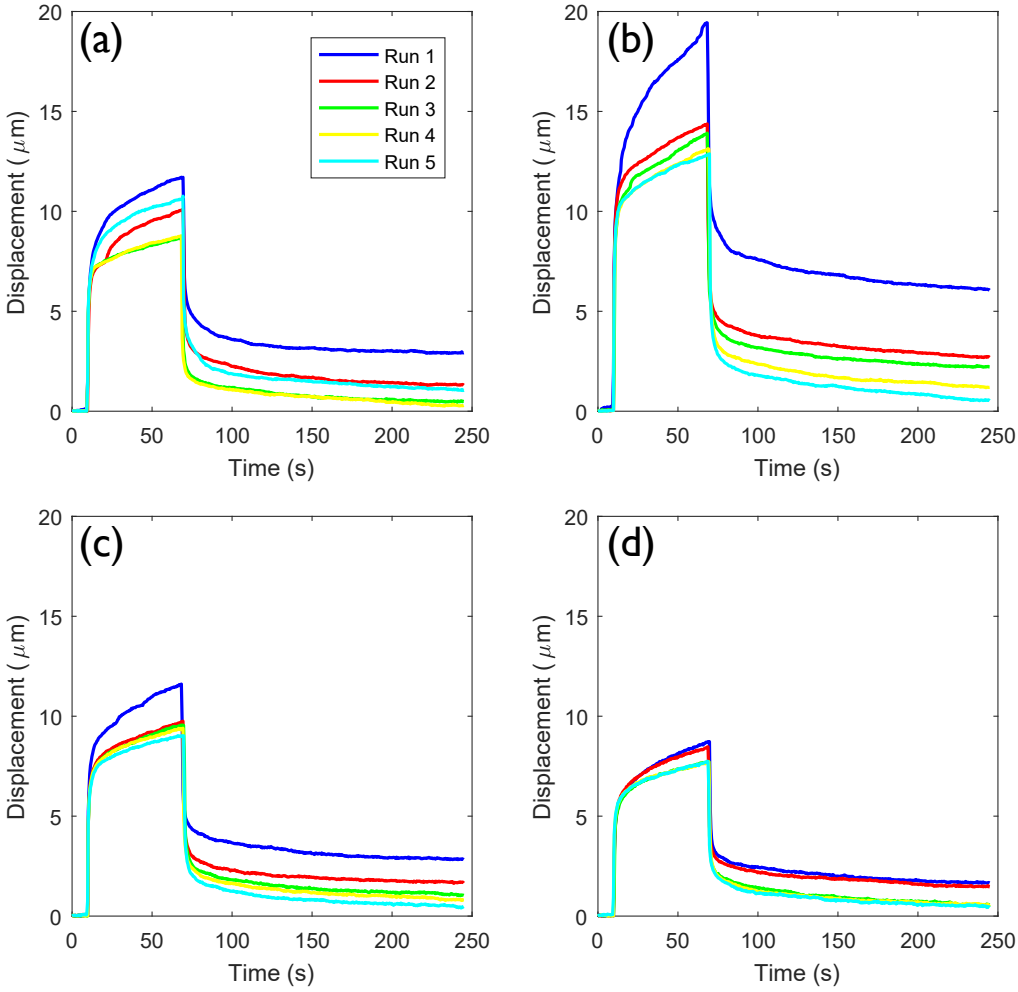

Fig. 7.5 Displacements from the creep and recovery experiments using a magnetic beads in a dense vesicle tissue. Each plot shows five successive experiments testing the creep response of the material, with each plot corresponding to a different stage in the heat cycle: (a) the pre-heat response (b) post-heat 1, (c) post-heat 2 and (d) post-heat 3.

"jamming" could lead to an increase in the local density of vesicles, due to their deformability and their rearrangement allowing for the formation of multiple contacts between vesicles [52], locally creating a more wet-foam like structure with fewer interstices. This would lead to increase rigidity of the sample and explain the strain hardening effect observed, as increasing packing fraction leads to multiple contacts that effectively act as elastic springs; by lowering packing fraction the number of contacts decreases [268]. Indeed, jamming induced strain hardening has been observed in colloidal gels and attributed to the strengthening of the gel backbone [269]. We therefore conclude that upon heating, the vesicles relax from the strain-induced configuration, and upon cooling reform into a network with fewer contacts, less densely packed. However, this would still be more locally jammed than previously, therefore complete reversion to the original state, and thus initial creep behaviour, would not be expected.

7.4.3 Model Fits

We fit the two models described in Section 7.2 to describe the creep and recovery of the magnetic bead during our experiments. This is achieved by considering only the data taken when the bead is subjected to an applied magnetic field for the creep, and only the data once the magnetic field is removed for the recovery. Representative fits are shown in Fig. 7.6.

From these representative fits, we can see that both models reasonably describe the creep data (Fig. 7.6a&b), with the Jeffrey's model overestimating the sharpness of the transition between elastic and viscous deformation behaviour. In contrast, the Jeffrey's model consistently overestimates the rate of recovery, due to the lack of flexibility of only having one time constant with which to model the data. Conversely, the spring-pot, which represents a distribution of time constants, fits the recovery well, indicating the complex nature of recovery in our material.

Whilst adding more parameters to the Jeffrey's model could allow us to capture power-law behaviour, it takes us away from having intuitive physical parameters, and as such the spring-pot, which gives quasi-rheological properties whilst describing power-law behaviour, is preferred. We find that this fits both the creep and recovery better, even as a simpler two-parameter model. However, it is still informative to consider the physically intuitive parameters derived from the Jeffrey's model, notably in the better fitting creep experiments.

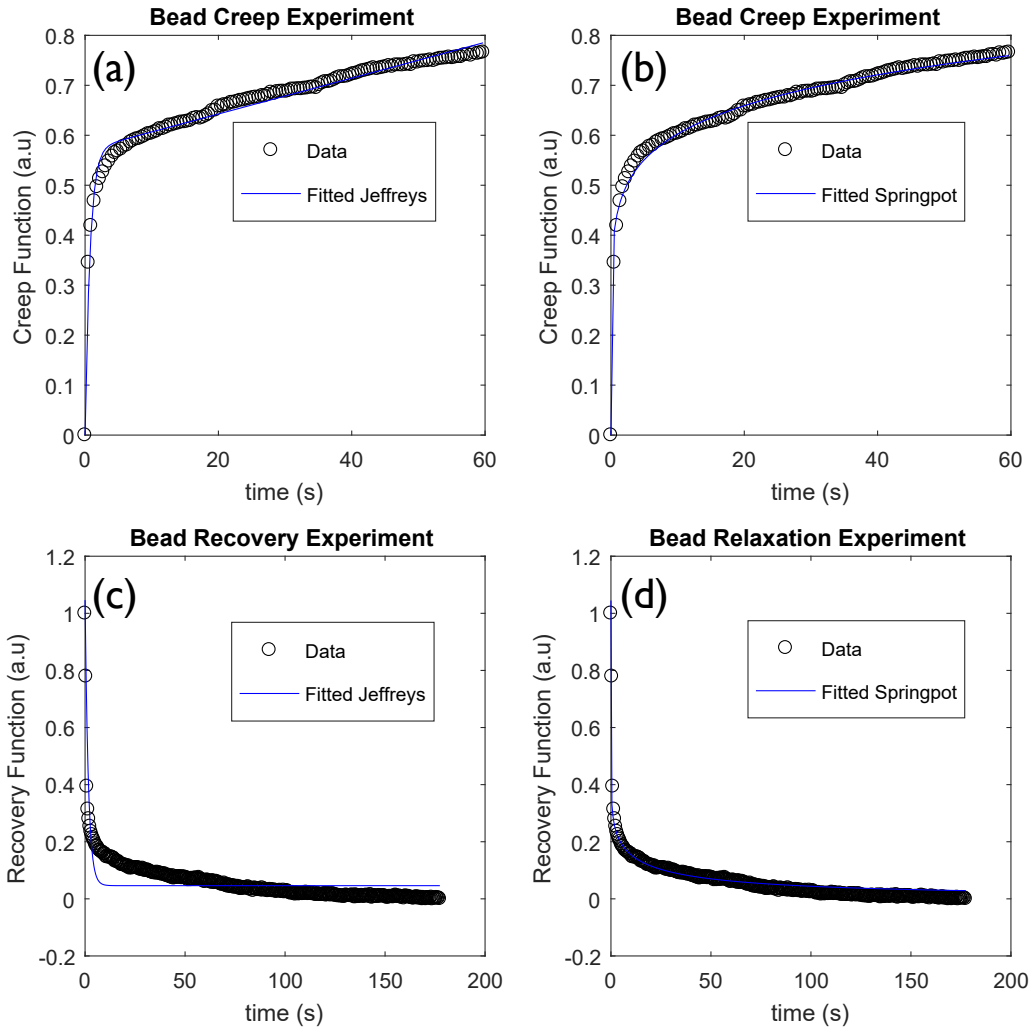

Fig. 7.6 Fits for the creep and recovery data for a representative run using both the Jeffrey's and Spring-pot model. (a) Fitted Jeffrey's Creep (b) fitted Spring-pot Creep (c) Fitted Jeffrey's Recovery (d) Fitted Spring-pot Recovery.

7.4.4 Model-derived Rheological insight

Jeffrey's Model

Fig. 7.7 shows the result of analysing the creep data. This analysis shows that, with the exception of the pre-heat data, all three elements in the model increase in value between subsequent heat steps. As such the material appears to stiffen and become more viscous between heat steps. Within each stage, η_1 increases with each repetition (Figure 7.7a). η_1 in our model represents the inter-vesicle viscosity and as such arises purely from the microscopic interactions between vesicles such as the friction/adhesion between vesicles;

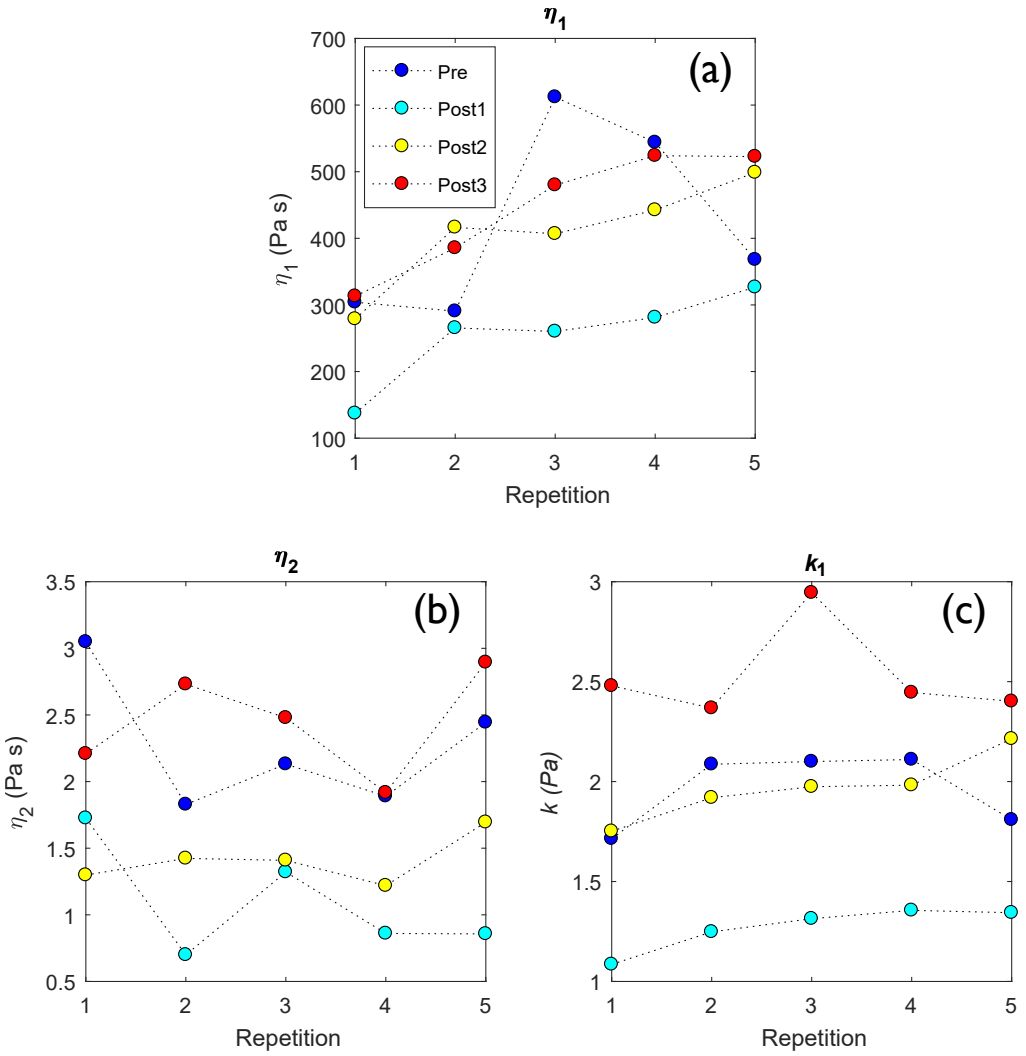

Fig. 7.7 Viscoelastic properties of the material derived from the fitting of the Jeffrey's model to the creep data for each repetition. (a-b) The two viscosity parameters from the dashpots in the model, η_1 and η_2, respectively. (c) The fitted hookean spring constant (k_1). Coloured dots represented different stages in the heating cycle as in the key, dotted lines connect repetitions within the same stage.

therefore the increase in η_1 is consistent with the local increase in packing fraction and thus local increase in friction/adhesive forces [270]. η_1 is somewhat reset after each heating cycle. As stated in the Section 7.4.2, this could be due to the reduction in physical contacts between vesicles due to the heating allowing the relaxation of the vesicles from strain induced locally dense configurations [268]. The other parameters, η_2 and k_1 show an upward trend between cycle, but no consistent discernible trends.

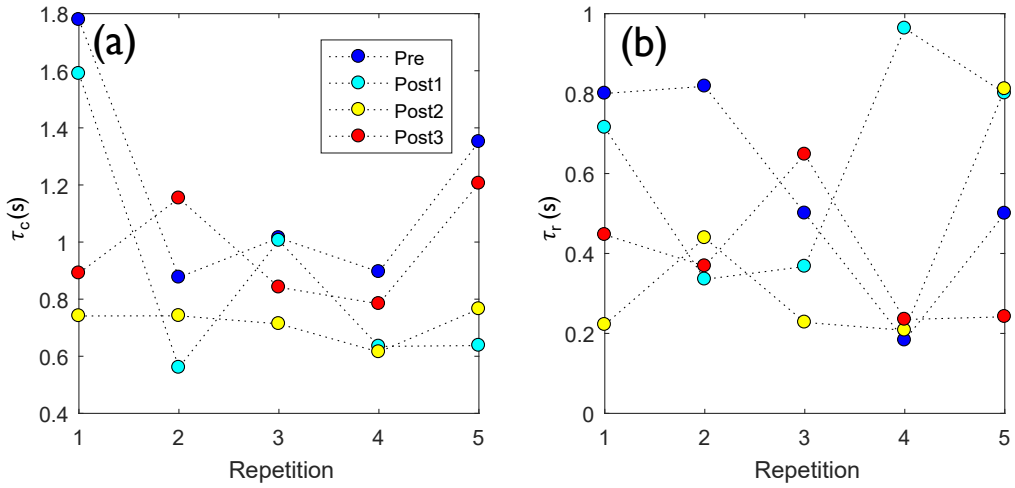

Fig. 7.8 Jeffrey's model derived timescales of deformation for both the (a) creep and (b) recovery data. Colours indicate different stages in the heat cycle and repetitions within the same heat cycle are connected using dashed lines.

We can derive the timescale of deformation for the creep data as $\tau_c = \frac{\eta_2}{k_1}$, and this is shown in Fig. 7.8a. Conversely, the timescale for the recovery, τ_r, is calculated independently, as it is not possible to obtain separate values for the model parameters from the recovery phase alone, and is shown in Fig. 7.8b. Fig. 7.8 shows that the creep timescale is predominantly greater than the recovery timescale, and with the exception of the pre-heat data, the timescale shows a general slow speeding up with each repetition. No such relationship with the repetition is seen in the case of recovery timescale. Whilst the fit of the creep (Fig. 7.6a) was relatively robust, this was not the case for the recovery (Fig. 7.6b), where the Jeffrey's model single timescale was insufficient to capture the recovery dynamics, overestimating the sharpness of the recovery. As such, the significance of comparisons between the deformation timescales observed in both models is limited.

In similar experiments in zebrafish embryos where the same model was used on creep experiments using magnetic tweezers (Ref. [255]), strain hardening of the biological tissue was also observed. The interesting difference in the creep response is the evolution of the fitted parameters. The two parameters that correspond to the cell mechanics, η_2 and k_1, increase with each stages but show no clear trend with each run in the biomimetic tissue presented here (Fig. 7.7b&c), in contrast to the results in Ref. [255], where there is an increase in the values of both parameters. There is a similar monotonic increase in η_1 in both the cell mechanics and the dashpot represents cell–cell adhesion. These experiments are not identical, however, it shows that the biomimetic tissue presented here allows for the

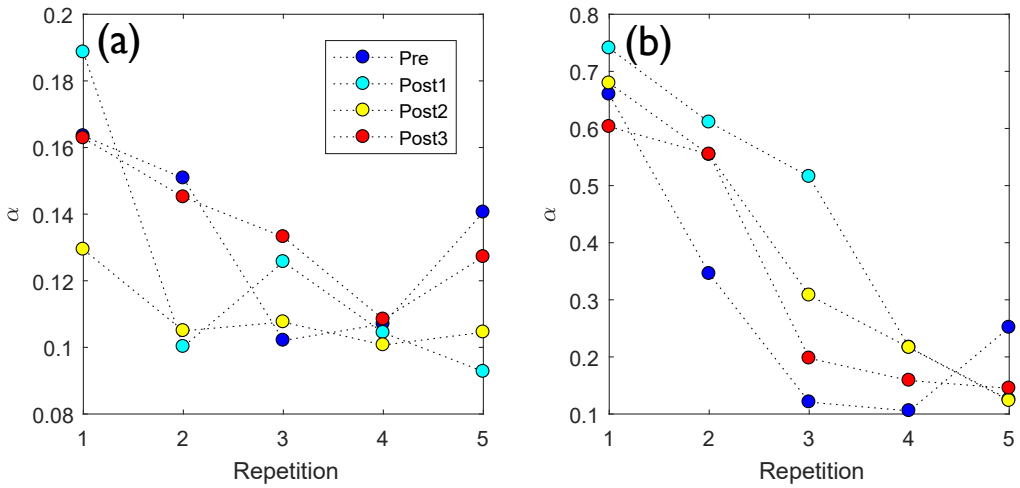

Fig. 7.9 The power of the fractional derivative of the strain within the spring-pot model, derived from the fit to the (a) creep and (b) recovery data for each repetition. Colours indicate different stages in the heat cycle and repetitions within the same heat cycle are connected using dashed lines.

decoupling of some of the trends observed in biological tissues from the active processes of the cells.

Spring-pot Model

In the case of the spring-pot model, we concern ourselves with the evolution of the α, the exponent of of the fractional derivative [133]. The fits (Fig. 7.6b&d) for both the creep and recovery were robust. We see a decrease in the power of the fractional derivative of the spring-pot, α, indicating that the model element is tending towards more spring-like, rather than dashpot-like behaviour during both the creep and recovery measurements, which aligns with the work of Bolton *et al.* where the increase in packing fraction leads to multiple contacts that effectively act as elastic springs [268].

There is an abundance of literature of using spring-pots within more complicated models, both with other spring-pots and linear viscoelastic elements [263, 271, 272]. We attempted fitting with a Fractional Maxwell Model, where two spring-pots are connected in series; this yielded a minimal improvement in the fit, for double the parameters. The use of a second spring-pot led to the one spring-pot consistently demonstrating a pure dashpot behaviour with a near 0 α, and with the spring-pot showing very similar values to those found from fitting the single spring-pot. Additionally, recent work has shown the ability to model the

rheology of epithelial monolayers with a fractional standard linear solid model, a spring in parallel with a spring and spring-pot in series, as well as a "special" model, described as a spring in parallel with a spring-pot and dashpot in series [263]. These fits did not show considerably improved fits for the extra parameters, and as such we settled on the the single spring-pot, as it gave a good fit to our data.

7.5 Deformation Length Scales

7.5.1 Measuring Tissue Deformation

In addition to tracking the movement of the bead itself, we extract information on the bead-induced deformations of the material across length scales by considering the evolution of the structure of the tissue, through the assessment of changes in the pixel intensity of brightfield images of the vesicle network. Firstly, we subtract the first frame of the image stack for each experiment from each frame in the stack to get a series of difference images. By masking pixels within the path of the bead during the experiment, we do not consider pixel differences directly due to the motion of the bead, causing the differences in values of the pixel considered to be due to bead-induced deformation of the vesicle network itself. We average the values of each pixel across all difference images to get an image for the average pixel difference across the stack ($\Delta\overline{Int}_{Pix}$), where the path of the bead has been masked (Fig. 7.10a). We take the centre of mass of the mask, and create a series of regions of interest allowing for the consideration of pixels in either an annular region at specific radii from the bead's path (Fig. 7.10b) or an angular segment of such an annular region (Fig. 7.10c).

7.5.2 Deformations: Lengthscale and Angular Dependency

In all cases we see a broadly monotonic decrease in $\Delta\overline{Int}_{Pix}$ as a function of distance from the bead path centre of mass (Fig. 7.11). This also consistently decreases with each run within each stage, and decreases with each subsequent stage, though $\Delta\overline{Int}_{Pix}$ for the first run of each stage reaches higher values than the last runs of the previous stage (Fig. 7.11). This indicates the material properties are somewhat reset by heating, which is in agreement with the results shown in Section 7.4, but also that force-induced deformation is less pronounced with increased distance from the bead.

We fit $\Delta\overline{Int}_{Pix}$ with a simple exponential function, in order to probe the length scale of the deformations, as shown in Fig. 7.12a. This length scale represents a characteristic length

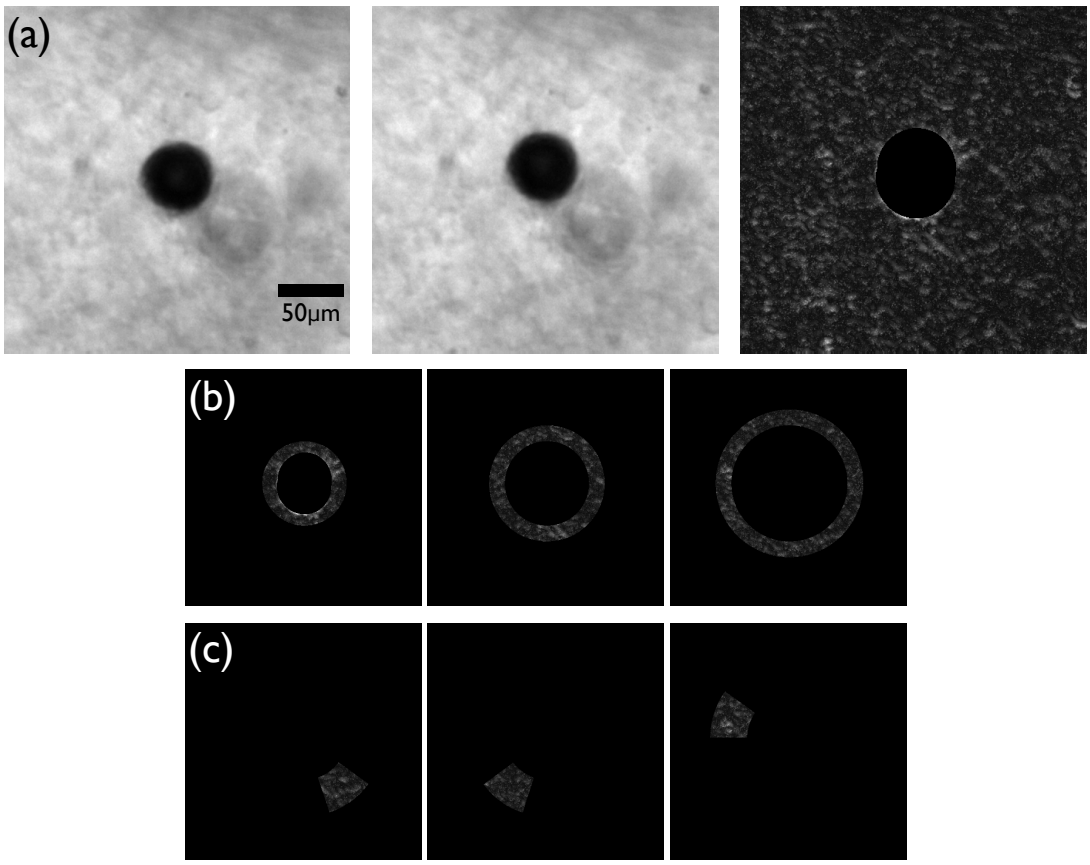

Fig. 7.10 Probing tissue deformation. (a) The positions of the beads for each frame, with two representative frames shown. (Left) a single frame at t=0 s and (Middle) a single frame at t=50 s, were used to create a mask for each frame. Difference images (between the first and all subsequent frames) were created, and each pixel value was averaged, except those within the masked region, over all difference images to create a mean pixel intensity difference ($\Delta\overline{Int}_{Pix}$) image shown in the (Right) panel. (b) Annular regions, defined at a series of radii from the centre of mass of the mask, were then considered to probe the length scales of deformation with 3 representative sections of inner radii of (Left) 70 μm, (Middle) 100 μm and (Right) 130 μm shown. (c) Angular segments, defined at a set radius (inner=100 μm, outer=150 μm) and a series of angular regions from the centre of mass of the mask, were considered to probe the directional dependence of the deformation with 3 representative 0.2π radian sections at angles (Left) 0.2π (Middle) 0.6π and (Right)1.0π radians shown.

scale (β) over which the deformation, and therefore force, decays. This is similar to the work by Clark *et al.*, where they also observed an exponential decay in force transmission away from the intruder [273]. We plot β as a function of repetition and heat cycle in Fig. 7.12b. Between repetitions there is a generally decreasing trend in the length scale of the deformations, indicating the local hardening of the material, and structural rearrangements leading to

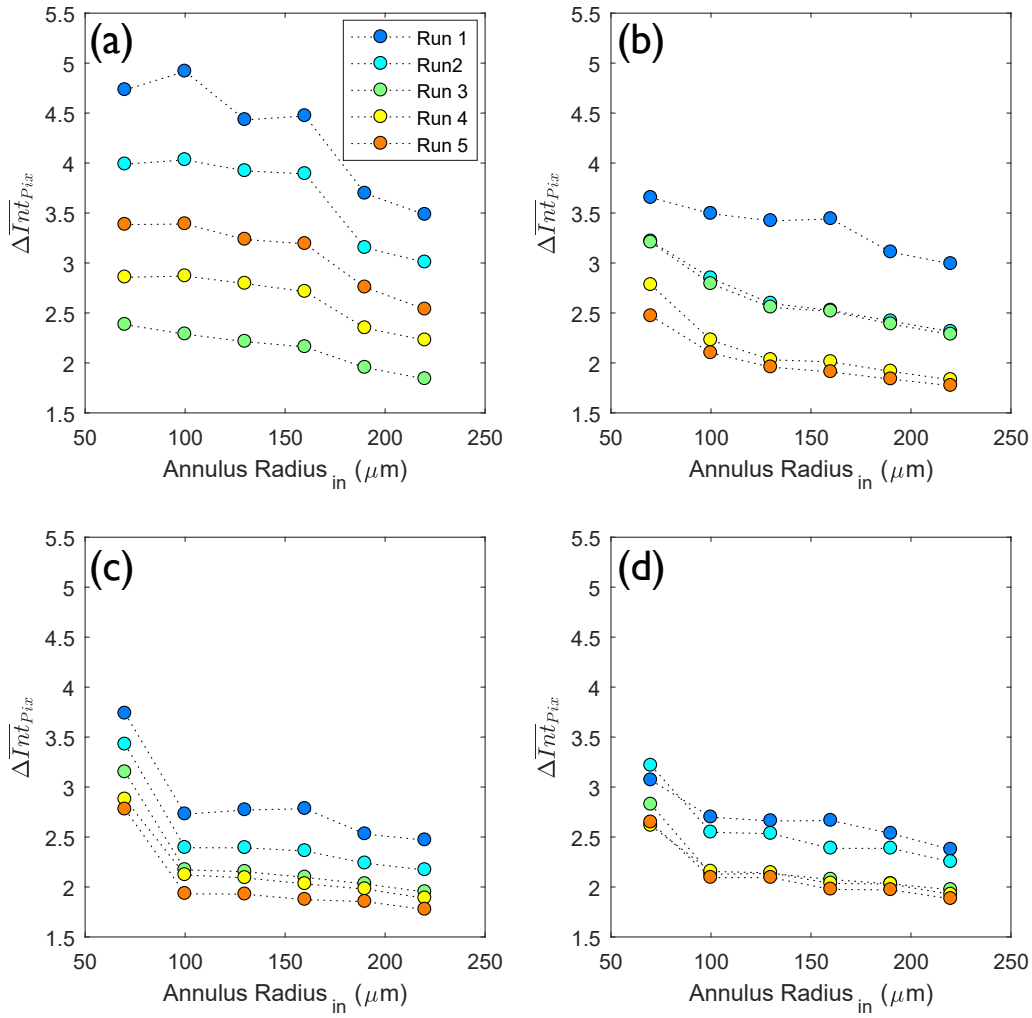

Fig. 7.11 Structural rearrangement represented through the mean pixel intensity difference ($\Delta\overline{Int}_{Pix}$) as a function of distance from the bead's path, in this case the inner radius of the annular region from which we find $\Delta\overline{Int}_{Pix}$ (Annulus Radius$_{in}$). The annular regions have a width of 30 µm. Each plot shows results from five successive experiments testing the creep response of the material (see figure legend), with each plot corresponding to a different stage in the heat cycle (a) shows the pre-heat response (b) post-heat 1, (c) post-heat 2 and (d) post-heat 3.

a minimisation of force chains, with rearrangements increasingly short range. Interestingly, despite the decrease in the absolute value of displacement between runs in the final stage (Fig. 7.12b), the lengthscales of deformations observed are larger than those in the previous stage. The mechanisms responsible for this dissipation and deformation are likely force-chain splitting or inter-vesicular friction in dense packings created through jamming [273, 274].

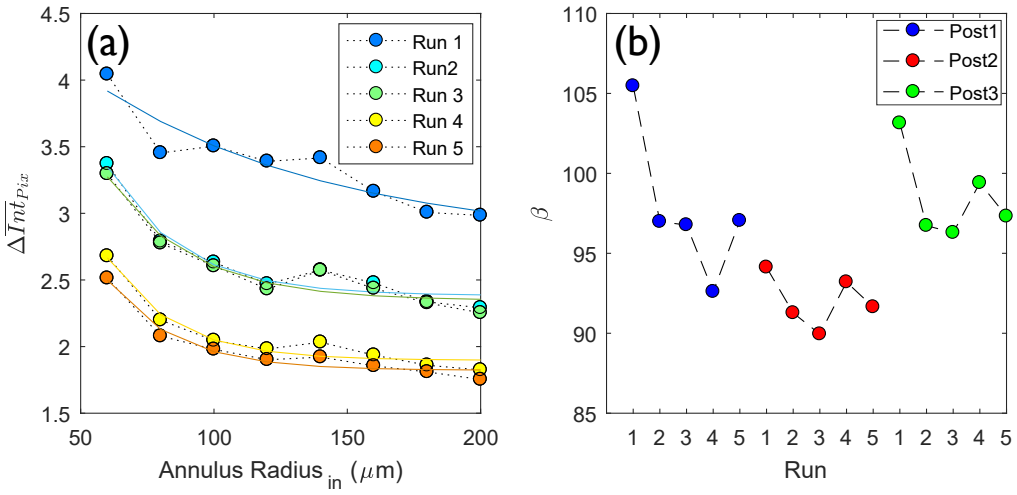

Fig. 7.12 Characteristic lengthscale of the bead induced deformation of the vesicle tissue. (a) Representative figure showing an exponential fit for the decay of the mean pixel intensity difference ($\Delta\overline{Int}_{Pix}$) as a function of distance from the bead's path, in this case the inner radius of the annular segment from which we find $\Delta\overline{Int}_{Pix}$ (Annulus Radius$_{in}$). From the fitted exponential, we derive a lengthscale, β, with coloured dots corresponding to points from the same run. (b) The evolution of β for each run in the 3 post-heat cycles. Coloured dots represented different stages in the heating cycle as in the key, dotted lines connect repetitions within the same heat cycle.

We also consider the angular variation in the $\Delta\overline{Int}_{Pix}$ by considering angular segments with an inner angle of θ_{in}. The segments are 0.2π radian segments of an annular region of inner radius 100 µm, and outer radius 150 µm. The direction of the motion of the bead during force application corresponds to the segment where θ_{in}=1.4π radians. We see no strong dependency on the direction of the motion of the bead (Fig. 7.13). There is however, a consistent peak at $\theta_{in} = 0.4\pi$ radians in Fig. 7.13a-c, which is the segment π radians (/opposite to) the direction of the bead motion. In the direction of the bead, we lose information on the deformation due to much of the deformation taking place within the masked region. Therefore, this peak might be an artefact of the masking. In studies on intruders acting under gravity on granular packings of 2D photoelastic spheres, force chain propagation was seen to be both denser and more homogeneous in the case of softer spheres, supporting our findings of negligible angular variation [275].

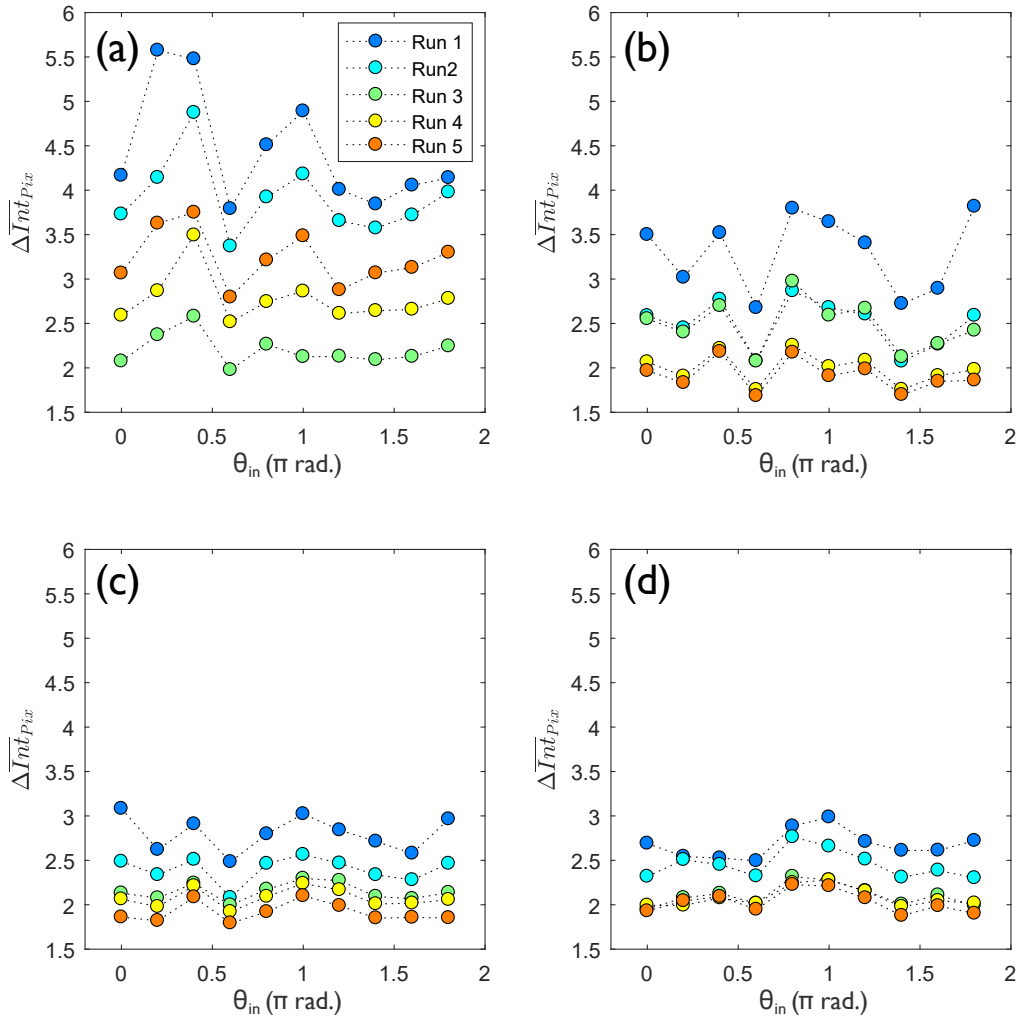

Fig. 7.13 Structural rearrangement represented through the mean pixel intensity difference ($\Delta\overline{Int}_{Pix}$) of 0.2π radians (rad.) spaced angular segments at with an inner radius of 100 µm and an outer radius of 150 µm. Each plot shows results from five successive experiments testing the creep response of the material (see figure legend), with each plot corresponding to a different stage in the heat cycling process (a) shows the pre-heat response (b) post-heat 1, (c) post-heat 2 and (d) post-heat 3.

7.6 Porosity Changes

7.6.1 Testing Sterically Stabilised Beads

Sterically stabilised beads were shown to have a broadly linear mean-sqaured displacement (MSD), corresponding to free diffusion of the particles (Fig. 7.3b). Additionally, visual inspection of videos corroborated the fact that the beads did not aggregate (Fig. 7.3a).

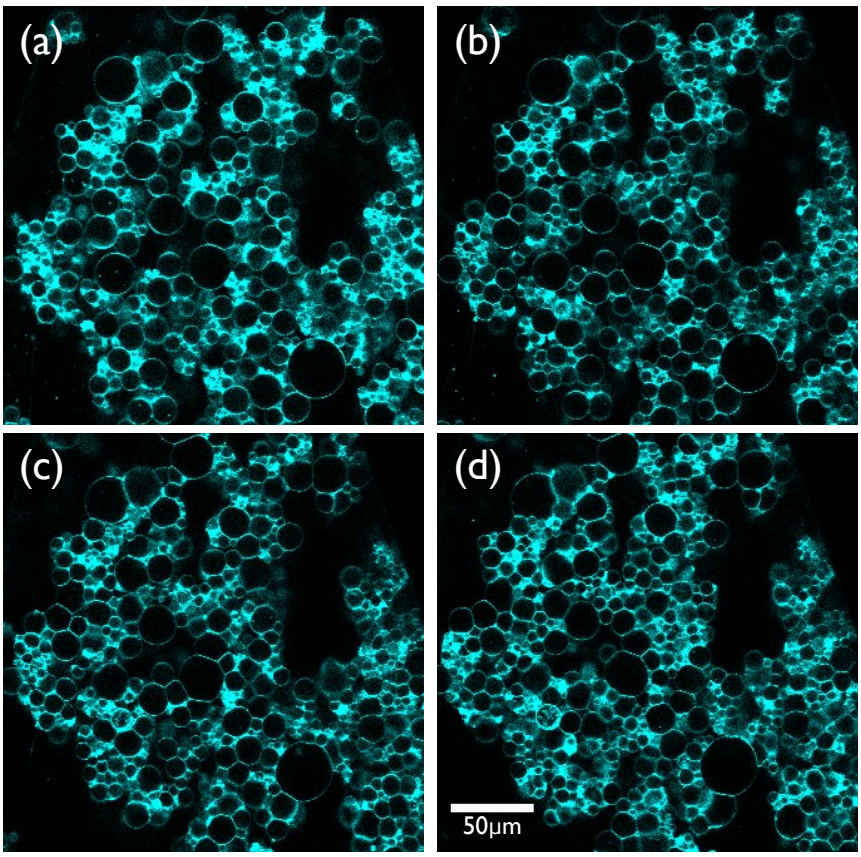

Fig. 7.14 Temperature evolution of a "tissue" of vesicles, where the same slice of a confocal z-stack at the same location is shown at (a) 20°C and (b) 30°C (c) 40°C (d) 50°C.

7.6.2 Temperature Variation

It can be observed from Fig. 7.14 that increasing the temperature changes the individual interactions of adhering vesicles, which parlays into changes in the bulk structure. The number, and size of contacts between vesicles can be observed to increase with increasing temperature, with larger, flatter adhesion contacts visible, and vesicles clearly deformed away from near-spherical structures. Furthermore, changes in the bulk structure are also observable; some pores have closed due to the densening of the structure, whereas in other cases pores have gotten larger as the structure contracts (Fig. 7.14).

At 20°C, at long delay times (delay$\gtrsim$55s), we start to see the gradient of the MSD decreasing towards a plateau. As we increase the temperature, the gradient of the MSD starts to decrease towards a plateau earlier, both in time and at lower MSDs, more clearly indicating subdiffusive, confined dynamics, and indeed a reduction in cage/pore size as we increase the

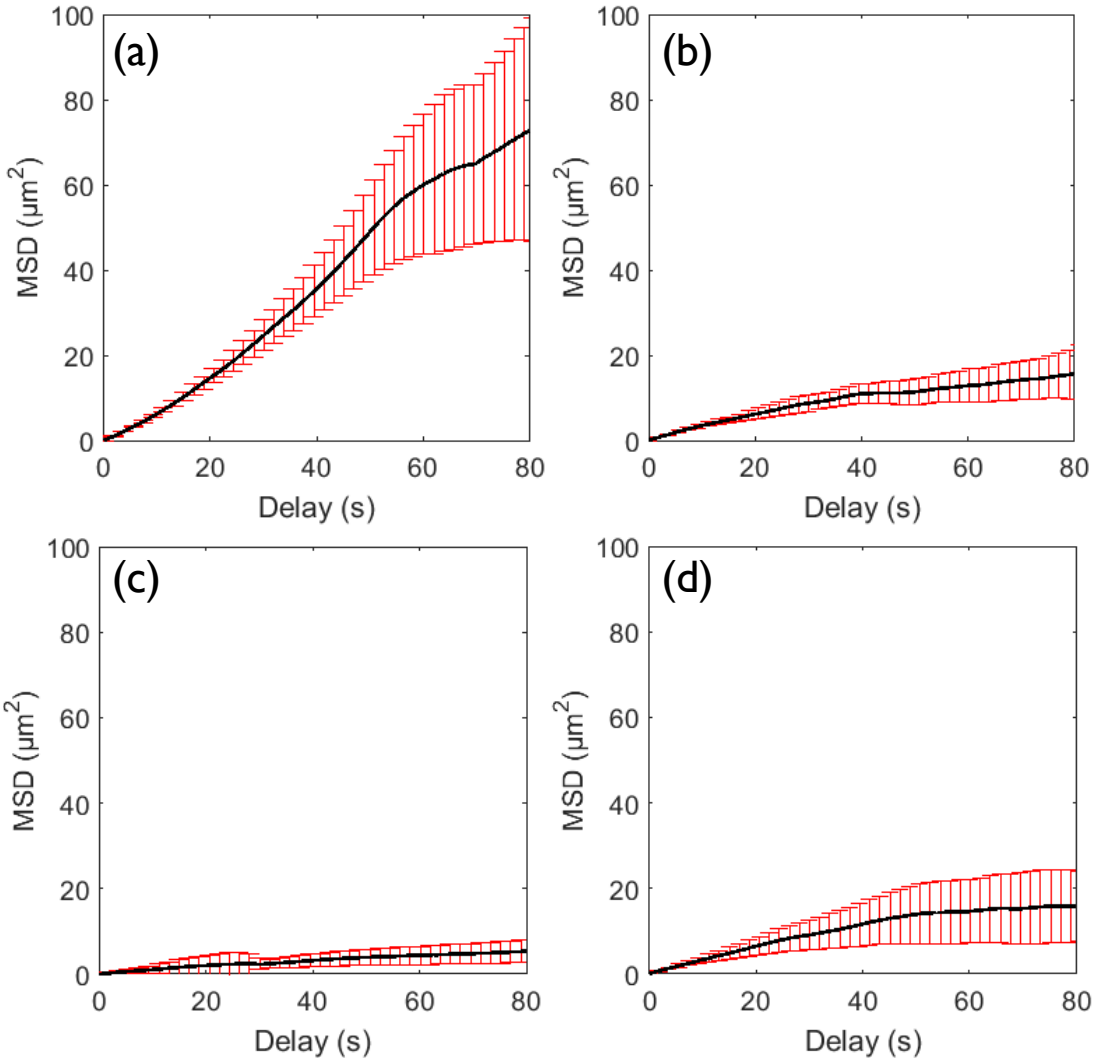

Fig. 7.15 Mean-Squared displacements from the tracking of sterically stabilised beads in a vesicle network at (a) 20°C and (b) 30°C (c) 40°C (d) 50°C. Errorbars indicate standard deviation of the values. The mean $N_{particles}$=60.

temperature towards the melting temperature of the tissue, where the cage/pore size can be defined as the square root of the plateau of the MSD [276]. At 50°C we see an increase in the location of the plateau of the MSD. The beads moving more whilst the material is still in a regime where the vesicles are adhering is initially surprising. However, the errorbars are large, presumably due to the heterogeneous structure of the material and the sampling occurring in different regions of the sample. Additionally, this re-entrant behaviour could be due to the coarsening to the structure; whilst the interstitial spaces between adhering vesicles will continue to decrease with increasing patch size and vesicle deformability, coarsening of the structure and rearrangement can lead to the presence of larger pores. Another possibility

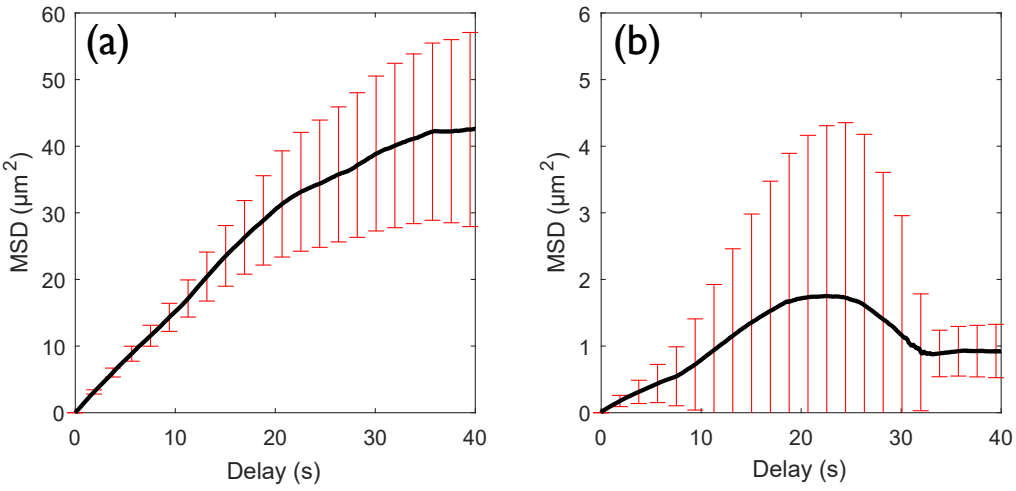

Fig. 7.16 Mean-Squared displacements from the tracking of sterically stabilised beads in a vesicle network formed with a DNA concentration of (a) and (b). Errorbars indicate standard deviation of the values. $N_{particles}$>35.

could be that the material is close enough to the melting temperature that some of the inter-vesicle adhesive connections have broken.

Previous work on both individual vesicles and networks of vesicles conducted by Parolini *et al.* contextualises these results [52]. They found that at low temperatures, the adhesion patches between vesicles become almost point-like, with the tissue taking on the structure of a packing of hard spheres, whereas conversely, at high temperatures the vesicle network forms a wet-foam like material with reduced interstices. This can be understood through the excess area of the vesicles; at low temperatures, vesicles are very stiff thus the formation of large adhesion patches and the associated deformations needed to achieve this are too energetically costly, whereas at higher temperatures the vesicles have a larger excess area and are easily deformable [52].

7.6.3 DNA Density

We increase the DNA concentration threefold in the sample, from 55nM to 160nM, and observe a ∼20 times decrease in the maximum observed value of the MSD (Fig. 7.16). By adding more DNA, there is more linker available to form patches. Therefore, there is the potential for both increased valency/contact number of the vesicles, or increased patch size and increased strength of adhesion due to the additive effects of multivalent linkers, allowing

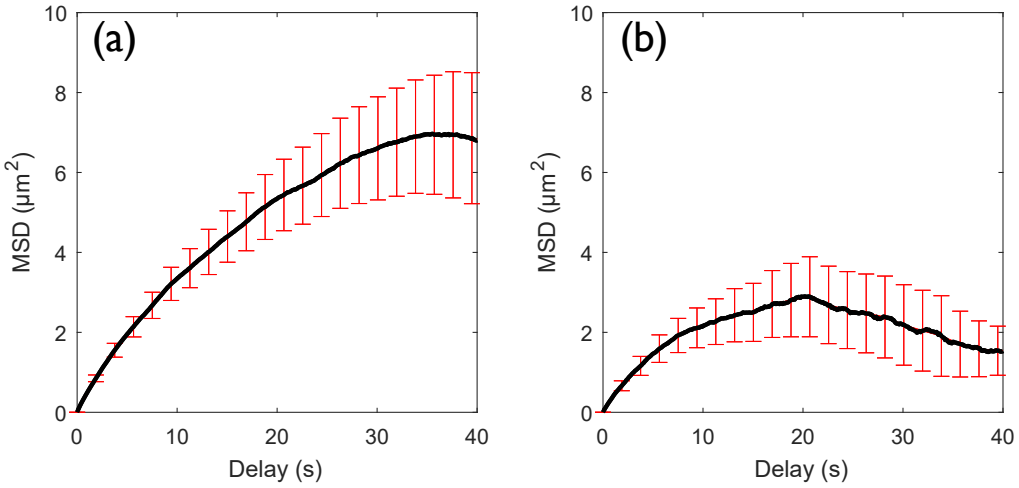

Fig. 7.17 Mean-Squared displacements from the tracking of sterically stabilised beads in a vesicle network at (a) t$\simeq$ 0s and (b) t$\simeq$ $1.21x10^6$s. Errorbars indicate standard deviation of the values. $N_{particles}$>38.

for a more densely packed network, with smaller interstitial spaces. This is corroborated by our experiment, where, as stated, we see an $\sim$20 times decrease in the maximum observed value of the MSD.

7.6.4 Aging

We investigated the possible effect of aging by considering the evolution of the MSD of the material over a long time period, where the time $t \simeq 1.21x10^6$. The MSD plateaued significantly quicker after the aging period, at a value $\sim 3\times$ smaller (Fig. 7.17). The reasoning for this could be due to thermal fluctuations that are sufficient to cause rearrangements in the structure of the material. Alternatively, it could simply be that at long times, only the particles constrained in small interstices, have not moved through the series of cages and escaped into the solution outside of the tissue.

7.7 Conclusions

In this chapter, we studied a biomimetic tissue consisting of GUVs adhering through complementary DNA-mediated interactions, and looked at its rheological and structural properties in the context of our understanding of vesicle-vesicle adhesion.

Magnetic tweezers are used to perturb a magnetic bead with a known force, with which we conducted creep measurements. Through consideration of two simple models: the Jeffrey's model, a constitutive model consisting of linear viscoelastic elements, and a spring-pot, a fractional element interpolating between a spring and a dashpot which captures power-law behaviour, we derive parameters with which to assess the material. We find both models reasonably fit the creep data, but only the spring-pot robustly fits the creep recovery. We find evidence of strain hardening in the material, which we posit is due to local jamming increasing contacts. This would lead to an increase in friction between the particles leading to a higher η_1 term from the constitutive model fit, and we observe this phenomena between runs. We find that the application of the Jeffrey's model to this biomimetic tissue, when compared to results on zebrafish embryos in the literature, supports the idea that this material represents a model for biological tissues free from the effects of active processes. Furthermore, the material should stiffen due to the adhesive contacts acting like elastic springs, and the formation of a backbone similar to a polymer gel network. The spring-pot becomes more "spring-like" with increasing runs, both in creep and recovery, indicating that the creep tests lead to further (local) solidification. The material shows the ability to "heal" somewhat; by melting the contacts through raising the temperature above the melting temperature of the system, the system is released from some of the strain induced configuration, though the material is still less deformable than as in the initial run of the previous cycle.

We are also able to assess the deformation due to the bead in the tissue itself, rather than through the movement of the bead, through analysis of the change in mean pixel intensity ($\Delta\overline{Int}_{Pix}$) of the tissue in response to bead induced deformation. We find that the deformation decreases monotonically with increasing distance from the bead, showing an exponential decay of $\Delta\overline{Int}_{Pix}$. We see no clear angular dependency of $\Delta\overline{Int}_{Pix}$; force chain distribution in soft materials has been shown to be more homogeneous than in harder granular systems. With each successive run we see the magnitude of the deformation decreasing, further demonstrating the hardening observed in the creep experiments.

Additionally, the porosity of the material is examined through particle tracking of small diffusive, sterically stabilised particles. We find that the structure of the tissue dramatically changes in response to temperature, where adhesion patches grow due to the increased deformability of the vesicles, and the interstices in the material shrink. We also see that the material ages: over $\sim 10^6$ s, the plateau of the MSD decreases from $\simeq 6\mu\text{m}^{-2}$ to $\simeq 2\mu\text{m}^{-2}$. This indicates slow aging dynamics in the material. We also probe the effect of DNA density. Increasing the DNA concentration $3\times$ resulted in $\simeq 20\times$ decrease in the MSD, indicating

the ability to dramatically, and non-linearly change the porosity of the material through DNA concentration.

We characterised aspects of this material's rheological, mechanical and structural properties, and contextualised the phenomenology within the context of our understanding of the microstructure. Much of this is preliminary; ongoing updates to the setup prevented full exploration of a number of ideas which will be considered in Section 8.2.2.

Chapter 8

Future Perspectives and Conclusions

In this chapter we present a summary of the findings from the work undertaken in this thesis alongside the future avenues of investigation that this work has pointed us towards, before making some holistic concluding remarks.

8.1 Thesis Summary

In Chapter 2 we introduced fundamental literature on lipids and lipid structures, before tying it together with a review on multivalent adhesion, focusing on systems using compliant subunits. To introduce some of the fundamental considerations for Chapters 5 and 7, we gave an overview of soft gels and the rheology of soft granular materials. Finally, to contextualise the work shown in Chapter 6, we introduced microfluidic methods of GUV formation. In Chapter 3 we reviewed some frequently employed experimental techniques, fundamental to the later work.

In Chapter 4 we showed a system of single lipid vesicles adhering to a flat supported lipid bilayer through multimeric multivalent interactions, which we studied to characterise the morphological and mechanical changes of the vesicles in response to external ligands. We showed that the mechanical properties of the vesicles, in particular their membrane tension, change dramatically on binding, and that the number of adhering vesicles is dependent on the concentration of the external ligand, with a "Goldilocks" situation of either too much, too little or just the right amount of ligand to enable adhesion, which we confirmed through consideration of a simple statistical mechanical model. This demonstrated concentration dependency confirms our assertion that this represents a proof-of-concept biosensing system.

In Chapter 5 we used Differential Dynamic Microscopy (DDM) to study the dynamics of a thermoreversible gel consisting of diffusive attractive soft colloids (small unimlamellar vesicles functionalised with complementary DNA constructs), allowing us to probe the spatial heterogeniety of the samples, and the aging, temperature and q-value dependency on melting of a deeply quenched gel, as well as upon quenching from a diffusive system. From the statics we found the gelation and melting temperatures of the system, whilst the dynamics of the diffusive system are well fit by a stretched/compressed exponential model. On quenching we found a gradual shift in dynamics, from those characterising diffusive behaviour to subdiffusive behaviour, with some evidence of small-scale interfacial coarsening events, where diffusive clusters coalesce. On melting, we saw a movement from subdiffusive dynamics to superdiffusive, characteristic of breaking events, and caging-like behaviour before the gel fully melts into diffusive vesicles. In both cases within the gel regime we frequently observed a low-q-value plateau of relaxation times which we ascribe to the material acting like an elastic solid at these length scales. The different regimes of dynamics can be well clustered through consideration of the two parameters characterising the intermediate scattering function. The use of spatially resolved DDM gave an insight into the spatial heterogeniety of the dynamics, which we found has a quench rate dependency, as well as corresponding to the coarsening that we observed through the consideration of the static measurements. The observed phenomenology, and its temperature dependence, can be reconciled with the existing work on low-volume fraction attractive colloidal systems, as well as novel behaviour driven by the changes in the mechanics of the vesicles themselves.

In Chapter 6 we introduced a method for high-throughput vesicle production. We characterise the method and the vesicles produced, as well as demonstrating novel applications, most notably the high-throughput production of vesicles encapsulating responsive DNA circuitry, highlighting the potential of this method in bottom-up synthetic biology and the design of programmable materials. Furthermore, we demonstrated the possibility of on-chip functionalisation of constructs into the lipid membranes, in this case cholesterol-anchored DNA constructs. Monodisperse vesicles which can be functionalised and encapsulated on chip represent an important step towards using such vesicles in viable engineering applications, such as as the fundamental building block of responsive materials for molecular diagnostics.

In Chapter 7 we studied dense packings of polydisperse GUVs assembled using multivalent complementary DNA interactions, through passive tracking of diffusive colloidal particles and active microrheology, in this case using magnetic tweezers. We found no-

ticeable changes in the structure in response to increased temperature, DNA concentration and aging leading to reduced pore sizes. From a rheological standpoint, we observed strain hardening of the material through repeated creep tests. Interestingly, despite the particles being non-Brownian, significant stress relaxation is observed through resetting the material by increasing the temperature above the melting point of the system. The material stiffens and becomes more viscous, which we observed through the application of a constitutive and fractional model respectively. When considering the tissue itself, we also see evidence of strain hardening, through reduced deformation with repeated runs. We also extracted a characteristic length scale of deformation, which we observe to broadly decrease with increasing run number. We relate this to our understanding of the physics of the microstructure of the material. This testing allowed for both the characterisation of the material, as well as gaining some insight through this biomimetic tissue into the physical non-active mechanisms underlying the rheology of biological tissues.

8.2 Future Perspectives

8.2.1 Molecular Sensing

As stated in Chapter 1, the motivations for this work lie in the development of novel responsive materials, in particular the development of materials that respond to external stimuli. Such materials have a clear application in molecular sensing. We have shown in Chapter 4 that the morphology and mechanical properties of adhering vesicles can be responsive to the concentration of an external "bridging" ligand. In Chapter 7 we demonstrated that the porosity of a network of lipid vesicles varies in response to morphological changes of the vesicles (in this case due to temperature). We hypothesise that both dense packings of lipid vesicles and indeed vesicles adhering to a supported lipid bilayer (or indeed another substrate) could be used as molecular sensing systems.

By conducting similar studies to those shown in Chapter 4 with other multimeric receptor-ligand complexes, for example with membrane functionalised antibodies or specifically designed aptamers, we could characterise the response to specific antigens/analytes of interest. By scaling up from these individual interactions mediated by the receptor-ligand pairs of interest, we conceptualised two designs of molecular sensing devices, both with the ability to give a simple electronic readout.

In the first device, functionalised GUVs will be loaded into a microfluidic chamber, with integrated electrodes as in Ref. [148]. In the presence of a linker being added/flowed through, the vesicles will adhere and the resultant mesophase coarsen, and form smaller pores. The electrodes will enable read out by impedance or ionic current measurements, which will vary in response to the porosity of the network. The second design, which has been studied in a side project, is the use of surface impedance spectroscopy, in a method analogous to electric cell-substrate impedance spectroscopy [277–279]. In this we simply "count" the number of vesicles adhering to a substrate (in this case a functionalised supported lipid bilayer formed on an electrode) by analysing the surface impedance which corresponds to the coverage of the electrode by adhering vesicles.

Both methods would allow for the customisation of sensor-target device (through choice of functionalisation, vesicle size/stiffness etc.) which makes it suitable also for parallel multiplexing detection of numerous specific targets. The possibility of an electrical readout of the results would make this technology particularly convenient as compared to competing strategies, which rely on complex spectroscopic measurements (e.g. absorbance spectroscopy, spectrofluorimetry, etc) and/or the use of molecular probes (e.g. fluorescent tags). To achieve this engineering application, standardised (monodisperse and similarly functionalised) vesicles such as those created in Chapter 6 would be required.

8.2.2 Biomimetic Tissues

The work shown in Chapter 7 demonstrated the insight that can be gleaned from work with magnetic tweezers, but ongoing development of the experimental set-up limited the ability to complete some of the tests we began. However, the improvements will give more insight into the properties of the material in the future. The recent implementation of the set-up with a light sheet microscope allows for improved sectioning in the z-axis, allowing for 3D reconstruction of the structure and consideration of 3D strain fields. The implementation of a heat bath will give precise control of the temperature simultaneously to the imaging and magnetic tweezer capabilities of the set-up.

A first direction using the water bath would be to study the temperature dependent rheological dependent properties that we observe; from our understanding of the response of vesicle-vesicle adhesion to temperature, whereby we can adjust the stiffness of the particles, we can correlate this knowledge of the microstructure to bulk/local rheological properties. Also of interest would be to study these rheological properties in relationship with the density

of linker; by changing the functionalisation (either the number or type of linker used) of the vesicles, we can adjust the potential contact number and/or the adhesion strength. Additionally, we can use different sized and different composition vesicles to vary the subunit properties. Other tests looking into oscillatory measurements and looking at response to forces of different magnitudes and directions could also be performed. All of these measurements could be directly compared to measurements on biological tissues, in particular the zebrafish embryos that our collaborators have already investigated [255], in order to compare this model tissue free from the active process of the cell (such as the actin cytoskeleton) to a biological tissue to determine the differing contributions of active and physical processes in tissue rheology [50]. Another interesting experiment would be to probe the interactions of a binary mixture of vesicles, where type A can only bind to type A and type B only to type B. Initially the system would be mixed randomly and kinetically arrested in the dense network, but if stimulated by a force, these could be driven to rearrange and undergo demixing due to the self-adhesive nature of type A and type B vesicles, in a manner similar to that achieved in a colloidal system in Ref. [193], This can be of particular interest in biology due to the similarity of cell-sorting; and could yield a demonstration of adhesion driven physical segregation of cells/vesicles as hypothesised by the differential adhesion hypothesis [252].

In regards to the use of bead tracking for pore size, differential dynamic microscopy, as employed in Chapter 5, would give better statistics for characterising the porosity of the material.

8.2.3 DNA-LUV gels

The system introduced in Chapter 5 offers multiple avenues for further exploration. Looking at how the dynamics change in response to changes in the vesicle size, functionalisation density and quench rate and depth would all offer interesting insight into the programmable nature of the materials dynamics, and correspond well with similar studies in hard colloidal systems and some existing work on soft systems. Indeed, applying DNA-mediated strand displacement through a toehold exchange mechanism could marry the responsiveness to an external stimuli and demonstrate how dynamics of such a gel could be programmed outside of the considerations discussed in the earlier [90, 89]. Different temperature ramps, and cycles of heating and cooling around the gel/melting points were also attempted, and further investigation into this is warranted. It would also be interesting to investigate the longer time dynamics. By taking longer videos at a reduced framerate, we could investigate the slow relaxations of the material [114].

8.2.4 Microfluidics

The microfluidic method presented in Chapter 6 presents multiple avenues for future work. Firstly, developing the method for phase separated vesicles on-chip would be exciting, and consideration of the effects of oil on the lipid mixture concentrations required for phase separation in the work on phase transfer methods and varying the choice of lipids may lead to more promising results in this space [235]. Indeed controllable phase separation could lead to the ability to form soft "patchy" particles with controlled valency due to preferential segregation of membrane bound constructs into different phases, which could allow for soft particles with an extra degree of control. The proof-of principle on the generation high-throughput communicating artificial cells encourages further study, and coupling it with the functionalisation of lipid vesicles on-chip would be an exciting avenue for the bottom up high-throughput creation of artificial tissues on-chip, where the constitutive vesicles communicate through signalling mediated by the production of diffusive small molecules.

8.3 Concluding Remarks

This thesis outlines fundamental physical characterisation of systems involving multivalent assembly of lipid vesicles, from single vesicle adhesion studies to self-assembled structures, demonstrating the range of properties such materials can exhibit. In particular, the study of ligand concentration dependent adhesion has obvious ramifications for using such systems in sensing applications, and our subsequent work on mesophases of lipid vesicles shows the tunability of such materials to external stimuli. In particular we demonstrate the sensitivity of the structure, dynamics and rheology to external stimuli such as linker concentration or temperature, showing the programmable nature of such materials. In conjunction with the work developing a microfluidic method for lipid vesicle production, we can envisage engineering applications to create responsive materials with a range of properties suitable for fields such as sensing, nanofiltration and synthetic biology.

References

[1] J. R. McNamara, G. R. Warnick, and G. R. Cooper. A brief history of lipid and lipoprotein measurements and their contribution to clinical chemistry. *Clinica Chemica Acta*, 369:158–67, 2006.

[2] A. Jesorka and O. Orwar. Liposomes: Technologies and Analytical Applications. *Annual Review of Analytical Chemistry*, 1:801–832, 2008.

[3] Y. M. Chan and S. G. Boxer. Model membrane systems and their applications. *Current Opinion in Chemical Biology*, 3:3615–3617, 2007.

[4] J. N. Israelachvili, D. J. Mitchell, and B. W. Ninham. Theory of self-assembly of hydrocarbon amphiphiles into micelles and bilayers. *Journal of the Chemical Society, Faraday Transactions 2: Molecular and Chemical Physics*, 2:1525–1568, 1976.

[5] P. A. Beales and T. K. Vanderlick. Application of nucleic acid–lipid conjugates for the programmable organisation of liposomal modules. *Advances in Colloid Interface Science*, 207(0):290–305, 5 2014.

[6] J. M. Halbleib and W. J. Nelson. Cadherins in development: Cell adhesion, sorting, and tissue morphogenesis. *Genes and Development*, 20:3199–214, 2006.

[7] D. M. Walker, S. Oghumu, G. Gupta, B. S. McGwire, M. E. Drew, and A. R. Satoskar. Mechanisms of cellular invasion by intracellular parasites. *Cellular and Molecular Life Sciences*, 71(7):1245–63, 2014.

[8] J. Yang, M. Li, X. Shen, and S. Liu. Influenza A virus entry inhibitors targeting the hemagglutinin. *Viruses*, 5(1):352–73, 2013.

[9] D. Nykypanchuk, M. M. Maye, D. van der Lelie, and O. Gang. DNA-guided crystallization of colloidal nanoparticles. *Nature*, 451(7178):549–552, 2008.

[10] J. Macfarlane, R, B. Lee, M. R. Jones, N. Harris, George C. Schatz, and C. A. Mirkin. Nanoparticle superlattice engineering with DNA. *Science*, 334(6053):204–208, 2011.

[11] L. Di Michele and E. Eiser. Developments in understanding and controlling self assembly of DNA-functionalized colloids. *Physical Chemistry Chemical physics*, 15(9):3115–29, 2013.

[12] M. Hadorn, E. Boenzli, K. T. Sørensen, H. Fellermann, P. Eggenberger Hotz, and M. M. Hanczyc. Specific and reversible DNA-directed self-assembly of oil-in-water emulsion droplets. *Proceedings of the National Academy of Sciences of the United States of America*, 109(50):20320–20325, 2012.

[13] S. A. J. Van Der Meulen and M. E. Leunissen. Solid colloids with surface-mobile DNA linkers. *Journal of the American Chemical Society*, 135(40):15129–15134, 2013.

[14] M. I. Gurr and J. L. Harwood. *Lipid Biochemistry: An Intoduction*. Chapman & Hall, 4th edition, 1991.

[15] John A. Hunt. A short history of soap. *Pharmaceutical Journal*, 263:985–989, 1999.

[16] J. N. Israelachvili. *Intermolecular and Surface Forces*. Academic Press, 3rd edition, 2011.

[17] S. A. Safran. *Statistical Thermodynamics of Surfaces, Interfaces, and Membranes*. Frontiers in Physics, 1st edition, 1994.

[18] I. R. Cooke and M. Deserno. Coupling between lipid shape and membrane curvature. *Biophysical Journal*, 91:487–495, 2006.

[19] Frederick A. Heberle and Gerald W. Feigenson. Phase separation in lipid membranes. *Cold Spring Harbor Perspectives in Biology*, 3:a004630, 2011.

[20] A. Akbarzadeh, R. Rezaei-Sadabady, S. Davaran, S. W. Joo, N. Zarghami, Y. Hanifehpour, M. Samiei, M. Kouhi, and K. Nejati-Koshki. Liposome: Classification, preparation, and applications. *Nanoscale Research Letters*, 8:102, 2013.

[21] T. Bhatia, P. Husen, J. Brewer, L. A. Bagatolli, P. L. Hansen, J. H. Ipsen, and O. G. Mouritsen. Preparing giant unilamellar vesicles (GUVs) of complex lipid mixtures on demand: Mixing small unilamellar vesicles of compositionally heterogeneous mixtures. *Biochimica et Biophysica Acta - Biomembranes*, 1848:3175–3180, 2015.

[22] K. Langowska, C. G. Palivan, and W. Meier. Polymer nanoreactors shown to produce and release antibiotics locally. *Chemical Communications*, 49:128–30, 2012.

[23] V. Noireaux, Y. T. Maeda, and A Libchaber. Development of an artificial cell, from self-organization to computation and self-reproduction. *Proceedings of the National Academy of Sciences of the United States of America*, 108(9):3473–3480, 2011.

[24] R. J. R. W. Peters, I. Louzao, and J. C. M. van Hest. From polymeric nanoreactors to artificial organelles. *Chemical Science*, 3(2):335–342, 2012.

[25] S. L. Veatch and S. L. Keller. Seeing spots: Complex phase behavior in simple membranes. *Biochimica et Biophysica Acta - Molecular Cell Research*, 1746:172–85, 2005.

[26] K. Simons and W. L.C. Vaz. Model Systems, Lipid Rafts, and Cell Membranes. *Annual Review of Biophysics and Biomolecular Structure*, 33:269–295, 2004.

[27] S. L. Veatch and S. L. Keller. Separation of Liquid Phases in Giant Vesicles of Ternary Mixtures of Phospholipids and Cholesterol. *Biophysical Journal*, 85:3074–3083, 2003.

[28] J. R. Silvius. Partitioning of membrane molecules between raft and non-raft domains: Insights from model-membrane studies. *Biochimica et Biophysica Acta - Molecular Cell Research*, 1746:193–202, 2005.

[29] R. Lipowsky. Coupling of bending and stretching deformations in vesicle membranes. *Advances in Colloid and Interface Science*, 208:14–24, 2014.

[30] W. Rawicz, K. C. Olbrich, T. McIntosh, D. Needham, and E. A. Evans. Effect of chain length and unsaturation on elasticity of lipid bilayers. *Biophysical Journal*, 79:328–339, 2000.

[31] M. Deserno. Fluid lipid membranes – a primer. https://www.cmu.edu/biolphys/deserno/pdf/membrane_theory.pdf, 2007. Accessed: 2019-01-11.

[32] R. Lipowsky and U. Seifert. Adhesion of Vesicles and Membranes. *Molecular Crystals and Liquid Crystals*, 202:17–25, 1991.

[33] U. Seifert and R. Lipowsky. Adhesion of vesicles. *Physical Review A*, 42:4768–4771, 1990.

[34] A. Ramachandran, T. H. Anderson, L. G. Leal, and J. N. Israelachvili. Adhesive interactions between vesicles in the strong adhesion limit. *Langmuir*, 27(1):59–73, 2011.

[35] M. Mammen, S. Chio, and G. M. Whitesides. Polyvalent interactions in biological systems: implications for design and use of multivalent ligands and inhibitors. *Angewandte Chemie*, 37:2754–2794, 1998.

[36] L. Shapiro and W. I. Weis. Structure and biochemistry of cadherins and catenins. *Cold Spring Harbor Perspectives in Biology*, 1(3), 2009.

[37] A.M Krachler and K. Orth. Functional characterization of the interaction between bacterial adhesin multivalent adhesion molecule 7 (MAM7) protein and its host cell ligands. *The Journal of Biological Chemistry*, 286(45):38939–47, November 2011.

[38] O.A. Amjad, B.M. Mognetti, P. Cicuta, and L. Di Michele. Membrane Adhesion through Bridging by Multimeric Ligands. *Langmuir*, 33(5), 2017.

[39] R. S Kane. Thermodynamics of multivalent interactions: Influence of the linker. *Langmuir*, 26:8636–8640, 2010.

[40] H. D. Hill, R. J. Macfarlane, A. J. Senesi, B. Lee, S. Y. Park, and C. A. Mirkin. Controlling the lattice parameters of gold nanoparticle FCC crystals with duplex DNA linkers. *Nano Letters*, 8(8):2341–2344, 2008.

[41] S. Y. Park, A. K. R. Lytton-Jean, B. Lee, S. Weigand, G. C. Schatz, and C. A. Mirkin. DNA-programmable nanoparticle crystallization. *Nature*, 451(7178):553–556, 2008.

[42] C. A. Mirkin, R. L. Letsinger, R. C. Mucic, and J. J. Storhoff. A DNA-based method for rationally assembling nanoparticles into macroscopic materials. *Nature*, 382(6592):607–609, 1996.

[43] A. P. Alivisatos, K. P. Johnsson, X. Peng, T. E. Wilson, C. J. Loweth, M. P. Bruchez, and P. G. Schultz. Organization of 'nanocrystal molecules' using DNA. *Nature*, 382(6592):609–611, 1996.

[44] C. S. Thaxton, R. Elghanian, A. D. Thomas, S. I. Stoeva, J. Lee, N. D. Smith, A. J. Schaeffer, H. Klocker, W. Horninger, G. Bartsch, and C. A. Mirkin. Nanoparticle-based bio-barcode assay redefines "undetectable" PSA and biochemical recurrence after radical prostatectomy. *Proceedings of the National Academy of Sciences of the United States of America*, 106(44):18437–18442, 2009.

[45] K. L. Young, M. B. Ross, M. G. Blaber, M. Rycenga, M. R. Jones, Chuan Zhang, A. J. Senesi, B. Lee, G. C. Schatz, and Chad A. Mirkin. Using DNA to design plasmonic metamaterials with tunable optical properties. *Advanced Materials*, 26(4):653–659, 2014.

[46] M. E. Leunissen, R. Dreyfus, R. Sha, Tong Wang, N. C. Seeman, D. J. Pine, and P. M. Chaikin. Towards self-replicating materials of DNA-functionalized colloids. *Soft Matter*, 5(12):2422, 2009.

[47] M. M. Maye, M. T. Kumara, D. Nykypanchuk, W. B. Sherman, and O. Gang. Switching binary states of Nanoparticle superlattices and dimer clusters by DNA strands. *Nature Nano.*, 5(2):116–120, 2010.

[48] C. K. Tison and V. T Milam. Reversing DNA-mediated adhesion at a fixed temperature. *Langmuir*, 23(19):9728–9736, 2007.

[49] W. B. Rogers and V. N Manoharan. Programming colloidal phase transitions with DNA strand displacement. *Science*, 347(6222):639–642, 2015.

[50] L.-L. Pontani, I. Jorjadze, V. Viasnoff, and J. Brujic. Biomimetic emulsions reveal the effect of mechanical forces on cell-cell adhesion. *Proceedings of the National Academy of Sciences*, 109(25):9839–9844, 2012.

[51] S. F. Shimobayashi, B. M. Mognetti, L. Parolini, D. Orsi, P. Cicuta, and L. Di Michele. Direct measurement of DNA-mediated adhesion between lipid bilayers. *Physical Chemistry Chemical Physics*, 17(24):15615–15628, 2015.

[52] L. Parolini, B. M. Mognetti, E. Kotar, J.and Eiser, P. Cicuta, and L. Di Michele. Volume and porosity thermal regulation in lipid mesophases by coupling mobile ligands to soft membranes. *Nature Communications*, 6:5948, 2015.

[53] L. Parolini, J. Kotar, L. Di Michele, and B. M. Mognetti. Controlling self-assembly kinetics of DNA-functionalized liposomes using toehold exchange mechanism. *ACS Nano*, 10(2):2392–2398, 2016.

[54] P. A. Beales and T. K. Vanderlick. Application of nucleic acid–lipid conjugates for the programmable organisation of liposomal modules. *Advances in Colloid and Interface Science*, 207:290 – 305, 2014.

[55] P. A. Beales, J. Nam, and T. K. Vanderlick. Specific adhesion between DNA-functionalized "Janus" vesicles: size-limited clusters. *Soft Matter*, 7(5):1747–1755, 2011.

[56] P. A. Beales and T. K. Vanderlick. Specific binding of different vesicle populations by the hybridization of membrane-anchored DNA. *Journal of Physical Chemistry A*, 111(49):12372–12380, 2007.

[57] M. Hadorn, E. Boenzli, K. T. S, D. De Lucrezia, M. M. Hanczyc, and T. Yomo. Defined DNA-mediated assemblies of gene-expressing giant unilamellar vesicles. *Langmuir*, 29(49):15309–15319, 2013.

[58] M. Hadorn and P. Eggenberger Hotz. DNA-Mediated Self-Assembly of Artificial Vesicles. *PLoS ONE*, 5:1–9, 2010.

[59] J. Y. Wong and T. L. Kuhl. Dynamics of membrane adhesion: The role of polyethylene glycol spacers, ligand-receptor bond strength, and rupture pathway. *Langmuir*, 24:1225–1231, 2008.

[60] F. J. Martinez-Veracoechea and M. E. Leunissen. The entropic impact of tethering, multivalency and dynamic recruitment in systems with specific binding groups. *Soft Matter*, 9:3213–3219, 2013.

[61] J. M. Warner, E. Karatekin, and B. O'Shaughnessy. Model of SNARE-Mediated Membrane Adhesion Kinetics. *PLoS ONE*, 4(8):e6375, 2009.

[62] P. G. de Gennes, P. H. Puech, and F. Brochard-Wyart. Adhesion induced by Mobile Stickers: A list of Scenarios. *Langmuir*, 19(17):7112–7119, 2003.

[63] T. R. Weikl and R. Lipowsky. Membrane adhesion and domain formation. *Advances in planar lipid bilayers and liposomes*, 5:63–127, 2007.

[64] T. R. Weikl, M. Asfaw, H. Krobath, B. Rózycki, and R. Lipowsky. Adhesion of membranes via receptor-ligand complexes: Domain formation, binding cooperativity, and active processes. *Soft Matter*, 5:3213–3224, 2009.

[65] S. F. Fenz and K. Sengupta. Giant vesicles as cell models. *Integrative Biology*, 4(9):982–995, 2012.

[66] P. Ratanabanangkoon, M. Gropper, R. Merkel, E. Sackmann, and A. P. Gast. Mechanics of streptavidin-coated giant lipid bilayer vesicles: A micropipet study. *Langmuir*, 19(4):1054–1062, 2003.

[67] E. A. Bayer and M. Wilchek. Avidin- and streptavidin-containing probes. *Methods in Enzymology*, 184:174–187, 1990.

[68] D. A. Noppl-Simson and D. Needham. Avidin-Biotin Interactions at Vesicle Surfaces: Adsorption and Binding, Cross-Bridge Formation, and Lateral Interactions. *Biophysical Journal*, 70:1391–1401, 1996.

[69] S. Chiruvolu, S. Walker, J. Israelachvili, F. J. Schmitt, D. Leckband, and J. A. Zasadzinski. Higher order self-assembly of vesicles by site-specific binding. *Science*, 264(5166):1753–1756, 1994.

[70] C. Boyer and J. A. Zasadzinski. Multiple lipid compartments slow vesicle contents release in lipases and serum. *ACS Nano*, 1:176–182, 2007.

[71] T. Bihr, S. Fenz, E. Sackmann, R. Merkel, U. Seifert, K. Sengupta, and A. C. Smith. Association Rates of Membrane-Coupled Cell Adhesion Molecules. *Biophysical Journal*, 107:L33–L36, 2014.

[72] S. F. Fenz, R. Merkel, and K. Sengupta. Diffusion and Intermembrane Distance: Case Study of Avidin and E-Cadherin Mediated Adhesion. *Langmuir*, 25(2):1074–1085, 2009.

[73] S. F. Fenz, A. C. Smith, R. Merkel, and K. Sengupta. Inter-membrane adhesion mediated by mobile linkers: Effect of receptor shortage. 7:952–962, 2011.

[74] A Albersdorfer, T Feder, and E Sackmann. Adhesion-induced Domain Formation by Interplay of Long-Range Repulsion and Short-Range Attraction Force: A Model Membrane Study. *Biophysical Journal*, 73:245–257, 1997.

[75] J. Nam and M. M. Santore. The Adhesion Kinetics of Sticky Vesicles in Tension: The Distinction between Spreading and Receptor Binding. *Langmuir*, 23:10650–10660, 2007.

[76] J. D. Watson and F. H. C. Crick. A Structure for Deoxyribose Nucleic Acid. *Nature*, 171(4356):737–738, 1953.

[77] J. D. Watson and F. H.C. Crick. Genetical implications of the structure of deoxyribonucleic acid. *Nature*, 171:964–967, 1953.

[78] J. Mergny and L. Lacroix. Analysis of Thermal Melting Curves. *Oligonucleotides*, 13:515–537, 2004.

[79] J. SantaLucia. A unified view of polymer, dumbbell, and oligonucleotide DNA nearest-neighbor thermodynamics. *Proceedings of the National Academy of Sciences of the United States of America*, 95:1460–1465, 1998.

[80] R. Owczarzy, P. M. Vallone, F. J. Gallo, T. M. Paner, M. J. Lane, and A. S. Benight. Predicting Sequence-Dependent Melting Stability of Short Duplex DNA Oligomers. *Biopolymers*, 44:217–239, 1998.

[81] B. M. Mognetti, M. E. Leunissen, and D. Frenkel. Controlling the temperature sensitivity of DNA-mediated colloidal interactions through competing linkages. *Soft Matter*, 8:2213–2221, 2012.

[82] B. Tinland, A. Pluem, J. Sturm, and G. Weill. Influenza A virus entry inhibitors targeting the hemagglutinin. *Macromolecules*, 30:5763–5765, 1997.

[83] I. Pfeiffer and F. Höök. Bivalent cholesterol-based coupling of oligonucletides to lipid membrane assemblies. *Journal of the American Chemical Society*, 126(33):10224–10225, 08 2004.

[84] P. A. Beales and T. K. Vanderlick. Specific binding of different vesicle populations by the hybridization of membrane-anchored DNA. *Journal of Physical Chemistry A*, 111(49):12372–12380, 2007.

[85] L. Feng, L. L. Pontani, R. Dreyfus, P. Chaikin, and J. Brujic. Specificity, flexibility and valence of DNA bonds guide emulsion architecture. *Soft Matter*, 9:9816–9823, 2013.

[86] S. J. Bachmann, J. Kotar, L. Parolini, A. Šarić, P. Cicuta, L. Di Michele, and B. M. Mognetti. Melting transition in lipid vesicles functionalised by mobile DNA linkers. *Soft Matter*, 12:7804–7817, 2016.

[87] P. A. Beales, J. Nam, and T. K. Vanderlick. Specific adhesion between DNA-functionalized "Janus" vesicles: size-limited clusters. *Soft Matter*, 7(5):1747–1755, 2011.

[88] M. Chung, B. J. Koo, and S. G. Boxer. Formation and analysis of topographical domains between lipid membranes tethered by DNA hybrids of different lengths. *Faraday Discussions*, 161:333–345, 2012.

[89] L. Parolini, J. Kotar, L. Di Michele, and B. M. Mognetti. Controlling Self-Assembly Kinetics of DNA-Functionalized Liposomes Using Toehold Exchange Mechanism. *ACS Nano*, 10(2):2392–2398, 02 2016.

[90] D. Y. Zhang and E. Winfree. Control of DNA strand displacement kinetics using toehold exchange. *Journal of the American Chemical Society*, 131:17303–17314, 2009.

[91] M. M. Maye, M. T. Kumara, D. Nykypanchuk, W. B. Sherman, and O. Gang. Switching binary states of nanoparticle superlattices and dimer clusters by DNA strands. *Nature Nanotechnology*, 5(2):116–120, 2010.

[92] C. K. Tison and V. T. Milam. Reversing DNA-mediated adhesion at a fixed temperature. *Langmuir*, 23:9728–9736, 2007.

[93] Y. M. Chan, B. van Lengerich, and S. G. Boxer. Lipid-anchored DNA mediates vesicle fusion as observed by lipid and content mixing. *Biointerphases*, 3:17–21, 2008.

[94] Y.-H. M. Chan, B. van Lengerich, and S. G. Boxer. Effects of linker sequences on vesicle fusion mediated by lipid-anchored DNA oligonucleotides. *Proceedings of the National Academy of Sciences*, 106:979–984, 2009.

[95] J. Yang, Z. Meng, Q. Liu, Y. Shimada, R.C.L. Olsthoorn, H. P. Spaink, A. Herrmann, and A. Kros. Performing DNA nanotechnology operations on a zebrafish. *Chemical Science*, 9:7271–7276, 2018.

[96] V. D. Gordon, T. J. O'Halloran, and O. Shindell. Membrane adhesion and the formation of heterogeneities: biology, biophysics, and biotechnology. *Physical Chemistry Chemical Physics*, 17:15522–15533, 2015.

[97] G. Bendas, J. Vogel, U. Bakowski, A. Krause, J. Müller, and U. Rothe. A liposome-based model system for the simulation of lectin-induced cell adhesion. *Biochimica et Biophysica Acta - Biomembranes*, 1325:297–308, 1997.

[98] E. Reister-Gottfried, K. Sengupta, B. Lorz, E. Sackmann, U. Seifert, and A. S Smith. Dynamics of specific vesicle-substrate adhesion: From local events to global dynamics. *Physical Review Letters*, 101:208103, 2008.

[99] Z. Guttenberg, B. Lorz, E. Sackmann, and A. Boulbitch. First-order transition between adhesion states in a system mimicking cell-tissue interaction. *Europhysics Letters*, 54:826–832, 2001.

[100] A.-S. Smith, K. Sengupta, S. Goennenwein, U. Seifert, and E. Sackmann. Force-induced growth of adhesion domains is controlled by receptor mobility. *Proceedings of the National Academy of Sciences*, 105:6906–6911, 2008.

[101] S. Villringer, J. Madl, T. Sych, C. Manner, A. Imberty, and W. Römer. Lectin-mediated protocell crosslinking to mimic cell-cell junctions and adhesion. *Scientific Reports*, 8:1932, 2018.

[102] R. J. Mart, K. P. Liem, X. Wang, and S. J. Webb. The effect of receptor clustering on vesicle-vesicle adhesion. *Journal of the American Chemical Society*, 128:14462–14463, 2006.

[103] S. J. Webb, L. Trembleau, R. J. Mart, and X. Wang. Membrane composition determines the fate of aggregated vesicles. *Organic and Biomolecular Chemistry*, 3:3615–3617, 2005.

[104] M. Ma, Y. Gong, and D. Bong. Lipid membrane adhesion and fusion driven by designed, minimally multivalent hydrogen-bonding lipids. *Journal of the American Chemical Society*, 131:16919–16926, 2009.

[105] V. Marchi-Artzner, T. Gulik-Krzywicki, M. A. Guedeau-Boudeville, C. Gosse, J. M. Sanderson, J. C. Dedieu, and J. M. Lehn. Selective adhesion, lipid exchange and membrane-fusion processes between vesicles of various sizes bearing complementary molecular recognition groups. *ChemPhysChem*, 2:367–376, 2001.

[106] W. Alshaer, H. Hillaireau, and E. Fattal. Aptamer-guided nanomedicines for anticancer drug delivery. *Advanced Drug Delivery Reviews*, 134:122–137, 2018.

[107] G.N.C. Chiu, M. B. Bally, and L. D. Mayer. Targeting of antibody conjugated, phosphatidylserine-containing liposomes to vascular cell adhesion molecule 1 for controlled thrombogenesis. *Biochimica et Biophysica Acta - Biomembranes*, 1613:115–121, 2003.

[108] Y. M. Joshi. Dynamics of Colloidal Glasses and Gels. *Annual Review of Chemical and Biomolecular Engineering*, 5:181–202, 2014.

[109] E. Zaccarelli. Colloidal gels: Equilibrium and non-equilibrium routes. *Journal of Physics Condensed Matter*, 19:323101, 2007.

[110] Francesco Sciortino. Disorderd materials: One liquid, two glasses. *Nature Materials*, 1:145–146, 2002.

[111] P. J. Lu and D. A. Weitz. Colloidal Particles: Crystals, Glasses, and Gels. *Annual Review of Condensed Matter Physics*, 4:217–233, 2013.

[112] L. Cipelletti and L. Ramos. Slow dynamics in glassy soft matter. *Journal of Physics Condensed Matter*, 17:R253–R285, 2005.

[113] W. van Megen, T. C. Mortensen, S. R. Williams, and J. Müller. Measurement of the self-intermediate scattering function of suspensions of hard spherical particles near the glass transition. *Physical Review E*, 58:6073–6085, 1998.

[114] Y. Gao, J. Kim, and M. E. Helgeson. Microdynamics and arrest of coarsening during spinodal decomposition in thermoreversible colloidal gels. *Soft Matter*, 11:6345–6528, 2015.

[115] S. Mazoyer, L. Cipelletti, and L. Ramos. Origin of the slow dynamics and the aging of a soft glass. *Physical Review Letters*, 97:238301, 2006.

[116] L. Cipelletti, L. Ramos, S. Manley, E. Pitard, D. A. Weitz, E. E. Pashkovski, and M. Johansson. Universal non-diffusive slow dynamics in aging soft matter. *Faraday Discussions*, 123:237–251, 2003.

[117] J. P. Bouchaud and E. Pitard. Anomalous dynamical light scattering in soft glassy gels. *European Physical Journal E*, 6:231–236, 2002.

[118] J. P. Bouchaud. Anomalous Relaxation in Complex Systems: From Stretched to Compressed Exponentials. In *Anomalous Transport: Foundations and Applications*. Wiley, 2008.

[119] A. H. Krall and D. A. Weitz. Internal dynamics and elasticity of fractal colloidal gels. *Physical Review Letters*, 80:778–781, 1998.

[120] B. Abou, D. Bonn, and J. Meunier. Aging dynamics in a colloidal glass. *Physical Review E*, 64:021510, 2001.

[121] M. Bellour, A. Knaebel, J. L. Harden, F. Lequeux, and J. P. Munch. Aging processes and scale dependence in soft glassy colloidal suspensions. *Physical Review E*, 67:031405, 2003.

[122] M. J. Solomon and P. Varadan. Dynamic structure of thermoreversible colloidal gels of adhesive spheres. *Physical Review E*, 63:051402, 2001.

[123] N. B. Simeonova and W. K. Kegel. Gravity-induced aging in glasses of colloidal hard spheres. *Physical Review Letters*, 93:035701, 2004.

[124] L. Cipelletti, S. Manley, R. C. Ball, and D. A. Weitz. Universal aging features in the restructuring of fractal colloidal gels. *Physical Review Letters*, 84:2275–2278, 2000.

[125] L. Ramos and L. Cipelletti. Ultraslow dynamics and stress relaxation in the aging of a soft glassy system. *Physical Review Letters*, 87:245503, 2001.

[126] A. Duri and L. Cipelletti. Length scale dependence of dynamical heterogeneity in a colloidal fractal gel. *Europhysics Letters*, 76:972–978, 2006.

[127] M. Bouzid, J. Colombo, L. V. Barbosa, and E. Del Gado. Elastically driven intermittent microscopic dynamics in soft solids. *Nature Communications*, 8:15846, 2017.

[128] G. Petekidis, A. Moussaïd, and P. N. Pusey. Rearrangements in hard-sphere glasses under oscillatory shear strain. *Physical Review E*, 66:051402, 2002.

[129] F. Ozon, T. Narita, A. Knaebel, G. Debrégeas, P. Hébraud, and J. P. Munch. Partial rejuvenation of a colloidal glass. *Physical Review E*, 68:032401, 2003.

[130] D. Bonn, S. Tanase, B. Abou, H. Tanaka, and J. Meunier. Laponite: Aging and shear rejuvenation of a colloidal glass. *Physical Review Letters*, 79:011501, 2002.

[131] S. Mazoyer, L. Cipelletti, and L. Ramos. Direct-space investigation of the ultraslow ballistic dynamics of a soft glass. *Physical Review E*, 79:011501, 2009.

[132] P. Kollmannsberger and B. Fabry. Linear and Nonlinear Rheology of Living Cells. *Annual Review of Materials Research*, 41:75–97, 2011.

[133] A. Jaishankar and G. H. McKinley. Power-law rheology in the bulk and at the interface: Quasi-properties and fractional constitutive equations. *Proceedings of the Royal Society A: Mathematical, Physical and Engineering Sciences*, 469:20120284, 2013.

[134] N. Demirci and E. Tönük. Non-integer viscoelastic constitutive law to model soft biological tissues to in-vivo indentation. *Acta of Bioengineering and Biomechanics*, 16:13–21, 2014.

[135] M. L Gardel, M. T Valentine, and D. A Weitz. *Microrheology*. Springer-Verlag, 2005.

[136] F. Radjai, M. Jean, J. J. Moreau, and S. Roux. Force Distributions in Dense Two-Dimensional Granular Systems. *Physical Review Letters*, 77:274–277, 1996.

[137] D. T. N. Chen, Q. Wen, P. A. Janmey, J. C. Crocker, and A. G. Yodh. Rheology of soft materials. *Annual Review of Condensed Matter Physics*, 1(1):301–322, 2010.

[138] C. H. Liu, S. R. Nagel, D. A. Schecter, S. N. Coppersmith, S. Majumdar, O. Narayan, and T. A. Witten. Force fluctuations in bead packs. *Science*, 269:513–515, 1995.

[139] D. T. Chiu, A. J. DeMello, D. Di Carlo, P. S. Doyle, C. Hansen, R. M. Maceiczyk, and R. C.R. Wootton. Small but Perfectly Formed? Successes, Challenges, and Opportunities for Microfluidics in the Chemical and Biological Sciences. *Chem*, 2, 2017.

[140] E. K. Sackmann, A. L. Fulton, and D. J. Beebe. The present and future role of microfluidics in biomedical research. *Nature*, 133:2798–2800, 2014.

[141] A. B. Theberge, F. Courtois, Y. Schaerli, M. Fischlechner, C. Abell, F. Hollfelder, and W.T.S. Huck. Microdroplets in microfluidics: An evolving platform for discoveries in chemistry and biology. *Angewandte Chemie - International Edition*, 49:5846–5868, 2011.

[142] S. Y. Teh, R. Khnouf, H. Fan, and A. P. Lee. Stable, biocompatible lipid vesicle generation by solvent extraction-based droplet microfluidics. *Biomicrofluidics*, 5:044113, 2011.

[143] K. Karamdad, R. V. Law, J. M. Seddon, N. J. Brooks, and O. Ces. Preparation and mechanical characterisation of giant unilamellar vesicles by a microfluidic method. *Lap Chip*, 15:557–562, 2015.

[144] S. Deshpande, Y. Caspi, A. E. C. Meijering, and C. Dekker. Octanol-assisted liposome assembly on chip. *Nature Communications*, 7:10447, 2016.

[145] X. Niu, S. Gulati, J. B. Edel, and A. J. Demello. Pillar-induced droplet merging in microfluidic circuits. *Lab on a Chip*, 8:1837–1841, 2008.

[146] X. Z. Niu, B. Zhang, R. T. Marszalek, O. Ces, J. B. Edel, D. R. Klug, and A. J. Demello. Droplet-based compartmentalization of chemically separated components in two-dimensional separations. *Chemical Communications*, pages 6159–6161, 2009.

[147] H. Song, M. R. Bringer, J. D. Tice, C. J. Gerdts, and R. F. Ismagilov. Experimental test of scaling of mixing by chaotic advection in droplets moving through microfluidic channels. *Applied Physics Letters*, 83:4664–4666, 2003.

[148] T. W. Herling, T. Müller, L. Rajah, J. N. Skepper, M. Vendruscolo, and T. P. J. Knowles. Integration and characterization of solid wall electrodes in microfluidic devices fabricated in a single photolithography step. *Applied Physics Letters*, 102(18):184102, 2013.

[149] H. C Shum, D. Lee, I. Yoon, T. Kodger, and D. A. Weitz. Double emulsion templated monodisperse phospholipid vesicles. *Langmuir*, 24:7651–7653, 2008.

[150] Y. Park, D. Lee, E. Um, and J. Park. On-chip generation of monodisperse giant unilamellar lipid vesicles containing quantum dots. *ELECTROPHORESIS*, 37(10):1353–1358, 2016.

[151] D. van Swaay and A. DeMello. Microfluidic methods for forming liposomes. *Lab on a chip*, 13(5):752–67, 2013.

[152] A. Vian, V. Favrod, and E. Amstad. Reducing the shell thickness of double emulsions using microfluidics. *Microfluidics and Nanofluidics*, 20:159, 2016.

[153] D. Vallejo, S. Lee, and A. Lee. *Functionalized Vesicles by Microfluidic Device*, pages 489–510. Springer New York, New York, NY, 2017.

[154] N. Deng, M. Yelleswarapu, and W. T.S. Huck. Monodisperse Uni- and Multicompartment Liposomes. *Journal of the American Chemical Society*, 138:7584–7591, 2016.

[155] S. Deshpande, A. Birnie, and C. Dekker. On-chip density-based purification of liposomes. *Biomicrofluidics*, 11:034106, 2017.

[156] J. C. Stachowiak, D. L. Richmond, T. H. Li, A. P. Liu, S. H. Parekh, and D. A. Fletcher. Unilamellar vesicle formation and encapsulation by microfluidic jetting. *Proceedings of the National Academy of Sciences of the United States of America*, 105:4697–4702, 2008.

[157] Y. Elani. Construction of membrane-bound artificial cells using microfluidics: a new frontier in bottom-up synthetic biology. *Biochemical Society Transactions*, 44:723–730, 2016.

[158] Manouk Abkarian, Etienne Loiseau, and Gladys Massiera. Continuous droplet interface crossing encapsulation (cDICE) for high throughput monodisperse vesicle design. *Soft Matter*, 7:4610–4614, 2011.

[159] S. Matosevic and B. M. Paegel. Stepwise synthesis of giant unilamellar vesicles on a microfluidic assembly line. *Journal of the American Chemical Society*, 133:2798–2800, 2011.

[160] S. Matosevic and B. M. Paegel. Layer-by-layer cell membrane assembly. *Nature Chemistry*, 5:958–963, 2013.

[161] Y. C. Tan, K. Hettiarachchi, M. Siu, Y. R. Pan, and A. P. Lee. Controlled microfluidic encapsulation of cells, proteins, and microbeads in lipid vesicles. *Journal of the American Chemical Society*, 128:5656–5658, 2006.

[162] C. W. Coyne, K. Patel, J. Heureaux, J. Stachowiak, D. A. Fletcher, and A. P. Liu. Lipid bilayer vesicle generation using microfluidic jetting. *Journal of visualized experiments : JoVE*, (84):e51510, 2014.

[163] A. Jahn, W. N. Vreeland, M. Gaitan, and L. E. Locascio. Controlled Vesicle Self-Assembly in Microfluidic Channels with Hydrodynamic Focusing. *Journal of the American Chemical Society*, 126:2674–2675, 2004.

[164] M. I. Angelova and D. S. Dimitrov. Liposome electroformation. *Faraday Discuss. Chem. Soc.*, 81:303–311, 1986.

[165] H. Kaiser, D. Lingwood, I. Levental, J. L. Sampaio, L. Kalvodova, L. Rajendran, and K. Simons. Order of lipid phases in model and plasma membranes. *Proceedings of the National Academy of Sciences*, 106(39):16645–16650, 2009.

[166] A. Varnier, F. Kermarrec, I. Blesneac, C. Moreau, L. Liguori, J. L. Lenormand, and N. Picollet-D'hahan. A simple method for the reconstitution of membrane proteins into giant unilamellar vesicles. *Journal of Membrane Biology*, 233(1):85–92, 2010.

[167] T. Pott, H. Bouvrais, and P. Méléard. Giant unilamellar vesicle formation under physiologically relevant conditions. *Chemistry and Physics of Lipids*, 154(2):115 – 119, 2008.

[168] C. Herold, G. Chwastek, P. Schwille, and E. P. Petrov. Efficient electroformation of supergiant unilamellar vesicles containing cationic lipids on ito-coated electrodes. *Langmuir*, 28(13):5518–5521, 2012.

[169] P. Taylor, C. Xu, P. D. I. Fletcher, and V. N. Paunov. Fabrication of 2D arrays of giant liposomes on solid substrates by microcontact printing. *Physical Chemistry Chemical Physics*, 5:4918–4922, 2003.

[170] F. Olson, C. A. Hunt, F. C. Szoka, W. J. Vail, and D. Papahadjopoulos. Preparation of liposomes of defined size distribution by extrusion through polycarbonate membranes. *Biochimica et Biophysica Acta - Biomembranes*, 557(1):9 – 23, 1979.

[171] B. A. Korgel, J. H. van Zanten, and H. G. Monbouquette. Vesicle size distributions measured by flow field-flow fractionation coupled with multiangle light scattering. *Biophysical Journal*, 74(6):3264 – 3272, 1998.

[172] T. Kaasgaard, O. G. Mouritsen, and K. Jørgensen. Freeze/thaw effects on lipid-bilayer vesicles investigated by differential scanning calorimetry. *Biochimica et Biophysica Acta - Biomembranes*, 1615(1):77 – 83, 2003.

[173] R. Cerbino and V. Trappe. Differential dynamic microscopy: Probing wave vector dependent dynamics with a microscope. *Physical Review Letters*, 100:188102, May 2008.

[174] F. Ferri, A. D'Angelo, M. Lee, A. Lotti, M. C. Pigazzini, K. Singh, and R. Cerbino. Kinetics of colloidal fractal aggregation by differential dynamic microscopy. *The European Physical Journal Special Topics*, 199(1):139–148, 2011.

[175] F. Giavazzi, D. Brogioli, V. Trappe, T. Bellini, and R. Cerbino. Scattering information obtained by optical microscopy: Differential dynamic microscopy and beyond. *Physical Review E*, 80:031403, 2009.

[176] R. Cerbino and P. Cicuta. Perspective: Differential dynamic microscopy extracts multi-scale activity in complex fluids and biological systems. *The Journal of Chemical Physics*, 147(11):110901, 2017.

[177] J. D. C. Jacob, K. He, S. T. Retterer, R. Krishnamoorti, and J. C. Conrad. Diffusive dynamics of nanoparticles in ultra-confined media. *Soft Matter*, 11:7515–7524, 2015.

[178] I. Hanasaki and Y. Ooi. Particle image diffusometry: Resolving diffusion coefficient field from microscopy movie data without particle tracking. *AIP Advances*, 8(6):065014, 2018.

[179] P. Edera, D. Bergamini, V. Trappe, F. Giavazzi, and R. Cerbino. Differential dynamic microscopy microrheology of soft materials: A tracking-free determination of the frequency-dependent loss and storage moduli. *Physical Review Materials*, 1:073804, 2017.

[180] Y. Gao, J. Kim, and M. E. Helgeson. Microdynamics and arrest of coarsening during spinodal decomposition in thermoreversible colloidal gels. *Soft Matter*, 11:6360–6370, 2015.

[181] L. G. Wilson, V. A. Martinez, J. Schwarz-Linek, J. Tailleur, G. Bryant, P. N. Pusey, and W. C. K. Poon. Differential dynamic microscopy of bacterial motility. *Physical Review Letters*, 106:018101, 2011.

[182] M. Drechsler, F. A Giavazzi, R. Cerbino, and I. M Palacios. Active diffusion and advection in drosophila oocytes result from the interplay of actin and microtubules. *Nature Communications*, 8:1520, 2017.

[183] M. Chioccioli, L. Feriani, J. Kotar, P. E. Bratcher, and P. Cicuta. Phenotyping ciliary dynamics and coordination in response to cftr-modulators in cystic fibrosis respiratory epithelial cells. *Nature Communications*, 10:1763, 2019.

[184] L. Feriani, M. Juenet, C. J. Fowler, N. Bruot, M. Chioccioli, S. M. Holland, C. E. Bryant, and P. Cicuta. Assessing the Collective Dynamics of Motile Cilia in Cultures of Human Airway Cells by Multiscale DDM. *Biophysical Journal*, 113:109–119, 2017.

[185] H. P. Duwe, J Kaes, and E. Sackmann. Bending elastic moduli of lipid bilayers : modulation by solutes. *Journal de Physique*, 51:945–961, 1990.

[186] W. Helfrich and R. M. Servuss. Undulations, steric interaction and cohesion of fluid membranes. *Il Nuovo Cimento D*, 3(1):137–151, 1984.

[187] B. C. Borro, L. Parolini, P. Cicuta, V. Foderà, and L. Di Michele. Interaction with prefibrillar species and amyloid-like fibrils changes the stiffness of lipid bilayers. *Physical Chemistry Chemical Physics*, 19:27930–27934, 2017.

[188] C. Esposito, A. Tian, S. Melamed, C. Johnson, and T. Tee, S. Baumgart. Flicker spectroscopy of thermal lipid bilayer domain boundary fluctuations. *Biophysical Journal*, 93:3169–3181., 2007.

[189] Y. Z. Yoon, H. Hong, A. Brown, C. K. Dong, J. K. Dae, V. L. Lew, and P. Cicuta. Flickering analysis of erythrocyte mechanical properties: Dependence on oxygenation level, cell shape, and hydration level. *Biophysical Journal*, 97(6):1606–1615, 2009.

[190] J. Pécréaux, H. G. Döbereiner, J. Prost, J. F. Joanny, and P. Bassereau. Refined contour analysis of giant unilamellar vesicles. *European Physical Journal E*, 13(3):277–290, 2004.

[191] J. N. Zadeh, C. Steenberg, J. S. Bois, B. R. Wolfe, M. B. Pierce, A. R. Khan, R. M. Dirks, and N. A. Pierce. *Journal of Computational Chemistry*, 32:170–173, 2011.

[192] L Di Michele, S. J. Bachmann, L Parolini, and B. M. Mognetti. Free energy of lingand-receptor systems forming multimeric complexes. *Journal of Chemical Physics*, 144:161104, 2016.

[193] L. Di Michele, F. Varrato, J. Kotar, S. H. Nathan, G. Foffi, and E. Eiser. Multistep kinetic self-assembly of DNA-coated colloids. *Nature Communications*, 4(May):1–7, 2013.

[194] B. Schmid, J. Schindelin, A. Cardona, M. Longair, and M. Heisenberg. A high-level 3D visualization API for Java and ImageJ. *BMC Bioinformatics*, 11:274, 2010.

[195] M. A. Koussa, K. Halvorsen, A. Ward, and W. P Wong. DNA nanoswitches: a quantitative platform for gel-based biomolecular interaction analysis. *Nature Methods*, 12(2):123–126, 02 2015.

[196] A. Pommella, N. J. Brooks, J. M. Seddon, and V. Garbin. Selective flow-induced vesicle rupture to sort by membrane mechanical properties. *Scientific Reports*, 5:13163, 2015.

[197] H. Zhou, B. Burrola Gabilondo, W. Losert, and W. Van De Water. Stretching and relaxation of vesicles. *Physical Review E*, 83:011905, 2011.

[198] L. Ramos and L. Cipelletti. Intrinsic aging and effective viscosity in the slow dynamics of a soft glass with tunable elasticity. *Physical Review Letters*, 94:158301, 2005.

[199] A. M. Philippe, D. Truzzolillo, J. Galvan-Myoshi, P. Dieudonné-George, V. Trappe, L. Berthier, and L. Cipelletti. Glass transition of soft colloids. *Physical Review E*, 97:040601, 2018.

[200] M. Gradzielski. Vesicles and vesicle gels - Structure and dynamics of formation. *Journal of Physics Condensed Matter*, 16:R655–R697, 2003.

[201] F. Ferri, A. D'Angelo, M. Lee, A. Lotti, M. C. Pigazzini, K. Singh, and R. Cerbino. Kinetics of colloidal fractal aggregation by differential dynamic microscopy. *European Physical Journal: Special Topics*, 2011.

[202] M. Zupkauskas, Y. Lan, D. Joshi, Z. Ruff, and E. Eiser. Optically transparent dense colloidal gels. *Chemical Science*, 8:5559–5566, 2017.

[203] K He, M. Spannuth, J. C. Conrad, and R. Krishnamoorti. Diffusive dynamics of nanoparticles in aqueous dispersions. *Soft Matter*, 8(47):11933–11938, 2012.

[204] M. S. Safari, R. Poling-Skutvik, P. G. Vekilov, and J. C. Conrad. Differential dynamic microscopy of bidisperse colloidal suspensions. *npj Microgravity*, 3, 2017.

[205] B. J. Frisken. Revisiting the method of cumulants for the analysis of dynamic light-scattering data. *Applied Optics*, 40(24):4087, 2007.

[206] M. S. Safari, M. A. Vorontsova, R. Poling-Skutvik, P. G. Vekilov, and J. C. Conrad. Differential dynamic microscopy of weakly scattering and polydisperse protein-rich clusters. *Physical Review E*, 92(4):042712, 2015.

[207] D. G. Hunter and B. J. Frisken. Effect of extrusion pressure and lipid properties on the size and polydispersity of lipid vesicles. *Biophysical Journal*, 74:2996–3002, 1998.

[208] E. Zaccarelli, P. J. Lu, F. Ciulla, D. A. Weitz, and F. Sciortino. Gelation as arrested phase separation in short-ranged attractive colloid-polymer mixtures. *Journal of Physics Condensed Matter*, 20:494242, 2008.

[209] C. Gögelein. *Phase Behaviour of Proteins and Colloid-Polymer Mixtures*. PhD thesis, Heinrich-Heine-Universitat Dusseldorf, 2008.

[210] B. Chung, S. Ramakrishnan, R. Bandyopadhyay, D. Liang, C. F. Zukoski, J. L. Harden, and R. L. Leheny. Microscopic dynamics of recovery in sheared depletion gels. *Physical Review Letters*, 96:228391, 2006.

[211] H. Bissig, S. Romer, L. Cipelletti, V. Trappea, and P. Schurtenberger. Intermittent dynamics and hyper-aging in dense colloidal gels. *PhysChemComm*, 6:21–23, 2003.

[212] H. Guo, S. Ramakrishnan, J. L. Harden, and R. L. Leheny. Gel formation and aging in weakly attractive nanocolloid suspensions at intermediate concentrations. *Journal of Chemical Physics*, 135:154903, 2011.

[213] E. D. Siggia. Late stages of spinodal decomposition in binary mixtures. *Physical Review A*, 20:595–605, 1979.

[214] R. Sánchez and A. Huerta. Dynamics and avalanches in a system exhibiting granular collapse. *Physica A: Statistical Mechanics and its Applications*, 437, 2015.

[215] E. Zaccarelli and W. C. K. Poon. Colloidal glasses and gels: The interplay of bonding and caging. *Proceedings of the National Academy of Sciences*, 106:15203–15208, 2009.

[216] D. El Masri, L. Berthier, and L. Cipelletti. Subdiffusion and intermittent dynamic fluctuations in the aging regime of concentrated hard spheres. *Physical Review E*, 82:031503, 2010.

[217] S. Manley, H. M. Wyss, K. Miyazaki, J. C. Conrad, V. Trappe, L. J. Kaufman, D. R. Reichman, and D. A. Weitz. Glasslike arrest in spinodal decomposition as a route to colloidal gelation. *Physical Review Letters*, 95:238302, 2005.

[218] E. Del Gado and W. Kob. A microscopic model for colloidal gels with directional effective interactions: Network induced glassy dynamics. *Soft Matter*, 6:1547–1558, 2010.

[219] O. Dauchot, G. Marty, and G. Biroli. Dynamical heterogeneity close to the jamming transition in a sheared granular material. *Physical Review Letters*, 95:265701, 2005.

[220] P. M. Reis, R. A. Ingale, and M. D. Shattuck. Caging dynamics in a granular fluid. *Physical Review Letters*, 98:188301, 2007.

[221] E. E. Ferrero, K. Martens, and J. L. Barrat. Relaxation in yield stress systems through elastically interacting activated events. *Physical Review Letters*, 113:248301, 2014.

[222] C. P. Royall and A. Malins. The role of quench rate in colloidal gels. *Faraday Discussions*, 158:301–311, 2012.

[223] S. B. Lindström, T. E. Kodger, J. Sprakel, and D. A. Weitz. Structures, stresses, and fluctuations in the delayed failure of colloidal gels. *Soft Matter*, 8:3657–3664, 2012.

[224] J. E. Martin, D. Adolf, and J. P. Wilcoxon. Viscoelasticity near the sol-gel transition. *Physical Review A*, 39:1325–1332, 1989.

[225] H. H. Winter and M. Mours. Rheology of Polymers Near Liquid-Solid Transitions. In *Neutron Spin Echo Spectroscopy Viscoelasticity Rheology*. Springer, 1997.

[226] A. Coniglio, L. De Arcangelis, E. Del Gado, A. Fierro, and N. Sator. Percolation, gelation and dynamical behaviour in colloids. *Journal of Physics Condensed Matter*, 16:S4831–S4839, 2004.

[227] A. S. Negi, C. G. Redmon, S. Ramakrishnan, and C. O. Osuji. Viscoelasticity of a colloidal gel during dynamical arrest: Evolution through the critical gel and comparison with a soft colloidal glass. *Journal of Rheology*, 58(5):1557–1579, 2014.

[228] A. Duri, D. A. Sessoms, V. Trappe, and L. Cipelletti. Resolving long-range spatial correlations in jammed colloidal systems using photon correlation imaging. *Physical Review Letters*, 102:085702, 2009.

[229] A. Mamane, C. Frétigny, F. Lequeux, and L. Talini. Surface fluctuations of an aging colloidal suspension: Evidence for intermittent quakes. *Europhysics Letters*, 88:58002, 2009.

[230] L. Cipelletti and E. R. Weeks. Glassy dynamics and dynamical heterogeneity in colloids. In *Dynamical Heterogeneities in Glasses, Colloids, and Granular Media*. Oxford University Press, 2011.

[231] R. Angelini, L. Zulian, A. Fluerasu, A. Madsen, G. Ruocco, and B. Ruzicka. Dichotomic aging behaviour in a colloidal glass. *Soft Matter*, 9:10955–10959, 2013.

[232] A. Coniglio, T. Abete, A. De Candia, E. Del Gado, and A. Fierro. Static and dynamic heterogeneities in irreversible gels and colloidal gelation. *Journal of Physics Condensed Matter*, 19:205103, 2007.

[233] P. Charbonneau and D. R. Reichman. Dynamical heterogeneity and nonlinear susceptibility in supercooled liquids with short-range attraction. *Physical Review Letters*, 99:135701, 2007.

[234] A. Zaccone, H. Wu, and E. Del Gado. Elasticity of arrested short-ranged attractive colloids: Homogeneous and heterogeneous glasses. *Physical Review Letters*, 103:208301, 2009.

[235] K. Karamdad, J. W. Hindley, G. Bolognesi, M. S. Friddin, R. V. Law, N. J. Brooks, O. Ces, and Y. Elani. Engineering thermoresponsive phase separated vesicles formed: Via emulsion phase transfer as a content-release platform. *Chemical Science*, 9:4851, 2018.

[236] L. R. Arriaga, Y. Huang, S. H. Kim, J. L. Aragones, R. Ziblat, S. A. Koehler, and D. A. Weitz. Single-step assembly of asymmetric vesicles. *Lab on a Chip*, 19(5):749–756, 2019.

[237] T. Trantidou, M. S. Friddin, A. Salehi-Reyhani, O. Ces, and Y. Elani. Droplet microfluidics for the construction of compartmentalised model membranes. *Lab on a Chip*, 18(17):2488–2509, 2018.

[238] L. R. Arriaga, E. Amstad, and D. A. Weitz. Scalable single-step microfluidic production of single-core double emulsions with ultra-thin shells. *Lab on a Chip*, 15:3335, 2015.

[239] J. Petit, I. Polenz, J. C. Baret, S. Herminghaus, and O. Bäumchen. Vesicles-on-a-chip: A universal microfluidic platform for the assembly of liposomes and polymersomes. *European Physical Journal E*, 39:59, 2016.

[240] G. T. Vladisavljević, R. Al Nuumani, and S. A. Nabavi. Microfluidic production of multiple emulsions. *Micromachines*, 8:75, 2017.

[241] S. Deshpande and C. Dekker. On-chip microfluidic production of cell-sized liposomes. *Nature Protocols*, 13:856–874, 2018.

[242] J. R. Elliott and D. A. Haydon. The interaction of n-octanol with black lipid bilayer membranes. *BBA - Biomembranes*, 557:259–263, 1979.

[243] A. H. Demond and A. S. Lindner. Estimation of interfacial tension between organic liquids and water. *Environmental Science & Technology*, 27:2318–2331, 1993.

[244] E. Karatekin, O. Sandre, H. Guitouni, N. Borghi, P. H. Puech, and F. Brochard-Wyart. Cascades of transient pores in giant vesicles: Line tension and transport. *Biophysical Journal*, 84:1734–49, 2003.

[245] F. K. Hansen and G. Rødsrud. Surface tension by pendant drop. I. A fast standard instrument using computer image analysis. *Journal of Colloid And Interface Science*, 141:1–9, 1991.

[246] H. H. Girault, D. J. Schiffrin, and B. D.V. Smith. Drop image processing for surface and interfacial tension measurements. *Journal of Electroanalytical Chemistry*, 44:723–730, 1982.

[247] A. Vian, B. Reuse, and E. Amstad. Scalable production of double emulsion drops with thin shells. *Lab on a Chip*, 18:1936, 2018.

[248] J. Y. Wang, J. Marks, and K. Y. C. Lee. Nature of interactions between PEO-PPO-PEO triblock copolymers and lipid membranes: (I) Effect of polymer hydrophobicity on its ability to protect liposomes from peroxidation. *Biomacromolecules*, 13:2624–2633, 2012.

[249] Q. T. H. Shubhra, J. Tóth, J. Gyenis, and T. Feczkó. Poloxamers for surface modification of hydrophobic drug carriers and their effects on drug delivery. *Polymer Reviews*, 54:112–138, 2014.

[250] P. Rørth. Collective cell migration. *Annual Review of Cell and Developmental Biology*, 25(1):407–429, 2009.

[251] E. Scarpa and R. Mayor. Collective cell migration in development. *Journal of Cell Biology*, 212:143, 2016.

[252] R. A. Foty and M. S. Steinberg. The differential adhesion hypothesis: A direct evaluation. *Developmental Biology*, 278:255–63, 2005.

[253] J. Lipfert, X. Hao, and N. H. Dekker. Quantitative modeling and optimization of magnetic tweezers. *Biophysical Journal*, 96:5040–5049, 2009.

[254] A. R. Bausch, F. Ziemann, A. A. Boulbitch, K. Jacobson, and E. Sackmann. Local measurements of viscoelastic parameters of adherent cell surfaces by magnetic bead microrheometry. *Biophysical Journal*, 75:2038–2049, 1998.

[255] Q. Cheng. *Characterisation of Local Mechanical Properties in Living Tissues*. PhD thesis, University of Cambridge, 2017.

[256] D. Blair and E. Dufresne. The MATLAB Particle Tracking Code Repository. *The MATLAB Particle Tracking Code Repository*, 2008.

[257] R. C. Koeller. Applications of Fractional Calculus to the Theory of Viscoelasticity. *Journal of Applied Mechanics*, 51:299–307, 1984.

[258] G. W. Scott Blair and F. M. V. Coppen. The Subjective Conception of the Firmness of Soft Materials. *The American Journal of Psychology*, 55:215–229, 1942.

[259] H. Schiessel and A. Blumen. Hierarchical analogues to fractional relaxation equations. *Journal of Physics A: Mathematical and General*, 26:5057–5069, 1993.

[260] F. Mainardi. *Fractional calculus and waves in linear viscoelasticity: An introduction to mathematical models*. Imperial College Press, 2010.

[261] H. Schiessel, R. Metzler, A. Blumen, and T. F. Nonnenmacher. Generalized viscoelastic models: Their fractional equations with solutions. *Journal of Physics A: General Physics*, 1995.

[262] D. Craiem and R. L. Magin. Fractional order models of viscoelasticity as an alternative in the analysis of red blood cell (RBC) membrane mechanics. *Physics in Medicine and Biology*, 53:4543–54, 2010.

[263] A. Bonfanti, J. Fouchard, N. Khalilgharibi, G. Charras, and A. Kabla. A unified rheological model for cells and cellularised materials. *bioRxiv*, 2019.

[264] A. J. Kim, V. N. Manoharan, and J. C. Crocker. Swelling-based method for preparing stable, functionalized polymer colloids. *Journal of the American Chemical Society*, 127:1592–1593, 2005.

[265] N. Tarantino, J. Y. Tinevez, E. F. Crowell, B. Boisson, R. Henriques, M. Mhlanga, F. Agou, A. Israël, and E. Laplantine. Tnf and il-1 exhibit distinct ubiquitin requirements for inducing NEMO-IKK supramolecular structures. *Journal of Cell Biology*, 204:231–245, 2014.

[266] J. P. Rich, J. Lammerding, G. H. McKinley, and P. S. Doyle. Nonlinear microrheology of an aging, yield stress fluid using magnetic tweezers. *Soft Matter*, 7:9933–9943, 2011.

[267] J. Colombo and E. Del Gado. Stress localization, stiffening, and yielding in a model colloidal gel. *Journal of Rheology*, 58(5):1089–1116, 2014.

[268] F. Bolton and D. Weaire. Rigidity loss transition in a disordered 2D froth. *Physical Review Letters*, 65:34449–3451, 1990.

[269] T. Gisler, R. C. Ball, and D. A. Weitz. Strain hardening of fractal colloidal gels. *Physical Review Letters*, 82:1064–1067, 1999.

[270] G. L. Hunter and E. R. Weeks. The physics of the colloidal glass transition. *Reports on Progress in Physics*, 75:066501, 2012.

[271] A. J. Holder, N. Badiei, K. Hawkins, C. Wright, P. R. Williams, and D. J. Curtis. Control of collagen gel mechanical properties through manipulation of gelation conditions near the sol-gel transition. *Soft Matter*, 14:574–580, 2018.

[272] M. Bouzid, B. Keshavarz, M. Geri, T. Divoux, E. Del Gado, and G. H. McKinley. Computing the linear viscoelastic properties of soft gels using an optimally windowed chirp protocol. *Journal of Rheology*, 62(4):1037–1050, 2018.

[273] A. H. Clark, L. Kondic, and R. P. Behringer. Particle scale dynamics in granular impact. *Physical Review Letters*, 109:238302, 2012.

[274] T. S. Majmudar and R. P. Behringer. Contact force measurements and stress-induced anisotropy in granular materials. *Nature*, 435:1079–1082, 2005.

[275] A. H. Clark, A. J. Petersen, L. Kondic, and R. P. Behringer. Nonlinear force propagation during granular impact. *Physical Review Letters*, 114:144502, 2015.

[276] F. W. Starr, J. F. Douglas, and S. Sastry. The relationship of dynamical heterogeneity to the Adam-Gibbs and random first-order transition theories of glass formation. *Journal of Chemical Physics*, 138(12):12A541, 2013.

[277] I Giaever and C R Keese. Monitoring fibroblast behavior in tissue culture with an applied electric field. *Proceedings of the National Academy of Sciences of the United States of America*, 81:3761–3764, 1984.

[278] P. Mitra, C. R. Keese, and I. Giaever. Electric measurements can be used to monitor the attachment and spreading of cells in tissue culture. *BioTechniques*, 11:504–511, 1991.

[279] I. Giaever and C. R. Keese. A morphological biosensor for mammalian cells. *Nature*, 366:591–592, 1993.